Evolution of carbon-enhanced metal-poor stars originating from mass transfer in stellar binaries

Dissertation
zur
Erlangung des Doktorgrades (Dr. rer. nat.)
der
Mathematisch-Naturwissenschaftlichen Fakultät
der
Rheinischen Friedrich-Wilhelms-Universität Bonn

von
Elvijs Matrozis
aus
Liepaja, Lettland

Bonn, 19.10.2017

Dieser Forschungsbericht wurde als Dissertation von der Mathematisch-Naturwissenschaftlichen Fakultät der Universität Bonn angenommen und ist auf dem Hochschulschriftenserver der ULB Bonn http://hss.ulb.uni-bonn.de/diss_online elektronisch publiziert.

1. Gutachter:	Dr. Richard J. Stancliffe
2. Gutachter:	Prof. Dr. Norbert Langer
Tag der Promotion:	02.02.2018
Erscheinungsjahr:	2018

Abstract

As the hydrogen and helium created shortly after the Big Bang is gradually processed into heavier elements by successive generations of stars, the overall metal content of the Universe increases. Metal-poor stars which, owing to their low mass, evolve slowly and have ages comparable to the age of the Universe are thus relics of the earliest stellar generations, and recent decades have seen dedicated efforts to discover these stars in ever greater numbers. An unexpected outcome of these efforts is the discovery that a large fraction of these stars are rich in carbon compared to the Sun.

These carbon-enhanced metal-poor (CEMP) stars are a chemically diverse population, and this work concerns the evolution of CEMP stars rich in elements produced by slow neutron capture nucleosynthesis (CEMP-*s* stars), which are believed to have originated from accreting chemically enriched material from a binary companion in a thermally pulsing asymptotic giant branch (AGB) stage. As such, CEMP-*s* stars are commonly used to test models of metal-poor AGB stars, an important contributor to the chemical evolution of the Universe.

The evolution of CEMP-*s* stars is modelled from the zero-age main sequence through the accretion phase and up to the end of the red giant branch with an updated version of the STARS stellar evolution code. Particular attention is paid to the evolution of the surface chemical composition of CEMP-*s* stars, which is shown to be modified following mass transfer as a result of the competition between various mixing processes taking place within these stars. The mixing processes considered here in detail are thermohaline convection, atomic diffusion, and rotational mixing. Thermohaline convection dilutes the transferred material by rapidly (compared to the main sequence lifetime) mixing it with the material originally present in the star. As a result, the accreted material is diluted by a factor from two to more than ten depending mostly on how much mass is accreted. Atomic diffusion, and radiative forces in particular, accelerate different chemical elements discriminately and tend to make the surface layers of CEMP-*s* stars poor in carbon but rich in other metals like iron. This is at odds with observations and suggests that some other process is actively counteracting atomic diffusion. It is then demonstrated that this other process could be the turbulent mixing arising in rotating CEMP-*s* stars. At surface rotation velocities consistent with those observed, atomic diffusion is found to have little effect on the chemical composition of the surface of CEMP-*s* stars as a result.

It is also found that the amount of mass that can be accreted by the progenitors of CEMP-*s* and related stars may be limited by the angular momentum content of the transferred material. In particular, explaining the most chemically enriched stars, which have likely accreted the most mass, may require that the material loses most of its angular momentum during the accretion. The rotation velocities observed in CEMP-*s* stars are also suggestive of angular momentum loss, either during the accretion or the evolution following mass transfer.

Contents

CHAPTER 1

Introduction

Carbon-enhanced metal-poor stars are some of the oldest stars in the local Universe. The carbon-enhanced metal-poor stars rich in chemical elements produced by slow neutron capture nucleosynthesis are believed to originate from mass transfer in stellar binary systems. These are the stars whose evolution this thesis is concerned with. Because of their age and origin, these stars allow us to probe a wide range of astrophysical topics. Among them are the evolution of low-mass stars, the chemical evolution of our Galaxy, the evolution and interaction of binary stars, neutron capture nucleosynthesis of the first asymptotic giant branch stars, and physical mechanisms leading to chemical mixing in stars.

1.1 Evolution of low-mass stars

Stars are massive balls of gas held together by gravity that sustain themselves by nuclear fusion reactions. Stars form when giant molecular gas clouds, consisting mostly of hydrogen and helium, become unstable and undergo gravitational collapse. Many different fragments of these giant gas clouds locally contract until the temperature and density in the cores of these fragments rises sufficiently to ignite nuclear fusion of hydrogen. At that moment a star is born, and many (hundreds of) thousands of stars can form out of a single molecular cloud.

The fusion of hydrogen liberates energy and establishes an equilibrium between the gravitational force, which tends to compress the star, and pressure gradient forces, which tend to expand it. The subsequent evolution of a star is a constant struggle to maintain this equilibrium. The outcome of this struggle depends crucially on the mass of the star. Single stars more massive than about eight solar masses end their lives as core collapse supernovae and are typically referred to as massive stars. This thesis instead concerns the evolution of stars of lower mass, which are much more numerous and longer-lived, and we begin by reviewing the basic stages of their evolution. The following applies, with some caveats, to single stars with masses between about a half and eight solar masses (at solar-like chemical composition).

1.1.1 From the zero-age main sequence to the asymptotic giant branch

When the central temperature and density of the contracting object reach values sufficient for hydrogen fusion, the star is said to have reached the zero-age main sequence (ZAMS). Thus begins the longest phase of the evolution (lasting about 90% of the total lifetime) known as the main sequence, during which the surface temperature and the brightness of the star change relatively little. Hence, in a diagram of luminosity versus effective temperature (the Hertzsprung-Russell diagram; Fig. 1.1) most stars lie along

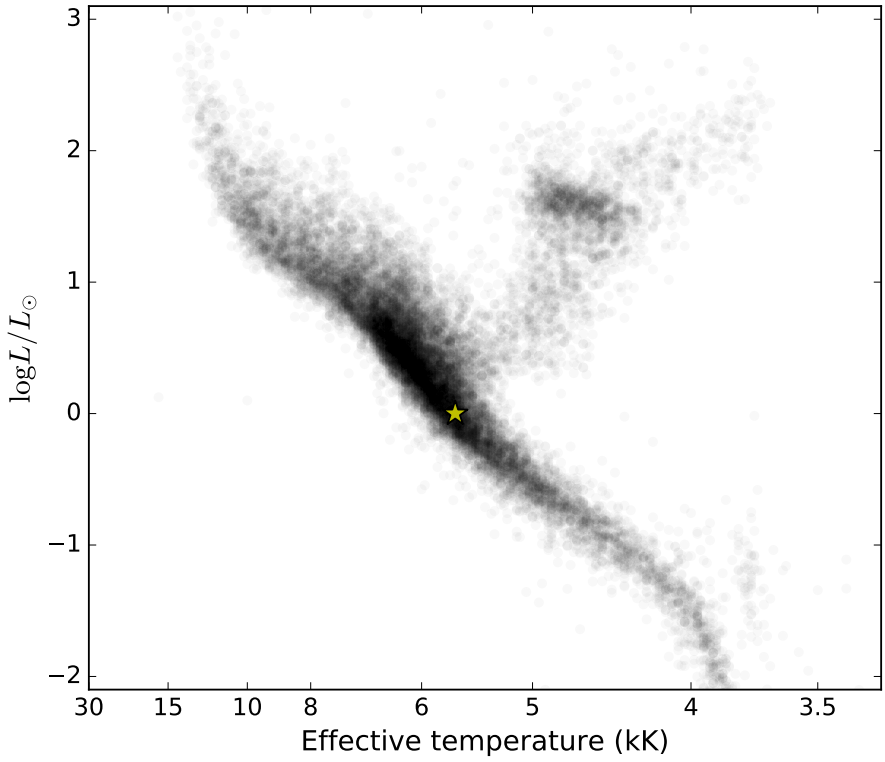

Figure 1.1: The Hertzsprung-Russell diagram of about 17000 stars observed by the Hipparcos satellite (ESA, 1997). The diagonal strip running from the bottom right (less massive stars) to the top left (more massive stars) is the main sequence. The stars to the upper right of the main sequence are red giants. The over-density of stars close to $\log L/L_\odot = 2$ and $T_{\rm eff} = 5000$ K is the horizontal branch. The position of the Sun is marked by the yellow star.

this (main) sequence. On the main sequence the star is supported by the energy released from converting its hydrogen into helium. There are two main channels by which this conversion happens.

In the lowest mass stars ($M \lesssim 1.5\ M_\odot$) the helium production occurs mainly via the proton-proton (pp) chains. These are series of reactions initiated by the fusion of two protons (^{1}H):

$$\begin{aligned} {}^1\mathrm{H} + {}^1\mathrm{H} &\rightarrow {}^2\mathrm{H} + e^+ + \nu_e \\ {}^2\mathrm{H} + {}^1\mathrm{H} &\rightarrow {}^3\mathrm{He} + \gamma \\ {}^3\mathrm{He} + {}^3\mathrm{He} &\rightarrow {}^4\mathrm{He} + {}^1\mathrm{H} + {}^1\mathrm{H}. \end{aligned} \tag{1.1}$$

In this ppI chain the first two steps have to occur twice to produce one ^{4}He nucleus out of four protons. Alternatively, the ^{3}He nucleus can also fuse with a ^{4}He nucleus to yield ^{7}Be:

$$ {}^3\mathrm{He} + {}^4\mathrm{He} \rightarrow {}^7\mathrm{Be} + \gamma, \tag{1.2}$$

which opens up two alternative branches along which the burning can proceed. These are the ppII:

$$\begin{aligned} {}^7\mathrm{Be} + e^- &\rightarrow {}^7\mathrm{Li} + \nu_e \\ {}^7\mathrm{Li} + {}^1\mathrm{H} &\rightarrow {}^4\mathrm{He} + {}^4\mathrm{He}, \end{aligned} \tag{1.3}$$

and the ppIII chains:

$$\begin{aligned} {}^{7}\mathrm{Be} + {}^{1}\mathrm{H} &\rightarrow {}^{8}\mathrm{B} + \gamma \\ {}^{8}\mathrm{B} &\rightarrow {}^{8}\mathrm{Be} + e^{+} + \nu_e \\ {}^{8}\mathrm{Be} &\rightarrow {}^{4}\mathrm{He} + {}^{4}\mathrm{He}. \end{aligned} \tag{1.4}$$

The energies released in the different chains range from 19.6 MeV (ppIII) to 26.5 MeV (ppI) per helium nucleus as a result of the different fractions of energy carried away by neutrinos. As the mass of the star (and thus its central temperature) is increased, the contribution of the ppI chain declines and that of the ppIII chain increases.

In stars more massive than about 1.5 $M_\odot$ the central temperatures reach high enough values ($T \gtrsim 20$ MK) that another channel takes over the helium production. This is the CNO cycle, which can also have branchings. The CNO-I (or CN) cycle is made up by this chain of reactions:

$$\begin{aligned} {}^{12}\mathrm{C} + {}^{1}\mathrm{H} &\rightarrow {}^{13}\mathrm{N} + \gamma \\ {}^{13}\mathrm{N} &\rightarrow {}^{13}\mathrm{C} + e^{+} + \nu_e \\ {}^{13}\mathrm{C} + {}^{1}\mathrm{H} &\rightarrow {}^{14}\mathrm{N} + \gamma \\ {}^{14}\mathrm{N} + {}^{1}\mathrm{H} &\rightarrow {}^{15}\mathrm{O} + \gamma \\ {}^{15}\mathrm{O} &\rightarrow {}^{15}\mathrm{N} + e^{+} + \nu_e \\ {}^{15}\mathrm{N} + {}^{1}\mathrm{H} &\rightarrow {}^{12}\mathrm{C} + {}^{4}\mathrm{He}. \end{aligned} \tag{1.5}$$

Once every thousand reactions or so the last reaction can instead produce ^{16}O, which starts starts the CNO-II (or ON) cycle:

$$\begin{aligned} {}^{15}\mathrm{N} + {}^{1}\mathrm{H} &\rightarrow {}^{16}\mathrm{O} + \gamma \\ {}^{16}\mathrm{O} + {}^{1}\mathrm{H} &\rightarrow {}^{17}\mathrm{F} + \gamma \\ {}^{17}\mathrm{F} &\rightarrow {}^{17}\mathrm{O} + e^{+} + \nu_e \\ {}^{17}\mathrm{O} + {}^{1}\mathrm{H} &\rightarrow {}^{14}\mathrm{N} + {}^{4}\mathrm{He}. \end{aligned} \tag{1.6}$$

Some CNO processing will also occur in lower mass stars in which the main energy source is one of the pp chains. In fact, the conversion of ^{12}C into ^{14}N occurs at lower temperatures than the fusion of two protons. The slowest of the reactions is $^{14}\mathrm{N}(^{1}\mathrm{H}, \gamma)^{15}\mathrm{O}$. This means that in an equilibrium, where the production rate of each nucleus equals its destruction, the abundance of ^{14}N must be larger than that of ^{12}C and ^{16}O. Note that the CNO nuclei play the role of catalysts in these reactions: their total number is not changed during the CNO cycle.

The main sequence ends when the star exhausts the hydrogen supply (comprising about 70% by mass originally) in its central regions. The lack of energy release means that gravity takes over, so the central regions contract and heat up. This enables nuclear burning to transition to a shell surrounding the centre. As this shell converts hydrogen into helium, it moves outward in mass, leaving behind a helium core.[1] While the layers below the burning shell continue contracting, the layers above the shell expand and become convective. The star becomes cool and luminous as it moves up the red giant branch (RGB; Fig. 1.2a). Meanwhile, the outer convective region gradually moves inwards in mass, bringing helium-

[1] This applies to stars like the Sun, in which the energy from the central regions is carried away by radiation. Stars slightly more massive than the Sun instead have convective cores in which material is efficiently mixed. At the end of their main sequence evolution such stars already have distinct helium cores. Nevertheless, in these stars too the burning transitions to a shell around this hydrogen-exhausted core.

and nitrogen-enriched material to the surface of the star during a phase known as first dredge-up (FDU; Fig. 1.2b). FDU stops when the envelope is forced outwards by the advancing burning shell.

The next lightest element available for burning is helium. But because of the short lifetime of the ^{8}Be nucleus, the next stable and accessible isotope is ^{12}C. The production of carbon from helium thus requires two reactions to occur in rapid succession:

$$\begin{aligned} {}^{4}\mathrm{He} + {}^{4}\mathrm{He} &\rightleftarrows {}^{8}\mathrm{Be} \\ {}^{8}\mathrm{Be} + {}^{4}\mathrm{He} &\rightarrow {}^{12}\mathrm{C} + \gamma. \end{aligned} \tag{1.7}$$

This so-called 3α reaction requires very high temperatures ($T \simeq 80$ MK), and the hydrogen-free core needs to grow sufficiently massive ($M_{\mathrm{c}} \simeq 0.48\ M_{\odot}$) to attain them. Until that point the star continues climbing the RGB.

The RGB terminates when the 3α reaction begins converting helium into carbon in the core. In stars with initial mass $M \gtrsim 2.3\ M_{\odot}$ this is a rather seamless transition. But in lower mass stars the core is largely degenerate at the onset of helium burning. The temperature increases but the core does not expand, because the pressure of a degenerate electron gas does not depend on temperature. This leads to a runaway increase in the burning rate in an event known as a core helium flash. This finally lifts the degeneracy, and the core expands and cools, which reduces the temperature (and thus luminosity) of the hydrogen burning shell. The star as a whole contracts and settles onto the horizontal branch (Fig. 1.2a).

During the horizontal branch evolution, much of the produced carbon is further processed into oxygen via

$$ {}^{12}\mathrm{C} + {}^{4}\mathrm{He} \rightarrow {}^{16}\mathrm{O} + \gamma. \tag{1.8}$$

Once helium is exhausted in the core, the star consists of an inert CO core surrounded by a layer of almost pure helium, and a hydrogen-rich envelope on top of it. Nuclear burning proceeds in a helium shell around the CO core and in a hydrogen shell around the helium core (Fig. 1.3). Transition to shell-burning again forces the outer layers to expand, and the star once more becomes a cool giant (Fig. 1.2a). This is known as the asymptotic giant branch stage, for which a more detailed introduction is warranted owing to its particular significance to carbon-enhanced metal-poor stars.

1.1.2 The asymptotic giant branch and thermal pulses

Early on during the asymptotic giant branch (AGB) evolution the helium shell provides most of the total luminosity. However, as the helium shell burns through its fuel, it becomes thinner and eventually experiences what is known as the thin-shell instability (Schwarzschild and Härm, 1965; Yoon, Langer and van der Sluys, 2004). As a result of this instability, the helium shell expands but heats up in the process. This increases the burning rate in the shell, which further raises the temperature. The result is a thermonuclear runaway.

In what is known as a thermal pulse, the sudden large energy release drives a convection zone throughout much of the intershell (Fig. 1.4). The energy released during a thermal pulse (with luminosity momentarily reaching $\log L_{\mathrm{He}}/L_{\odot} \simeq 4$–$9$, depending on stellar mass and pulse number; Stancliffe, Tout and Pols, 2004) does not reach the surface of the star but instead goes into expanding the intershell and the layers above it. This expansion reduces the temperature in the hydrogen shell sufficiently for it to shut down. It also expands the helium shell sufficiently for it to no longer be subject to the thin-shell instability. The temperature in the helium shell drops (and hence the energy generation within it), and the intershell convection zone disappears. Helium burning proceeds quiescently under radiative conditions.

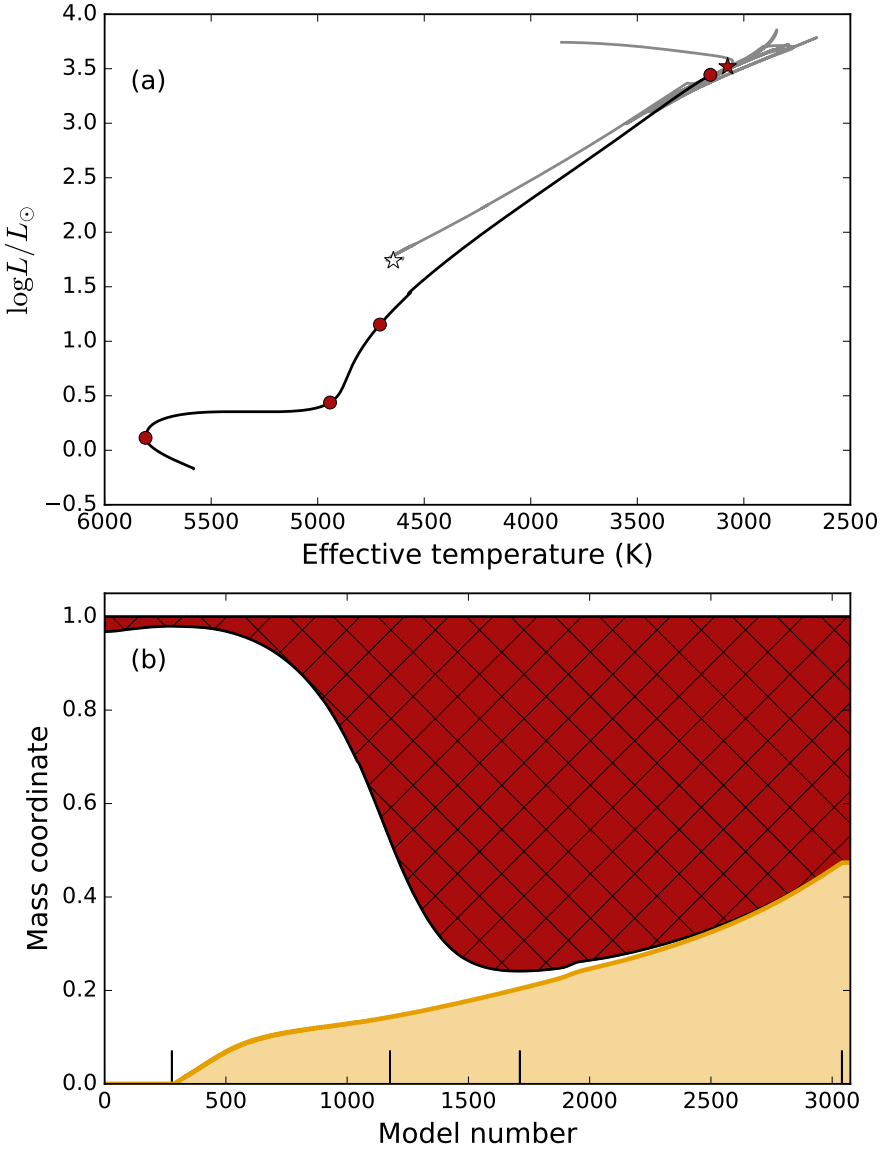

Figure 1.2: (a) The evolution of a star with a mass of one solar mass and solar-like chemical composition in the Hertzsprung-Russell diagram. Evolution from the zero-age main sequence (ZAMS) to the end of the red giant branch (RGB) is in black, and the evolution following the core helium flash is in grey. (b) The internal evolution from the ZAMS to the end of the RGB. The model number serves as a proxy for the age of the star. Mass coordinate of zero (one) corresponds to the centre (surface) of the star. The red hatched region shows layers that are convective. The orange line shows the hydrogen burning shell, and the shaded region below it shows the growth of the helium core. The four ticks along the bottom x axis correspond to the four red dots in panel (a) and mark, in order, the main sequence turn-off (maximum effective temperature), the beginning of first dredge-up, the end of first dredge-up, and the end of the RGB. The empty and filled stars indicate, respectively, the horizontal branch and the onset of thermal pulses.

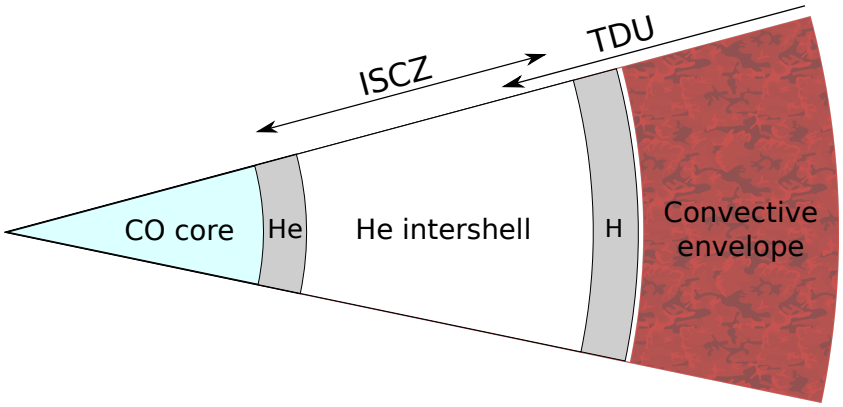

Figure 1.3: Schematic structure of an asymptotic giant branch star. From the centre outwards, the star consists of an inert carbon-oxygen core, a helium burning shell, a layer of mostly helium (intershell), a hydrogen burning shell, and a convective envelope consisting of mostly hydrogen. The approximate extent of the intershell convection zone (ISCZ) during a thermal pulse and the depth of the envelope during third dredge-up (TDU) are also sketched.

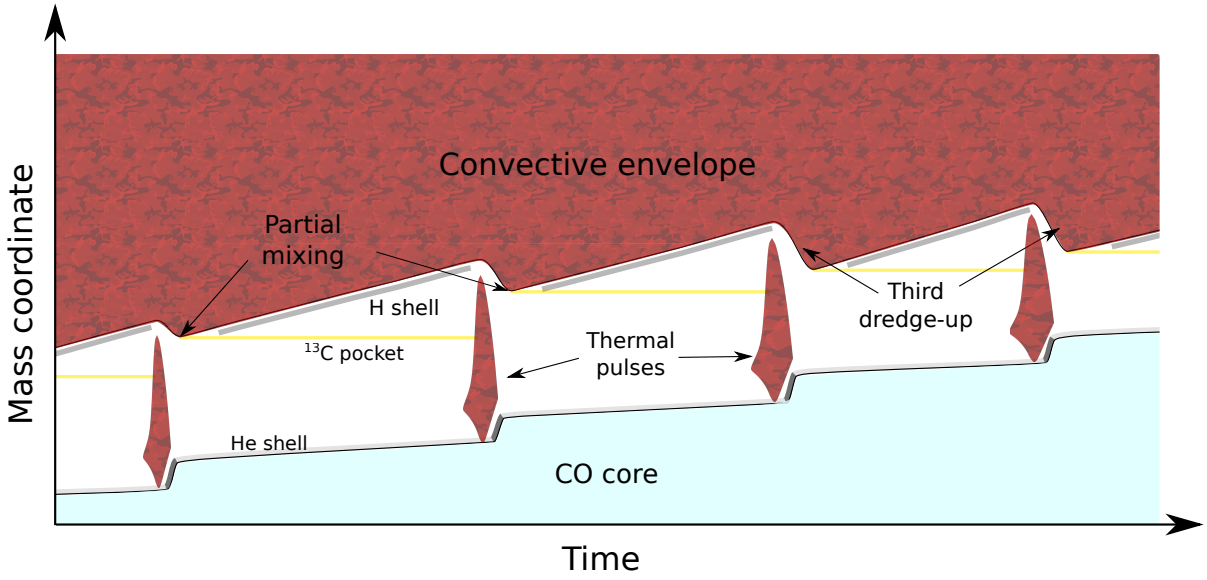

Figure 1.4: Schematic illustration of the evolution of a star during the thermally pulsing asymptotic giant branch (TP-AGB) stage. The star alternates between predominantly hydrogen and helium shell burning phases. The ignition of the helium shell triggers an intershell convection zone that efficiently mixes the intershell region. The extinguishing of the hydrogen shell allows the convective envelope to penetrate inwards in mass, leading to dredge-up of the intershell material. At the deepest point reached by the envelope partial mixing of protons into the radiative region results in the creation of a "^{13}C pocket" (see Sect. 1.1.5).

The cooling resulting from the expansion during a thermal pulse also increases the opacity near the base of the convective envelope, which causes the envelope to move inwards in mass. If the envelope moves into a region that was homogenised during the thermal pulse by the intershell convection zone, helium-burning products (chiefly carbon) are brought to the surface of the star. This mixing episode is known as third dredge-up (TDU).

Following a thermal pulse the star contracts, which heats up the intershell and reignites the hydrogen shell. The luminosity of the star is then provided almost entirely by the hydrogen shell, which leaves its ashes, i.e. helium, on top of the intershell. The hydrogen shell, due to its much greater luminosity ($\log L_{\mathrm{H}}/L_{\mathrm{He}} \gtrsim 3$), now burns through its material faster than the helium shell. As burning proceeds and the intershell becomes more massive, it and the helium shell at its base get increasingly compressed. Eventually, the helium shell again undergoes the thin-shell instability, triggering the next thermal pulse. This sequence of alternating shell-burning episodes is the thermally pulsing AGB (TP-AGB) stage (Iben and Renzini, 1983; Herwig, 2005; Karakas and Lattanzio, 2014).

During most of the TP-AGB stage (the interpulse phases) the luminosity is provided by the hydrogen shell. The helium-burning phases are comparatively short (about 100 yr versus about 10^4 yr; Karakas and Lattanzio, 2014), but they get more energetic and frequent with time (Straniero, Chieffi, Limongi et al., 1997; Stancliffe et al., 2004; Weiss and Ferguson, 2009).

1.1.3 Mass loss and termination of the AGB evolution

The TP-AGB stage cannot continue indefinitely. The helium-exhausted core will collapse into a neutron star once it reaches the Chandrasekhar mass (Ritossa, García-Berro and Iben, 1999; Doherty, Gil-Pons, Siess et al., 2015). But this may happen only in the most massive AGB stars (initial $M \gtrsim 8\ M_{\odot}$), if at all. Normally, the evolution is terminated much earlier by mass loss.

Early on during the AGB evolution the mass-loss rates are fairly low ($\dot{M} \lesssim 10^{-8}\ M_{\odot}\,\mathrm{yr}^{-1}$). But as the stars become cooler and more luminous, their mass-loss rates increase by many orders of magnitude (Vassiliadis and Wood, 1993). While mass loss from cool stars is a poorly understood phenomenon and its description usually relies on empirical relations (Willson, 2000), dust formation in the increasingly cool and extended atmospheres of AGB stars is believed to play a crucial role. Dust absorbs radiation very effectively, and the mass-loss rates increase because the gas is dragged along with the dust away from the star.

Dust-driven mass loss depends on the molecular species in the atmosphere. Particularly, the ratio between carbon and oxygen atoms plays a crucial role because the kind of molecular species present (and thus the opacity) changes as the C/O ratio crosses unity. The reason is the high binding energy of the CO molecule (Marigo, 2002), which means that either all of the carbon (C/O < 1) or all of the oxygen (C/O > 1) will be locked up in carbon monoxide. The remaining carbon or oxygen can go on to form other molecules (e.g. CN, C_2 and CH when C/O > 1). Stars begin their lives as oxygen-rich, i.e. C/O < 1. But with each TDU the carbon abundance in the envelope increases (at least in AGB stars with initial masses below about $4\ M_{\odot}$). Once C/O exceeds unity, the chemistry of the atmosphere becomes carbon-dominated, which leads to a reduction in the effective temperature by about 300 K (Marigo, 2002). Since the mass-loss rates are very temperature sensitive (empirically $\dot{M} \propto T_{\mathrm{eff}}^{-6.5}$; Wachter, Schröder, Winters et al., 2002; van Loon, Cioni, Zijlstra et al., 2005), such a change accelerates the mass-loss rates up to almost $10^{-4}\ M_{\odot}\,\mathrm{yr}^{-1}$ (Vassiliadis and Wood, 1993; Ramstedt and Olofsson, 2014). At such high rates the stars lose the remaining envelope after a few thermal pulses (some tens of thousands of years), exposing the hydrogen exhausted core (van Winckel, 2003). Having lost the envelope, the stars become white dwarfs within a few (tens of) thousands of years (Miller Bertolami, 2016).

The remnant masses are typically $M < 1\ M_{\odot}$ (Catalán, Isern, García-Berro et al., 2008; Salaris,

Serenelli, Weiss et al., 2009). Most of the difference between the remnant and initial masses (which can be multiple solar masses) is returned to the interstellar medium during the TP-AGB stage via slow ($v_{\rm w} \simeq 5$–$20\ {\rm km\,s^{-1}}$; Vassiliadis and Wood, 1993; Goldman, van Loon, Zijlstra et al., 2017) wind mass loss. From this material, which has likely undergone substantial nuclear processing (Sect. 1.1.5), the next generation of stars can form (Sect. 1.1.6).

1.1.4 Neutron capture nucleosynthesis

Stars support themselves against gravity by releasing energy via nuclear fusion reactions involving multiple charged particles. When a fuel is exhausted, gravity temporarily takes over until the central regions contract and heat up sufficiently to enable the ignition of the ashes of the previous burning stage. So far the fusion of successively heavier nuclei up to oxygen has been described. In massive stars still heavier nuclei are fused, until their cores consist of iron. Proceeding further is impossible, because the binding energy per nucleon peaks around ^{56}Fe, which means that further fusion reactions require a net input of energy. The star can no longer resist gravity, and the outcome is gravitational collapse.

Production of the chemical elements located beyond iron in the periodic table occurs by a different kind of nucleosynthesis – neutron capture. Neutron capture nucleosynthesis operates as follows. An element (Z, A) with atomic number Z and mass number A captures a neutron, which increases its mass number by one:

$$(Z, A) + n^0 \rightarrow (Z, A + 1) + \gamma. \tag{1.9}$$

At some point (say, after capturing k neutrons) the resulting nucleus is unstable and can undergo β-decay:

$$(Z, A + k) \rightarrow (Z + 1, A + k) + e^- + \bar{\nu}_e. \tag{1.10}$$

The element $(Z + 1, A + k)$ can go on to capture neutrons and eventually decay to element with atomic number $Z + 2$, and so on.

Whether the unstable isotope $(Z, A + k)$ actually decays depends crucially on the availability of neutrons. When the density of neutrons is low, β decays can generally occur before the isotope encounters another neutron. On the other hand, when the neutron density is sufficiently high, the isotope may capture another neutron before it decays, and then another, and so on until a point where the binding energy of the next neutron is negative (thus reaching a limit known as the neutron drip line), at which point the then very neutron-rich isotope must β-decay (Meyer, 1994). In either case, dependence on temperature is low, because neutrons are electrically neutral and thus there is no Coulomb barrier to overcome.

The case of low neutron densities, where the timescales of β decays are typically shorter than those of neutron captures, is known as the slow (or *s*-) process nucleosynthesis. The case of high neutron densities, where nucleosynthesis proceeds near the neutron drip line, is known as the rapid (or *r*-) process nucleosynthesis. In more quantitative terms, the *s*-process takes place at neutron number densities around $10^7\ {\rm cm^{-3}}$ (Busso, Gallino and Wasserburg, 1999), whereas the *r*-process requires densities in excess of $10^{20}\ {\rm cm^{-3}}$ (Wehmeyer, Pignatari and Thielemann, 2015). The distribution of elements in the solar system bears the signature of both processes (Seeger, Fowler and Clayton, 1965; Anders and Grevesse, 1989). Some elements are almost exclusively created in the *s*-process (such as barium, lead, strontium), whereas others (such as europium, platinum, gold) are produced in the *r*-process (Arlandini, Käppeler, Wisshak et al., 1999). Given the very different conditions of the *s*- and *r*-processes, the main production sites of these elements are likely different, although they are yet to be fully localised. The high neutron densities of the *r*-process imply violent conditions, and core-collapse supernovae (Woosley, Wilson, Mathews et al., 1994; Takahashi, Witti and Janka, 1994; Fryer, Herwig, Hungerford et al., 2006; Winteler, Käppeli, Perego et al., 2012) and mergers of neutron stars (Eichler, Livio, Piran et al., 1989; Freiburghaus,

Rosswog and Thielemann, 1999; Korobkin, Rosswog, Arcones et al., 2012) have been proposed as possible sites for the *r*-process. The *s*-process is believed to mainly take place in AGB stars during the thermally pulsing phase (Gallino, Busso, Picchio et al., 1988; Gallino, Arlandini, Busso et al., 1998; Käppeler, Gallino, Bisterzo et al., 2011).

1.1.5 Neutron capture nucleosynthesis in AGB stars

As illustrated in Sect. 1.1.2, repeated episodes of TDU should enrich the convective envelope of TP-AGB stars in material subjected to nuclear processing during hydrogen and helium burning. This is mainly helium and carbon, but (some isotopes of) other elements like fluorine, sodium, and neon are also expected to be produced in energetically less important reactions (Stancliffe and Glebbeek, 2008; Karakas, 2010). Beyond these light elements, AGB stars are also believed to be responsible for much of the *s*-process content of the Universe (Arlandini et al., 1999; Travaglio, Galli, Gallino et al., 1999; Travaglio, Gallino, Arnone et al., 2004; Nomoto, Kobayashi and Tominaga, 2013; Bisterzo, Travaglio, Gallino et al., 2014).

The first direct evidence of neutron capture nucleosynthesis occurring in AGB stars was the detection of technetium by Merrill (1952) in some evolved giants. Technetium ($Z = 43$) has no stable isotopes. The isotope produced during the *s*-process (^{99}Tc) has a half-life of about 0.2 Myr, which is much shorter than the main sequence lifetime, and hence any initial abundance of technetium would have long since disappeared. This means that the element must have been synthesised relatively recently by the star itself. At the same time, the decay time is much longer than the interpulse period, so any technetium produced deep inside the star and brought up to the surface during a TDU can be expected to be still detectable.

Producing neutron capture elements such as technetium requires neutrons. Free neutrons decay into protons in about fifteen minutes and thus are generally not present in stars. Therefore, some reaction has to take place in AGB stars that releases them. In the context of the *s*-process, two such reactions have been identified (Cameron, 1955; Cameron, 1960). These are

$$^{13}\mathrm{C} + {}^{4}\mathrm{He} \rightarrow {}^{16}\mathrm{O} + n^{0}, \tag{1.11}$$

$$^{22}\mathrm{Ne} + {}^{4}\mathrm{He} \rightarrow {}^{25}\mathrm{Mg} + n^{0}. \tag{1.12}$$

The high temperatures needed for an efficient activation of the ^{22}Ne reaction ($T > 300$ MK) largely limit its relevance to massive AGB stars ($M \gtrsim 4\ M_{\odot}$), as well as massive stars during helium and carbon burning (Couch, Schmiedekamp and Arnett, 1974; Lamb, Howard, Truran et al., 1977; Raiteri, Gallino, Busso et al., 1993). Moreover, in TP-AGB stars it only activates during a thermal pulse, so the neutron exposures are low, and only lighter *s*-process elements like strontium and zirconium ($Z \simeq 40$) are produced in abundance. The ^{13}C source is believed to operate in lower mass AGB stars ($M \lesssim 4\ M_{\odot}$) and produce neutrons for most of the interpulse period. Hence, although the neutron density is lower, the time-integrated neutron fluxes are larger (Busso, Gallino, Lambert et al., 2001), which allows the *s*-process to proceed all the way up to nuclei like lead and bismuth ($Z \simeq 80$).

^{13}C is produced via $^{12}\mathrm{C}(^{1}\mathrm{H}, \gamma)^{13}\mathrm{N}(\beta^{+})^{13}\mathrm{C}$. The intershell is rich in ^{12}C, but devoid of protons. Some ^{13}C is produced in the hydrogen burning shell, but any neutrons released there by burning ^{13}C would just be captured by ^{14}N, which has a much greater abundance and a very large neutron capture cross-section. Hence, what one requires to produce the heavy elements is that there are some protons present in the intershell, but not enough for the CN cycle to proceed to equilibrium. These protons are believed to mix into the intershell at the end of TDU ("partial mixing", Fig. 1.4) but how to achieve this self-consistently and produce large quantities of *s*-process elements is an unsolved problem (Herwig, 2000; Herwig, Langer and Lugaro, 2003; Piersanti, Cristallo and Straniero, 2013; Denissenkov and Tout, 2003). Current

predictions of the resulting *s*-process output rely on artificial insertion of a small number of protons in a model after a TDU, which results in a "^{13}C pocket" at the deepest point reached by the convective envelope during TDU (Fig. 1.4; Busso et al., 2001; Straniero, Cristallo and Gallino, 2009; Karakas, 2010; Bisterzo, Gallino, Straniero et al., 2010; Bisterzo et al., 2014). During a thermal pulse, the intershell convection zone engulfs the region where the pocket is (or was) located, and the *s*-process elements can then be dredged to the surface during the next TDU episode. Naturally, the expected yields of the *s*-process elements depend somewhat on the structure and mass of the pocket.

1.1.6 Stellar metallicity, metal-poor stars and Galactic chemical evolution

Other than the initial mass, the metallicity (or chemical composition in general) of a star is the other major factor that hugely influences its evolution. The chemical composition of a star determines the opacity of stellar material, and thus also the structure of the star. It can determine which nucleosynthesis processes operate. As an extreme example, note the catalytic nature of the CNO nuclei in the CNO cycle – in hydrogen fusion via the CNO cycle the total number of CNO nuclei does not change. In the nearly metal-free first stars hydrogen burning thus must have occurred via the pp chains in stars of all masses because of the absence of CNO nuclei. Mass loss and internal transport processes also depend on the chemical composition.

There are two quantities that are often referred to as the metallicity of the star. To theorists, the metallicity of a star usually means the fraction of total mass made up by elements other than hydrogen (X) and helium (Y):

$$Z = 1 - X - Y. \tag{1.13}$$

According to standard cosmology, the Universe was initially nearly free of metals ($Z \approx 0$), consisting of only hydrogen ($X \approx 0.75$) and helium ($Y \approx 0.25$; Cyburt, Fields, Olive et al., 2016). For observers, using spectroscopic methods, measuring the total metallicity Z is impossible. For one, spectroscopy only probes the region of the star where the escaping radiation is formed. This is the photosphere of the star. Moreover, many abundant elements, including helium, are very difficult to measure. As a result, even the total metal content of the Sun is rather uncertain with older studies finding $Z \approx 0.02$ (Anders and Grevesse, 1989; Grevesse and Sauval, 1998) and newer studies arguing for $Z \approx 0.014$ (Lodders, 2003; Asplund, Grevesse, Sauval et al., 2009; Scott, Grevesse, Asplund et al., 2015b; Scott, Asplund, Grevesse et al., 2015a; Grevesse, Scott, Asplund et al., 2015).

Observers thus use iron as a proxy of the total metallicity. This element is responsible for a large number of spectral lines, making its abundance relatively easy to measure, and its abundance in young stars should reflect the initial, presumably homogeneous, composition of the star. The other definition of metallicity of a star is thus a measure of its surface iron content compared to the Sun:

$$[\mathrm{Fe/H}] = \log\left(\frac{N_{\mathrm{Fe}}}{N_{\mathrm{H}}}\right) - \log\left(\frac{N_{\mathrm{Fe}}}{N_{\mathrm{H}}}\right)_{\odot}, \tag{1.14}$$

where N is the number fraction of the element. For stars on the zero-age main sequence the two metallicities are related by

$$[\mathrm{Fe/H}] = \log\left(\frac{Z}{X}\right) - \log\left(\frac{Z}{X}\right)_{\odot} \approx \log\left(Z/Z_{\odot}\right). \tag{1.15}$$

The bracket notation is used to express the abundances of other elements as well:

$$[\mathrm{A/B}] = \log\left(\frac{N_\mathrm{A}}{N_\mathrm{B}}\right) - \log\left(\frac{N_\mathrm{A}}{N_\mathrm{B}}\right)_\odot . \tag{1.16}$$

By definition, all [A/B] of the Sun are 0. Stars with [Fe/H] < 0 are deficient in metals and stars with [Fe/H] < -1 are usually referred to as metal-poor. Elements with [A/Fe] > 0 are enhanced or over-abundant. Elements with [A/Fe] < 0 are under-abundant.

As noted, the Universe was initially nearly metal-free. The formation of the first stars irrevocably changed this, and over time more and more of the primordial hydrogen is converted into heavier elements by successive generations of stars. This astrated material is then returned back to the interstellar medium from which the next generation of slightly more metal-rich stars form. Due to their age, surviving metal-poor stars allow a wide range of astrophysically important questions to be investigated, like the nature of the first stars, the formation and chemical evolution history of the Galaxy, the production of light elements (Li, Be) shortly after the Big Bang, and stellar nucleosynthesis at low metallicity (this is by no means an exhaustive list, see Beers and Christlieb, 2005; Frebel and Norris, 2015, and references therein).

1.2 Binary stars

The majority of stars are members of multiple star systems (Duquennoy and Mayor, 1991; Raghavan, McAlister, Henry et al., 2010). In the simplest (and probably most common) case of binary stars, two gravitationally bound stars (or their remnants) orbit their common centre of mass. Interactions between the components of such binary systems are (partially) responsible for a diverse range of astrophysical phenomena (De Marco and Izzard, 2017; Eggleton, 2006), such as symbiotic binaries (Belczyński, Mikołajewska, Munari et al., 2000; Mikołajewska, 2012), cataclysmic variables (Warner, 2003; Bode and Evans, 2012), algols and other semi-detached systems (Budding, Erdem, Çiçek et al., 2004), X-ray binaries (Podsiadlowski, Rappaport and Pfahl, 2002; Liu, van Paradijs and van den Heuvel, 2006; Lewin and van der Klis, 2006), blue stragglers (Bailyn, 1995), Type Ia supernovae (Maoz, Mannucci and Nelemans, 2014), gamma-ray bursts (Berger, 2014), and the newly discovered gravitational wave signals (Abbott, Abbott, Abbott et al., 2016b; Abbott, Abbott, Abbott et al., 2016a; Abbott, Abbott, Abbott et al., 2017), to name a few.

A prototypical example of an interaction between the components of a binary system is mass transfer. Mass transfer can occur in one of several ways depending on the internal structure of the stars and the orbital configuration. To understand how mass transfer comes about, it is helpful to introduce the concept of the Roche potential. In a frame co-rotating with the binary system one can write this potential as

$$\Phi(x,y) = \Phi_\mathrm{g}(x,y) + \Phi_\mathrm{c}(x,y) = -\frac{1}{1+q}\left[\frac{q}{\sqrt{\left(x-\frac{1}{1+q}\right)^2+y^2}} + \frac{1}{\sqrt{\left(x+\frac{q}{1+q}\right)^2+y^2}}\right] - \frac{1}{2}\left(x^2+y^2\right), \tag{1.17}$$

where Φ_g and Φ_c are the gravitational and centrifugal parts of the potential, respectively, and $q \leq 1$ is the mass ratio of the two stars.[2] Figure 1.5 shows the potential in a system with $q = 0.5$. Two potential wells centred on the x axis delineate regions around the stars where their gravitational influence dominates, and the potential is large and negative. The potential is also large and negative at large distances from the

[2] The potential has been normalised such that the orbital separation a, the gravitational constant G, and the total mass of the two stars all equal unity.

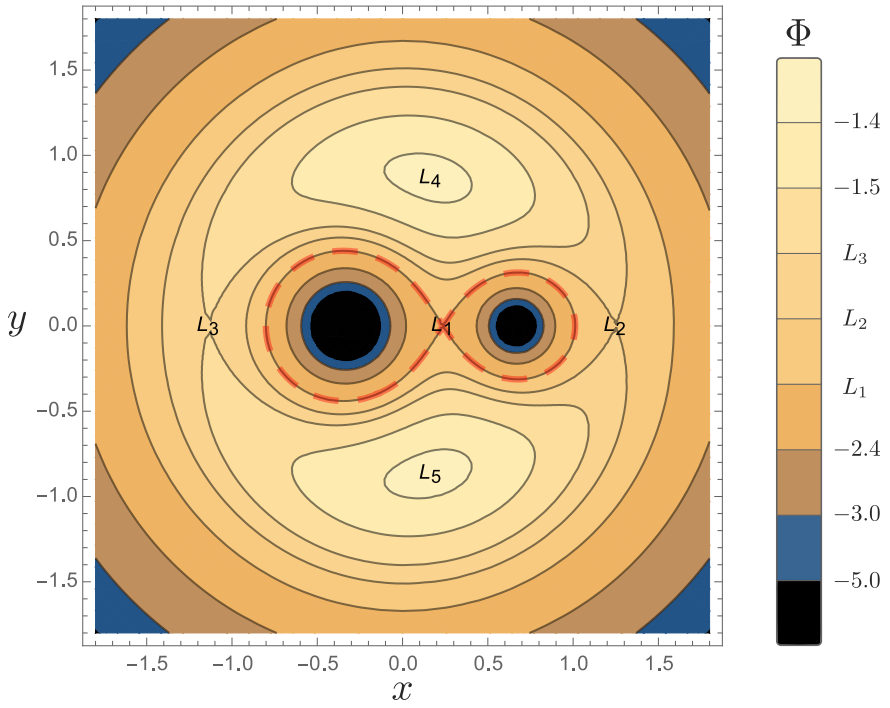

Figure 1.5: The Roche potential in a binary system with $q = 0.5$ and $a = 1$ (arbitrary units). With the barycentre at the origin, the stars are located at $\{x, y\} = \{-1/3, 0\}$ and $\{2/3, 0\}$. The five Lagrange points are indicated as L_i and the Roche surface corresponding to $\Phi(x, y) = \Phi(L_1)$ is shown by the dashed red line.

barycentre, where the centrifugal term dominates. The five points indicated as L_i are the Lagrange points. They correspond to locations where $\nabla\Phi = 0$.

The significance of the Lagrange points follows from the fact that the acceleration of a test particle placed in a potential field Φ is given by $-\nabla\Phi$. As shown in Fig. 1.5, the first three Lagrange points lie on the x axis ($y = 0$). The potential along this axis is shown in Fig. 1.6, from which one sees that a particle co-rotating with the system and located between L_1 and L_3 (L_2) will experience an acceleration towards, and eventually be accreted by, the more (less) massive star, while a particle located beyond L_2 or L_3 will drift away from the system. It can be shown that L_1, L_2 and L_3 are unconditionally unstable – small perturbations in the position of a particle will grow over time – while L_4 and L_5 are only stable for $q \lesssim 0.04$, and are thus more relevant for star-planet systems.

1.2.1 Roche lobe overflow

The L_1 point has particular significance in binary star physics. During the course of their evolution stars usually become bigger (even if their mass remains unchanged), filling up more of their potential wells. If the surface of the star reaches $\Phi(x, y) = \Phi(L_1)$, the star is said to fill its Roche lobe (the equipotential with $\Phi(x, y) = \Phi(L_1)$ is indicated in Fig. 1.5 with a dashed line). Further expansion causes mass to flow through the L_1 point to the companion star (Fig. 1.6b). This type of mass transfer is known as Roche lobe overflow (RLOF).

When a star fills its Roche lobe and begins to lose mass, the Roche potential of the system changes, and thus so does the size of the Roche lobe (R_L) of the mass-losing star. At the same time, the radius of the star (R) also changes. Depending on how $\dot{R}$ compares to $\dot{R}_L$, RLOF can be stable ($\dot{R} \leq \dot{R}_L$) or

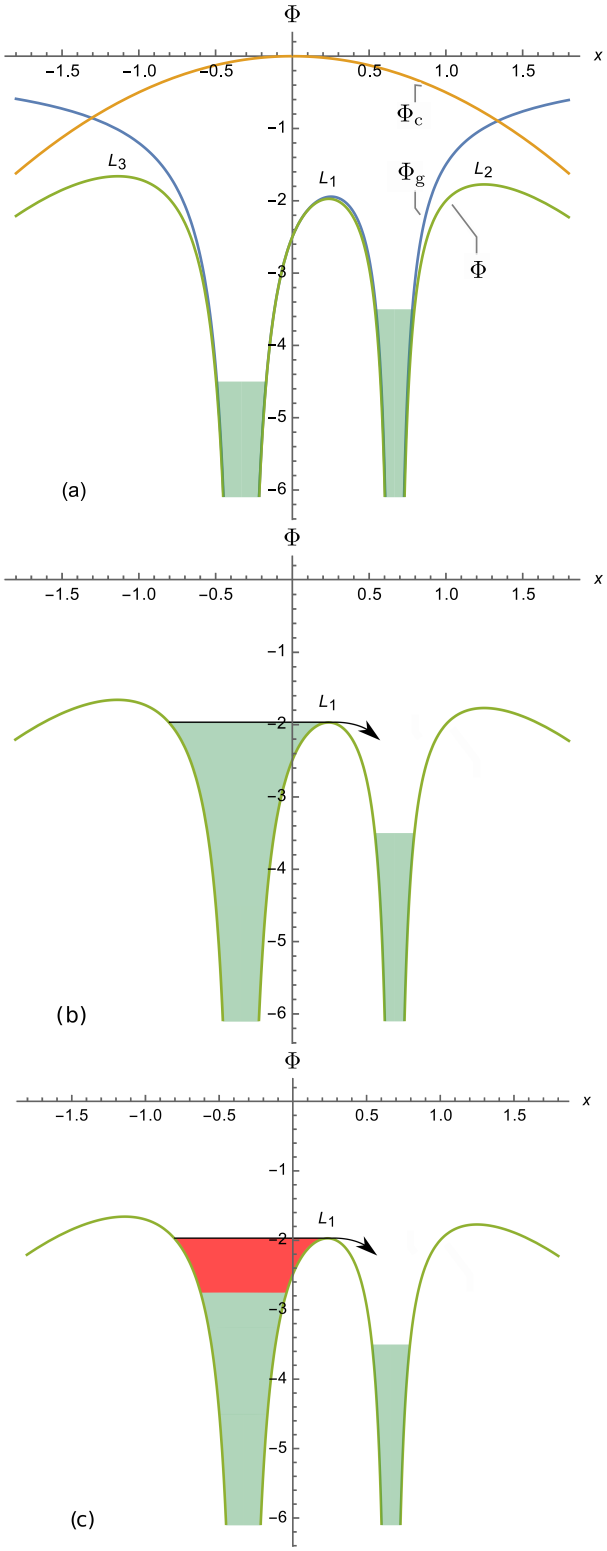

Figure 1.6: (a) The Roche potential at $y = 0$ in a system with $q = 0.5$ and $a = 1$ with the gravitational and centrifugal contributions shown separately. The shaded regions schematically show the extent to which two stars occupy their potential wells in a detached binary; (b) Roche lobe overflow: if a star expands beyond its Roche lobe, material at its surface flows through the L_1 Lagrange point to the other star; (c) wind Roche lobe overflow: if a slow and dense wind is accelerated beyond the Roche lobe of the star, material flows through the L_1 Lagrange point to the other star even though the star itself is within its Roche lobe.

unstable ($\dot{R} > \dot{R}_L$).[3] In the latter case, the radius of the star does not shrink enough in response to mass loss for the star to remain within R_L (if $\dot{R}_L < 0$), or the star expands faster than its Roche lobe (if $\dot{R}_L > 0$), and an ever increasing fraction of the stellar material is no longer bound to the mass-losing star. If the mass-accreting star cannot accommodate all of this extra material, the stars enter a common envelope phase: two stars orbiting within a shared envelope of material.

Whether mass transfer will be stable or unstable depends on the mass ratio of the two stars, as well as on their internal structure. Generally, when no mass is lost from the system, mass transfer from the more massive component to the less massive component reduces the separation between the components. The size of the donor's Roche lobe thus decreases. At the same time, if a substantial fraction of the outer part of the star is convective, losing mass makes the star expand (Paczyński, 1965). In binaries where the star overflowing its Roche lobe is a more massive red giant or an AGB star, mass transfer tends to be unstable and the stars enter a common envelope phase. The physics of common envelope evolution is still poorly understood (Ivanova, Justham, Chen et al., 2013), but it is believed that even if the stars succeed in ejecting the envelope prior to merging, the mass-accreting component will have accreted little to no mass (Ricker and Taam, 2008).

1.2.2 Wind mass transfer

Roche lobe overflow is not the only means of mass transfer. In wider binaries, where the stars remain within their Roche lobes at all times, mass transfer may still occur via a stellar wind. The problem of wind accretion was first studied by Hoyle and Lyttleton (1939) and Bondi and Hoyle (1944). In their model the accreting star is assumed to move through a homogeneous gas cloud at a constant relative velocity $v_{\rm rel}$ (for a review, see Edgar, 2004). While only material within the radius R of the star is swept up directly, more material is accreted indirectly because of the gravitational influence of the star (Fig. 1.7). The impact radius within which material is accreted is given by

$$\zeta = \frac{2GM_2}{v_{\rm rel}^2}, \tag{1.18}$$

and the amount of mass accreted depends on the density of the wind $\rho_{\rm w}$:

$$\dot{M}_2 = \pi\zeta^2 v_{\rm rel}\rho_{\rm w} = \frac{4\pi G^2 M_2^2 \rho_{\rm w}}{v_{\rm rel}^3}, \tag{1.19}$$

with M_2 the mass of the star. The case of spherically symmetric accretion was considered by Bondi (1952) and resulted in a very similar expression for the accretion rate. The overall problem has thus come to be known as Bondi-Hoyle-Lyttleton (BHL) accretion.

For binary systems the accretion rate can be more conveniently expressed as a function of the mass-loss rate of the primary, if the wind is assumed to be spherically symmetric (Boffin and Jorissen, 1988):

$$\dot{M}_2 = -\left(\frac{GM_2}{a}\right)^2 \left(\frac{1}{1 + [v_{\rm orb}/v_{\rm w}]^2}\right)^{\frac{3}{2}} \frac{\dot{M}_1}{v_{\rm w}^4}, \tag{1.20}$$

with M_1 the mass of the donor star and $v_{\rm orb} = \sqrt{G(M_1 + M_2)/a} = 2\pi a/P_{\rm orb}$ for an orbital period $P_{\rm orb}$. The accretion rate is predicted to be very sensitive to the wind velocity $v_{\rm w}$. However, when the wind velocity becomes comparable to the orbital velocity of the accretor, the applicability of the BHL prescription

[3] A dot over a symbol denotes the time derivative of the respective quantity.

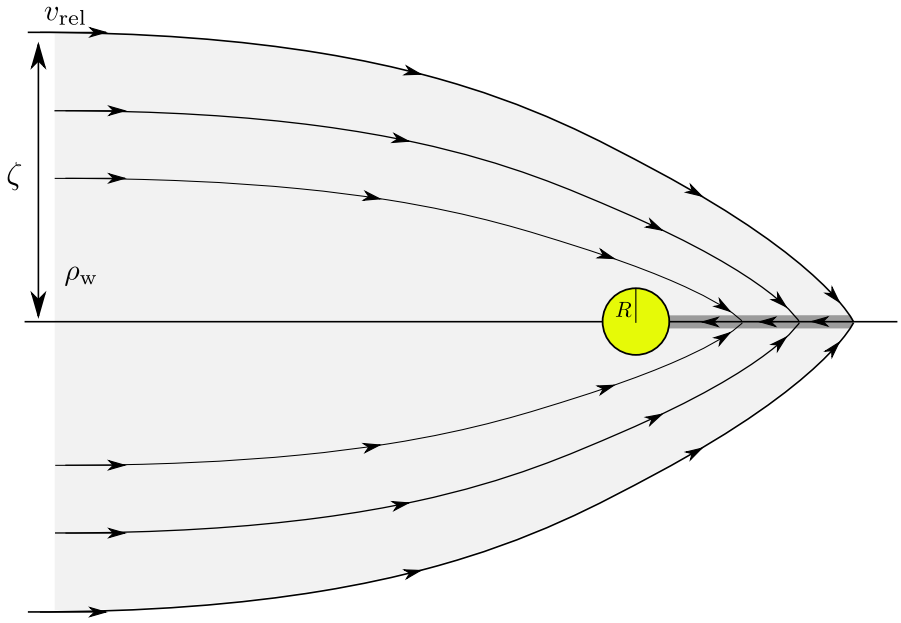

Figure 1.7: Sketch of Bondi-Hoyle-Lyttleton accretion by an object with radius R moving with a velocity $v_{\rm rel}$ with respect to a homogeneous medium with density $\rho_{\rm w}$. While only material within R is directly accreted, material within the impact radius ζ (light shaded region) is accreted along the accretion column (dark shaded region) because of gravitational focusing. Adapted from Edgar (2004).

becomes questionable, as the flow around the accreting star will certainly not look like that sketched in Fig. 1.7. In particular, as the star moves in its orbit, material attempting to accrete will be deflected by the Coriolis force and gain angular momentum. In such cases one can only use the BHL accretion rate to get a rough idea of the expected accretion rates.

Recently another mode of mass transfer, wind Roche lobe overflow (WRLOF), has been discovered in multi-dimensional simulations (Mohamed and Podsiadlowski, 2007; Mohamed and Podsiadlowski, 2012; Podsiadlowski and Mohamed, 2007). This is an intermediate mode of mass transfer, applicable to stars with dense dust-accelerated winds, such as AGB stars near the end of their lives (Abate, Pols, Izzard et al., 2013). In this case, the star is ejecting material with slow speeds, and the acceleration of the wind happens only once the ejected material is cool enough that it can form dust. This dust formation radius $r_{\rm d}$ can be several radii from the surface of the star. When $r_{\rm d} > R_L$, the ejected material can flow to the companion through the L_1 point, even though the donor itself is within its Roche lobe (Fig. 1.6c). WRLOF can increase the accretion efficiency in systems with $R < R_L < r_{\rm d}$ by orders of magnitude (Abate et al., 2013).

1.2.3 Chemical pollution and origin of carbon-enriched stars

If the chemical composition of the wind is different from that of the surface of the accretor, the surface composition of the accretor will be altered. This can be expected to happen when a main sequence star accretes material from a TP-AGB donor, which should be enriched in helium, carbon, and a range of heavy elements produced by the *s*-process. After the TP-AGB star evolves to become a white dwarf, the binary consists of a white dwarf and, in most cases, a main sequence star whose surface composition should reflect the composition of the accreted material (Fig. 1.8).

The first stars that were proposed to be an example of this scenario are the so-called barium (Ba)

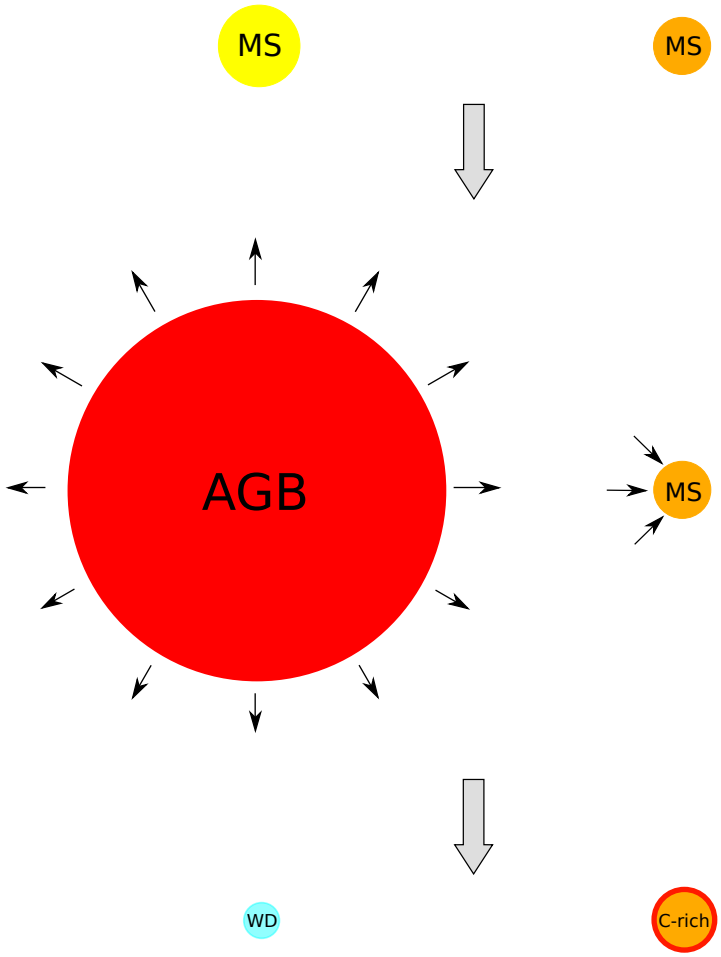

Figure 1.8: Sketch of the evolution of a binary system leading to the formation of a carbon-enriched star. The more massive of the two stars evolves faster and eventually becomes a TP-AGB star. Towards the end of its life the star experiences large mass loss via a stellar wind, some of which is accreted by the companion. After the AGB stage terminates, the binary consists of a white dwarf and a main sequence star whose surface has been enriched in carbon and other elements produced by the TP-AGB star.

and CH stars. Barium stars are giants of spectral types G and K that, compared to normal giants, show anomalously strong lines of barium and some molecular species of carbon (Bidelman and Keenan, 1951). The spectra of CH stars also showcase prominent bands of carbon molecules, the CH molecule in particular, as well as strong lines of strontium and barium (Keenan, 1942; Bond, 1974). Members of this class span the subgiant and giant branches. In general, the heavy element abundances of both Ba and CH stars are indicative of the *s*-process (Vanture, 1992; Smith, Coleman and Lambert, 1993; Busso, Lambert, Beglio et al., 1995).

Surface enrichment in carbon and *s*-process elements in low-mass stars is not expected prior to the TP-AGB stage. Attempts to explain the surface chemistry as resulting from internal processes occurring within the star (Warner, 1965; Bond, 1974; Paczynski and Tremaine, 1977) thus ultimately proved unsatisfactory for such relatively unevolved stars (Scalo, 1976; Smith and Demarque, 1980; Luck and Bond, 1991). That these stars originate from binary mass transfer was first suggested by McClure, Fletcher and Nemec (1980) who monitored the radial velocity variations of Ba stars over the course of about a year. Unless the orbital plane is exactly perpendicular to the line of sight, the spectrum of a star is periodically red- and blueshifted with respect to the observer as the star orbits the centre of mass of the system. From observing such periodic shifts McClure et al. (1980) concluded that all Ba stars may be in binaries with an unseen low-mass companion (see also McClure, 1983), compared to less than a half for normal giants (Harris and McClure, 1983). They also suggested that CH stars too may have binary companions, and presented preliminary evidence in favour of this suggestion soon after (McClure, 1984). Continued radial velocity monitoring over the following decades has put these conclusions on much firmer grounds, and it is now well established that Ba and CH stars have faint companions with masses of about 0.6 $M_\odot$ at orbital separations of an astronomical unit or more (McClure and Woodsworth, 1990; Jorissen, Van Eck, Mayor et al., 1998; Jorissen, Van Eck, Van Winckel et al., 2016). In some closer and younger systems the companions (white dwarfs) have even been directly detected (Böhm-Vitense, Carpenter, Robinson et al., 2000). Ba-rich dwarfs, the putative progenitors of classical Ba stars, have also now been found (North and Lanz, 1991; North, Berthet and Lanz, 1994; Edvardsson, Andersen, Gustafsson et al., 1993) and fit the hypothesis of mass accretion from a now-extinct AGB star (North, Jorissen and Mayor, 2000; Gray, McGahee, Griffin et al., 2011).

1.2.4 Carbon-enhanced metal-poor stars

The barium and CH stars form the same way, but they belong to different populations. CH stars are older, less massive and more metal-poor on average than barium stars (De Marco and Izzard, 2017). Carbon-enhanced metal-poor (CEMP) stars, not unlike Ba and CH stars, are relatively unevolved stars whose atmospheres show large over-abundances of carbon. These stars were discovered in surprisingly large numbers once large scale surveys focused on discovering the most metal-poor ([Fe/H] < -2) and oldest stars in our Galaxy were underway (Beers, Preston and Shectman, 1985; Beers, Preston and Shectman, 1992; Christlieb, Green, Wisotzki et al., 2001).

High-resolution spectroscopic follow-up studies then revealed that CEMP stars ([C/Fe] $\gtrsim 1$; Beers and Christlieb, 2005; Aoki, Beers, Christlieb et al., 2007; Masseron, Johnson, Plez et al., 2010) are actually a mixed bag of objects, which has prompted the introduction of several sub-classes in the CEMP family based on their heavy (neutron capture) element abundance patterns. For example, Masseron et al. (2010) propose:[4]

- CEMP-*s*: [Ba/Fe] > 1 and [Ba/Eu] > 0;

[4] Other authors use somewhat different limits (cf. Beers and Christlieb, 2005; Allen, Ryan, Rossi et al., 2012) but the same four classes.

- CEMP-*r*: [Ba/Eu] < 0;
- CEMP-*r*/*s*: [Eu/Fe] > 1 and [Ba/Eu] > 0;
- CEMP-no: [Ba/Fe] < 1.

Stars in the CEMP-no sub-class do not display large enhancements in neutron capture elements.

Unlike the Ba and and CH stars, which make up no more than a couple of percent of normal (sub)giants (MacConnell, Frye and Upgren, 1972; Scalo and Miller, 1979; Luck and Bond, 1991), CEMP stars are much more prevalent among metal-poor stars. Multiple authors have investigated the metallicity dependence of the frequency of the CEMP star phenomenon, and a consistent finding is that the prevalence of CEMP stars increases towards lower metallicities. For example, below [Fe/H] = −2 about 15–20% of all stars are CEMP stars, but this fraction rises to about 30–40% below [Fe/H] = −3 (Carollo, Beers, Bovy et al., 2012; Lee, Beers, Masseron et al., 2013; Norris, Yong, Bessell et al., 2013; Yong, Norris, Bessell et al., 2013), and below [Fe/H] = −4 the majority of stars are carbon-enhanced (Placco, Frebel, Beers et al., 2014).

The relative fractions of the different sub-classes too change with metallicity. At metallicities of [Fe/H] < −3 nearly all CEMP stars belong to the -no or -*r* subclasses (Norris et al., 2013; Spite, Caffau, Bonifacio et al., 2013; Frebel and Norris, 2015). At higher metallicities the -*s* and -*r*/*s* subclasses are predominant, and so the majority of all CEMP stars are enriched in elements associated with the *s*-process (Aoki et al., 2007) because of the rarity of stars with [Fe/H] < −3.

This dissimilar metallicity dependence, in addition to the fact that the *s*- and *r*- processes require very different conditions to operate (Sect. 1.1.4), indicates that the CEMP-no, CEMP-*r* and CEMP-*s* stars likely have very different formation channels. The binary characteristics of CEMP stars too betray their different origins. The binary frequency among CEMP stars without *s*-process enrichment is about the same as that for carbon-normal metal-poor stars (about 15–20%; Starkenburg, Shetrone, McConnachie et al., 2014; Hansen, Andersen, Nordström et al., 2016a; Carney, Latham, Stefanik et al., 2003), and the chemical enrichment of these stars is suspected to be due to local pollution events in the early Universe, such as the first rapidly rotating massive stars (Meynet, Ekström and Maeder, 2006; Hirschi, 2007; Maeder, Meynet and Chiappini, 2015) and faint supernovae (Umeda and Nomoto, 2003; Nomoto et al., 2013). Meanwhile, the overwhelming majority, if not all, *s*-process-rich CEMP stars are members of binary systems (Lucatello, Tsangarides, Beers et al., 2005b; Starkenburg et al., 2014; Hansen, Andersen, Nordström et al., 2016b) with orbital periods typically between a few hundred and a few thousand days.

The origin of CEMP-*r*/*s* stars is currently unclear. On one hand they are found in similar numbers to CEMP-*s* stars (Masseron et al., 2010; Suda, Katsuta, Yamada et al., 2008; Suda, Yamada, Katsuta et al., 2011; Abate, Stancliffe and Liu, 2016) and are probably members of binary systems as well (Hansen et al., 2016b). But explaining their richness in both elements that are associated with the *s*- and the *r*-processes is very difficult under currently proposed formation scenarios, which usually involve multiple and, for the most part, independent pollution episodes (Abate et al., 2016). In fact, the abundance pattern of most of these stars can be well fit with an *i*-process, with neutron densities intermediate between the *s*- and *r*- processes ($n \sim 10^{15}$ cm^{-3}, Cowan and Rose, 1977), so a more appropriate name for this subclass may be CEMP-*i* (Hampel, Stancliffe, Lugaro et al., 2016). But whether TP-AGB stars can routinely generate the necessary neutron densities for the *i*-process to operate remains to be determined.

In any case, it is thus the CEMP stars with *s*-process enrichment (CEMP-*s* and possibly CEMP-*r*/*s*) that are the lower-metallicity counterparts to CH and Ba stars (Lucatello et al., 2005b; Jorissen et al., 2016), and with which this thesis is concerned. CEMP-*s* stars offer us a way to indirectly study the nucleosynthesis of their long-extinct companions, low-metallicity TP-AGB stars with masses $M \gtrsim 0.9\ M_{\odot}$, which have undoubtedly played a key role in the chemical evolution of the Universe,

particularly in the dissemination of carbon and elements with primarily *s*-process isotopes such as barium, lead, yttrium, strontium, zirconium, and lanthanum among many others (Travaglio et al., 1999; Travaglio, Gallino, Busso et al., 2001; Roederer, Cowan, Karakas et al., 2010; Kobayashi, Karakas and Umeda, 2011; Bisterzo et al., 2014). By observing the surviving CEMP-*s* stars, we can try to infer the nucleosynthesis output of their TP-AGB companions, provided we understand their evolution following mass accretion.

1.3 Evolution following mass transfer

This thesis is principally concerned with the evolution of CEMP stars with *s*-process enrichment following mass transfer and investigating the fate of the accreted material. One of the key questions is under what circumstances the surface composition of these stars can be trusted to reflect the composition of the accreted material.

The accreted material will mix within the outer convection zone of the star, if there is one. But the surface convection zone of many CEMP star progenitors (low metallicity stars with $M \lesssim 0.8\ M_{\odot}$) is very small (containing less than a hundredth of a solar mass), and thus it is sometimes supposed that no mixing of the accreted material occurs prior to first dredge-up. The surface composition of the star would then directly reflect the composition of the accreted material (e.g. Sivarani, Bonifacio, Molaro et al., 2004; Lucatello, Gratton, Beers et al., 2005a), and only when the star transitions to the RGB and develops a large convective envelope would the accreted material be homogeneously diluted by the comparatively pristine material of the CEMP star. However, owing to the different chemical composition and angular momentum content of the accreted material, various instabilities can be expected to set in long before first dredge-up.

1.3.1 Thermohaline mixing

The accreted material will be considerably enriched in helium, carbon, and other heavy elements as a result of the advanced nucleosynthesis occurring in AGB stars. This material is, in a sense, heavier than the material at the surface of the star prior to mass accretion. In particular, the mean molecular weight μ of the material comprising the accreted layers will be higher than that of the layers below. While such a situation can be convectively stable, it is secularly unstable, which means that mixing can still occur but over longer timescales.

The situation of having a higher mean molecular weight material on top of material with lower molecular weight is unstable because the diffusivity of heat in astrophysical fluids is greater than that of chemicals. Thus, for example, a blob of material displaced from the accreted layer into the pristine layer below will reach thermal equilibrium with its surroundings prior to reaching chemical equilibrium (Fig. 1.9). Then, owing to its higher molecular weight, it will find itself denser than its surroundings and sink deeper. There, it will again find itself denser after reaching thermal equilibrium and sink farther, until it finally loses the excess molecular weight. The situation is analogous for blobs displaced upwards, since they will find themselves less dense than their surroundings and buoyancy will make them rise.

This form of mixing is known as thermohaline or fingering convection, and was first described as occurring in oceans where salinity plays the role of the molecular weight (Stern, 1960; Kunze, 2003). When warm salty water finds itself on top of cold and less salty water, fingering convection can set in. Such a configuration can be realised in warm climates when there is little precipitation: the evaporation of water leaves behind an increased concentration of salt in the warm surface waters.

The first to apply this process to the stellar context were Ulrich (1972) and Kippenhahn, Ruschenplatt

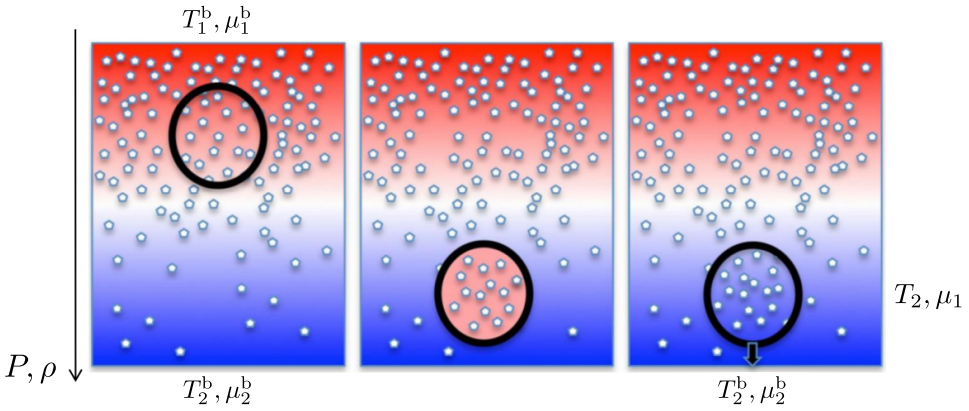

Figure 1.9: Illustration of thermohaline mixing following mass accretion. The original material of the star (blue) and the accreted layer (red) will have different molecular weights μ_i. A blob of material displaced from the accreted layer into the pristine layer will reach thermal equilibrium with its surroundings prior to reaching chemical equilibrium. Because of its higher mean molecular weight, it will keep sinking until it dissolves. Adapted from Garaud (2014).

and Thomas (1980). These first formulations of the theory contain a free parameter that effectively characterises the shape of the fingers and thus determines the rate and extent of the mixing. Ulrich (1972) estimated the structures to be finger-like (deriving a length-to-diameter ratio of about seven, Denissenkov, 2010), similar to the oceanic case, whereas Kippenhahn et al. (1980) argued that the mixing elements will lose their identity much sooner, and thus be more blob-like (with a length-to-diameter ratio of around unity). Recently, multidimensional hydrodynamical simulations have tried to address this uncertainty (Denissenkov, 2010; Traxler, Garaud and Stellmach, 2011; Brown, Garaud and Stellmach, 2013; Zemskova, Garaud, Deal et al., 2014). While these simulations are still far from the stellar regimes in terms of the fluid conditions, they agree that the structure of the mixing elements is probably more blob-like.

The ways in which thermohaline mixing could be relevant to stars (e.g. burning of ^{3}He, accretion of material with a higher molecular weight, and off-centre onset of the 3α reaction in low-mass stars prior to core helium flash) were recognised already by Ulrich (1972) but then seemingly forgotten for many years until a revival in the interest of thermohaline mixing was sparked by Eggleton, Dearborn and Lattanzio (2006). The importance of thermohaline mixing to the secondaries in binary systems hosting a TP-AGB primary was recognised by Stancliffe, Glebbeek, Izzard et al. (2007), who computed model sequences for different combinations of primary and secondary masses and amount of mass transferred. They found that nearly all of the accretor can be mixed if a sufficient amount of high-μ material is accreted. In other words, the material accreted by the star is substantially diluted shortly after mass transfer, so that the surface of the accreting star is no longer composed solely of the material ejected by the AGB star, even before the star evolves off the main sequence.

1.3.2 Rotation and mixing

All stars rotate, even if very slowly. For single stars this is a legacy of their formation. As a fragment of a molecular gas cloud collapses, some of its angular momentum will be conserved by the newly formed star, resulting in a non-zero rotation rate on the zero-age main sequence. In fact, the rotation rate should typically be an appreciable fraction of the critical (maximum possible) rotation rate (at critical rotation the centrifugal acceleration on a fluid element at the surface of the star balances the gravitational acceleration,

and the material is no longer bound to the star). The low-mass metal-poor progenitors of CEMP-*s* stars, however, rotate rather slowly, with equatorial velocities rarely higher than about 5 km s^{-1} (Lucatello and Gratton, 2003; Cortés, Silva, Recio-Blanco et al., 2009), which is well below their critical velocities of about 300 km s^{-1}. This suggests that these stars have lost most of their angular momentum during their main sequence evolution, similar to their counterparts at solar metallicity (Kraft, 1967; Kawaler, 1988).

The wind material accreted by the progenitors of CEMP-*s* stars could instead possess substantial angular momentum. In particular, wind mass transfer from a giant with slow winds to a low-mass companion has been extensively modelled in 3D simulations (Theuns, Boffin and Jorissen, 1996; Mastrodemos and Morris, 1998; de Val-Borro, Karovska and Sasselov, 2009; Huarte-Espinosa, Carroll-Nellenback, Nordhaus et al., 2013; Chen, Frank, Blackman et al., 2017; Liu, Stancliffe, Abate et al., 2017). What such simulations typically find is that the material gains enough specific angular momentum while falling to the secondary that an accretion disk forms around it. Accretion onto the secondary should then proceed via the disk. The angular momentum of the accreted material should thus be rather high, and the accreting star should rotate more and more rapidly as it grows in mass.

Such spin-up can limit the amount of mass that a star can accrete. Particularly, if enough material possessing high specific angular momentum is added to the star, the star should eventually be spun up to critical rotation. Even if the star is able to rapidly redistribute the angular momentum internally, the amount of mass it can accrete from a disk can be as little as a couple of percent of its own mass before it reaches critical rotation and can accrete no more (Packet, 1981).

Since the accreted material deposits additional angular momentum near the surface of the star, newly formed CEMP-*s* stars are likely to rotate differentially, which means that the angular rotation velocity Ω varies with depth within the star. Under such circumstances rotating stellar layers are especially prone to various instabilities that can redistribute the angular momentum content within the star and trigger mixing of chemical elements in the process. Given the potentially large velocity contrast between the original surface and the accreted material, the shear instability could be of particular importance.

In a very basic analysis concerning stability against shear one considers two neighbouring fluid elements at slightly different distances r_0 and $r_0 + \delta r$ travelling with respective velocities v_0 and $v_0 + \delta v$ in a fluid with density ρ (Fig. 1.10; Chandrasekhar, 1961; Maeder, 2009). If, as a result of some turbulent displacement, the two elements are exchanged and homogenised, such that their velocities become $v_0 + \frac{\delta v}{2}$, work must be done to change their potential energy by $\delta W = g\delta\rho\delta r$, where $\delta\rho$ is the density excess of the fluid elements over their surroundings after the displacement. In the adiabatic case the energy available to do this work is the kinetic energy difference between the initial and final states:

$$\delta K = \frac{1}{2}\rho\left[v_0^2 + (v_0 + \delta v)^2\right] - \rho\left(v_0 + \frac{\delta v}{2}\right)^2 = \frac{1}{4}\rho\,(\delta v)^2\,. \tag{1.21}$$

The shear instability can set in if this energy is greater than the work needed to overcome the restoring force (gravity), i.e. $\delta K > \delta W$. Thus, the medium will be stable when

$$\mathcal{R}i = \frac{g}{\rho}\frac{\mathrm{d}\rho\,/\,\mathrm{d}r}{(\mathrm{d}v\,/\,\mathrm{d}r)^2} = \frac{g}{\rho}\frac{\mathrm{d}\rho\,/\,\mathrm{d}r}{(\mathrm{d}\Omega\,/\,\mathrm{d}\ln r)^2} > \frac{1}{4} = \mathcal{R}i_\mathrm{c}. \tag{1.22}$$

This is known as the Richardson criterion, and $\mathcal{R}i$ ($\mathcal{R}i_\mathrm{c}$) is the (critical) Richardson number. Naturally, the shear instability is more likely to arise for large differential rotation. Equation (1.22) was derived ignoring thermal exchange between the elements and their surroundings. But when thermal effects are considered, an instability can arise even for $\mathcal{R}i \gtrsim \mathcal{R}i_\mathrm{c}$, giving rise to secular (as opposed to dynamical) shear that operates on a longer (thermal) timescale.

Another important transport process arises in rotating stars. Its origin can be sketched by considering

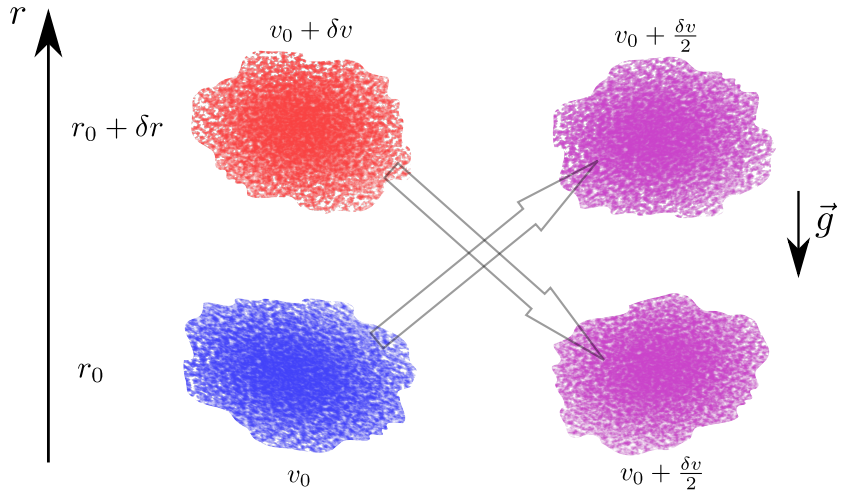

Figure 1.10: Illustration of the shear instability. Two fluid elements at different distances from the centre of the star travel at slightly different velocities. If the work required to equalize their momenta is less than the kinetic energy difference between the elements, the medium is unstable to shear.

the radiative flux in a uniformly rotating (i.e. Ω is constant everywhere) star in hydrostatic equilibrium:

$$\mathcal{F} = -k\nabla T = -k\frac{\mathrm{d}T}{\mathrm{d}P}\nabla P = -k\frac{\mathrm{d}T}{\mathrm{d}P}\rho \boldsymbol{g}_{\mathrm{eff}} = \mathcal{K}\nabla\Psi. \tag{1.23}$$

Here k is the thermal conductivity, T is temperature, P is pressure, $\boldsymbol{g}_{\mathrm{eff}} = \boldsymbol{g} + \boldsymbol{g}_{\mathrm{c}}$ is the effective gravity (i.e. gravitational acceleration corrected for centrifugal acceleration so that $|\boldsymbol{g}_{\mathrm{eff}}| \leq |\boldsymbol{g}|$), and Ψ is the total potential ($\nabla\Psi = -\boldsymbol{g}_{\mathrm{eff}}$). Energy conservation requires that in radiative equilibrium the divergence of the flux be zero in the absence of energy generation:

$$\begin{aligned} \nabla\cdot\mathcal{F} &= \nabla\mathcal{K}\nabla\Psi + \mathcal{K}\nabla\cdot(\nabla\Psi) = \frac{\mathrm{d}\mathcal{K}}{\mathrm{d}\Psi}(\nabla\Psi)^2 + \mathcal{K}\Delta\Psi \\ &= \frac{\mathrm{d}\mathcal{K}}{\mathrm{d}\Psi}(\nabla\Psi)^2 + \mathcal{K}\left(4\pi G\rho - 2\Omega^2\right) = 0, \end{aligned} \tag{1.24}$$

where use has been made of the Poisson equation ($\Delta\Psi = 4\pi G\rho - 2\Omega^2$). However, Eq. (1.24) cannot generally hold in a rotating star – since the effective gravity is larger near the poles ($g_{\mathrm{c}} \to 0$) than at the equator ($g_{\mathrm{c}} \to \Omega^2 r$), on surfaces of constant Ψ all the terms are constant except for the term involving $(\nabla\Psi)^2$. This implies a local breakdown of radiative equilibrium, which was first pointed out by von Zeipel (1924). While on average $\nabla\cdot\mathcal{F}$ must vanish on an equipotential (in the absence of energy generation), local breakdown of radiative equilibrium implies that too much energy is carried away by radiation from some regions of the star, while not enough energy is carried away from others. Some regions thus cool down, while others heat up. To maintain a stationary state, large scale meridional flows must arise. These flows, known as meridional, Eddington-Sweet or Eddington-Vogt circulation (Eddington, 1925; Vogt, 1925; Sweet, 1950), slowly advect entropy, angular momentum, and contribute to the transport of chemical species (Fig. 1.11).

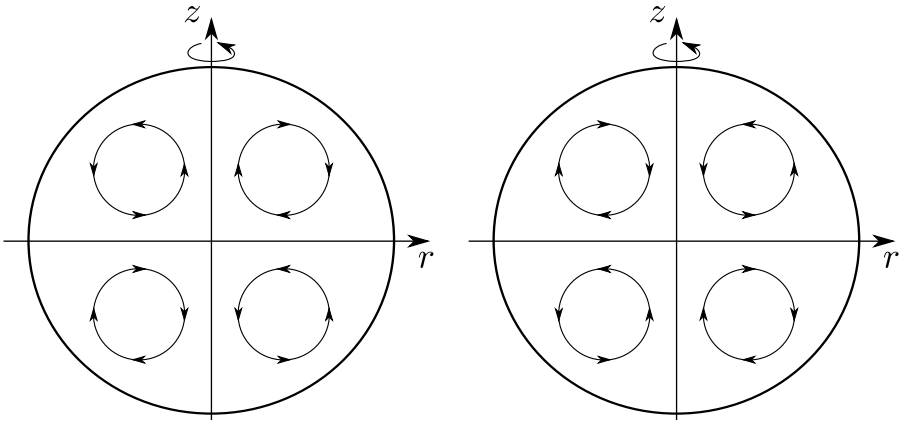

Figure 1.11: To maintain thermal equilibrium, large scale meridional currents must arise in a rotating star. With the star rotating around the z axis as indicated, the flow rises along the poles and descends along the equator leading to a net inward transport of angular momentum when the circulation velocity is positive (left) and vice versa when the circulation velocity is negative (right).

1.3.3 Atomic diffusion

The instabilities expected to arise from accretion of material should interact with a process that to some extent must operate in all low-mass metal-poor stars: atomic (or microscopic) diffusion. Atomic diffusion leads to a separation of the chemical species of the medium when the particles of some species i experience a net force F_i with respect to the particles of all other species. In stars this can occur in stable (radiative) layers that are not mixed as a result of some other process. To first order atomic diffusion can be described with a characteristic velocity

$$w_i = -D_i\left(\frac{1}{X_i}\frac{\partial X_i}{\partial r} - \frac{F_i}{k_\mathrm{B}T}\right), \tag{1.25}$$

where D_i is the diffusion coefficient, X_i is the mass fraction (abundance) of the species, and k_B is the Boltzmann constant. The net forces result from gradients in one or more of several quantities, such as pressure or temperature.

Pressure diffusion leads to gravitational settling of elements more massive than the mean molecular weight of the stellar plasma (through most of the evolution, this means all elements other than hydrogen). Likewise, thermal diffusion also separates hydrogen from heavier elements. What this means is that in a main sequence star heavier elements will tend to sink deeper into the star towards the centre, while the surface layers become increasingly hydrogen rich. These processes are opposed, to some extent, by concentration diffusion, the first term in Eq. (1.25), which attempts to erase any abundance gradients.

The importance of atomic diffusion has been demonstrated in multiple contexts. For example, the agreement between stellar models and helioseismic inferences of the interior structure of the Sun improved considerably once the models included atomic diffusion (Christensen-Dalsgaard, Proffitt and Thompson, 1993; Richard, Vauclair, Charbonnel et al., 1996; Christensen-Dalsgaard, 2002). Inclusion of diffusion in models of low-metallicity dwarfs brought their ages into better agreement with expectations based on the age of the Universe (Chaboyer, Deliyannis, Demarque et al., 1992; VandenBerg, Richard, Michaud et al., 2002). The purity of the atmosphere of many white dwarfs (either pure hydrogen or helium) is also believed to result from their large surface gravities leading to rapid gravitational settling (Muchmore, 1984; Dupuis, Fontaine, Pelletier et al., 1992).

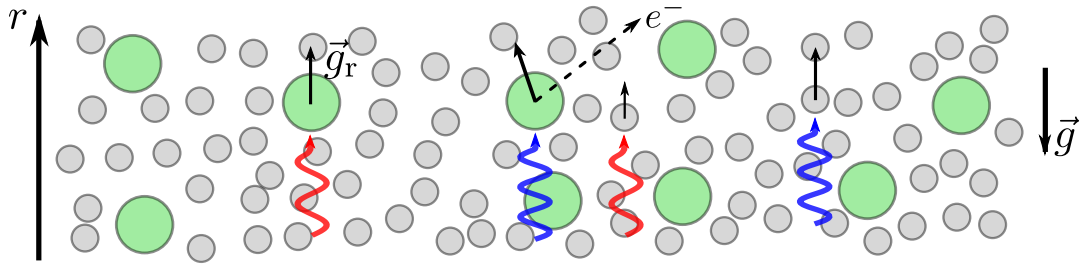

Figure 1.12: Schematic illustration of radiative levitation. The atoms of the stellar plasma in a net outward radiation field experience different levels of acceleration depending primarily on their abundance (number) and contribution to the opacity of the medium (size).

The possible importance of atomic diffusion for CEMP-*s* stars was raised by Thompson, Ivans, Bisterzo et al. (2008). They correctly argued that the combined action of gravitational settling and thermal diffusion should succeed in establishing a μ-gradient throughout the star. This μ-gradient might then present a sufficient barrier to thermohaline mixing, such that its importance would be significantly reduced. This hypothesis was investigated by Stancliffe and Glebbeek (2008), who concluded that the μ-barrier established by atomic diffusion is too small to have a significant influence on thermohaline mixing, as long as the accreted layer is not very small ($\Delta M \lesssim 10^{-3}\ M_\odot$).

At the same time, Stancliffe and Glebbeek (2008) found that in the absence of other mixing processes atomic diffusion is expected to influence the evolution of CEMP-*s* stars in a manner similar to regular low-mass stars, i.e. by reducing their lifetimes and leading to surface abundance anomalies. This complicates the interpretation of their surface abundances in the context of TP-AGB nucleosynthesis. Given the importance of gravitational settling and thermal diffusion, Stancliffe and Glebbeek (2008) suggested that radiative forces might also have to be accounted for.

Radiative forces are a consequence of energy transport by radiation. The energy in a main sequence star is produced in the central regions, slowly transported outwards, and radiated away from the surface. This transport is slow because the stellar material is opaque to radiation – the photons produced by nuclear reactions in the central regions are scattered, absorbed and re-emitted countless numbers of times by the ions in the plasma before they emerge from the star. During these interactions the photons impart (some of) their momentum to the ions. Since the net flux of photons in a star is directed outwards, the ions are accelerated in a direction opposite to gravity. When the acceleration exceeds the gravity, the element as a whole can be transported upwards towards the surface until a level where the radiative acceleration is roughly compensated by the gravity. This process is thus commonly referred to as radiative levitation (Fig. 1.12).

Radiative levitation is believed to at least partially cause the surface abundance anomalies of stars somewhat more massive than the Sun ($M \simeq 1.5$–$3\ M_\odot$), such as the AmFm stars that display strong metallic lines and the HgMn stars which display large over-abundances of mercury and manganese (Turcotte, Richer and Michaud, 1998; Richer, Michaud and Turcotte, 2000). Part of the reason why radiative forces are able to modify the surface abundances of these stars is that outside of their core these stars are almost fully radiative up to their surface, in contrast to lower mass stars that have surface convection zones. Interestingly, these convection zones are very thin in lower metallicity stars, even at masses as low as $M \simeq 0.8\ M_\odot$, which suggests that radiative levitation might be similarly important.

1.4 Outline of this thesis

This thesis focuses on modelling the evolution of CEMP-*s* stars under the assumption that they form when a low-mass star accretes material from a binary companion which is in the thermally pulsing AGB stage.

The tool to use for modelling the evolution of stars is a stellar evolution code. Chapters 2 and 3 describe the code used here, with particular emphasis on the code development resulting as part of this research. Chapters 4, 5, and 6 describe the scientific results of this work, and are largely reproductions of peer-reviewed published articles. In particular, in Chapter 4 the consequences of atomic diffusion and radiative levitation on the evolution of CEMP-*s* stars and their surface abundances are investigated (Matrozis and Stancliffe, 2016), while Chapters 5 and 6 concern rotation. Chapter 5 expands on the previous chapter by accounting for rotational mixing (Matrozis and Stancliffe, 2017). In Chapter 6 the chemical aspects, as well as the post-mass-transfer evolution, are set aside to investigate the following question: how much mass and angular momentum can the progenitors of carbon-enriched stars accrete (Matrozis, Abate and Stancliffe, 2017)? Finally, in Chapter 7 the results obtained during this work are summarised prior to highlighting possible future avenues of research.

CHAPTER 2

Modelling the structural evolution of stars

In this and the next chapter the methods used to tackle the evolution of carbon-enhanced metal-poor stars are described. The principal tool employed in this thesis is a stellar evolution code, a piece of software that solves the equations of stellar structure and evolution. The code used here is commonly referred to as STARS. Since its introduction in a series of papers by Peter Eggleton (Eggleton, 1971; Eggleton, 1972; Eggleton, Faulkner and Flannery, 1973), the code has spawned multiple offshoots and undergone many updates by various authors (e.g. Pols, Tout, Eggleton et al., 1995; Glebbeek, Pols and Hurley, 2008; Stancliffe and Eldridge, 2009; Potter, Tout and Eldridge, 2012b). The version of the code built upon here is available at `http://www.ast.cam.ac.uk/~stars/index.htm`. Many of the processes detailed here, such as simulating the accretion of mass of a different chemical composition and angular momentum, radiative levitation, and stellar rotation and rotational mixing are not present in the public version. They are described in more detail here.

2.1 Equations governing the evolution of a star[1]

As mentioned in the introduction, a star is a massive ball of gas held together by gravity. Since such objects can be closely approximated to be spherical (at least in the non-rotating case), a star can be taken to consist of spherical shells (Fig. 2.1), which means the equations of stellar structure can be written with respect to only one spatial coordinate. The independent coordinates are then the time t and either the radial distance r from the centre of the star (Eulerian formulation) or the corresponding mass coordinate m (i.e. enclosed mass; Lagrangian formulation).

The equations of stellar structure express the conservation of various quantities a closed system must have. These are the conservation of mass, momentum, and energy, with an additional equation describing energy transport.

2.1.1 Equations of stellar structure

The mass of the shell in Fig. 2.1 at some time t_0 can be written as $\mathrm{d}m = 4\pi r^2 \rho(r)\,\mathrm{d}r$, where ρ is the density in the shell. This immediately leads to the equation for conservation of mass:

$$\frac{\partial m}{\partial r} = 4\pi r^2 \rho, \tag{2.1}$$

[1] This section briefly summarises relevant material from any textbook on stellar structure and evolution, such as that of Kippenhahn, Weigert and Weiss (2012).

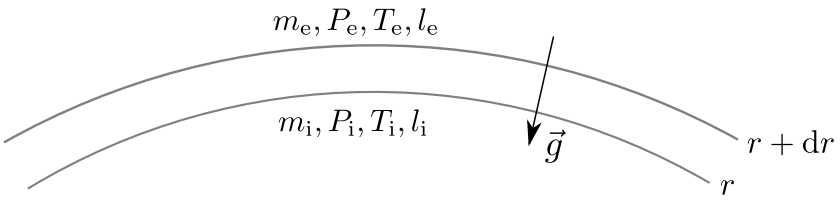

Figure 2.1: Schematic illustration of a shell of stellar matter between coordinates r and $r + \mathrm{d}r$ in a spherically symmetric star. Over the distance $\mathrm{d}r$ various quantities change by amounts of, e.g. $\mathrm{d}m = m_\mathrm{e} - m_\mathrm{i}$, $\mathrm{d}P = P_\mathrm{e} - P_\mathrm{i}$, $\mathrm{d}T = T_\mathrm{e} - T_\mathrm{i}$, $\mathrm{d}l = l_\mathrm{e} - l_\mathrm{i}$. $\boldsymbol{g}$ indicates the direction of gravitational acceleration.

The second equation expresses the conservation of linear momentum. A global acceleration $\ddot{r}$ of a stellar layer will result if the gravitational force $g\,\mathrm{d}m$ with acceleration $g = Gm/r^2$ is not balanced by the pressure gradient force $\frac{\partial P}{\partial r}\,\mathrm{d}r\,4\pi r^2$:

$$\frac{\partial^2 r}{\partial t^2} = -\frac{Gm}{r^2} - \frac{1}{\rho}\frac{\partial P}{\partial r}. \tag{2.2}$$

In all our models we assume hydrostatic equilibrium ($\ddot{r} = 0$). This is a good approximation for our purposes since a star will readjust to any perturbation from hydrostatic equilibrium on the dynamical timescale (a star that is not about to explode or collapse, that is, but we do not deal with such stars here), which is much shorter than any timescales of interest in this study (e.g. the dynamical timescale of the Sun is about 25 minutes). The second equation of stellar structure thus becomes:

$$\frac{\partial P}{\partial r} = -\rho g. \tag{2.3}$$

Conservation of energy requires that the energy generated (or consumed) by the shell $\mathrm{d}l$ equals the energy generation rate per unit mass ε times the mass $\mathrm{d}m$ of the shell, which gives the third equation of stellar structure:

$$\frac{\partial l}{\partial r} = 4\pi r^2 \rho \varepsilon. \tag{2.4}$$

The final equation of stellar structure is that of energy transport (Sect. 2.1.3). In the interiors of stars the radiative transport of energy can be well described in the diffusion approximation because the mean-free-path of photons is very small (of the order of centimetres) compared to the size of the star. The energy transport equation can then be written as

$$\frac{\partial T}{\partial r} = -\frac{3}{16\pi ac}\frac{\kappa\rho l}{r^2 T^3}, \tag{2.5}$$

where T is temperature, a is the radiation density constant, c is the speed of light, and κ is the opacity of the stellar matter (Sect. 2.1.4).

2.1.2 Lagrangian formulation

It is more convenient to consider m as the independent variable instead of r because then the movement of a shell over time is accounted for implicitly. Applying the chain rule $\partial_m = \partial_r \frac{\partial r}{\partial m}$ to m and using Eq. (2.1), the conservation of mass can be expressed as

$$\frac{\partial r}{\partial m} = \frac{1}{4\pi r^2 \rho}. \tag{2.6}$$

Applying the same rule to the other equations gives

$$\frac{\partial P}{\partial m} = -\frac{g}{4\pi r^2} = -\frac{Gm}{4\pi r^4}, \tag{2.7}$$

$$\frac{\partial l}{\partial m} = \varepsilon, \tag{2.8}$$

$$\frac{\partial T}{\partial m} = -\frac{3}{64\pi^2 ac}\frac{\kappa l}{r^4 T^3}. \tag{2.9}$$

In Eq. (2.8) ε consists of multiple terms owing to, e.g. nuclear energy generation, gravitational expansion or contraction, and neutrino emission. Equations (2.6)-(2.9) determine the structure of a star of a given composition at a given time. To follow the evolution of a star over time, the changes in its chemical composition as a result of nuclear reactions and mixing of the stellar matter need to be tracked. This discussion is deferred until Chapter 3.

The equations of stellar structure and evolution need to be supplemented by an equation of state that relates the density to the other thermodynamic quantities and the composition, i.e. a relation $\rho = \rho(P, T, X_i)$ has to be specified, where X_i is the mass fraction of species i. The energy generation terms encapsulated in ε and the opacity need to be similarly expressed, i.e. $\varepsilon = \varepsilon(P, T, X_i)$ and $\kappa = \kappa(P, T, X_i)$.

In the case of rotating stars an additional equation needs to be introduced describing the internal evolution of specific angular momentum. Furthermore, Eqs. (2.7) and (2.9) need to be modified, and the interpretation of some of the variables changes. These complications are described in Sect. 2.2.

2.1.3 Radiative and convective energy transport

Equation (2.9) can be written with the help of Eq. (2.7) as

$$\frac{\partial T}{\partial m} = \frac{T}{P}\frac{\partial \ln T}{\partial \ln P}\frac{\partial P}{\partial m} = -\frac{Gm}{4\pi r^4}\frac{T}{P}\nabla, \tag{2.10}$$

where we have defined $\nabla = \frac{\partial \ln T}{\partial \ln P}$, a quantity that describes the variation of temperature with depth measured in terms of pressure. The value of ∇ depends on the convective stability of the medium. In convectively stable (radiative) regions

$$\nabla = \nabla_{\rm rad} = \frac{3}{16\pi acG}\frac{\kappa l P}{m T^4}. \tag{2.11}$$

$\nabla_{\rm rad}$ is the temperature gradient required for radiation (and conduction, when κ is appropriately defined, see Sect. 2.1.4) to be able to carry all of the energy flux. If the actual temperature gradient (∇) is smaller than $\nabla_{\rm rad}$, only a part of the energy flux,

$$\mathcal{F}_{\rm rad} = \frac{4acG}{3}\frac{mT^4}{\kappa P r^2}\nabla, \tag{2.12}$$

can be transported by radiation. The rest needs to be carried by convection. When convection is efficient, the temperature gradient tends to the adiabatic value

$$\nabla \to \nabla_{\rm ad} = \left(\frac{\partial \ln T}{\partial \ln P}\right)_s = \frac{P\delta}{T\rho c_P}, \tag{2.13}$$

where s is the specific entropy, $\delta = -(\partial \ln \rho / \partial \ln T)_{P,\mu}$, and c_P is the specific heat capacity at constant pressure. A region is dynamically stable against convection when

$$\nabla_{\rm rad} < \nabla_{\rm ad}. \tag{2.14}$$

This is known as the Schwarzschild criterion. Properly evaluating ∇ when $\nabla_{\rm rad} > \nabla_{\rm ad}$ requires a theory of convection, which is a notoriously difficult problem. In the stellar context convection is typically modelled using the mixing length theory (MLT; Böhm-Vitense, 1958).

The basic picture of MLT envisions convective motions to consist of single-sized macroscopic blobs of material. Buoyancy forces make blobs hotter than their surroundings rise while blobs cooler than their surroundings sink. Such motions result in a net energy flux $\mathcal{F}_{\rm conv}$, which carries a fraction of the total energy flux given by

$$\mathcal{F}_{\rm conv} + \mathcal{F}_{\rm rad} = \frac{4acG}{3} \frac{mT^4}{\kappa P r^2} \nabla_{\rm rad}. \tag{2.15}$$

The blobs travel some distance ℓ (a mixing length) before dissolving in the surroundings. This distance is taken to be some multiple $\alpha_{\rm MLT}$ of the local pressure scale height H_P. Hence,

$$\ell = \alpha_{\rm MLT} H_P \tag{2.16}$$

with

$$H_P = -\frac{{\rm d}r}{{\rm d} \ln P} = \frac{P}{g\rho}. \tag{2.17}$$

Estimates of the velocity of the blobs, their temperature excess, and the convective flux in terms of temperature gradients yield additional equations to Eqs. (2.12) and (2.15). The resulting system of equations can be reduced to a single cubic equation, the sole real root of which gives ∇.

The value of $\alpha_{\rm MLT}$ is a free parameter in the mixing length theory. It is typically calibrated by requiring that a model with $M = 1\ M_\odot$ has $R = 1\ R_\odot$ and $L = 1\ L_\odot$ at the solar age, which yields values of $\alpha_{\rm MLT}$ around two (Stancliffe, Fossati, Passy et al., 2016). All models presented in this thesis have $\alpha_{\rm MLT} = 2$.

2.1.4 Opacity of stellar matter

The opacity κ appearing first in Eq. (2.5) characterises the transparency of stellar material to energy transport. A large opacity implies that energy transport is inefficient. For example, as indicated by Eq. (2.12), for radiation to carry a certain amount of energy, a larger temperature gradient is required in regions of higher opacity.

The opacity of material is generally frequency dependent, so the value of κ appearing in Eq. (2.5) must be some proper average over frequency. The radiation flux inside the star can be well approximated as that from a black-body radiator with temperature T. The energy density of such radiation is given by

$$U_\nu(T) = \frac{4\pi}{c} B_\nu(T) = \frac{8\pi h}{c^3} \frac{\nu^3}{\exp(h\nu / k_{\rm B} T) - 1}, \tag{2.18}$$

where h is the Planck constant, $k_{\rm B}$ is the Boltzmann constant, and B_ν is the intensity of radiation. The radiation flux in the frequency range $[\nu, \nu + {\rm d}\nu]$ in the diffusion approximation can be written as $\mathcal{F}_\nu = -D_\nu \frac{\partial U_\nu}{\partial r}$, where

$$D_\nu = \frac{1}{3} c \ell_\gamma = \frac{1}{3} \frac{c}{\kappa_\nu \rho} \tag{2.19}$$

is the diffusion coefficient for radiation, ℓ_γ is the mean free path of photons, and κ_ν is the absorption

cross-section per unit mass, i.e. the opacity of the material in the frequency range $[\nu, \nu + \mathrm{d}\nu]$. Integrated over all frequencies, the monochromatic radiation flux has to equal the total radiative flux:

$$\mathcal{F}_{\mathrm{rad}} = \int \mathcal{F}_\nu \,\mathrm{d}\nu = -\frac{1}{3}\frac{c}{\rho}\int \frac{1}{\kappa_\nu}\frac{\partial U_\nu}{\partial r}\,\mathrm{d}\nu = -\frac{4\pi}{3\rho}\frac{\partial T}{\partial r}\int \frac{1}{\kappa_\nu}\frac{\partial B_\nu}{\partial T}\,\mathrm{d}\nu\,. \tag{2.20}$$

Replacing $\partial T/\partial r$ by Eq. (2.5) and $\mathcal{F}_{\mathrm{rad}}$ by $l/\left(4\pi r^2\right)$ and simplifying gives

$$\frac{1}{\kappa} = \frac{\pi}{acT^3}\int \frac{1}{\kappa_\nu}\frac{\partial B_\nu}{\partial T}\,\mathrm{d}\nu = \frac{1}{\kappa_{\mathrm{R}}}. \tag{2.21}$$

κ_{R} is known as the Rosseland mean opacity.

Combining Eqs. (2.20) and (2.21), one can write

$$\mathcal{F}_{\mathrm{rad}} = -\frac{4acT^3}{3\rho\kappa_{\mathrm{R}}}\frac{\partial T}{\partial r}. \tag{2.22}$$

Collisions of particles caused by their random thermal motion can also contribute to energy transport, particularly in dense, degenerate matter, such as the helium cores of low-mass post-main-sequence stars. This conductive energy flux can be written in analogy with the radiative flux as

$$\mathcal{F}_{\mathrm{cond}} = -\frac{4acT^3}{3\rho\kappa_{\mathrm{cond}}}\frac{\partial T}{\partial r}. \tag{2.23}$$

The total flux is thus

$$\mathcal{F}_{\mathrm{rad}} + \mathcal{F}_{\mathrm{cond}} = -\frac{4acT^3}{3\rho\kappa_{\mathrm{tot}}}\frac{\partial T}{\partial r} \tag{2.24}$$

with

$$\frac{1}{\kappa_{\mathrm{tot}}} = \frac{1}{\kappa_{\mathrm{R}}} + \frac{1}{\kappa_{\mathrm{cond}}}. \tag{2.25}$$

Independent opacities thus add harmonically instead of algebraically ($\kappa_{\mathrm{tot}} \neq \kappa_{\mathrm{R}} + \kappa_{\mathrm{cond}}$), which illustrates why opacity is a measure of the transparency of material to energy transport. It is the opacity given by Eq. (2.25) that is to be used in the stellar structure equations.

2.1.5 Numerical implementation

Non-Lagrangian mesh In a typical stellar evolution code the equations of stellar structure given by Eqs. (2.6)-(2.8), and (2.10) are discretised in the range $0 \leq m \leq M$ (where M is the total mass of the star) at a few hundreds to a few thousands of meshpoints. Regions where various quantities change rapidly (with respect to the mass coordinate) are assigned more meshpoints, whereas regions where quantities change slowly can be less well resolved. As a model is evolved, meshpoints are inserted or removed as necessary.

In the STARS code the number of meshpoints K is instead fixed at the beginning of a simulation. These meshpoints are then redistributed during a simulation such that more meshpoints are moved to regions where a higher resolution is required from regions where the requirements are not as high. The

c_1	c_2	c_3	c_4	c_5	c_6	c_7	c_8	c_9	c_{10}	c_{11}
0.02	−0.05	10^{18}	0.45	2×10^4	0.5	0.15	10^{15}	10^{99}	0.1	$5\times10^5/1.0$

Table 2.1: Typical values of the mesh spacing function coefficients, assuming the physical quantities in Eq. (2.26) are in cgs units. The value of c_{11} depends on whether the term concerns T or $\log P$. For stars without a convective envelope $c_{10} = 0$, and a different set of constants is normally used during the AGB phase.

distribution of the meshpoints is decided by a mesh spacing function given by

$$Q(m,r,T,P) = \ln\left(\frac{c_1}{c_1+(m/M)^{2/3}}\right) + c_2\ln\left(\frac{r^2}{c_3}+1\right) + c_4\ln\left(\frac{T}{T+c_5}\right) + \ln\left[P^{c_6}\left(\frac{P+c_8}{P+c_9}\right)^{c_7}\right] + c_{10}\left(\tanh\left(\frac{y-y_{\rm bce}}{c_{11}}\right)-1\right), \quad (2.26)$$

where $c_1 \ldots c_{11}$ are suitably chosen constants (Table 2.1).[2] The last term was introduced during this thesis to increase the resolution at the base of the convective envelope in low-mass stars: y here stands for either T or $\log P$ and $y_{\rm bce}$ is the corresponding value at the base of the envelope.

The meshpoints are distributed at equal intervals of Q, which requires solving an additional equation:

$$\frac{\partial m}{\partial k} = \frac{\mathrm{d}Q}{\mathrm{d}k}\left(\frac{\mathrm{d}Q}{\mathrm{d}m}\right)^{-1} = C\left(\frac{\partial Q}{\partial m} + \frac{\partial Q}{\partial r}\frac{\partial r}{\partial m} + \frac{\partial Q}{\partial T}\frac{\partial T}{\partial m} + \frac{\partial Q}{\partial P}\frac{\partial P}{\partial m}\right)^{-1} \quad (2.27)$$

where k is meshpoint number and C is a constant whose value depends on the total number of meshpoints, the mesh spacing function coefficients, and time. The stellar structure equations for quantities r, P, T, l then become

$$\frac{\partial}{\partial m} \rightarrow \frac{\partial}{\partial k} = \frac{\partial}{\partial m}\frac{\partial m}{\partial k}, \quad (2.28)$$

and time derivatives become

$$\frac{\partial}{\partial t} \rightarrow \frac{d}{dt} = \frac{\partial}{\partial t} + \frac{\partial}{\partial m}\frac{\partial m}{\partial t}. \quad (2.29)$$

The STARS code is thus unusual among stellar evolution codes in that it is not Lagrangian. The original intent behind this approach was that generally fewer meshpoints are required to resolve a stellar model adequately, which speeds up calculations, particularly during phases in which thin shell-burning sources are present (Eggleton, 1971). About 1000 meshpoints are more than sufficient for most applications (as in, increasing the number of meshpoints does not change the results), even for AGB modelling. Discretisation of the equations gives a linear system of equations, which is solved using a Henyey scheme (Henyey, Wilets, Böhm et al., 1959; Henyey, Forbes and Gould, 1964; Kippenhahn et al., 2012).

Time stepping The STARS code uses an adaptive timestep. After a model has converged, the changes δx_i^k in all the variables i at each meshpoint k from the previous model are summed up to get

$$\Delta = \sum_i \sum_k \left|\delta x_i^k\right|. \quad (2.30)$$

[2] Choosing "suitable" values is a rather arcane and dark art. To the author's disappointment, all attempts to find "better" values of $c_1 \ldots c_9$ have proved largely unfruitful.

To set the value of the next timestep, this quantity is compared to a pre-defined value Δ_0 so that the next timestep is

$$\delta t = \delta t_{\rm prev} \times \frac{\Delta_0}{\Delta} \frac{K}{K_0}. \tag{2.31}$$

Larger Δ_0 allows the code to use larger timesteps. The factor K/K_0 makes sure that changing the number of meshpoints does not change the timestep for a given value of Δ_0. To avoid large changes in the timestep from model to model, δt is limited to not differ from $\delta t_{\rm prev}$ too much (more than 15%, by default).

Simulating mass accretion The mass transfer process in real binary systems is a complicated process that depends on the structure of the two stars and the orbital separation and eccentricity. While the STARS code is capable of modelling the two stars simultaneously,[3] and the time-dependent transfer of material between them under different assumptions for the mass (and angular momentum) transfer efficiency, a simpler approach is employed here. To increase the mass of the star, one uses the surface boundary condition

$$\frac{dM}{dt} = \dot{M}_{\rm a}, \tag{2.32}$$

where $\dot{M}_{\rm a}$ is some constant. Since this will add new material to the star, one also needs to consider the surface boundary condition for chemical composition. To simply increase the mass of the model without changing the composition (e.g. to generate a series of models of different masses at a given evolutionary stage), one uses

$$X_i^K - X_i^{K-1} = 0 \tag{2.33}$$

for all species i (meshpoint K denotes the surface). To simulate the accretion of material of a different composition, one can instead use

$$X_i^K - X_i^{\rm a} = 0, \tag{2.34}$$

where $X_i^{\rm a}$ is the mass fraction of species i in the accreted material. The composition gradient between the material originally present in the star and the accreted material resulting from a direct application of Eq. (2.34) is often so steep that the code has convergence issues. To aid convergence, instead of $X_i^{\rm a}$ one typically uses $\frac{1}{2}(X_i^K + X_i^{\rm a})$, so the surface reaches $X_i^K \approx X_i^{\rm a}$ over a few models. This implies that the mass of the region with altered composition is actually slightly smaller than the amount by which the mass of the model is increased. However, since the initial timestep during accretion is small ($\delta t \sim$ yr), this inconsistency is inconsequential.

The values of $X_i^{\rm a}$ are pre-defined. They are set here according to the average ejecta compositions of the AGB models of Lugaro, Karakas, Stancliffe et al. (2012). In other words, $X_i^{\rm a}$ equals $\delta M_i/\delta M$, the total amount of element i lost compared to the total amount of mass lost by their AGB models. AGB models of different initial masses lose different amounts of mass (δM) of different composition (δM_i). Hence, by choosing an appropriate set of $X_i^{\rm a}$, accretion of material from different AGB stars can be simulated without modelling the two stars simultaneously. This allows us to focus only on the subsequent evolution of the accreting star.

This approach also allows us to create a regular grid of models in terms of mass accreted, which we denote by ΔM. Different values of ΔM can be taken to approximate different orbital separations: larger values of ΔM imply larger mass accretion efficiencies, which should be characteristic of more tightly bound binary systems. However, for convenience the mass accretion rate is set to $\dot{M}_{\rm a} = 10^{-6}\ M_\odot\,{\rm yr}^{-1}$ in all models presented in Chapters 4 and 5. This choice is inherited from Stancliffe, Glebbeek, Izzard

[3] In fact, modelling stellar binaries is built in at the very core of the STARS code: in single star mode the companion is simply treated as a point mass at an extremely large distance.

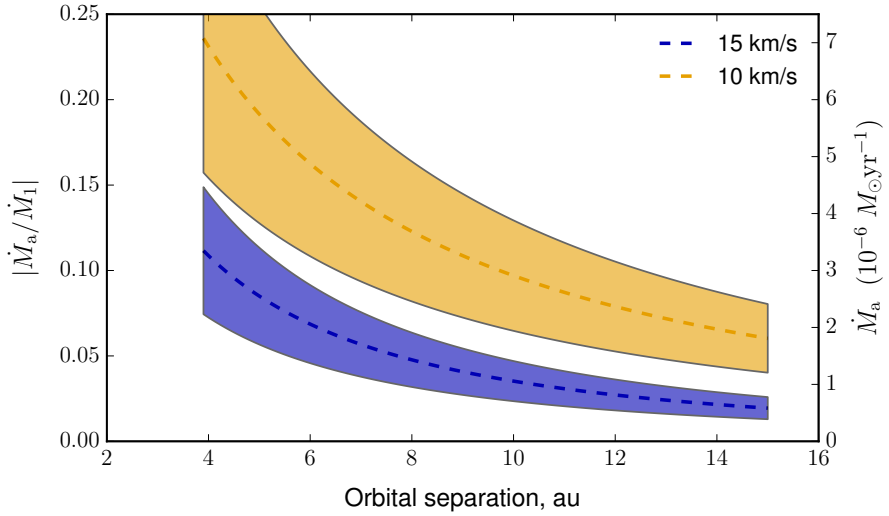

Figure 2.2: Mass accretion efficiency and rates in a system with $M_1 = 1\ M_\odot$ and $M_2 = 0.7\ M_\odot$ assuming BHL-like accretion. The dashed lines correspond to $\dot{M}_1 = 3 \times 10^{-5}\ M_\odot\,\mathrm{yr}^{-1}$ for two different wind velocities. The shaded area shows (on the right y-axis) $\dot{M}_a$ when $\dot{M}_1 = (2\text{–}4) \times 10^{-5}\ M_\odot\,\mathrm{yr}^{-1}$.

et al. (2007) and Stancliffe and Glebbeek (2008), who estimated this value based on the BHL rate given by Eq. (1.20). Figure 2.2 shows an example system with $M_1 = 1\ M_\odot$, $M_2 = 0.7\ M_\odot$. At $a = 10$ au, $\left|\dot{M}_a/\dot{M}_1\right|$ varies between 0.035 and 0.1 for wind velocities between 15 and 10 km s^{-1} (dashed lines). At $a = 5$ au the accretion efficiencies are between 0.085 and 0.19. The corresponding mass accretion rates are close to $10^{-6}\ M_\odot\,\mathrm{yr}^{-1}$ or greater, assuming mass-loss rates of $\dot{M}_1 \simeq (2\text{–}4) \times 10^{-5}\ M_\odot\,\mathrm{yr}^{-1}$ on the AGB (Vassiliadis and Wood, 1993; Ramstedt and Olofsson, 2014).

2.2 Rotating stars

The problem of stellar rotation is at least two-dimensional because of the centrifugal force, which makes the gravity in a rotating star depend not only on the radial coordinate, but also on the angle θ from the rotation axis (Fig. 2.3):

$$\boldsymbol{g}_{\mathrm{eff}} = \left(-\frac{Gm}{r(\theta)^2} + \Omega^2 r(\theta)\sin^2\theta\right)\boldsymbol{e}_r + \left(\Omega^2 r(\theta)\sin\theta\cos\theta\right)\boldsymbol{e}_\theta, \tag{2.35}$$

where Ω is the angular velocity.

Nevertheless, rotating stars can still be reasonably well modelled with a one-dimensional stellar evolution code, provided some modifications to the stellar structure equations are made. These modifications are described in Meynet and Maeder (1997) and generalise those described by Kippenhahn and Thomas (1970) and Endal and Sofia (1976). The following subsections summarise relevant material from the textbook of Maeder (2009).

2.2.1 Shellular rotation

Generally, Ω can depend on both r and θ. However, it was argued by Zahn (1992) that any horizontal shear would induce strong anisotropic turbulence because of the low viscosity of stellar material. By anisotropic,

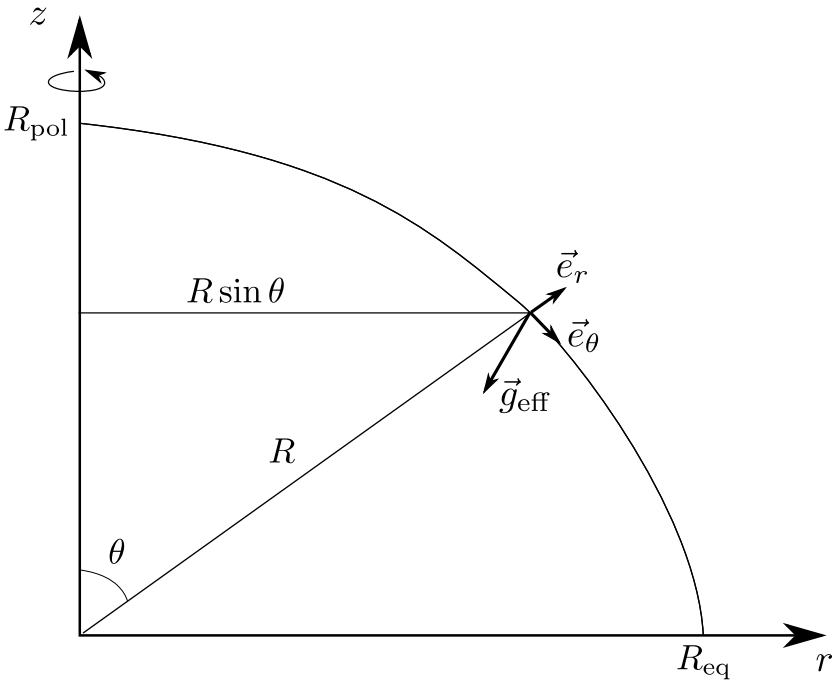

Figure 2.3: The two-dimensional nature of rotation. The radius of a non-rotating star is everywhere the same ($R(\theta) = R_{\rm pol} = R_{\rm eq}$) and the gravity $\boldsymbol{g}_{\rm eff}$ points towards the centre, but in a rotating star both R and $\boldsymbol{g}_{\rm eff}$ depend on the angle from the rotation axis θ because of the centrifugal acceleration.

he distinguished the r and θ directions: turbulence is free to develop only in the θ (horizontal) direction. Such turbulence would enforce $\Omega(r,\theta) \approx \Omega(P)$. This insight allowed Meynet and Maeder (1997) to adapt the earlier work of Kippenhahn and Thomas (1970) and Endal and Sofia (1976) and formulate the equations of stellar structure on isobars, which generally no longer coincide with equipotentials. In particular, the isobaric surfaces are given by constant values of

$$\Psi = -\frac{Gm}{r} - \frac{1}{2}\Omega^2 r^2 \sin^2\theta. \tag{2.36}$$

In cases with $\Omega(r,\theta) = \text{const}$ these are also equipotential surfaces because then $\vec{\nabla}\Psi = \left(\frac{\partial\Psi}{\partial r}, \frac{1}{r}\frac{\partial\Psi}{\partial\theta}, 0\right) = -\boldsymbol{g}_{\rm eff}$ (see Eq. (2.35)). But generally,

$$\frac{\partial\Psi}{\partial r} = \frac{Gm}{r^2} - \Omega^2 r\sin^2\theta - r^2\sin^2\theta\Omega\frac{\partial\Omega}{\partial r}, \tag{2.37}$$

$$\frac{1}{r}\frac{\partial\Psi}{\partial\theta} = -\Omega^2 r\sin\theta\cos\theta - r^2\sin^2\theta\Omega\frac{1}{r}\frac{\partial\Omega}{\partial\theta} \tag{2.38}$$

and hence

$$\boldsymbol{g}_{\rm eff} = -\vec{\nabla}\Psi - r^2\sin^2\theta\Omega\vec{\nabla}\Omega = \frac{1}{\rho}\vec{\nabla}P, \tag{2.39}$$

where the second equality expresses hydrostatic equilibrium.

Formulated on isobars, the equations of stellar structure largely remain the same, but the interpretation of some of the physical variables changes. In particular, for an isobaric surface with area S_P enclosing

volume V_P one can define the radius r_P of a sphere of the same volume:

$$r_P = \left(\frac{3V_P}{4\pi}\right)^{\frac{1}{3}}. \tag{2.40}$$

This is the radial coordinate to be used in rotating stars with shellular rotation. Geometrically, it corresponds roughly to $r(\theta_0) = r(54.7°)$ where $\sin^2\theta_0 = 2/3$. Other quantities q represent their averages on an isobar, formally defined according to

$$\langle q \rangle = \frac{1}{S_P}\int q \, \mathrm{d}s_P \,, \tag{2.41}$$

where $\mathrm{d}s_P$ is a surface element of the isobar.

2.2.2 Modifications to stellar structure equations

By introducing $\alpha = |\partial\Omega/\partial\Psi|$ such that $\nabla\Omega = -\alpha\nabla\Psi$, one can write the modulus of $\boldsymbol{g}_{\mathrm{eff}}$ as

$$g_{\mathrm{eff}} = \left(1 - r(\theta)^2 \sin^2\theta\Omega\alpha\right)\frac{\partial\Psi}{\partial r_P}, \tag{2.42}$$

which gives for the equation of hydrostatic equilibrium

$$\frac{\partial P}{\partial r_P} = -\rho g_{\mathrm{eff}} = -\rho\left(1 - r(\theta)^2 \sin^2\theta\Omega\alpha\right)\frac{\partial\Psi}{\partial r_P}. \tag{2.43}$$

If the mass enclosed by an isobaric surface is m_P, then $\mathrm{d}m_P = \int \rho \, \mathrm{d}r_P \, \mathrm{d}s_P = \mathrm{d}\Psi \int \rho \, (\partial r_P/\partial\Psi) \, \mathrm{d}s_P$. With the above two equations and Eq. (2.41) this becomes

$$\frac{\partial P}{\partial m_P} = -\frac{1}{\langle g_{\mathrm{eff}}^{-1}\rangle S_P}. \tag{2.44}$$

If we define

$$f_P = \left(\frac{4\pi r_P^2}{S_P}\right)\frac{1}{\left(Gm_P/r_P^2\right)\langle g_{\mathrm{eff}}^{-1}\rangle}, \tag{2.45}$$

we get the equation of hydrostatic equilibrium in shellular rotation (cf. Eq. (2.7)):

$$\frac{\partial P}{\partial m_P} = -\frac{Gm_P}{4\pi r_P^4} f_P. \tag{2.46}$$

The continuity equation also remains similar to its non-rotating form,

$$\frac{\partial r_P}{\partial m_P} = \frac{1}{4\pi r_P^2 \bar{\rho}}, \tag{2.47}$$

if one uses the density in the volume element between neighbouring isobars $\bar{\rho}$ (approximately equal to the average density on an isobar, although formally not the same). To this measure of density, one can assign a temperature $\bar{T}$ via the equation of state. If the energy generation rates and opacities are then

evaluated at this pair of $\bar{\rho}$ and $\bar{T}$ to yield $\bar{\varepsilon}$ and $\bar{\kappa}_{\rm tot}$, Eq. (2.8) becomes

$$\frac{\partial l_P}{\partial m_P} = \bar{\varepsilon}, \tag{2.48}$$

and from Eqs. (2.10) and (2.46) the energy transport equation becomes

$$\frac{\partial \bar{T}}{\partial m_P} = -\frac{G m_P}{4\pi r_P^4}\frac{\bar{T}}{P} f_P \bar{\nabla}. \tag{2.49}$$

In convective regions $\bar{\nabla} \approx \bar{\nabla}_{\rm ad}$ (Eq. (2.13)). In radiative regions we have, via Eqs. (2.24), (2.43) and (2.44),

$$\mathcal{F}_{\rm rad} + \mathcal{F}_{\rm cond} = \frac{l_P}{S_P} = -\frac{4ac\bar{T}^3}{3\bar{\kappa}}\frac{\partial \bar{T}}{\partial m_P} g_{\rm eff}\langle g_{\rm eff}^{-1}\rangle S_P. \tag{2.50}$$

From here we get via Eq. (2.11) that

$$\frac{\partial \bar{T}}{\partial m_P} = -\frac{G m_P}{4\pi r_P^4}\frac{\bar{T}}{P}\bar{\nabla}_{\rm rad}\left[\left(\frac{4\pi r_P^2}{S_P}\right)^2 \frac{1}{\langle g_{\rm eff}\rangle\langle g_{\rm eff}^{-1}\rangle}\right], \tag{2.51}$$

where $g_{\rm eff}$ has been replaced by $\langle g_{\rm eff}\rangle$. To retain the form of Eq. (2.49), we require in radiative regions $\bar{\nabla} = \frac{f_T}{f_P}\bar{\nabla}_{\rm rad}$, which defines the second deformation parameter:

$$f_T = \left(\frac{4\pi r_P^2}{S_P}\right)^2 \frac{1}{\langle g_{\rm eff}\rangle\langle g_{\rm eff}^{-1}\rangle}. \tag{2.52}$$

Thus the equations of stellar structure of stars with shellular rotation profiles remain the same as those for their non-rotating counterparts, except for the deformation parameters f_P and f_T, which tend to unity as the rotation rate goes to zero.

2.2.3 The surface of the star and critical rotation

The surface of a star is given by $\Psi = \text{const}$. Since at the pole $\theta = 0$, $\Psi = -GM/R_{\rm pol}$, and from Eq. (2.36) we have that the surface is given by the isobar

$$\frac{GM}{R(\theta)} + \frac{1}{2}\Omega^2 R(\theta)^2 \sin^2\theta = \frac{GM}{R_{\rm pol}}. \tag{2.53}$$

Unless our star is to have mountains, this surface must also be an equipotential.[4]

When the centrifugal acceleration equals the gravitational acceleration, the star is said to be at critical rotation. This happens first at the equator, where the centrifugal acceleration is largest ($\sin\theta = 1$). The radial component of $\boldsymbol{g}_{\rm eff}$ disappears when

$$\Omega = \Omega_{\rm c} = \sqrt{\frac{GM}{R_{\rm eq,c}^3}}, \tag{2.54}$$

[4] To be precise, the surface is indeed an equipotential but not exactly an isobar. Rigorously, owing to Eq. (2.39) the equation should have another (comparatively small) term on the left-hand side (Maeder, 2009). However, Eq. (2.53) still applies to the outermost isobar, as well as any isobar within the star when M, R and $R_{\rm pol}$ are replaced by the local values (m_P, r and $r_{\rm pol}$, respectively).

where $R_{\rm eq,c}$ is the equatorial radius at critical rotation. Inserting this into the surface equation above gives

$$R_{\rm eq,c} = \frac{3}{2} R_{\rm pol,c}. \tag{2.55}$$

Hence, at critical rotation the equatorial radius is 1.5 times as large as the polar radius. It is the equatorial radius that changes substantially as the rotation rate is increased. The polar radius stays approximately constant (Ekström, Meynet, Maeder et al., 2008), i.e. $R_{\rm pol,c} \approx R_{\rm pol}$. Introducing $x = R/R_{\rm pol}$ and $\omega = \Omega/\Omega_{\rm c}$ into Eq. (2.53) we get (Georgy, Meynet and Maeder, 2011)

$$4x^3\omega^2 \sin^2\theta - 27x + 27 = 0. \tag{2.56}$$

For a given $\omega \in [0, 1]$ the equation has three roots, the only physical one of which relates the isobaric radius R_P to the polar radius $R_{\rm pol}$. At critical rotation

$$R_{P,\rm c} \approx 1.15 R_{{\rm pol},c}. \tag{2.57}$$

As the effective gravity disappears when $\Omega_{\rm c}^2 R_{\rm eq} = GM/R_{\rm eq}^2$, at the isobaric radius, where $\sin^2\theta = 2/3$, we have instead

$$\frac{\frac{2}{3}\Omega_{\rm c}^2 R_P}{GM/R_P^2} = \frac{2}{3}\left(\frac{R_{P,\rm c}}{R_{\rm eq,c}}\right)^3 \approx \frac{2}{3}\left(\frac{1.15}{1.5}\right)^3 \approx 0.3, \tag{2.58}$$

and hence in terms of the isobaric radius the critical rotation rate is given by

$$\Omega_{\rm c} \approx \sqrt{0.45\frac{GM}{R_{P,\rm c}^3}}. \tag{2.59}$$

2.2.4 Transport of angular momentum

The internal transport of specific angular momentum $j = \Omega r_P^2$ is in general governed by an advection-diffusion equation that expresses the internal conservation of angular momentum:

$$\frac{\partial j}{\partial t} = \frac{1}{5\bar{\rho} r_P^2}\frac{\partial}{\partial r_P}\left(\bar{\rho} r_P^2 j U\right) + \frac{1}{\bar{\rho} r_P^2}\frac{\partial}{\partial r_P}\left(\bar{\rho} r_P^4 \left(D_{\rm rot} + D_{\rm conv}\right)\frac{\partial \Omega}{\partial r_P}\right), \tag{2.60}$$

where $D_{\rm rot} = D_{\rm rot}(r_P)$ is the diffusion coefficient for diffusive transport in radiative zones, $D_{\rm conv} = D_{\rm conv}(r_P)$ is the diffusion coefficient in convective zones (Sect. 3.2.1), and $U = U(r_P)$ accounts for advective transport. The meridional circulation velocity U arises as a result of the local breakdown of radiative equilibrium (Sect. 1.3.2). Its evaluation is very complicated and involves spatial derivatives of Ω of up to third order, making the equation fourth order in space (Zahn, 1992; Maeder and Zahn, 1998). In an attempt to capture this complexity at lower spatial order, Potter et al. (2012b), on whose work the current implementation of rotation in the STARS code is based on (Sect. 2.2.6), introduced additional constants in the evaluation of U that have to be calibrated against observations or other models, which makes the approach rather ad-hoc.

Alternatively, the meridional circulation can also be modelled as a diffusive process associated with a diffusion coefficient that enters $D_{\rm rot}$. This reduces Eq. (2.60) to a diffusion equation:

$$\frac{\partial j}{\partial t} = \frac{\partial}{\partial m_P}\left(\mathcal{D}_{\rm rot} r_P^2 \frac{\partial \Omega}{\partial m_P}\right), \tag{2.61}$$

with $\mathcal{D}_{\rm rot} = \left(4\pi r_P^2 \bar{\rho}\right)^2 (D_{\rm rot} + D_{\rm conv})$. This approach to modelling the internal transport of angular momentum has a long tradition and is adopted in many actively used stellar evolution codes (e.g. Pinsonneault, Kawaler, Sofia et al., 1989; Heger, Langer and Woosley, 2000; Yoon and Langer, 2004; Paxton, Cantiello, Arras et al., 2013).

2.2.5 Diffusion coefficients

The diffusive approach to modelling the internal evolution of angular momentum is also adopted in this work, and this section gives the terms entering Eq. (2.61) via $D_{\rm rot}$. The medium in a rotating star is subject to a host of instabilities that can result in angular momentum redistribution. Two of the more important transport processes, meridional (Eddington-Sweet) circulation and shear (dynamical and secular) mixing, were already mentioned in Sect. 1.3.2. Following Heger et al. (2000), the STARS code also accounts for the GSF (Goldreich and Schubert, 1967; Fricke, 1968) and Solberg-Høiland instabilities (Wasiutynski, 1946).

In most cases, the diffusion coefficients associated with each instability are expressed as a product of some characteristic velocity v and a typical length-scale (typically the scale height H_v of the corresponding velocity). For example, the diffusion coefficient associated with the Eddington-Sweet circulation is written as $D_{\rm ES} = H_{v,{\rm ES}} v_{\rm ES}$. The separate diffusion coefficients are then summed up to get the total diffusion coefficient $D_{\rm rot}$ (Heger et al., 2000):

$$D_{\rm rot} = D_{\rm ES} + D_{\rm SSI} + D_{\rm DSI} + D_{\rm GSF} + D_{\rm SH}. \tag{2.62}$$

The velocities corresponding to the Eddington-Sweet circulation (Kippenhahn, 1974), the secular shear instability (Endal and Sofia, 1978), and the GSF instability (Endal and Sofia, 1978) are, respectively,[5]

$$v_{\rm ES} = \max\left\{|v_{\rm e}| - |v_\mu|, 0\right\}, \tag{2.63}$$

$$v_{\rm SSI} = \sqrt{\frac{\left(\mu_{\rm p} + \mu_{\rm r}\right)}{\rho \mathcal{R}e_{\rm c}} \left(r \frac{\partial \Omega}{\partial r}\right)}, \tag{2.64}$$

$$v_{\rm GSF} = \max\left\{\left|\frac{2H_T}{H_j} \frac{\partial \ln \Omega}{\partial \ln r} v_{\rm e}\right| - |v_\mu|, 0\right\} \tag{2.65}$$

with

$$v_{\rm e} = \frac{2\nabla_{\rm ad}}{\delta\left(\nabla_{\rm ad} - \nabla_{\rm rad}\right)} \frac{\Omega^2 r^5}{(Gm)^2} \left(\varepsilon_{\rm nuc} + \varepsilon_\nu - \frac{l}{m} - \frac{3l}{8\pi r^3 \rho}\right), \tag{2.66}$$

$$v_\mu = \frac{H_P r\left(l - m\varepsilon_\nu\right)}{Gm^2} \frac{\frac{\varphi}{\delta}\nabla_\mu}{\left(\nabla_{\rm rad} - \nabla_{\rm ad}\right)}. \tag{2.67}$$

In these equations, $\mu_{\rm p}$ and $\mu_{\rm r}$ are the plasma and radiation viscosity coefficients (Schatzman, 1977; Maeder, 2009); $\mathcal{R}e_{\rm c}$ is the critical Reynolds number; H_T and H_j are the temperature and angular momentum scale heights; $\varepsilon_{\rm nuc}$ and ε_ν are the energy generation rates due to nuclear reactions and neutrino losses ($\varepsilon_\nu < 0$); $\delta = -\left(\partial \ln \rho / \partial \ln T\right)_{P,\mu}$; $\varphi = \left(\partial \ln \rho / \partial \ln \mu\right)_{P,T}$ and ∇_μ is defined in analogy with $\nabla_{\rm rad}$ as the variation of the mean molecular weight with depth:

$$\nabla_\mu = \frac{\partial \ln \mu}{\partial \ln P}. \tag{2.68}$$

[5] Henceforth the subscripts and over-bars are generally omitted for simplicity.

As sketched in Sect. 1.3.2, the Richardson number has to exceed a certain value for the medium to be dynamically stable against shear, i.e. $\mathcal{R}i > \mathcal{R}i_\mathrm{c} = 1/4$. This can be more conveniently expressed as

$$\mathcal{R}i = N^2 \left(r \frac{\partial \Omega}{\partial r} \right)^{-2} > \mathcal{R}i_\mathrm{c}, \tag{2.69}$$

where

$$N^2 = N_T^2 + N_\mu^2 = \frac{g_\mathrm{eff} \delta}{H_P} \left(\nabla_\mathrm{ad} - \nabla_\mathrm{rad} \right) + \frac{g_\mathrm{eff} \varphi}{H_P} \nabla_\mu \tag{2.70}$$

is the Brunt-Väisälä frequency. Medium with $N^2 < 0$ is unstable to convection according to the Ledoux criterion. In chemically homogeneous regions the condition $N^2 < 0$ reduces to the Schwarzschild criterion given by Eq. (2.14). The diffusion coefficient associated with the dynamical shear instability is taken to be

$$D_\mathrm{DSI} = \frac{H_P^2}{\tau_\mathrm{dyn}} \min \left[1, \left(1 - \min \left\{ \mathcal{R}i / \mathcal{R}i_\mathrm{c}, 1 \right\} \right)^2 \right], \tag{2.71}$$

where $\tau_\mathrm{dyn} = \sqrt{r^3 / (Gm)}$ is the local dynamical timescale, and the term in the brackets gradually turns on the instability in the range $0 < \mathcal{R}i < \mathcal{R}i_\mathrm{c}$. The secular shear instability sets in if $\mathcal{R}i > \mathcal{R}i_\mathrm{c}$ but

$$\max \left\{ \frac{\mathcal{R}e_\mathrm{c}}{8} \frac{\left(\mu_\mathrm{p} + \mu_\mathrm{r} \right)}{\kappa_T \rho} N_T^2, N_\mu^2 \right\} \left(r \frac{\partial \Omega}{\partial r} \right)^{-2} < \mathcal{R}i_\mathrm{c}. \tag{2.72}$$

The thermal diffusivity κ_T is given by Eq. (3.6).

There is no condition for stability against meridional circulation other than $\Omega(r) = 0$. In other words, meridional currents will arise in a rotating star (Eq. (2.66)). For the GSF instability to set in, it is sufficient to violate $\partial \Omega / \partial z = 0$, where z is the vertical coordinate parallel to the rotation axis. This is always the case in shellular rotation, so we expect the medium to be GSF-unstable as long as there is some differential rotation (Eq. (2.65)). Nevertheless, the transport of angular momentum resulting from both of these instabilities is inhibited in chemically inhomogeneous regions (Mestel, 1953; Pinsonneault et al., 1989). This effect is modelled by the so-called μ-current velocity v_μ in Eqs. (2.63) and (2.65), following Kippenhahn (1974). However, various observational constraints indicate that applying v_μ as given by Eq. (2.67) tends to inhibit the transport too much. Thus, the effectiveness of μ-gradients is artificially reduced by replacing ∇_μ with $f_\mu \nabla_\mu$ (Pinsonneault et al., 1989). By default, $f_\mu = 0.05$ (Heger et al., 2000).

Finally, the Solberg-Høiland instability leads to mixing on the dynamical timescale if

$$\mathcal{R}_\mathrm{SH} = N^2 + \frac{1}{r^3} \frac{\partial j^2}{\partial r} < 0. \tag{2.73}$$

Thus, a region in a star will be stabilised against convection if j locally increases outwards and destabilised if j locally decreases outwards. The associated diffusion coefficient is taken to be

$$D_\mathrm{SH} = \frac{H_P^2}{\tau_\mathrm{dyn}} \left(\frac{r \mathcal{R}_\mathrm{SH}}{g_\mathrm{eff}} \right)^2. \tag{2.74}$$

2.2.6 Numerical implementation

The implementation follows closely that of Adrian Potter, who was kind enough to share the version of the STARS code described in Potter et al. (2012b) and Potter, Tout and Brott (2012a) and his PhD thesis

(Potter, 2012).

The main approximation, compared to what is described above, is that the density is assumed to be uniform on isobars, i.e. $\bar{\rho} = \langle\rho\rangle = \rho$. This approximation is based on the assumption that the horizontal (θ-direction) turbulence is strong enough to make density variations on isobars negligible (Zahn, 1992).

Isobaric surfaces The surface element of a spherical surface can be written as $\mathrm{d}s = r^2 \sin\theta \,\mathrm{d}\theta \,\mathrm{d}\varphi$, where φ is the longitude such that $\dot{\varphi} = \Omega$ and $\int \mathrm{d}\varphi = 2\pi$. The surface element of an isobaric surface is instead (Maeder, 2009)

$$\mathrm{d}s_P = \frac{r(\theta)^2 \sin\theta}{\cos\epsilon} \,\mathrm{d}\theta \,\mathrm{d}\varphi\,, \tag{2.75}$$

where ϵ is the angle between $-\boldsymbol{g}_{\mathrm{eff}}$ and $\boldsymbol{e}_r$ in Fig. 2.3. With the effective gravity written in terms of ω and x (Sect. 2.2.3) as

$$g_{\mathrm{eff}} = \frac{Gm}{r_{\mathrm{pol}}^2} \sqrt{\left(-\frac{1}{x^2} + \frac{8}{27}\omega^2 x \sin^2\theta\right)^2 + \left(\frac{8}{27}\omega^2 x \sin\theta\cos\theta\right)^2}\,, \tag{2.76}$$

the angle ϵ is given by the cosine theorem:

$$\cos\epsilon = -\frac{\boldsymbol{g}_{\mathrm{eff}} \cdot \boldsymbol{e}_r}{|\boldsymbol{g}_{\mathrm{eff}}|\,|\boldsymbol{e}_r|} = \frac{\frac{1}{x^2} - \frac{8}{27}\omega^2 x \sin^2\theta}{\sqrt{\left(-\frac{1}{x^2} + \frac{8}{27}\omega^2 x \sin^2\theta\right)^2 + \left(\frac{8}{27}\omega^2 x \sin\theta\cos\theta\right)^2}}. \tag{2.77}$$

x and ω are obtained by solving Eq. (2.56) using the Newton-Raphson method. In the current version of the code the integral in Eq. (2.41) is first evaluated using the trapezium rule, dividing the integration domain into a few segments of $\delta\theta$. Then Romberg's method (Romberg, 1955) is used, which combines halving the size of $\delta\theta$ with Richardson extrapolation (Richardson, 1911) to converge to a given precision. The number of segments required to reach a specified precision is much smaller than without Romberg's method. However, the models presented in this thesis were computed with an earlier version of the code, in which the integral of Eq. (2.41) is replaced with a sum, with the quantities evaluated at forty angles $\theta_i \in [0, \pi]$, as in Potter et al. (2012b).

Angular momentum accretion Angular momentum accretion is treated in the same way as accretion of non-standard chemical composition (Sect. 2.1.5). The mass added in a timestep is assigned specific angular momentum j_{a} so that adding a mass ΔM to a model results in adding angular momentum $\Delta J = j_{\mathrm{a}} \Delta M$. To implement this, the surface boundary condition is modified from

$$\Omega_K - \Omega_{K-1} = 0, \tag{2.78}$$

which in absence of mass loss or gain prevents angular momentum loss or gain at the surface, to

$$j_K - j_{\mathrm{a}} = 0. \tag{2.79}$$

As for X_i^{a}, this boundary condition is softened by using $\frac{1}{2}(j_K + j_{\mathrm{a}})$ instead of j_{a}.

CHAPTER 3

Modelling the chemical evolution of stars

The chemical structure of the star changes with time as a result of nuclear burning and internal transport of material by different mechanisms. Formally this is expressed by an advection-diffusion equation:

$$\frac{\partial X_i}{\partial t} = R_i + \frac{\partial}{\partial m}\left(\mathcal{D}_{\mathrm{mix},i}\frac{\partial X_i}{\partial m}\right) - \frac{\partial}{\partial m}\left(\mathcal{W}_i X_i\right), \tag{3.1}$$

where X_i is the mass fraction of species i, R_i accounts for its nuclear production/destruction, $\mathcal{D}_{\mathrm{mix},i} = \left(4\pi r^2 \rho\right)^2 D_{\mathrm{mix},i}$, and $\mathcal{W}_i = 4\pi r^2 \rho w_i$. This chapter principally describes the evaluation of the transport terms entering Eq. (3.1). The diffusion coefficient $D_{\mathrm{mix},i}$ is developed in Sect. 3.2 and the velocity w_i in Sect. 3.3.

3.1 Chemical species and nuclear network

By default, the STARS code solves Eq. (3.1) for seven chemical species: ^{1}H, ^{3}He, ^{4}He, ^{12}C, ^{14}N, ^{16}O, ^{20}Ne. Three others – ^{24}Mg, ^{28}Si and ^{56}Fe – are included in the computation of, e.g. the mean molecular weight of the medium, but no equations corresponding to their abundances are solved. Their abundances thus remain fixed at all times. We have added equations for these three species, such that their abundances can change as a result of mixing processes (nuclear conversion of these species does not occur in unevolved low-mass stars).

In astronomical parlance the total abundance of "metals" is

$$Z = \sum_{i \neq \mathrm{H,He}} X_i. \tag{3.2}$$

However, in stellar evolution codes the size of the network is limited. Therefore, the sum of the mass fractions of the metals included in the network will be smaller than the desired $Z = 1 - X_{\mathrm{H}} - X_{\mathrm{He}}$ when the abundances are set to some physical scale (such as the Sun). A typical solution is to add the remainder (in the STARS case this is about $\delta Z \approx 0.05Z$) to one of the more massive species, but then the abundance of that element is no longer representative of any physical scale. To avoid this, we have introduced an extra pseudo-species in the code whose abundance is set to δZ. This pseudo-species is assigned the properties (atomic and mass numbers) of one of the existing species (by default ^{28}Si), but its abundance remains fixed at all times throughout the star. In this way, the pseudo-species contributes to the density and molecular weight, but allows the abundances of all real elements to remain consistent.

Reaction chain	Q value (MeV)
$^1H + {}^1H \rightarrow {}^2H + {}^1H \rightarrow {}^3He$	6.936
$^3He + {}^3He \rightarrow {}^4He + {}^1H + {}^1H$	12.860
$^4He + {}^3He \rightarrow {}^7Be \rightarrow {}^7Li + {}^1H \rightarrow {}^4He + {}^4He$	19.796
$^4He + {}^3He \rightarrow {}^7Be + {}^1H \rightarrow {}^8B \rightarrow {}^8Be \rightarrow {}^4He + {}^4He$	18.774
$^{12}C + {}^1H \rightarrow {}^{13}N \rightarrow {}^{13}C + {}^1H \rightarrow {}^{14}N$	11.715
$^{14}N + {}^1H \rightarrow {}^{15}O \rightarrow {}^{15}N + {}^1H \rightarrow {}^{12}C + {}^4He$	15.017
$^{14}N + {}^1H \rightarrow {}^{15}O \rightarrow {}^{15}N + {}^1H \rightarrow {}^{16}O$	22.179
$^{16}O + {}^1H \rightarrow {}^{17}F \rightarrow {}^{17}O + {}^1H \rightarrow {}^{14}N + {}^4He$	5.573
$^4He + {}^4He + {}^4He \rightarrow {}^{12}C$	7.275

Table 3.1: Nuclear reaction chains relevant for evolution of low-mass stars up to core helium flash and the associated energy release.

The species from ^1H to ^{24}Mg are part of a nuclear reaction network, meaning they can be converted into other species as a result of nuclear reactions. All the models computed during this research were terminated at the tip of the red giant branch. The relevant nuclear reactions up to that point of evolution are those making up the pp chains and the CNO cycle. Some of the nuclei involved in these reaction chains, e.g. ^2H and ^{13}C are not followed by the STARS code. These minor nuclei are assumed by the code to be in equilibrium with their progenitor nuclei. For example, the pp chain is assumed to convert three protons directly into ^3He at the rate at which ^1H is converted into ^2H. The energy release, however, takes into account all the stages. Table 3.1 summarises the reaction chains in the code relevant for evolution up to the core helium flash. Most of the individual reaction rates are from Caughlan and Fowler (1988).

3.2 Diffusive mixing

3.2.1 Convection

Regions with $\nabla_{\rm rad} > \nabla_{\rm ad}$ are unstable to convection. Convective mixing is modelled as a diffusive process with a diffusion coefficient

$$D_{\rm conv} = \frac{1}{3} v \ell, \tag{3.3}$$

where v is given by the mixing length theory and ℓ by Eq. (2.16). For convergence reasons, near the boundaries of convective regions the diffusion coefficient is reduced and behaves like $D_{\rm conv} \sim (\nabla_{\rm rad} - \nabla_{\rm ad})^2$ (Eggleton, 1972). A harmonic mean between this modified coefficient and the one given by MLT ensures a smooth transition between the two coefficients.

3.2.2 Thermohaline mixing

The regime of thermohaline mixing (Sect. 1.3.1) corresponds formally to $0 \leq \mathcal{R} \equiv \frac{(R_0-1)}{(\kappa_T/\kappa_\mu-1)} \leq 1$ (Brown, Garaud and Stellmach, 2013), where κ_T and κ_μ are the thermal and compositional diffusivities, and

$$R_0 = \frac{\nabla_{\rm rad} - \nabla_{\rm ad}}{\frac{\varphi}{\delta}\nabla_\mu}. \tag{3.4}$$

Outside the regime of thermohaline mixing the fluid is stable if $\mathcal{R} > 1$ ($R_0 > \kappa_T/\kappa_\mu > 1$) and unstable to regular convection if $\mathcal{R} < 0$ ($R_0 < 1$). The mixing is modelled as a diffusion process, and the formulation

used here comes from Denissenkov (2010) who derives

$$D_\mu = C\frac{\left(\kappa_T - \kappa_\mu R_0\right)}{(R_0 - 1)}, \tag{3.5}$$

where $C \approx 5$ is a factor deriving from geometrical considerations. The corresponding effective finger length-to-diameter ratio is about 0.5, similar to that derived by Kippenhahn, Ruschenplatt and Thomas (1980).[1] The diffusivities are

$$\kappa_T = \frac{4acT^3}{3\kappa_{\rm tot}\rho^2 c_P}, \tag{3.6}$$

$$\kappa_\mu = 1.84\times10^{-17}\frac{T^{5/2}}{\rho}\left(1+7X_{\rm H}\right)\ {\rm cm^2\,s^{-1}}. \tag{3.7}$$

3.2.3 Rotational mixing

The rate and extent of angular momentum transport is determined by the diffusion coefficient $D_{\rm rot}$ described in Sect. (2.2.5). Transport of chemical species by meridional currents should introduce horizontal μ-gradients. However, according to the work of Zahn (1992), horizontal turbulence works to rapidly smear out these gradients (Maeder, 1999; Mathis, Palacios and Zahn, 2004), severely limiting the transport of chemicals to a slow diffusive process (Chaboyer and Zahn, 1992; Maeder and Zahn, 1998). Chaboyer and Zahn (1992) derive that the rate of chemical transport by meridional circulation and shears is thus only about 1/30 that of the transport of angular momentum. Observed surface abundances of stars also indicate that mixing of chemicals cannot be very efficient. As in Pinsonneault, Kawaler, Sofia et al. (1989) and Heger, Langer and Woosley (2000), we thus reduce the rotational mixing diffusion coefficient and use $f_c D_{\rm rot} = f_c\left(D_{\rm ES} + D_{\rm SSI} + D_{\rm DSI} + D_{\rm GSF} + D_{\rm SH}\right)$ for chemical mixing with $f_c = 1/30$ (Heger et al., 2000).

3.2.4 Total mixing coefficient

To summarise, the full diffusion coefficient $D_{{\rm mix},i}$ entering Eq. (3.1) via $\mathcal{D}_{{\rm mix},i}$ is given by

$$D_{{\rm mix},i} = D_{\rm conv} + D_\mu + D_i + f_c D_{\rm rot}, \tag{3.8}$$

where D_i is the concentration diffusion coefficient (Paquette, Pelletier, Fontaine et al., 1986). In convective regions $D_{{\rm mix},i} \approx D_{\rm conv}$, whereas in radiative regions $D_{\rm conv} = 0$ and $D_{{\rm mix},i} = D_\mu + D_i + f_c D_{\rm rot}$.

3.3 Atomic diffusion

The advective term on the right-hand-side of Eq. (3.1) was introduced into the STARS code by Stancliffe and Glebbeek (2008) based on the earlier work of Pelletier, Fontaine, Wesemael et al. (1986), Paquette et al. (1986) and Proffitt and Michaud (1991). After briefly describing their implementation in Sect. 3.3.1, we describe how radiative forces have been accounted for as part of the framework in Sect. 3.3.2.

[1] We have since updated the STARS code, providing the option to also model thermohaline mixing according to the parameter-free model of Brown et al. (2013). The results are rather similar among the three prescriptions (i.e. Kippenhahn et al., 1980; Denissenkov, 2010; Brown et al., 2013) in the context of mass accretion from an AGB donor.

3.3.1 The diffusion velocity

The expression for the diffusion velocity $w_i = \mathcal{W}_i / \left(4\pi r^2 \rho\right)$ entering Eq. (3.1) is based on the kinetic theory of gases (Burgers, 1969; Chapman and Cowling, 1970) and consists of three terms (Talon, 2008):

$$w_i = \frac{D_i}{k_\mathrm{B} T} \left[g\,(\mu - \mu_i) + k_\mathrm{B} \alpha_{\mathrm{T},i} \frac{\partial T}{\partial r} + \mu_i g_{\mathrm{r},i} \right]. \tag{3.9}$$

Here D_i and $\alpha_{\mathrm{T},i}$ are the atomic and thermal diffusion coefficients, both taken from Paquette et al. (1986), and g and $g_{\mathrm{r},i}$ are the gravitational and radiative accelerations. The mean molecular weight μ of the plasma is given by

$$\mu = \left(\sum \frac{X_i}{m_i} \left[1 + \bar{Z}_i \right] \right)^{-1}, \tag{3.10}$$

and the molecular weights μ_i of the constituent elements with atomic masses m_i are $\mu_i = m_i / \left(1 + \bar{Z}_i\right)$. The effective charges of the elements are given by

$$\bar{Z}_i = \sum_{j=0}^{Z_i} j N_{i,j}, \tag{3.11}$$

where $N_{i,j}$ is the number fraction of ions of element i in the ionisation stage j ($j = 0$ corresponds to the neutral state; by definition, $0 \leq \bar{Z}_i \leq Z_i$ and $\sum_j N_{i,j} = 1$).

The first term in Eq. (3.9) accounts for pressure diffusion and expresses the fact that elements heavier than the mean molecular weight of the plasma experience an excess gravitational force $g\,(\mu_i - \mu)$, as a result of which they tend to gradually sink with respect to the lighter elements. This is commonly referred to as gravitational settling. In a main sequence star only hydrogen is lighter than the mean molecular weight. Gravitational settling thus leads to an increasingly hydrogen-rich surface as all other elements settle deeper into the star. The second term in Eq. (3.9) accounts for temperature diffusion, which causes a similar effect. These two processes are opposed by concentration diffusion, which is already included in Eq. (3.1) via Eq. (3.8). The fundamental theory describing these types of diffusion is given in Burgers (1969) and Chapman and Cowling (1970). The third term in Eq. (3.9) has been added as part of this research as an extension of the work of Stancliffe and Glebbeek (2008). This term accounts for radiative forces selectively accelerating the elements in the plasma against gravity (Sect. 3.3.2).

The STARS treatment of element diffusion is appropriate for trace elements, meaning $n_i \ll n_b$ for some background species b. We take hydrogen to be the background at all times. For hydrogen itself the diffusion velocity is obtained from imposing mass conservation: $X_\mathrm{H} w_\mathrm{H} = -\sum_{i \neq \mathrm{H}} X_i w_i$. Diffusion in regions where hydrogen is not dominant is ignored. In the models presented here this only concerns the hydrogen-exhausted core that develops near the end of the main sequence, and should have no effect on the evolution of surface abundances.

3.3.2 Radiative accelerations

To estimate the magnitude of the radiative accelerations $g_{\mathrm{r},i}$ in Eq. (3.9), we consider a mixture of different elements in a radiation field as sketched in Fig. 1.12. The momentum flux in the frequency range between ν and $\nu + \mathrm{d}\nu$ associated with a radiation flux $\mathcal{F}_\nu$ is $\frac{1}{c}\mathcal{F}_\nu\,\mathrm{d}\nu$. If the particles of element i with mass m_i absorb some of this flux with a cross-section $s_i(\nu)$, the change in their momentum can be written as

$s_i(\nu)\frac{1}{c}\mathcal{F}_\nu \,\mathrm{d}\nu$. The total change in the momentum of the particles, i.e. the force acting on them, is then

$$F_{\mathrm{r},i} = m_i g_{\mathrm{r},i} = \frac{1}{c}\int_0^\infty s_i(\nu)\mathcal{F}_\nu \,\mathrm{d}\nu\,. \tag{3.12}$$

With (see Eq. (2.18))

$$\int_0^\infty \frac{\partial B_\nu}{\partial T}\,\mathrm{d}\nu = \frac{acT^3}{\pi} = \frac{\partial B}{\partial T}, \tag{3.13}$$

the monochromatic flux of Eq. (2.20) can be expressed in terms of the total flux:

$$\mathcal{F}_\nu = -\frac{4acT^3}{3\rho}\frac{\partial T}{\partial r}\frac{1}{\kappa_\nu}\frac{(\partial B_\nu/\partial T)}{(\partial B/\partial T)} = \frac{\kappa_\mathrm{R}}{\kappa_\nu}\frac{(\partial B_\nu/\partial T)}{(\partial B/\partial T)}\mathcal{F}_\mathrm{rad}. \tag{3.14}$$

Inserting this into Eq. (3.12) gives for the radiative acceleration of element i:

$$g_{\mathrm{r},i} = \frac{\bar{m}}{m_i}\frac{\kappa_\mathrm{R}\mathcal{F}_\mathrm{rad}}{c}\int_0^\infty \frac{s_i(\nu)}{\sigma_\nu}\frac{(\partial B_\nu/\partial T)}{(\partial B/\partial T)}\,\mathrm{d}\nu\,, \tag{3.15}$$

where σ_ν is the total radiative cross-section given by $\sigma_\nu = \kappa_\nu\bar{m}$ for an average atomic mass $\bar{m} = \rho/n$. The ratio $s_i(\nu)/\sigma_\nu = f_i(\nu)$ is the fraction contributed by element i to the total cross-section at frequency ν, i.e. $\sigma_\nu \approx \sum N_j s_j(\nu)$, where N_j is the number fraction of element j. Further defining

$$\gamma_i \equiv \int_0^\infty f_i(\nu)\frac{(\partial B_\nu/\partial T)}{(\partial B/\partial T)}\,\mathrm{d}\nu \tag{3.16}$$

finally gives

$$g_{\mathrm{r},i} = \frac{\bar{m}}{m_i}\frac{\kappa_\mathrm{R} l}{4\pi r^2 c}\gamma_i. \tag{3.17}$$

According to Eqs. (3.15) and (3.17), radiative accelerations will be important in strong radiation fields (large l) and for elements able to capture more of the radiation (large f_i), which will depend on what other elements are present in the mixture. These relations make intuitive sense. Another important dependence, that of composition, is revealed when the ratio of cross-sections is expressed in terms of opacities ($s_i(\nu) = \kappa_i(\nu)\rho/n_i = \kappa_i(\nu)m_i/X_i$) to give

$$g_{\mathrm{r},i} = \frac{\kappa_\mathrm{R}\mathcal{F}_\mathrm{rad}}{X_i c}\int_0^\infty \frac{\kappa_i(\nu)}{\kappa_\nu}\frac{(\partial B_\nu/\partial T)}{(\partial B/\partial T)}\,\mathrm{d}\nu\,. \tag{3.18}$$

Hence, the greater the abundance X_i of the element, the lower the acceleration. This again makes intuitive sense – all the particles of a given element compete for the same fixed amount of photons.

3.3.3 Atomic processes and absorption cross-sections

The quantity $f_i(\nu)$ in Eq. (3.16) is what makes evaluating $g_{\mathrm{r},i}$ computationally challenging (see Seaton, 1997). That is because evaluating the absorption cross-sections $s_i(\nu)$ requires knowledge of the absorption probabilities of the elements at all wavelengths, which, in turn, depend on the electronic structure of the elements at all ionisation stages and the thermal conditions of the plasma. Furthermore, a photon of a given frequency may be absorbed by an ion of element i, lifting one of its electrons to a higher energy state (bound-bound or bb interaction), but ionise an ion j' of a different element i'. In this bound-free (bf) case, some of the momentum is imparted to ion $j'+1$, while the rest is carried away by the liberated electron. The photon can also take part in a three body interaction with an ion and an electron (free-free

Type	Interaction	Momentum
bound-bound (bb)	$[i, j, k] + h\nu \rightarrow [i, j, k']$	imparted to ion
bound-free (bf)	$[i, j, k] + h\nu \rightarrow [i, j + 1, k] + e$	shared by ion in the next ionisation stage and electron
free-free (ff)	$[i, j, k] + h\nu + e \rightarrow [i, j, k] + e$	redistributed between ion and electron

Table 3.2: Summary of atomic processes between ions and photons. $[i, j, k]$ is a shorthand for element i in ionisation stage j in excitation stage k.

or ff interaction), redistributing the momenta between the interacting particles (Table 3.2). Generally, each chemical element in a mixture will be distributed over multiple ionisation stages (depending on the temperature and density of the plasma), so deriving the average acceleration of an element requires taking all of these processes into account.

With these considerations we can write that the cross-section for momentum absorption $s_i(\nu)$ for the element i is its radiative cross-section for absorption $\sigma_i(\nu)$, corrected for the fraction of momentum carried away by electrons:

$$s_i(\nu) = \sigma_i(\nu) - \sigma_i^e(\nu). \tag{3.19}$$

Meanwhile, the total monochromatic absorption cross-section is generally given by

$$\sigma_\nu = \sum_i N_i \sigma_i(\nu) + \sigma_s(\nu, n_e), \tag{3.20}$$

where $\sigma_s(\nu, n_e)$ is the cross-section for scattering of photons, which depends on the number density of electrons n_e. More explicitly,

$$\sigma(\nu) = \sum_i \sum_{j=0}^{Z_i} \sum_{k=0}^{\infty} N_{i,j,k} \sigma_{i,j,k}(\nu) + \sigma_s(\nu, n_e), \tag{3.21}$$

where indices i, j, k correspond to element, ionisation stage, and excitation stage, respectively, and Z_i is the atomic number of element i. The total quantity $f_i(\nu)$ can finally be expressed as

$$f_i(\nu) = \frac{\sigma_i(\nu) - \sigma_i^e(\nu)}{\sum_j N_j \sigma_j(\nu) + \sigma_s(\nu, n_e)}. \tag{3.22}$$

3.3.4 Monochromatic data

Evaluation of the radiative accelerations requires knowledge of $\sigma_i(\nu)$, $\sigma_i^e(\nu)$, and $\sigma_s(\nu)$ for all temperatures and densities of interest. The atomic data used here are those made available as part of the Opacity Project (OP; Seaton, 1997; Badnell, Bautista, Butler et al., 2005; Seaton, 2007). The Opacity Project (version 3.3[2]) provides the monochromatic cross-sections $\sigma_i(\nu)$ and corrections $\sigma_i^e(\nu)$ for 17 chemical elements (H, He, C, N, O, Ne, Na, Mg, Al, Si, S, Ar, Ca, Cr, Mn, Fe, Ni), which include all of the elements in the STARS network.

The data are tabulated on a $(\log T, \log n_e)$ grid in the temperature range $\log T = 3.5$–8.0 with a spacing of $\Delta \log T = 0.025$. The n_e range depends on temperature and has a spacing of $\Delta \log n_e = 0.25$. At

[2] http://cdsweb.u-strasbg.fr/topbase/TheOP.html

each grid point (about 1500 in total), the monochromatic data are tabulated at 10^4 frequency points (see Appendix A for details). The memory requirement for storing all of the monochromatic data is about 1 GB.

Photon scattering in most of the temperature and density range is dominated by free electrons. The cross-section $\sigma_s(\nu, n_e)$ is thus normally proportional to the Thomson cross-section for electrons:

$$\sigma_s(\nu, n_e) = \sigma_s(n_e) = \left(\frac{n_e}{n}\right)\sigma_T^e = \left(\frac{n_e}{n}\right)\left(\frac{8\pi}{3}\right)\left(\frac{e^2}{m_e c^2}\right)^2, \tag{3.23}$$

where e is the elementary charge. Some frequency-dependent modifications are made at low temperatures (Rayleigh scattering by hydrogen and helium) and at high temperatures and densities (Boercker, 1987; Seaton, 1997).

3.3.5 Numerical implementation

The OP data come bundled with OPserver (Mendoza, Seaton, Buerger et al., 2007), a Fortran module that is intended to facilitate the computation of opacities and radiative accelerations from OP data in stellar evolution calculations. While the OPserver module contains routines with slightly different strategies for computing κ_R and γ_i, the strategy for computing κ_R at some specified temperature T_0, density ρ_0 and composition $\boldsymbol{X}_0$ generally involves computing κ_R on the entire $(\log T, \log n_e)$ grid, interpolating the data to a $(\log T, \log \rho)$ grid, and computing derivatives with respect to T and ρ prior to interpolating to (T_0, ρ_0). The strategy for computing γ_i is similar, except the acceleration of only one element in the mixture can be computed at a time, and derivatives with respect to the abundance of that element are computed.

This strategy, in particular the computation of γ_i, was found to be very costly for stellar evolution calculations. A conceptually straight-forward alternative would be to take the local properties of the plasma (temperature, density, composition), compute the opacities and accelerations from the monochromatic data on neighbouring $(\log T, \log n_e)$ gridpoints, and interpolate to the desired temperature and density. This approach was found to be computationally prohibitive, at least with the numerical routines packaged with OPserver, and was not pursued fully.

In the end we settled for a heavily modified version of the OPserver strategy that is sketched in Fig. 3.1. The idea is to compute and save the values of κ_R and γ_i on the entire $(\log T, \log n_e)$ grid for each new chemical composition that is encountered during the evolution (optionally, γ_i can be computed only on a fraction of the full grid). Subsequently, only interpolation to the required temperature and density is required when the corresponding composition is encountered.[3] The number of computationally expensive steps (the computation of new tables, which takes about a second per table on a 2.2 Ghz AMD processor) is thus reduced at the expense of storing thousands of tables in memory (about 2000 tables per 1 GB of memory when the full temperature range is used). Since computing the models described in Chapter 4, the computation of new tables has been parallelised with OpenMP[4], which, when using up to $n \approx 20$ threads, allows a speed-up of close to n.

Since the derivatives with respect to composition are no longer calculated, a new table has to be computed every time the composition changes as a result of nuclear burning or chemical mixing. At the same time, since computing the tables takes a lot of time, one would like to compute them as rarely as possible. The question then becomes what amount of change in composition warrants the computation of a new table. The answer may depend on the intended application. For modelling the abundance changes

[3] The models presented in Chapter 4 were computed with an earlier version of the code where an intermediate step was made: the $(\log T, \log n_e)$ grid was first interpolated to a $(\log T, \log \rho)$ grid.

[4] http://www.openmp.org/

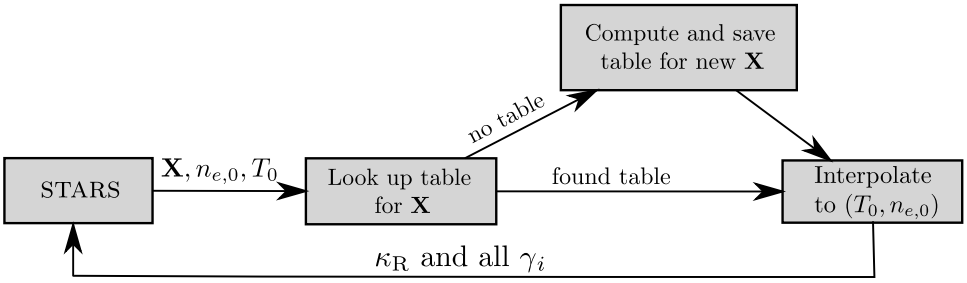

Figure 3.1: Schematic illustration of the computational strategy for computing the opacity κ_R and radiative accelerations γ_i from the Opacity Project data during stellar evolution calculations.

arising from atomic diffusion in CEMP-*s* stars, we found it sufficient to introduce the following criteria for using a previously computed table – absolute deviation in the hydrogen abundance $\Delta X_{H,0}$, and relative deviations in the metal abundances $r_{Z,0}$. Interpolation in a previously computed table (with abundances X'_i) is made when

1. deviation in the hydrogen abundance is below $\Delta X_{H,0}$, i.e. $|X_H - X'_H| \leq \Delta X_{H,0}$;
2. for all metals with an abundance above Z_0 the relative deviation is below $r_{Z,0}$, i.e. $|X_i - X'_i|/X_i \leq r_{Z,0}$ for all metals with $X_i > Z_0$.

When no table is found that satisfies both conditions, a new table of opacities and accelerations is computed and saved for later use. The models described in Chapter 4 were computed with thresholds $\Delta X_{H,0} = 5 \times 10^{-4}$, $r_{Z,0} = 0.05$, and $Z_0 = 10^{-5}Z$. Figure 3.2 shows that lowering the thresholds would result in a negligible effect in a $M = 0.825$, $Z = 10^{-4}$ model, in which the effects of diffusion are large.

Conductive opacities The conductive contribution to κ_{tot} is not available from the OP data. In the models described in Chapter 4 we gradually switch over to the tabulated OPAL-based opacities (Iglesias and Rogers, 1996; Eldridge and Tout, 2004) between $\log T = 7.1$–7.3, as these include the conductive opacities of Hubbard and Lampe (1969) and Canuto (1970). Subsequently, we have coupled the STARS code to the code of Cassisi, Potekhin, Pietrinferni et al. (2007)[5] to obtain the conductive opacities independently. This allows using the OP opacities up to their temperature limit of $\log T = 8$ also in partially degenerate regions. There are some noticeable differences in the central conditions of a model as a result (Fig. 3.3), but the differences in the evolution of surface abundances are nevertheless negligible (Fig. 3.4).

[5] http://www.ioffe.ru/astro/conduct

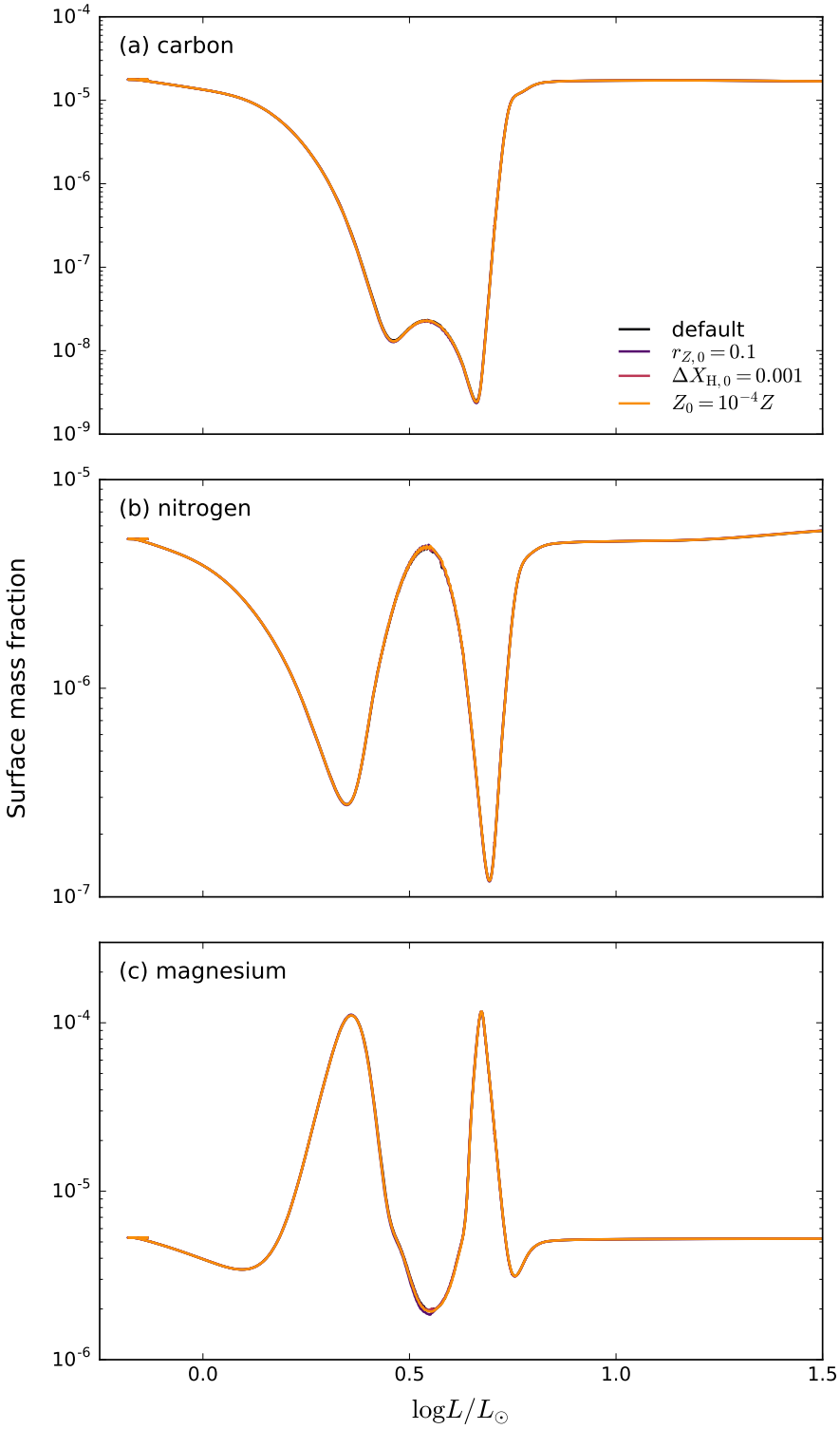

Figure 3.2: Evolution of surface abundances in a model with $M = 0.825\ M_\odot$ and $Z = 10^{-4}$ with radiative levitation. The model grid was computed with numerical parameters $r_{Z,0} = 0.05$, $\Delta X_{\mathrm{H},0} = 5 \times 10^{-4}$, and $Z_0 = 10^{-5} Z$ (default). The other three curves show how the results (do not) change when making one of these parameters less stringent.

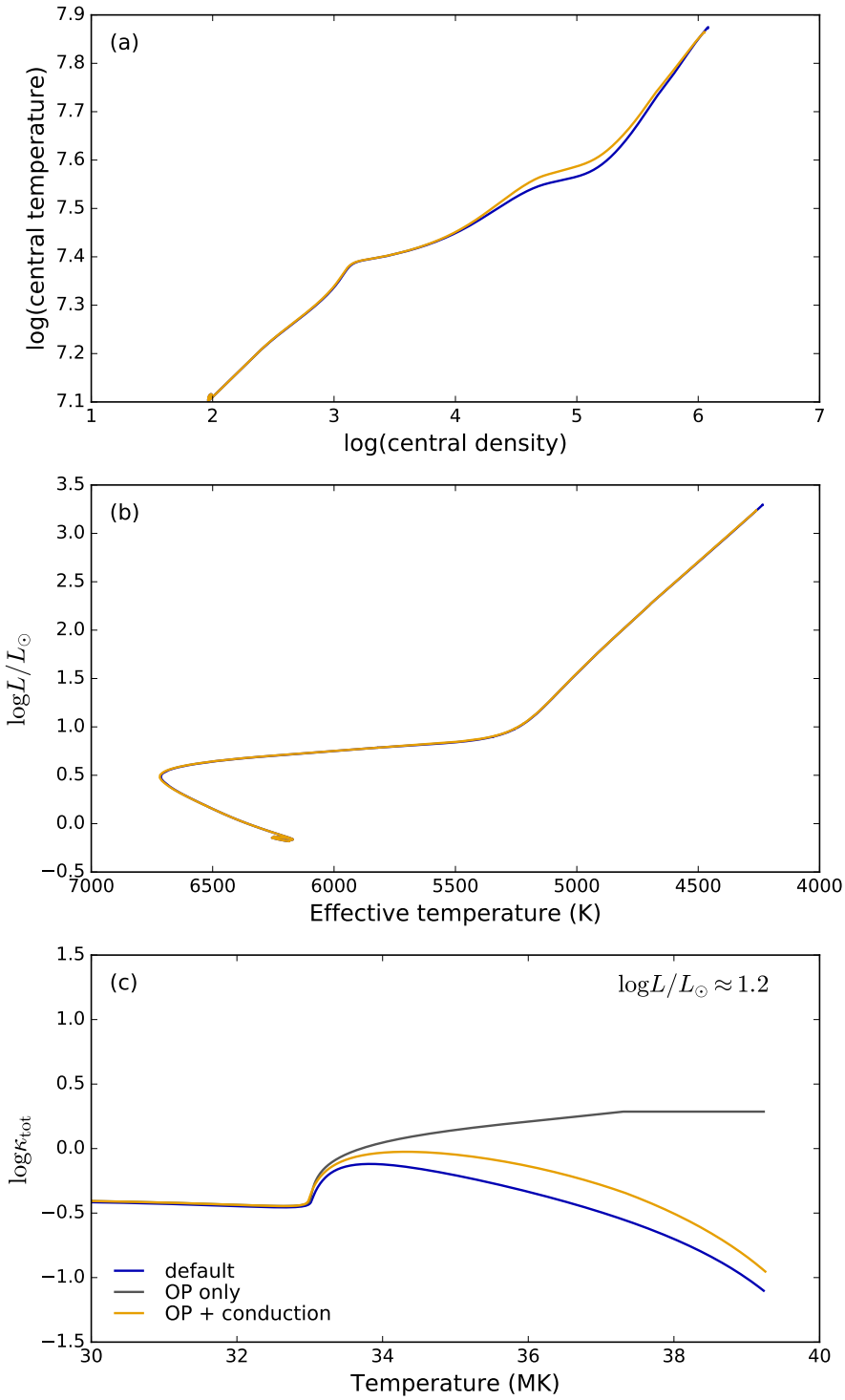

Figure 3.3: (a) Evolution of central temperature and density, and (b) the Hertzsprung-Russell diagram of a model with $M = 0.825\ M_\odot$ and $Z = 10^{-4}$ with radiative levitation, and (c) the opacity in the central regions in a model near the base of the red giant branch. The model grid was computed using the OP opacities up to $\log T = 7.1$, and then gradually switching over to pre-computed OPAL tables in the temperature range up to $\log T = 7.3$ (about 20 MK; default). The orange curve shows the case with using the OP opacities throughout together with the conductive opacities from Cassisi, Potekhin, Pietrinferni et al. (2007). The grey curve in the bottom panel shows the effect of ignoring conductive opacities in the core after the main sequence.

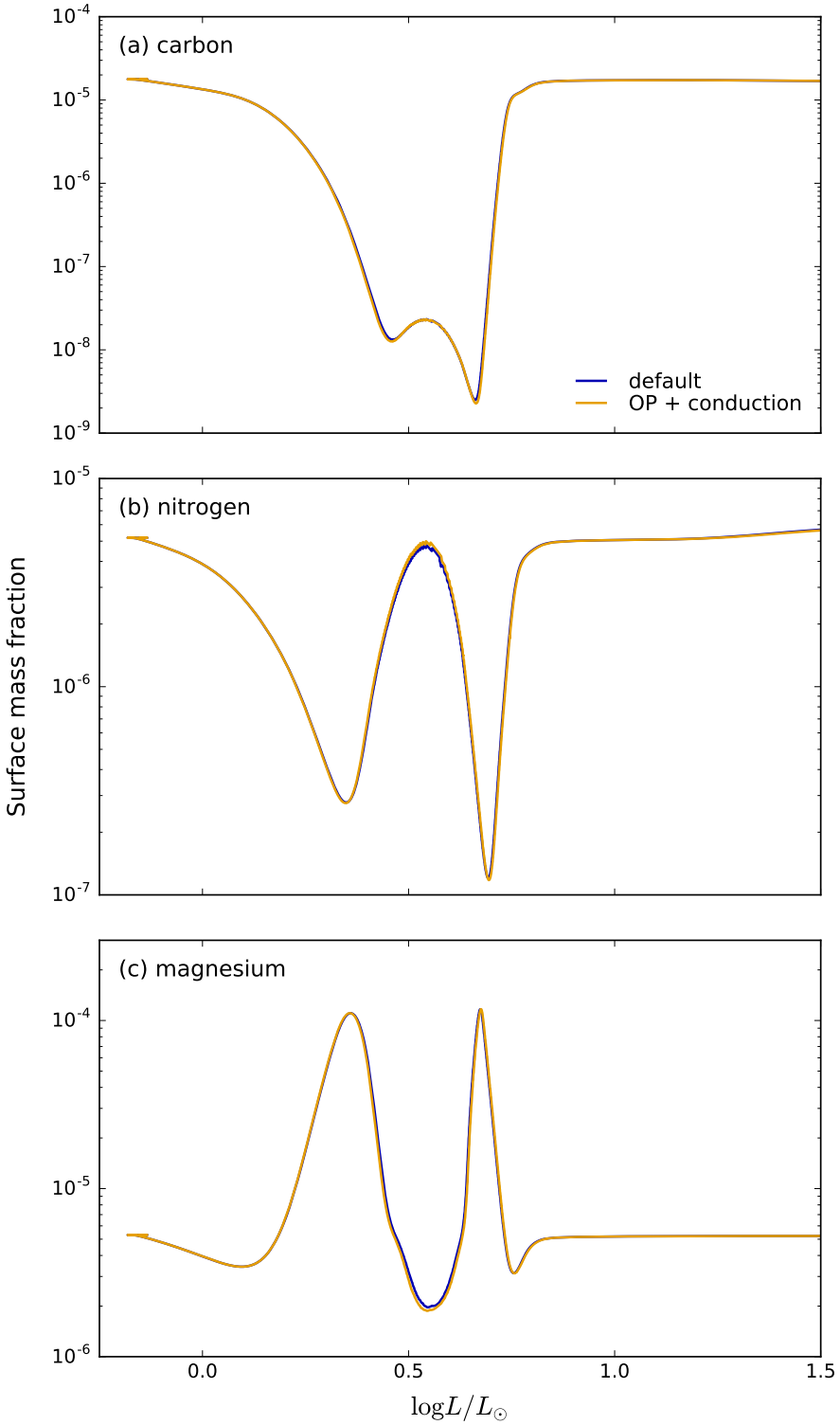

Figure 3.4: As Fig. 3.3, but showing the evolution of surface abundances.

CHAPTER 4

Radiative levitation in CEMP-*s* stars

Material from this chapter is published as:

E. Matrozis and R. J. Stancliffe (2016), *Radiative levitation in carbon-enhanced metal-poor stars with s-process enrichment*, A&A **592** A29, arXiv: 1605.02791 [astro-ph.SR].

In this chapter the effects of atomic diffusion (including radiative levitation) on the evolution of *s*-process-rich carbon-enhanced metal-poor (CEMP-*s*) stars are explored. As described in the introduction (Sect. 1.2.4), these stars are believed to form when a low-mass ($M \lesssim 0.8\ M_\odot$) metal-poor ([Fe/H] $\lesssim -2$) star accretes material from a thermally pulsing asymptotic giant branch (AGB) companion. The surface abundances of CEMP-*s* stars are thus commonly used to constrain the nucleosynthesis occurring in low-metallicity AGB stars (e.g. Lucatello, Gratton, Beers et al., 2005a; Stancliffe, Glebbeek, Izzard et al., 2007; Stancliffe and Glebbeek, 2008; Bisterzo, Gallino, Straniero et al., 2012; Abate, Pols, Izzard et al., 2015a).

A comparison of AGB nucleosynthesis models with abundances of CEMP-*s* stars is straightforward only if the accreted material remains on the surface of the star. This will certainly not be the case once it evolves off the main sequence and develops a deep convective envelope. But as demonstrated by Stancliffe et al. (2007), this is also unlikely on the main sequence because the higher mean molecular weight of the accreted material should trigger thermohaline mixing (Ulrich, 1972; Kippenhahn, Ruschenplatt and Thomas, 1980, Sect. 1.3.1). Furthermore, gravitational settling of heavier elements (Sect. 1.3.3) could modify both the extent of this mixing and the subsequent evolution of the secondary (Stancliffe and Glebbeek, 2008; Thompson, Ivans, Bisterzo et al., 2008; Stancliffe, 2009). If the overall effect is to dilute the accreted material by uniformly mixing it throughout some portion of the secondary, a comparison between AGB nucleosynthesis models and abundances of CEMP-*s* stars is still possible provided this amount of dilution can be estimated (e.g. as attempted by Bisterzo, Gallino, Straniero et al., 2011; Bisterzo et al., 2012). However, the rather impartial (leading to similar dilution of all elements) process of settling will be counteracted by the highly selective process of radiative levitation (Sect. 1.3.3). Metal-poor stars with masses around 0.8 $M_\odot$ have very shallow convective envelopes and, in absence of any counteracting processes, large abundance anomalies can result (e.g. Richard, Michaud and Richer, 2002a; Richard, Michaud, Richer et al., 2002b). If radiative levitation is important during the post-mass-transfer evolution of CEMP-*s* stars, the interpretation of their abundances in the context of AGB nucleosynthesis gets considerably more complicated.

In this chapter grids of CEMP-*s* stellar models corresponding to different combinations of the initial primary (AGB star) mass M_1, accreted mass ΔM, and initial secondary mass $M_{2,\mathrm{i}}$ (or, equivalently, final

Model	$t_{\rm mt}$ (Gyr)	Mass fraction		Mass fraction $\times 10^{-6}$								Abundance		μ
		H	^{4}He	^{3}He	C	N	O	Ne	Mg	Si	Fe	[Fe/H]	[C/Fe]	
ZAMS	...	0.75770	0.24217	30.30	17.72	5.190	42.95	9.390	5.300	4.980	9.680	−2.14	0.00	0.5934
Composition of AGB ejecta														
0.90 $M_\odot$	9.10	0.73302	0.26222	235.8	3680	135.1	217.5	457.0	12.77	4.943	8.895	−2.16	2.35	0.6046
1.00 $M_\odot$	6.30	0.74907	0.24956	261.4	933.0	21.47	92.47	37.29	5.395	4.913	8.910	−2.17	1.76	0.5972
1.25 $M_\odot$	3.06	0.71670	0.27604	228.9	6032	42.42	305.3	620.9	14.96	4.976	8.869	−2.15	2.57	0.6122
1.50 $M_\odot$	1.80	0.69878	0.28562	203.7	12840	56.60	590.2	1854	40.11	5.121	8.821	−2.14	2.90	0.6212

Table 4.1: Chemical composition of the secondaries on the zero-age main sequence (ZAMS; abundance distribution from Asplund, Grevesse, Sauval et al., 2009, scaled to $Z = 10^{-4}$) and of the ejecta from the AGB models of Lugaro, Karakas, Stancliffe et al. (2012). The second column lists the age when accretion of the corresponding composition begins ($t_{\rm mt}$). The last column gives the mean molecular weight (μ) of the composition. Mass fractions of all elements other than helium are sums over their isotopes.

CEMP-*s* star mass $M_{2,\rm f}$) are presented. These models are the first CEMP-*s* stellar models that consider the effects of radiative levitation. The focus is primarily on the evolution of carbon and iron surface abundances. Abundances of *s*-process elements are not modelled. However, levitation is expected to have a much greater impact on iron than on carbon (Gonzalez, LeBlanc, Artru et al., 1995; Seaton, 1997; Seaton, 2007). These two elements can therefore be used to constrain the overall importance of radiative levitation for CEMP-*s* stars. Qualitatively, our conclusions should apply to elements beyond iron, including those produced by the *s*-process.

4.1 Methods

The models presented in this chapter are produced with the version of the STARS stellar evolution code described in Chapters 2 and 3. To summarise the parts most relevant to this chapter, the mass fraction X_i of each chemical species i is governed by the advection-diffusion equation (3.1):

$$\frac{\partial X_i}{\partial t} = R_i + \frac{\partial}{\partial m}\left(\mathcal{D}_{{\rm mix},i}\frac{\partial X_i}{\partial m}\right) - \frac{\partial}{\partial m}\left(\mathcal{W}_i X_i\right), \tag{4.1}$$

where $\mathcal{D}_{{\rm mix},i} = \left(4\pi r^2 \rho\right)^2 D_{{\rm mix},i}$ and $\mathcal{W}_i = 4\pi r^2 \rho w_i$. The diffusive part of the equation accounts for convective mixing (Sect. 3.2.1), thermohaline mixing (Sect. 3.2.2), and concentration diffusion. The advective part accounts for atomic diffusion and is described in detail in Sect. 3.3. In particular, the diffusion velocity w_i of each element i is given by Eq. (3.9):

$$w_i = \frac{D_i}{k_{\rm B}T}\left[g\left(\mu - \mu_i\right) + k_{\rm B}\alpha_{{\rm T},i}\frac{\partial T}{\partial r} + \mu_i g_{{\rm r},i}\right], \tag{4.2}$$

with the radiative accelerations calculated according to Eq. (3.17):

$$g_{{\rm r},i} = \frac{\bar{m}}{m_i}\frac{\kappa_{\rm R} l}{4\pi r^2 c}\gamma_i. \tag{4.3}$$

Accretion of mass is simulated as described in Sect. 2.1.5. The composition of the accreted material is set to the average composition of the ejecta from the models of Lugaro, Karakas, Stancliffe et al. (2012). These yields together with the zero-age main sequence (ZAMS) abundances (Asplund, Grevesse, Sauval et al., 2009) are given in Table 4.1.

4.1.1 Grid selection

We consider those systems that are the most probable in the synthetic populations computed by Abate, Pols, Stancliffe et al. (2015c). According to their work, typical masses are $M_1 \simeq 0.9$–$1.25\ M_\odot$, $M_{2,\mathrm{f}} \simeq 0.8$–$0.9\ M_\odot$, and $\Delta M \simeq 0.05$–$0.2\ M_\odot$. These accreted masses and final masses of the secondaries are larger than considered in a related earlier study by Stancliffe and Glebbeek (2008). Therefore, we also consider some systems with smaller ΔM values, namely 0.001 and 0.01 $M_\odot$.

In summary, we evolve stellar models with initial masses of 0.60, 0.65, 0.70, 0.75, and 0.80 $M_\odot$ and metallicity $Z = 10^{-4}$ ([Fe/H] = −2.14) starting from the pre-main-sequence. At the ages listed in Table 4.1, somewhere between 0.001 and 0.2 $M_\odot$ of material of the corresponding composition is added to the models at a rate of $10^{-6}\ M_\odot\ \mathrm{yr}^{-1}$ yielding CEMP-*s* stellar models with masses between 0.8 and 0.95 $M_\odot$. These models are evolved up to the core helium flash or an age of 16 Gyr, whichever comes first.

4.2 Results

Two sets of models were initially evolved: in one set only thermohaline mixing, gravitational settling, thermal diffusion, and concentration diffusion were active; in the other, radiative levitation was also included. Table 4.2 lists some properties of these systems, including the [C/Fe] ratio at the surface at key points of the evolution: after thermohaline mixing, at the point where the convective envelope is smallest in mass (near the main sequence turn-off), and after first dredge-up.

4.2.1 An illustrative model sequence

To understand how the evolution of surface abundances is influenced by the different physical processes included in our simulations, let us consider a particular model sequence in detail. Figures 4.1 and 4.2 illustrate the case of a secondary with an initial mass of 0.75 $M_\odot$ that accretes 0.05 $M_\odot$ of material from a 1.25 $M_\odot$ primary. Multiple stages of evolution can be distinguished.

Prior to mass transfer the secondary slowly evolves as a 0.75 $M_\odot$ main sequence star (the part of the evolution labelled ‘1’ in Fig. 4.1). During this stage gravitational settling dominates and the abundance of every element other than hydrogen decreases at the surface.

At $t = 3.06$ Gyr mass transfer begins and the surface composition quickly becomes equal to that of the accreted material (‘2’). During the accretion the star becomes hotter and more luminous. This is common for many system configurations. In some models the effective temperature and luminosity can reach values as high as 9500 K and 30 $L_\odot$, respectively. But once accretion stops (‘3’), both luminosity and temperature rapidly drop, resulting in loops in the Hertzsprung-Russell diagram (HRD) as the star settles back on the main sequence. Generally, these loops are more characteristic of secondaries with larger initial masses (see also discussion in Sects. 5.2.1 and 6.2).

Shortly after accretion stops the accreted material starts to mix with the original material of the secondary as a result of the thermohaline instability (‘4’). As shown by Fig. 4.2a, some of the interior is already mixed by the time the surface abundances change. The mixing takes only a few hundred million years (about 150 Myr in this case) and is over before the star has settled back on the main sequence (‘5’). Ultimately, the surface carbon abundance is reduced by about 0.8 dex (regardless of radiative levitation), whereas the iron abundance is barely affected because it is virtually the same in the original and accreted compositions.

Over the rest of the post-mass-transfer main sequence lifetime the abundances are again modified by atomic diffusion (‘6’). At first gravitational settling prevails over radiative levitation and the surface

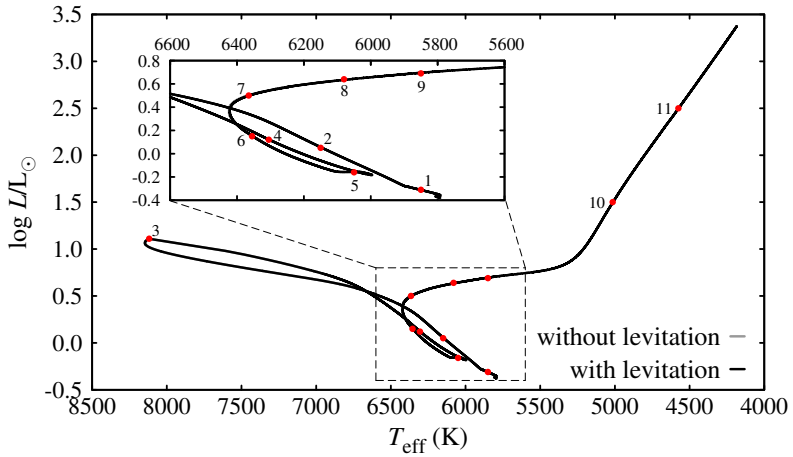

(a) Hertzsprung-Russell diagram

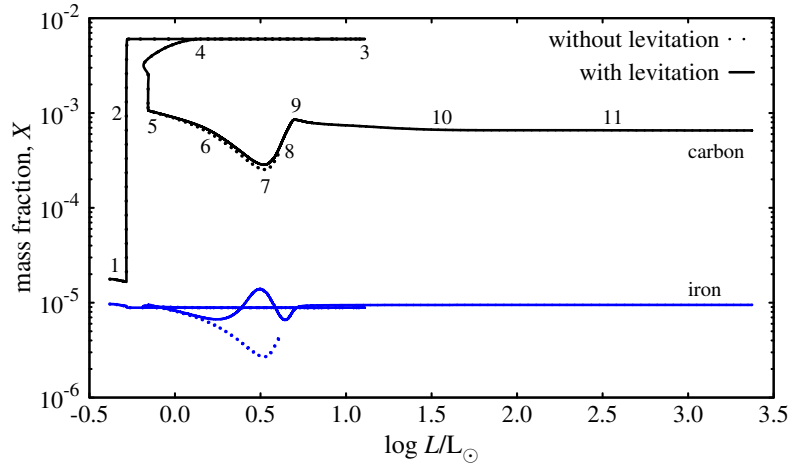

(b) Evolution of carbon and iron mass fractions

Figure 4.1: Evolution in the HRD and of the surface abundances of a $M_{2,\rm i} = 0.75\ M_\odot$ secondary accreting $\Delta M = 0.05\ M_\odot$ of material from a $M_1 = 1.25\ M_\odot$ primary. The numerical labels highlight specific parts of the evolution discussed in the text. The model sequences with and without radiative levitation overlap at this scale of the HRD.

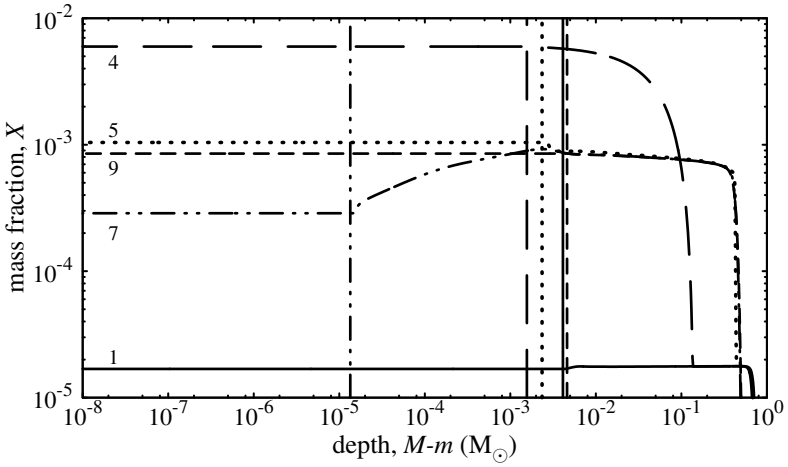

(a) Interior profiles of carbon

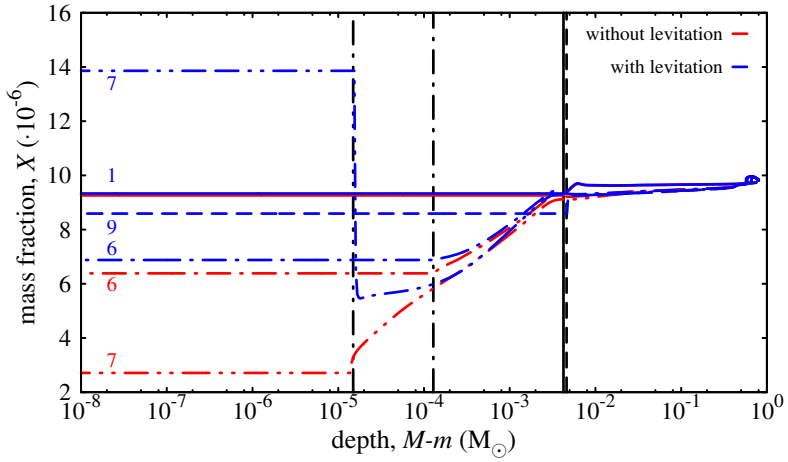

(b) Interior profiles of iron

Figure 4.2: Evolution of interior abundances in a $M_{2,\mathrm{i}} = 0.75\ M_\odot$ secondary accreting $\Delta M = 0.05\ M_\odot$ of material from a $M_1 = 1.25\ M_\odot$ primary. The profiles correspond to a few of the stages indicated in Fig. 4.1: before mass transfer ('1', solid); before thermohaline mixing ('4', long-dashed); after thermohaline mixing ('5', dotted); post-mass-transfer main sequence ('6', dot-dashed); minimum of convective envelope mass ('7', dot-dot-dashed); during first dredge-up ('9', short-dashed). The vertical lines indicate the position of the base of the convective envelope at the respective time. The interior profiles of carbon with and without levitation nearly coincide and only the case with levitation is shown.

Table 4.2: Results from simulations including atomic diffusion. The columns list the initial mass of the secondary ($M_{2,i}$); accreted mass (ΔM); whether levitation was included (g_r?); the deepest mass coordinate reached by thermohaline mixing (m_{thm}); [C/Fe] after thermohaline mixing ends; the age (t), luminosity (L), effective temperature (T_{eff}), surface gravity (g), envelope mass (M_{env}), metallicity ([Fe/H]), and [C/Fe] when the envelope mass reaches a minimum; [C/Fe] after first dredge-up. The table is sectioned according to the initial primary mass, M_1.

$M_{2,i}$	ΔM	g_r?	m_{thm}	[C/Fe]	At the time when envelope mass is smallest							[C/Fe][b]
				post-th.mix.	t (Gyr)	$\log(L/L_\odot)$	T_{eff}	$\log g$	M_{env}	[Fe/H][a]	[C/Fe][a]	post-FDU
					$M_1 = 0.9\ M_\odot$							
0.700	0.100	no	0.411	1.88	15.84	0.4461	6366	4.06	2.79(−5)	−2.54	1.82	…
		yes	0.410	1.88	15.83	0.4462	6365	4.06	2.90(−5)	−2.25	1.56	…
0.750	0.050	no	0.526	1.77	14.02	0.4573	6400	4.06	1.59(−5)	−2.61	1.71	…
		yes	0.525	1.78	14.00	0.4544	6402	4.06	1.69(−5)	−2.13	1.27	1.38
0.800	0.001	no	0.797	1.85	11.94	0.4986	6471	4.04	3.36(−6)	−3.05	1.86	…
		yes	0.797	1.83	11.93	0.4959	6465	4.04	3.98(−6)	−1.60	0.46	0.15
0.800*	0.010	no	0.760	1.76	11.79	0.4922	6464	4.05	5.28(−6)	−2.82	1.73	…
		yes	0.760	1.75	11.80	0.4930	6457	4.05	6.04(−6)	−1.73	0.67	0.72
0.750	0.100	no	0.462	1.91	13.24	0.5482	6581	4.05	3.94(−7)	−5.32	2.72	…
		yes	0.461	1.91	13.25	0.5490	6555	4.04	4.66(−7)	−0.63	−1.67	…
0.800	0.050	no	0.576	1.84	11.50	0.5567	6647	4.05	1.44(−7)	−7.71	3.95	…
		yes	0.578	1.76	11.48	0.5522	6616	4.05	1.56(−7)	−0.35	−2.60	1.34
0.700	0.200	no	0.361	2.06	12.76†	0.4587	6798	4.22	5.97(−8)	−inf	inf	…
		yes	0.360	2.05	12.99†	0.4907	6781	4.18	4.14(−8)	−0.44	−3.90	…
0.800	0.100	no	0.515	2.06	10.13†	0.4557	6858	4.23	2.91(−8)	−inf	inf	…
		yes	0.518	1.49	10.54†	0.5170	6874	4.18	1.03(−8)	−0.42	−3.17	…
					$M_1 = 1.0\ M_\odot$							
0.600	0.200	no	0.342	1.55	16.00‡	0.4132	6495	4.13	4.03(−6)	−3.05	1.50	…
		yes	0.341	1.55	16.00‡	0.4120	6486	4.13	4.80(−6)	−1.84	0.38	…
0.700	0.100	no	0.477	1.44	14.66	0.4815	6489	4.06	2.21(−6)	−3.44	1.48	…
		yes	0.479	1.44	14.67	0.4854	6476	4.05	2.66(−6)	−1.48	−0.37	1.11
0.750	0.050	no	0.602	1.36	13.45	0.4875	6498	4.06	1.82(−6)	−3.56	1.45	…
		yes	0.601	1.36	13.43	0.4871	6488	4.06	2.16(−6)	−1.37	−0.62	0.83
0.800	0.001	no	0.797	1.28	11.93	0.4992	6531	4.06	9.59(−7)	−4.11	1.56	…
		yes	0.797	1.28	11.92	0.4987	6515	4.05	1.18(−6)	−1.10	−1.25	0.03
0.800	0.010	no	0.778	1.34	11.73	0.5113	6558	4.06	5.99(−7)	−4.69	1.85	…
		yes	0.777	1.33	11.73	0.5109	6540	4.05	7.05(−7)	−0.85	−1.74	0.31
0.650	0.200	no	0.380	1.56	13.16†	0.4455	6764	4.20	7.90(−8)	−inf	inf	…
		yes	0.382	1.58	13.51†	0.5007	6759	4.14	3.76(−8)	−0.42	−4.47	…
0.750	0.100	no	0.528	1.48	11.33†	0.4298	6776	4.21	7.68(−8)	−inf	inf	…
		yes	0.528	1.48	11.78†	0.5005	6783	4.15	2.78(−8)	−0.42	−4.82	…
0.800*	0.050	no	0.655	1.42	10.32†	0.4584	6812	4.20	3.87(−8)	−inf	inf	…
		yes	0.654	1.39	10.31†	0.4566	6781	4.19	4.25(−8)	−0.44	−4.46	…
0.700	0.200	no	0.427	1.62	9.88†	0.3482	6879	4.35	5.60(−8)	−inf	inf	…
		yes	0.428	1.58	10.35†	0.3998	6918	4.31	1.68(−8)	−0.56	−7.12	…
					$M_1 = 1.25\ M_\odot$							
0.600	0.200	no	0.158	2.21	14.35	0.4497	6302	4.04	6.44(−5)	−2.46	2.15	2.04
		yes	0.156	2.21	14.34	0.4487	6302	4.04	6.63(−5)	−2.34	2.04	2.04
0.700*	0.100	no	0.263	1.94	13.31	0.4596	6358	4.05	2.42(−5)	−2.60	1.87	1.80
		yes	0.264	1.95	13.28	0.4534	6359	4.05	2.59(−5)	−2.26	1.57	1.80
0.750	0.050	no	0.370	1.78	12.68	0.4628	6400	4.06	1.19(−5)	−2.74	1.71	…
		yes	0.370	1.78	12.66	0.4598	6397	4.06	1.32(−5)	−2.11	1.12	1.58
0.800	0.001	no	0.796	1.90	11.90	0.4925	6457	4.04	3.56(−6)	−3.15	1.88	…
		yes	0.796	1.90	11.89	0.4914	6449	4.04	4.40(−6)	−1.69	0.50	…
0.800	0.010	no	0.600	1.52	11.58	0.5006	6507	4.05	1.46(−6)	−3.74	1.64	…
		yes	0.600	1.51	11.57	0.4979	6495	4.05	1.88(−6)	−1.30	−0.62	0.92
0.650	0.200	no	0.149	2.12	11.65	0.5482	6513	4.03	1.13(−6)	−3.96	2.32	…
		yes	0.150	2.12	11.62	0.5426	6501	4.03	1.47(−6)	−1.17	−0.29	…
0.750	0.100	no	0.309	1.96	10.90	0.5598	6589	4.04	3.02(−7)	−6.13	3.10	…
		yes	0.308	1.97	10.88	0.5578	6561	4.03	3.60(−7)	−0.56	−1.98	1.78
0.800	0.050	no	0.419	1.81	10.28	0.5552	6662	4.06	1.15(−7)	−inf	inf	…
		yes	0.421	1.81	10.30	0.5597	6625	4.05	1.27(−7)	−0.36	−3.19	…
					$M_1 = 1.5\ M_\odot$							
0.600	0.200	no	0.000	2.37	12.70	0.2746	6166	4.18	1.12(−3)	−2.29	2.35	2.28

Table 4.2: continued.

$M_{2,i}$	ΔM	g_r?	m_{thm}	[C/Fe] post-th.mix.	At the time when envelope mass is smallest							[C/Fe]^b post-FDU
					t (Gyr)	$\log(L/L_\odot)$	T_{eff}	$\log g$	M_{env}	[Fe/H]^a	[C/Fe]^a	
		yes	0.000	2.40	12.72	0.2751	6166	4.18	1.13(−3)	−2.28	2.34	2.28
0.800	0.010	no	0.495	1.67	11.56	0.4913	6449	4.05	4.15(−6)	−3.11	1.64	1.22
		yes	0.493	1.67	11.54	0.4886	6445	4.05	5.01(−6)	−1.73	0.35	1.22
0.650	0.200	no	0.000	2.37	10.44	0.3817	6307	4.14	1.30(−4)	−2.41	2.32	2.25
		yes	0.000	2.38	10.42	0.3804	6305	4.14	1.34(−4)	−2.35	2.28	2.25
						no accretion						
0.750	…	no	…	…	15.06	0.3914	6345	4.08	2.59(−5)	−2.63	−0.09	…
		yes	…	…	15.06	0.3901	6345	4.09	2.75(−5)	−2.33	−0.24	…
0.800	…	no	…	…	11.93	0.4951	6580	4.07	4.48(−7)	−5.38	0.73	…
		yes	…	…	11.94	0.4961	6558	4.07	5.27(−7)	−0.80	−3.33	−0.02
0.850	…	no	…	…	8.35†	0.3818	6819	4.27	6.75(−8)	−inf	inf	…
		yes	…	…	8.51†	0.4027	6814	4.25	5.28(−8)	−1.07	−4.25	…

Notes. All masses are in solar masses; other quantities are in cgs units unless indicated otherwise. Values of M_{env} are given in the format $n(m) = n \times 10^m$ for concision. $^{(a)}$ An 'inf' indicates that one of the mass fractions is below 10^{-12}. $^{(b)}$ Most of the models stop earlier. $^{(*)}$ Systems (with levitation) used in resolution tests (see Section 4.4). $^{(\dagger)}$ Models stop before reaching the minimum of M_{env}. The listed values are from the last converged model. $^{(\ddagger)}$ Models reach $t = 16$ Gyr before reaching the minimum of M_{env}. The listed values are for the final model.

becomes increasingly hydrogen-rich as all heavier elements settle out of the surface convection zone. As the star nears the main sequence turn-off, this convection zone becomes ever more superficial and radiative effects become increasingly important (Fig. 4.2b). Once an element's radiative velocity at the base of the convection zone exceeds its settling velocity, the surface abundance of this element increases. This is typically the case with iron. In contrast, if an element's settling velocity is always greater than its radiative velocity, the surface abundance of this element continues to decrease (although less so than in the case when radiative effects are ignored). This is always the case with helium and usually with carbon as well. The behaviour of other elements is not readily predicted because of the non-monotonic shape of the radiative accelerations (as a function of temperature) and the outward movement of the base of the envelope (decreasing temperature at the base). Therefore, the abundance of most elements alternates between increasing at those times when its radiative velocity exceeds its settling velocity and decreasing at others (e.g. see figure 2 of Richard et al., 2002b, or Fig. 3.2).

Eventually, the abundance anomalies, i.e. their values relative to those after thermohaline mixing, reach their maxima ('7'). At this stage the difference between the two sets of models is greatest – compared to the abundances after thermohaline mixing, in models without levitation the abundances of all elements are reduced (dotted lines in Fig. 4.1b), whereas in models with levitation this is not always the case (solid lines in Fig. 4.1b; in both cases only carbon and iron are shown for clarity) and readily levitated elements can be over-abundant. The anomalies are maximal shortly after the turn-off when the convective envelope is smallest (Fig. 4.2).[1] This occurs at the same time in models with and without levitation.

Next, as the convective envelope grows in mass, the material in it is mixed with that of the immediately adjacent, previously radiative layers. In models without diffusion no change in surface abundances would occur until the envelope reached depths where CN cycling had occurred (i.e. at first dredge-up). With diffusion, however, the composition of the envelope is different from that of the radiative layers below, and therefore the effect of the deepening of the envelope is to first undo all the work done by diffusion ('8'; cf. Fig. 1.2). When the envelope mass has reached a few thousandths of a solar mass, all surface evidence of atomic diffusion has been erased and the abundances are similar to those after thermohaline mixing ('9').

[1] In fact, the convective envelope has already slightly grown in mass. For a short time the diffusion timescale is shorter than the evolutionary timescale.

First dredge-up homogenises the composition in the layers above a mass coordinate of 0.3–0.35 $M_\odot$ (0.34 $M_\odot$ in this case). What effect this has on the surface abundances depends on how this depth compares to the depth of thermohaline mixing ($m_{\rm thm}$ = 0.37 $M_\odot$ in this case). If thermohaline mixing is not as deep as the maximum depth reached by the envelope at FDU, the accreted material is further diluted with the original material of the secondary. Otherwise, most abundances do not change. However, some of the accreted carbon will then have been converted into nitrogen. As shown by Stancliffe et al. (2007), during late FDU (which ends at around $\log L \approx 1.5$; '10') this nitrogen is dredged up to the surface.

Finally, after the luminosity bump ('11') ^{3}He-burning reduces the mean molecular weight above the hydrogen burning shell. Thus, a μ-inversion, which is magnified by the settling of ^{4}He (Michaud, Richer and Richard, 2010), develops between the shell and the receding convective envelope – a situation again unstable to thermohaline mixing. This alters the surface abundance of nitrogen by 0.1 dex at most. The much greater carbon abundance remains essentially unchanged. The abundance change after the bump is much smaller than found by Stancliffe, Church, Angelou et al. (2009) because the thermohaline mixing coefficient in this work is about 10^3 times smaller.

This model sequence illustrates the role each physical process plays in all models with atomic diffusion. We see that diffusion modifies the surface composition on the main sequence both before and after mass transfer. This modification is greatest around the turn-off, when the convective envelope is shallowest (point '7' in Figs. 4.1 and 4.2). We now turn to discussing the expected abundance changes for all CEMP-*s* stars in this evolutionary stage.

4.2.2 Abundance anomalies near the main sequence turn-off

During the main sequence the mass of the convective envelope, $M_{\rm env}$, of a low-mass star decreases. Therefore, the timescale for atomic diffusion, which is proportional to roughly the square root of $M_{\rm env}$ (Michaud, 1977), also decreases. In nearly all of our CEMP-*s* models the envelope mass reaches a minimum of less than 10^{-4} $M_\odot$ around the turn-off. The corresponding timescales are short enough compared to the nuclear timescale for atomic diffusion to notably modify the surface composition. Figure 4.3 summarises the extent of the abundance variations in our models with diffusion (Table 4.2). Specifically, the figure shows the [Fe/H], [C/H], and [C/Fe] abundances at the time when the convective envelope mass reaches the minimum in each of the CEMP-*s* models. In models with envelope masses always above about 2×10^{-5} $M_\odot$ the effect remains relatively minor – abundances are decreased by up to a factor of two from their values after thermohaline mixing. But in models with even smaller $M_{\rm env}$ at the turn-off abundances are modified by a factor of ten or more, and radiative levitation becomes important (Fig. 4.3a). The model discussed in Sect. 4.2.1 is close to this limit – its envelope mass has a minimum of about 1.2×10^{-5} $M_\odot$. At this minimum its [C/Fe] is 1.71 when levitation is ignored versus 1.12 when it is included (in both cases down from 1.78 after thermohaline mixing), and [Fe/H] is −2.74 and −2.11, respectively.

The results from many simulations plotted in Figs. 4.3a and 4.3c form two sequences corresponding to model sets with and without levitation. As shown by the solid lines, to a decent approximation we can interpret these sequences as describing the abundance evolution in a single simulation as the envelope mass changes. For example, as the envelope mass decreases from 10^{-5} to 10^{-6} $M_\odot$, [C/Fe] decreases by about two orders of magnitude in models with levitation because while carbon continues to settle, iron is levitated. On the other hand, in models without levitation [C/Fe] does not change because both elements settle at similar rates (Figs. 4.3a and 4.3b). At still smaller envelope masses, [C/Fe] increases because of the low degree of ionisation of iron at the base of the envelope. The small mean charge of iron gives a large diffusion coefficient because of the approximately $D \sim \bar{Z}^{-2}$ dependence (Paquette, Pelletier,

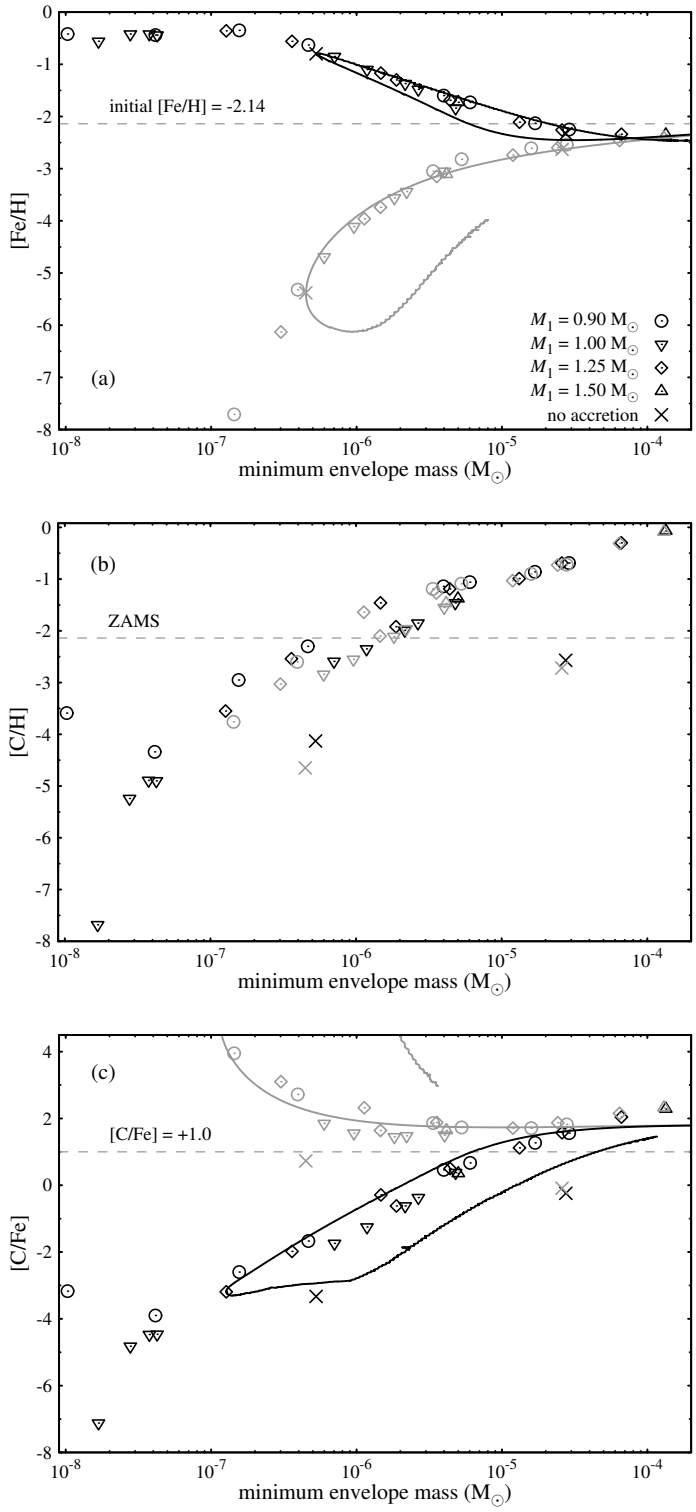

Figure 4.3: Symbols show [Fe/H] (a), [C/H] (b), and [C/Fe] (c) in each of the CEMP-*s* models at the point where the mass of the convective envelope is smallest, i.e. just before first dredge-up. Models with and without radiative levitation are plotted with black and grey symbols, respectively. All values for envelope masses below 10^{-7} $M_\odot$ denote upper or lower limits. The [Fe/H] plot also shows the metallicity evolution in a 0.8 $M_\odot$ model sequence with no accretion (solid lines). Similarly, the [C/Fe] plot shows the evolution in a model corresponding to $M_1 = 1.25$ $M_\odot$, $M_{2,\mathrm{i}} = 0.8$ $M_\odot$, and $\Delta M = 0.05$ $M_\odot$. Both sequences without levitation stop during the first dredge-up. The criterion for being classified as a carbon-enhanced metal-poor star ([C/Fe] ≥ 1.0) is from Beers and Christlieb (2005).

Fontaine et al., 1986) and, consequently, a large settling velocity.

Figure 4.3 shows that for given post-thermohaline-mixing abundances the abundance evolution prior to FDU can be parametrized as a function of only $M_{\rm env}$. But once FDU starts and the envelope deepens, a kind of hysteresis is seen in that the abundances at a given $M_{\rm env}$ are not the same as they were prior to FDU. This is because diffusion has modified the radiative layers below the envelope in the meantime.

Carbon-enhanced metal-poor stars are distinguished from other metal-poor stars based on their [C/Fe] value. Assuming that atomic diffusion is correctly predicted and no additional mixing processes operate in the radiative regions below the envelope, Fig. 4.3c implies that they must have envelope masses larger than $10^{-5}\ M_\odot$. Otherwise, they would not be classified as carbon-enhanced. While models without levitation do not have such a limit, the metallicity rapidly decreases below this value because of settling – at $M_{\rm env} \approx 10^{-6}\ M_\odot$ the surface [Fe/H] ≈ -4, which is much lower than typical of CEMP-*s* stars.

For a given combination of AGB and CEMP-*s* star masses (M_1 and $M_{2,\rm f}$, respectively) the convective envelope is deeper in models with larger accreted mass. For example, a 0.8 $M_\odot$ CEMP-*s* star with an initial mass of 0.6 $M_\odot$ retains a more massive envelope than one with an initial mass of 0.7 $M_\odot$. This is due to the higher average opacity of these stars (more metal-rich stars maintain thicker convective envelopes for the same reason). The difference in $M_{\rm env}$ can be a factor of 2–10 (depending on M_1, $M_{2,\rm f}$, and the range of $M_{2,\rm i}$) which can lead to substantially different abundances when the envelopes are small (Fig. 4.3).

As can be seen from Fig. 4.3 and Table 4.2, diffusion is extremely efficient in many of our models, leading to unrealistic abundance anomalies (e.g. [C/Fe] < -1 or [C/Fe] > 4). In most of our more massive CEMP-*s* models ($M_{2,\rm f} \geq 0.85\ M_\odot$) diffusion is so efficient that our code is incapable of handling the steep abundance gradients developing at the base of the envelope and we are forced to stop the computations before the main sequence turn-off. Such massive CEMP-*s* stars are nevertheless probable according to population synthesis calculations (Abate et al., 2015c) and would help explain the properties of some CEMP-*s* RR Lyrae stars (Stancliffe, Kennedy, Lau et al., 2013), so we would like to explore their connection to observations. Therefore, we proceed by assuming that diffusion, and possibly thermohaline mixing, is inhibited throughout these stars for one reason or another (leaving open the nature and cause of the underlying mechanism for now) and evolve two sets of model sequences without atomic diffusion: one set with thermohaline mixing and one without. The results from these simulations are summarised in Table 4.3.

These models have some key differences in global properties and surface abundances from the model sequences with atomic diffusion. First, the surface abundances do not change prior to mass transfer. More importantly, after thermohaline mixing has reached equilibrium no further abundance changes occur until FDU (i.e. between the stages labelled '5' and '9' in Fig. 4.1). The importance of FDU still depends on the depth of thermohaline mixing, as in models with diffusion. In models without thermohaline mixing the surface abundances do not change until FDU during which the accreted material is invariably diluted by mixing throughout most of the star (down to a mass coordinate of 0.3–0.35 $M_\odot$).

In agreement with previous studies, models with diffusion are younger (by a few percent) at a given evolutionary stage and have lower effective temperatures at the turn-off than models without diffusion, primarily because of the gravitational settling of helium throughout the star (e.g. Castellani and degl'Innocenti, 1999; VandenBerg, Richard, Michaud et al., 2002; Bressan, Marigo, Girardi et al., 2012). Our non-accreting models with diffusion are about 150 K cooler than models without diffusion (compare Table 4.2 and 4.3). Among our CEMP-*s* models, those with thermohaline mixing but without diffusion are generally between 100 to 300 K hotter than models without both. The latter, in which the accreted material remains unmixed on the surface, are cooler because of the high opacity of the outer layers owing to the metal-richness of the accreted material.

Table 4.3: Results from simulations without atomic diffusion. Columns have the same meaning as in Table 4.2 except for the third column (D_μ?) which here indicates whether thermohaline mixing is included.

$M_{2,i}$	ΔM	D_μ?	m_{thm}[a]	[C/Fe][a] post-th.mix.	At the time when envelope mass is smallest							[C/Fe][b] post-FDU
					t (Gyr)	$\log(L/L_\odot)$	T_{eff}	$\log g$	M_{env}	[Fe/H]	[C/Fe]	
					$M_1 = 0.9\ M_\odot$							
0.700	0.200	no	...	...	13.98	0.6032	6719	4.05	1.59(−6)	−2.16	2.35	1.89
		yes	0.329	1.91	13.93	0.6405	6990	4.08	1.37(−8)	−2.14	1.91	1.83
0.800	0.100	no	...	...	11.29	0.6136	6734	4.05	1.15(−6)	−2.16	2.35	1.58
		yes	0.461	1.72	11.23	0.6221	7079	4.12	6.39(−9)	−2.14	1.72	1.59
0.750	0.200	no	...	...	12.20	0.6829	7019	4.07	1.07(−8)	−2.16	2.35	1.85
		yes	0.372	1.91	12.05	0.6799	7359	4.16	2.84(−10)	−2.14	1.91	1.82
					$M_1 = 1.0\ M_\odot$							
0.650	0.200	no	...	...	14.18	0.5809	6841	4.08	1.59(−7)	−2.17	1.76	1.34
		yes	0.343	1.39	14.14	0.5877	6928	4.10	3.49(−8)	−2.15	1.39	1.32
0.750	0.100	no	...	...	12.39	0.5819	6836	4.08	1.73(−7)	−2.17	1.76	1.05
		yes	0.455	1.21	12.35	0.5838	6953	4.11	2.53(−8)	−2.15	1.21	1.06
0.800	0.050	no	...	...	11.17	0.5820	6849	4.08	1.38(−7)	−2.17	1.76	0.78
		yes	0.543	1.02	11.16	0.5861	6979	4.11	1.73(−8)	−2.14	1.01	0.79
0.700	0.200	no	...	...	12.04	0.6436	7198	4.13	6.53(−10)	−2.17	1.76	1.30
		yes	0.381	1.39	11.98	0.6391	7291	4.16	3.65(−10)	−2.15	1.39	1.30
0.800	0.100	no	...	...	10.31	0.6459	7190	4.13	6.91(−10)	−2.17	1.76	1.01
		yes	0.511	1.20	10.24	0.6369	7321	4.17	3.14(−10)	−2.15	1.20	1.02
0.850	0.050	no	...	...	9.17	0.6493	7193	4.12	6.71(−10)	−2.17	1.76	0.74
		yes	0.593	1.02	9.10	0.6384	7350	4.17	2.74(−10)	−2.14	1.02	0.75
0.750	0.200	no	...	...	10.20	0.6613	7544	4.22	1.52(−10)	−2.17	1.76	1.27
		yes	0.433	1.38	10.13	0.6538	7631	4.25	1.21(−10)	−2.15	1.38	1.27
					$M_1 = 1.25\ M_\odot$							
0.700	0.200	no	...	...	10.18	0.6008	6677	4.04	3.31(−6)	−2.15	2.57	...
		yes	0.194	2.03	10.08	0.6829	6963	4.03	2.76(−9)	−2.14	2.03	1.94
0.800	0.100	no	...	...	9.24	0.6103	6688	4.04	2.67(−6)	−2.15	2.57	...
		yes	0.324	1.83	9.02	0.6225	7091	4.13	6.12(−9)	−2.14	1.82	1.75
					no accretion							
0.750	...	no	...	...	15.44	0.4033	6509	4.12	2.31(−5)	−2.14	0.00	...
0.800	...	no	...	...	12.17	0.5013	6741	4.11	1.16(−6)	−2.14	0.00	−0.01
0.850	...	no	...	...	9.75	0.5897	7047	4.12	7.61(−9)	−2.14	0.00	−0.03

Notes. Values of M_{env} are given in the format $n(m) = n \times 10^m$ for concision. [(a)] Undefined for models without thermohaline mixing. [(b)] Some of the models stop earlier.

4.2.3 Thermohaline mixing

The fraction of the star mixed by thermohaline convection, which we shall call the thermohaline mixing efficiency, essentially depends on the mean molecular weight of the accreted material and its total mass compared to the final mass of the star. The more helium- and metal-rich the accreted material, the greater its molecular weight compared to the initial composition, and the greater the portion of the star that gets mixed. From the last column of Table 4.1 we therefore expect that, for a given amount of accreted material, thermohaline mixing should be most efficient when that material comes from a primary of 1.5 $M_\odot$ and least efficient when it comes from a primary of 1.0 $M_\odot$, which is indeed the case (Fig. 4.4).

Furthermore, the greater the amount of the high-μ material, the deeper the mixing must be for the μ-gradient to be removed. If an amount ΔM of AGB ejecta with a mean molecular weight μ_a is mixed with $M_{2,f} - \Delta M - m_{thm}$ of the unpolluted material with a molecular weight μ_i ($< \mu_a$) before the μ-gradient is removed, a mixed region $M_{2,f} - m_{thm}$ with molecular weight μ_f results (Fig. 4.5). Equating the states before and after mixing, one gets that the removal of the μ-gradient implies a linear relationship between the accreted-to-final mass ratio and mixing efficiency. Indeed, a linear relationship is a reasonable approximation in the range $0.05 \lesssim \Delta M/M_{2,f} \lesssim 0.2$ of accreted-to-final mass ratios. However, higher and lower ratios of $\Delta M/M_{2,f}$ require special consideration.

First, a high $\Delta M/M_{2,f}$ corresponds to a case where a lot of mass is transferred to a low-mass star, which

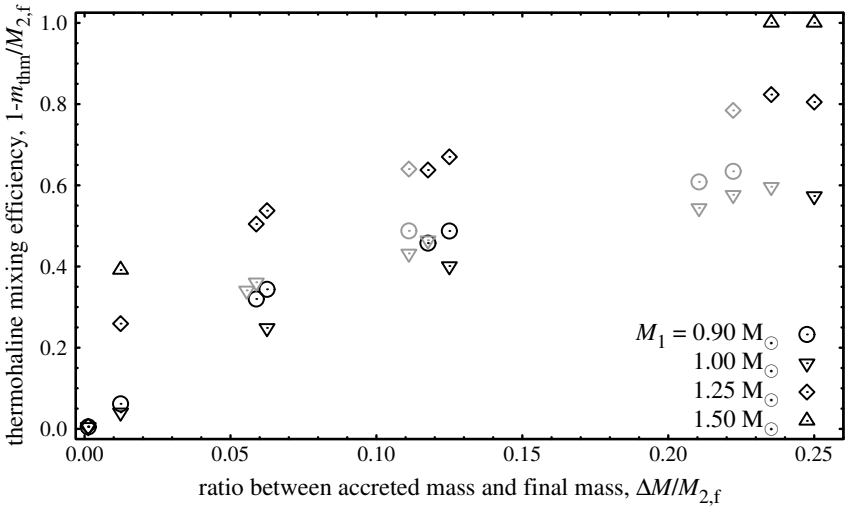

Figure 4.4: Thermohaline mixing efficiency (fraction of the star that is mixed) as a function of the ratio between accreted mass and final mass for different primaries. Black and grey symbols correspond to models with and without diffusion, respectively. Each symbol represents a unique combination of M_1, $M_{2,f}$, and ΔM.

implies that the mass transfer takes place when the secondary is still nearly on the ZAMS. Two outcomes are possible. If the accreted material has a sufficiently high molecular weight compared to the molecular weight throughout the star, thermohaline mixing affects the whole star, and the composition is nearly homogenised. For example, this occurs when a 0.65 $M_\odot$ secondary accretes 0.2 $M_\odot$ of material from a 1.5 $M_\odot$ primary. On the other hand, if the accreted material has a lower molecular weight than some central region of the star, increasing the accreted mass will not lead to a much deeper mixing because of the steepness of the μ-gradient near the centre. The mixing efficiency can therefore decrease for higher $\Delta M/M_{2,f}$ (although at this point almost all of the star will be mixed, anyway).

Second, in models with diffusion low accreted-to-final mass ratios lead to relatively inefficient thermohaline mixing. Contrary to models without diffusion, where the molecular weight is constant outside of nuclear burning regions, in these models there is a stabilising μ-gradient throughout the star owing to gravitational settling. This presents a "μ-barrier" to thermohaline mixing that must be overcome for mixing to happen (Thompson et al., 2008). If only a tiny amount of material is accreted ($\Delta M \lesssim 0.001\ M_\odot$), thermohaline mixing can be almost completely inhibited (left bottom corner of Fig. 4.4). Nevertheless, even in these cases the surface carbon content is depleted by a factor of two or more because the mass of the mixed region, $M_{2,f} - m_{thm}$, is always greater than ΔM.

For $\Delta M > 0.01\ M_\odot$ the μ-barrier is largely overwhelmed. However, the mixing is nevertheless slightly less efficient than in models without diffusion even for large amounts of accretion. Similar conclusions were reached by Stancliffe and Glebbeek (2008). Overall, the surface carbon abundance is typically reduced by somewhere between 0.3 to 1 dex depending on the relative amount of the accreted material and its molecular weight. Since radiative levitation has almost no influence on the molecular weight profile deep in the star, it has almost no influence on the efficiency of thermohaline mixing.

4.3 Comparison with observations

We have presented four sets of models of CEMP-*s* stars. Two of the sets comprise models with thermohaline mixing and atomic diffusion (one set with, one without radiative levitation). The other

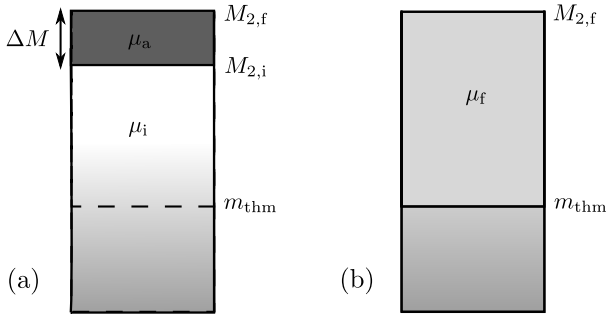

Figure 4.5: Schematic illustration of the mean molecular weight distribution in a star before (a) and after (b) thermohaline mixing. The shaded area around m_thm and below indicates a region in which the mean molecular weight has been raised as a result of nuclear processing.

two sets comprise models without diffusion (one set with, one without thermohaline mixing). We now compare the four sets of models with observations of CEMP stars.

The largest data set of Galactic metal-poor stellar spectra currently available is that from the Sloan Digital Sky Survey (SDSS; e.g. York, Adelman, Anderson et al., 2000; Ahn, Alexandroff, Allende Prieto et al., 2012; Ahn, Alexandroff, Allende Prieto et al., 2014) and its sub-survey, the Sloan Extension for Galactic Understanding and Exploration (SEGUE; Yanny, Rockosi, Newberg et al., 2009). Lee, Beers, Masseron et al. (2013) used the spectra collected by SDSS/SEGUE to derive the stellar parameters and carbon abundances ([C/Fe]) in close to 250 000 stars, around 10 000 of which have [Fe/H] < -2. We now use this homogeneous metal-poor sample (Lee et al., 2013, priv. comm.) to compare the observed carbon abundances with our models.

Comparing the observed [C/Fe] abundances with models must be done with care. Use of a fixed metallicity ([Fe/H]) range might not be adequate because of the diffusion of iron (Figs. 4.6a and 4.6b). Only the 0.8 $M_\odot$ models with levitation generally predict [Fe/H] to remain within a factor of about two of the initial value ([Fe/H] $= -2.14$) throughout the evolution, whereas the models without levitation have [Fe/H] $\lesssim -2.5$ near the turn-off. Meanwhile, most of the 0.85 $M_\odot$ models have [Fe/H] < -3 (without levitation) or [Fe/H] $\gtrsim -1$ (with levitation).

It is safer to first consider [C/H] because the largest [C/H] values should be close to 0.5 dex, independent of metallicity. In the metallicity range typical of CEMP-*s* stars ($-2.5 \leq$ [Fe/H] ≤ -2.0), this is indeed the case for subgiants ($\log g \lesssim 3.7$) but very few turn-off stars ($\log g \approx 4$) seem to have [C/H] > 0 (Figs. 4.6c and 4.6d). Is this difference in the maximum [C/H] values between the two groups in the observational data (Δ[C/H] ≈ 0.5) evidence of gravitational settling of carbon in CEMP stars? And does the similar 0.5 dex difference seen in the [C/Fe] data (Figs. 4.6e and 4.6f) then imply that iron is levitated just enough that its abundance stays roughly constant throughout the evolution? This seems rather unlikely because then the carbon-normal population should plausibly also have lower [C/H] (and [C/Fe]) values near the turn-off which is not the case. On the contrary, the observations suggest that the carbon abundance in carbon-normal metal-poor stars is increasing on the main sequence until they reach the turn-off. This is exactly the opposite behaviour that atomic diffusion predicts! Moreover, there is no obvious candidate for a physical process that could cause the surface carbon abundance to increase on the main sequence.

The carbon-normal metal-poor stars listed in the Stellar Abundances for Galactic Archeology database (SAGA; Suda, Katsuta, Yamada et al., 2008; Suda, Yamada, Katsuta et al., 2011) do not seem to show a similar behaviour of increasing carbon abundance on the main sequence (C. Abate, priv. comm.), although the relatively small number statistics (23 stars with $-2.5 \leq$ [Fe/H] ≤ -2.0, [C/Fe] < 1 and $\log g > 4.0$) and the heterogeneity of the data could perhaps hide such a trend. Unfortunately, whether

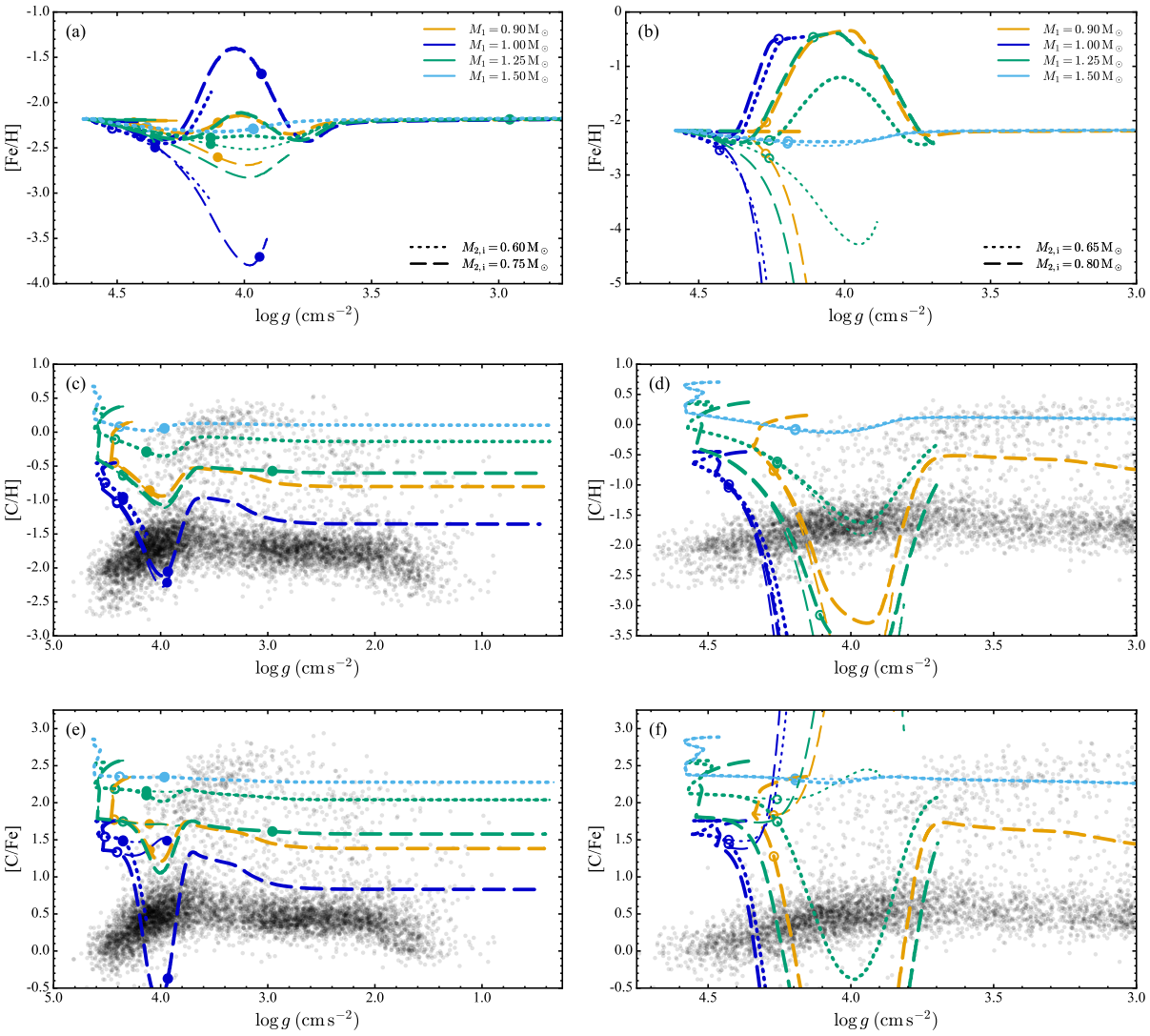

Figure 4.6: Evolution of [Fe/H] (upper panels), [C/H] (middle panels) and [C/Fe] (lower panels) in CEMP-*s* models of 0.8 $M_\odot$ (left panels) and 0.85 $M_\odot$ (right panels) with diffusion. Thick lines are models with radiative levitation, whereas thin lines are those without. Empty circles mark an age of 10 Gyr and filled circles mark an age of 13.8 Gyr, i.e. the part of the track between the circles covers the expected age range of CEMP-*s* stars. The small, grey circles show the metal-poor stars observed in the Sloan Digital Sky Survey in the metallicity range $-2.5 \leq$ [Fe/H] ≤ -2.0 (Lee, Beers, Masseron et al., 2013).

there is a real difference in the upper [C/H] and [C/Fe] values between turn-off stars and subgiants remains unclear.

Most of the models are at odds with the Lee et al. (2013) data, regardless of whether the abundance differences between turn-off stars and subgiants are caused by atomic diffusion. For example, while some of the 0.8 $M_\odot$ models predict abundances that are consistent with the observations, they only do so at very late times, i.e. at ages exceeding the age of the Universe (13.8 Gyr; Hinshaw, Larson, Komatsu et al. 2013). At earlier times stars with low-mass AGB companions (which thus accreted mass later) and/or with low initial masses (which were thus less evolved at the point of mass transfer) are still relatively unevolved. They should be observable as carbon-rich low-luminosity ($\log g \gtrsim 4.1$) objects. But such objects are conspicuous by their absence in the Lee et al. (2013) results (at all metallicities; their figure 6). Since there are plenty of carbon-normal low-luminosity stars in the data, it is difficult to imagine how this could be a selection effect, particularly since a few carbon-rich dwarfs have been found in the SDSS data in detailed abundance studies (Aoki, Beers, Sivarani et al., 2008; Behara, Bonifacio, Ludwig et al., 2010).[2] By contrast, the 0.85 $M_\odot$ CEMP-*s* models are sufficiently evolved but diffusion is so efficient that unrealistic abundances (e.g. [C/Fe] < -0.5 with levitation or [C/Fe] > 3.5 without levitation) are predicted in nearly all such stars around the turn-off (Fig. 4.6f). Clearly, in these more massive CEMP-*s* stars some physical process must be countering atomic diffusion, at least near their surface.

The disagreement between observations and models concerning the existence of low-luminosity carbon-rich stars has little to do with atomic diffusion – even if we identify a process that neatly counteracts diffusion near the surface, models will still predict many carbon-rich unevolved objects. In fact, if this process were to counteract diffusion throughout the star, the tension with observations would increase because diffusion starves the core of fuel and accelerates the evolution, making the star spend less time on the main sequence. Perhaps, the SDSS sample indicates that the mass ratio ($q \equiv M_{2,\mathrm{i}}/M_1$) in CEMP-*s* progenitor systems is biased towards unity, contrary to the common assumption of a flat distribution. If q is close to one, the mass transfer occurs relatively late, giving the secondary more time to evolve before it becomes a CEMP-*s* star.

Overall, models without diffusion are better able to envelop the observational data (Fig. 4.7). For example, CEMP-*s* models that have accreted less carbon-rich material (here coming from 1 $M_\odot$ primaries) have [C/Fe] < 1.5 with [C/Fe] increasing with accreted mass. Models that have accreted more carbon-rich material (from primaries with masses 1.25 $M_\odot$, 1.5 $M_\odot$) can have [C/Fe] $\gtrsim 2$ throughout evolution. Models with thermohaline mixing seem to be preferred because no sharp change in [C/Fe] at FDU is evident from the data, although there seem to be relatively fewer highly enriched (e.g. [C/Fe] > 2) stars after first dredge-up ($\log g < 3$). Lower mass models ($M_{2,\mathrm{f}} \approx 0.8\ M_\odot$) without diffusion would predict similar abundance evolution (Stancliffe et al., 2007; Stancliffe and Glebbeek, 2008). However, most of them, coming from systems with relatively low-mass AGB companions compared to earlier works, would be consistent with the data only for $t > 13.8$ Gyr.

Last, there are some objects with [C/Fe] $\gtrsim 2.5$ whose surface gravities ($\log g \lesssim 3$) imply that they are close to the end of FDU if not past it. How might we explain such objects, assuming that they were polluted by an AGB companion? Since carbon is not produced in the star, it is hard to imagine how the surface carbon abundance could be above the one in the accreted material. This limits the possible primaries to those that are able to produce at least this much carbon. From the models of Lugaro et al. (2012) these are AGB stars with $1.25 \lesssim M_1/M_\odot \lesssim 3$. Lower mass AGB stars do not produce enough carbon; and higher mass stars convert the carbon into nitrogen in the lower part of their convective

[2] Two examples are the CEMP-no (or -*r*) star SDSS0036-10 ([Fe/H] $= -2.4$, $\log g = 4.5$, [C/Fe] $= 2.3$, [Ba/Fe] $= 0.3$) and the CEMP-*s* (or -*r*/*s*) star SDSS2047+10 ([Fe/H] $= -2.1$, $\log g = 4.5$, [C/Fe] $= 2.0$, [Ba/Fe] $= 1.5$) from Aoki et al. (2008). Behara et al. (2010) present the CEMP-*r*/*s* star SDSSJ0912+0216 ([Fe/H] $= -2.5$, $\log g = 4.5$, [C/Fe] ≈ 1.5, [Ba/Fe] $= 1.5$, [Eu/Fe] $= 1.2$), which may, however, be more evolved with $\log g \approx 4.0$ (Aoki, Beers, Lee et al., 2013).

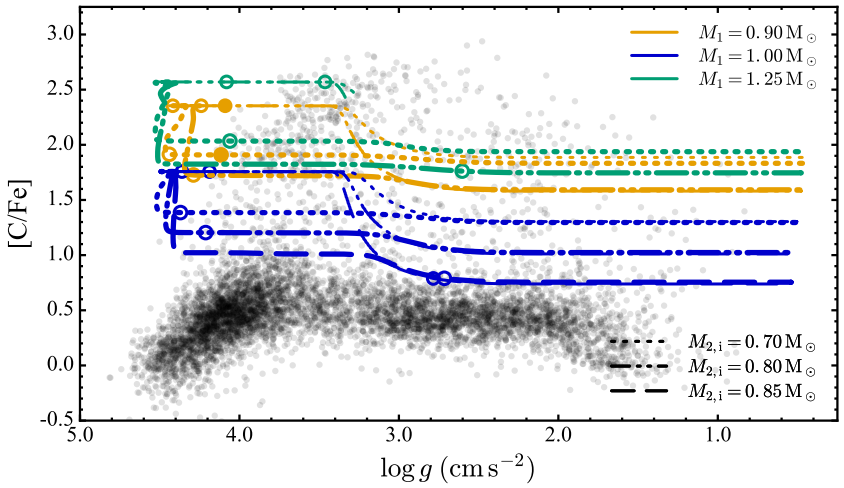

Figure 4.7: Similar to Figs. 4.6e and 4.6f, but here the lines correspond to CEMP-*s* models of 0.9 $M_\odot$ without diffusion. Thick lines are models with thermohaline mixing, whereas thin lines are those without.

envelope (a process known as hot-bottom-burning). Moreover, a large amount of mass must be transferred because the combined carbon reduction from thermohaline mixing and FDU can only be about 0.5 dex at most (the maximum [C/Fe] given by the AGB models of Lugaro et al., 2012, is about +3.2). This implies an accreted-to-initial mass ratio, $\Delta M/M_{2,\mathrm{i}}$, between about 0.25, if all the mixing occurs during FDU (where the envelope mass grows to about 0.5 $M_\odot$), and 0.5, if thermohaline mixing is efficient (as it will be in the absence of some inhibitory process because of how unevolved the progenitor of the CEMP-*s* star must be). The respective accreted-to-final mass ratios, $\Delta M/M_{2,\mathrm{f}}$, are between 0.2 and 0.35. Hence, the progenitor systems of the most carbon-rich evolved stars must be small mass-ratio binaries in which a lot of mass has been transferred to the secondary. It may be difficult to account for such stars without also predicting too many low-luminosity carbon-rich stars from cases where less mass has been transferred.

4.4 Discussion

The results presented in this chapter may lead one to wonder whether the abundance anomalies predicted by our diffusion models are overestimated. We have run multiple tests to address this concern. First, we have tried to reproduce the results of Richard et al. (2002b). In particular, we have compared the abundance evolution in a $M = 0.8\ M_\odot$ model with an initial composition taken from their table 1 ($Z = 1.7 \times 10^{-4}$; [Fe/H] = −2.31). We get good agreement in terms of the temperature and luminosity at the turn-off although our model is longer-lived by about 0.5 Gyr. The abundance anomalies from settling and/or levitation of He, C, N, and Fe agree within 0.1 dex. For other elements the abundances differ by 0.3–0.4 dex. Given that in our model the convective envelope mass is smaller by about a factor of two throughout most of the evolution (the minimum size of the convective envelope in our model is only about $3.7 \times 10^{-6}\ M_\odot$ whereas Richard et al. (2002b) get about $2.5 \times 10^{-5}\ M_\odot$), these differences are plausible. Judging from their figure 2, a smaller envelope mass in their model would lead to greater over-abundances of O, Ne, and Mg, and a smaller over-abundance of Si. All of these changes would reduce the discrepancies between their model and ours.

Second, we have tested whether the large abundance anomalies predicted by our models stem specifically from our simplified treatment of diffusion. For this purpose we have ported into our code the relevant

parts from the code used by Hu, Glebbeek, Thoul et al. (2010, priv. comm.)[3] and run a $M = 0.8\ M_\odot$, $Z = 10^{-4}$ diffusive model without radiative levitation (with the ZAMS chemical composition from Table 4.1). In this model diffusion reduces the helium and metal abundances in the envelope on much shorter timescales. The same $M = 0.8\ M_\odot$ model run with the MESA code (Paxton, Bildsten, Dotter et al., 2011; Paxton, Marchant, Schwab et al., 2015) yields similar results, which is reassuring given that the treatment of diffusion is based on the work of Burgers (1969) and Thoul, Bahcall and Loeb (1994) in both MESA and Hu et al. (2010). The abundances in the MESA model are depleted to a much greater degree: 5 dex for helium (compared to our 2.5 dex) and 5–6 dex (3–4 dex) for metals, even though the envelope masses are in a good agreement (the minimum envelope mass is $4.5 \times 10^{-7}\ M_\odot$ in STARS and $6.0 \times 10^{-7}\ M_\odot$ in MESA). The conclusion from all three of these tests is the same – if anything, the diffusion models presented here underestimate the amount of diffusion that we would get from a more rigorous treatment.

We have performed spatial resolution tests in three systems (denoted by an asterisk in Table 4.2) by varying the default number of meshpoints (999) by a factor of two. All models give consistent results (within a couple of percent) in terms of the global properties, depth of thermohaline mixing, abundance anomalies after turn-off, and post-FDU abundances. The size of the convective envelope at minimum is consistent within ten percent. We thus conclude that the models are sufficiently resolved.

Our approach of interpolating the opacities and accelerations from tables computed in real time necessitates the introduction of some numerical parameters. These parameters control mainly the amount by which some species has to change to warrant the computation of a new table. As discussed in Sect. 3.3.5, we have made sure that our results do not depend on the choice of these parameters, i.e. the tables are computed often enough (Fig. 3.2). The use of tabulated opacities above $\log T = 7.3$ similarly has virtually no effect on any of our results (Fig. 3.4).

The size of the convective envelope throughout the evolution depends somewhat on the choice of the mixing length parameter (Sect. 2.1.3) with larger values resulting in more massive envelopes. Our value, $\alpha_{\rm MLT} = 2.0$, is based on a calibration between the radius, effective temperature, and luminosity of a $Z = 0.0142$, $M = 1\ M_\odot$ diffusive model with OP opacities at an age of 4.56 Gyr and the Sun. Stars of masses, metallicities, and evolutionary stages different from the Sun should have other values of $\alpha_{\rm MLT}$ (e.g. Trampedach, Stein, Christensen-Dalsgaard et al., 2014) but meaningful quantitative predictions are virtually impossible. In a $0.8\ M_\odot$, $Z = 10^{-4}$ model increasing or decreasing $\alpha_{\rm MLT}$ by 5% accordingly changes the envelope mass by about 50%, which, given that $M_{\rm env} < 10^{-6}\ M_\odot$, translates into substantial changes in the surface abundances (Fig. 4.3). Since theoretical models suggest that at lower metallicities one should use lower $\alpha_{\rm MLT}$ values (at least for $-0.6 <$ [Fe/H] $< +0.3$; Bonaca, Tanner, Basu et al., 2012), it is unlikely that we have overestimated the importance of diffusion by underestimating the value of $\alpha_{\rm MLT}$.

4.4.1 Missing mixing processes

The strong abundance anomalies predicted by diffusive models are not observed in CEMP stars. This suggests that in real stars atomic diffusion is inhibited by some physical process that we have not included in our models. In the next chapter we investigate whether rotational mixing could be the culprit. For now, we examine a simple test case and add a "turbulent" diffusion term to $D_{{\rm mix},i}$ in Eq. (3.8) as proposed by Richer, Michaud and Turcotte (2000) and Richard, Michaud and Richer (2005):

[3] In their code the full set of Burgers flow equations (Burgers, 1969) is solved, and their treatment of diffusion is thus valid for arbitrary compositions.

$$D_{\mathrm{T}} = D_0 D_{\mathrm{He}}(T_0) \left[\frac{\rho}{\rho(T_0)}\right]^{-3}. \tag{4.4}$$

This type of parametrization extends the surface mixing region down to where the local temperature is somewhat larger than T_0. Richard et al. (2005) find that observations of lithium abundances in population II stars require $\log T_0 \approx 6.0$. Similar values have been found to reproduce the small systematic abundance differences between turn-off and giant stars in old globular clusters (Korn, Grundahl, Richard et al., 2006; Nordlander, Korn, Richard et al., 2012; Gruyters, Nordlander and Korn, 2014). Nevertheless, the ad-hoc nature of this prescription should be kept in mind. With this prescription we can primarily constrain the depth to which some form of mixing must occur to reconcile the models with observations, but not the physical processes responsible for this mixing.

We test the effect of turbulent diffusion on the evolution of a 0.75 $M_\odot$ star accreting 0.1 $M_\odot$ of material from a 1 $M_\odot$ primary. While in the absence of turbulence the resulting 0.85 $M_\odot$ model shows extremely large abundance anomalies ([Fe/H] > -0.5 with levitation and [Fe/H] < -9.2 without levitation), turbulence with $D_0 = 400$ (as used by Richard et al., 2005) and $\log T_0 = 6.0$ completely negates them (Fig. 4.8). Even much smaller turbulent diffusion coefficients (e.g. $D_0 = 1$) suffice to erase the anomalies. Indeed, the key parameter here is T_0 – as long as the mixing region remains large enough ($\log T_0 \gtrsim 5.5$ or $M_{\mathrm{env}} \gtrsim 10^{-4}\ M_\odot$), atomic diffusion is strongly suppressed. In terms of global properties, models with more pervasive turbulence are hotter and therefore more closely resemble models without diffusion. This can be seen from comparing the turbulent models with the model with thermohaline mixing only (solid grey line) in Fig. 4.8c.

Figure 4.8 also shows that while the turbulent diffusion prescription of Richard et al. (2005) can inhibit diffusion in the outer layers of a star, it has almost no influence on thermohaline mixing. This is not to say, however, that some form of turbulence (e.g. rotationally driven horizontal turbulence; Denissenkov and Pinsonneault, 2008a) could not inhibit thermohaline mixing as well. We return to this question in the next chapter (Sect. 5.3.2) when considering models with rotational mixing.

4.4.2 Mass loss

So far we have ignored mass loss. Simple estimates imply that it may be too important to neglect. With a mass-loss rate comparable to the current solar value, $2\text{–}3 \times 10^{-14}\ M_\odot\,\mathrm{yr}^{-1}$ (Wang, 1998), a star will lose more than $10^{-4}\ M_\odot$ over the roughly 10^{10} years it spends on the main sequence. This is a very large amount compared to the envelope masses of our models (Fig. 4.3) and could greatly interfere with atomic diffusion.

In the absence of mass loss the convective envelope of a star moves outwards in mass until the beginning of FDU. But when mass loss erodes the surface, this outward movement is halted and eventually reversed while the star is still on the main sequence. As the envelope now moves inwards, the surface abundances reflect the composition of the progressively deeper layers that get exposed. Qualitatively, if the mass-loss rate is sufficiently high, the removal of the outer layers is so fast that diffusion has not had enough time to modify the newly exposed layers and only small abundance anomalies can develop (Swenson, 1995). On the other hand, mass-loss rates below some limit must be negligible and have essentially no effect on the surface abundances.

We now estimate what mass-loss rates are necessary to prevent the development of abundance anomalies and what mass-loss rates are negligible. For simplicity, we use Reimers (1975) mass-loss formula with different factors η:

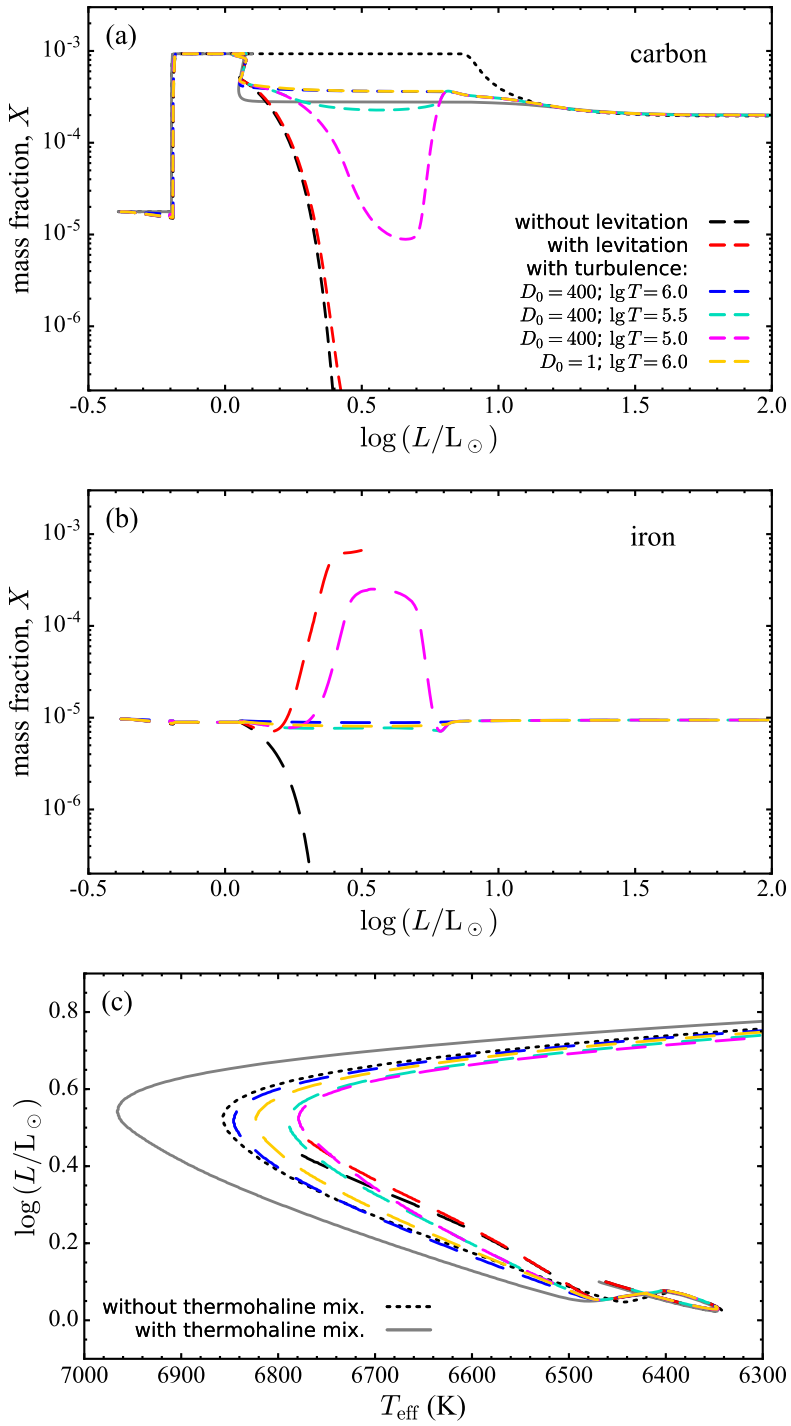

Figure 4.8: Effect of turbulence on the evolution of carbon (a) and iron (b) mass fractions, and the HRD (c) of a 0.75 $M_\odot$ star accreting 0.1 $M_\odot$ of material from a 1 $M_\odot$ primary. Large abundance variations are expected after accretion in absence of turbulence (black and red dashes). Inclusion of turbulence as in Eq. (4.4) erases all abundance signatures of atomic diffusion on the post-mass-transfer main sequence (dark blue) even for small turbulent diffusion coefficients (orange). Only when the temperature parameter is reduced to $\log T_0 \lesssim 5.5$ do the abundance variations start to reappear (light blue and magenta). The thermohaline-mixing-only model (solid grey) is hotter than the models with turbulence because in the latter diffusion still modifies the layers with $T \gtrsim T_0$ and thermohaline mixing is not as deep. For clarity, the HRD only shows the post-mass-transfer part of the evolutionary tracks.

$$\dot{M} = -4 \times 10^{-13} \eta \frac{LR}{M} \left(\frac{LR}{M} \right)_{\odot}^{-1} \; M_{\odot}\,\mathrm{yr}^{-1}. \tag{4.5}$$

Here we only consider metal-poor 0.8 $M_{\odot}$ and 0.85 $M_{\odot}$ models without accretion. We find that if $\eta \gtrsim 0.1$, the effects of atomic diffusion are almost entirely erased in both models (Figs. 4.9 and 4.10). This translates to mass-loss rates of a few times 10^{-14}–10^{-13} $M_{\odot}\,\mathrm{yr}^{-1}$ throughout the main sequence. In contrast, when the mass-loss rate falls below about 10^{-16} $M_{\odot}\,\mathrm{yr}^{-1}$, the abundance evolution proceeds as in models without mass loss. Intermediate mass-loss rates result in less extreme but non-negligible abundance variations. Note that the lost material is assumed to have the same composition as the surface at that time. Depending on the mass-loss rate and mechanism, some elements may be lost more readily than others, leading to more complicated abundance variations (e.g. Michaud, Dupuis, Fontaine et al., 1987; Vick, Michaud, Richer et al., 2010).

Is it reasonable to expect somewhat super-solar mass-loss rates from CEMP-*s* stars on the main sequence? That is difficult to say. The form of mass loss in these stars would presumably be the same as in solar-like main sequence stars – as magnetised winds originating in a hot corona (e.g. Suzuki, 2007; Cranmer and Saar, 2011). While mass-loss rates in these stars are too small to be directly observable, indirect measurements based on the interaction of the wind with the interstellar medium yield values within about an order of magnitude of the solar mass-loss rate (Wood, Müller, Zank et al., 2002; Wood, Müller, Zank et al., 2005). Various theoretical models also normally predict mass-loss rates in this range (e.g. Holzwarth and Jardine, 2007; Cranmer and Saar, 2011; Johnstone, Güdel, Brott et al., 2015). While most of these models concern stars with near solar metallicity, to first order the mass-loss rates are not expected to depend on metallicity.

In any case, if the mass-loss rates of CEMP-*s* dwarfs are at least a few times 10^{-15} $M_{\odot}\,\mathrm{yr}^{-1}$ throughout their evolution, mass loss should at least moderate the effects of atomic diffusion, which would help explain why turn-off stars with extreme abundance anomalies are not observed.

4.5 Conclusions

Our simulations with atomic diffusion indicate that CEMP-*s* stars should show large surface abundance variations on the main sequence, particularly as they approach the turn-off. This is because they have very shallow convective envelopes ($M_{\mathrm{env}} \lesssim 10^{-4}$ $M_{\odot}$ throughout most of the evolution and perhaps as little as 10^{-8} $M_{\odot}$ near the turn-off) and, therefore, short diffusion timescales. In stars whose envelope masses fall below about 10^{-5} $M_{\odot}$ (which happens in most of our models, including nearly all those with $M > 0.8$ $M_{\odot}$) the abundances should vary by a factor of about ten. This factor rapidly increases with decreasing envelope mass resulting in unrealistic abundances (Fig. 4.3). But even though our treatment of diffusion is not as detailed as in some other works, we do not find evidence that the surface abundance variations predicted by our models are exaggerated.

Radiative levitation has only a minor influence on carbon but a large one on iron. Whereas in diffusive models without levitation the metallicity ([Fe/H]) of the star decreases until first dredge-up, in models with levitation the metallicity can increase as the star evolves along the main sequence. Consequently, models with levitation predict reduced carbon abundances ([C/Fe]) around the turn-off. This implies a systematic difference between the [C/Fe] values of stars near the turn-off and those at the beginning of FDU. Unfortunately, whether there is any such difference is difficult to establish even from the largest homogeneous sample of observational data (from SDSS; Lee et al., 2013). Any such difference, however, would clearly be smaller than predicted by most of our models (Fig. 4.6). And while some of the 0.8 $M_{\odot}$ models do predict only a small variation in [C/Fe], at ages typical of metal-poor Halo stars most of them

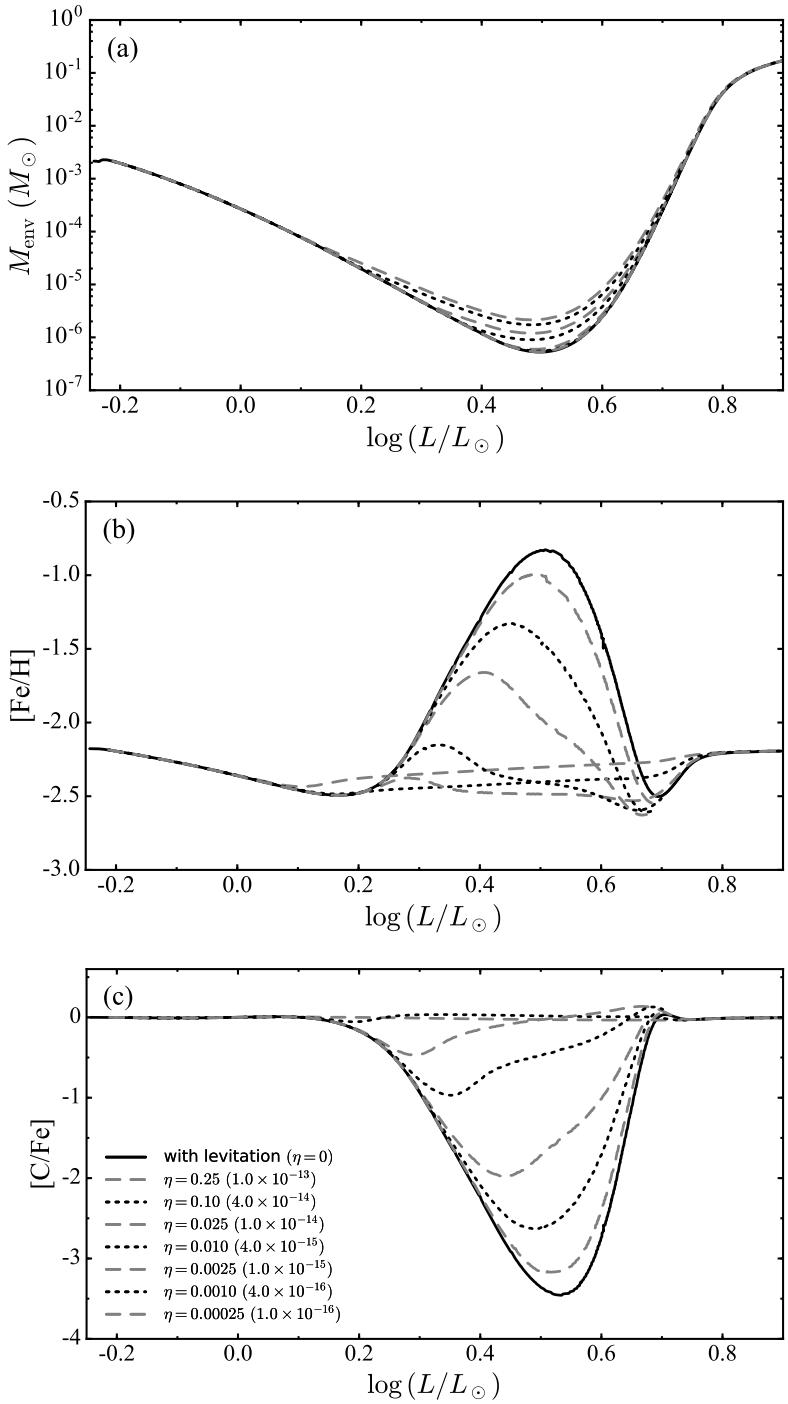

Figure 4.9: Envelope mass and abundance evolution in metal-poor 0.8 $M_\odot$ models with different Reimers-type mass-loss rates. The values in the parentheses are the mass-loss rates (in $M_\odot\,\mathrm{yr}^{-1}$) at $\log L \approx 0$; the average mass-loss rate during the main sequence is about 50% higher as a result of the mass, radius, and luminosity scaling in Reimers' law.

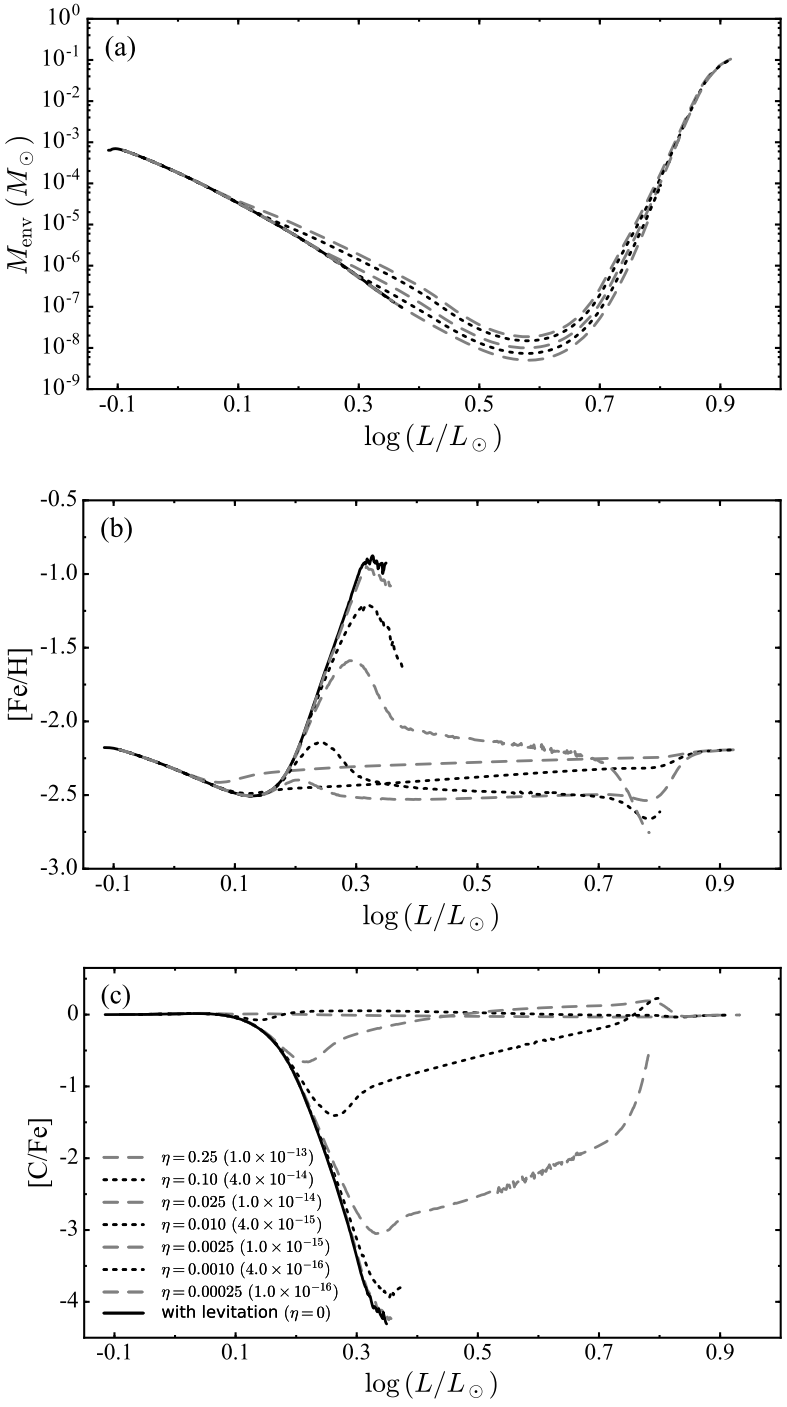

Figure 4.10: As Fig. 4.9 but for 0.85 $M_\odot$ models.

are still relatively unevolved and should be visible as carbon-rich low-luminosity objects. Very few such objects have been observed.

Although they too would predict many low-luminosity carbon-rich stars, models without atomic diffusion are generally much more successful at covering the range of observations (Fig. 4.7). We thus conclude that atomic diffusion cannot be acting alone near the surface convection zone of real CEMP-*s* stars and needs to be largely counteracted by some other physical process(es). The most extreme abundance variations (corresponding to stars with the smallest envelopes) could be moderated by mass loss as weak as $10^{-15}\ M_\odot\ \mathrm{yr}^{-1}$. In fact, a mass-loss rate of a few times the current solar value sustained throughout the evolution could on its own prevent substantial abundance anomalies from developing (Figs. 4.9 and 4.10). Otherwise, some additional internal mixing is required to inhibit atomic diffusion down to depths where the temperature exceeds about 10^6 K (about $10^{-4}\ M_\odot$ from the surface; Fig. 4.8). In the next chapter we investigate the question on how to inhibit atomic diffusion further by including angular momentum accretion in the models.

CHAPTER 5

Rotational mixing in CEMP-*s* stars

Material from this chapter is published as:

E. Matrozis and R. J. Stancliffe (2017), *Rotational mixing in carbon-enhanced metal-poor stars with s-process enrichment*, A&A **606** A55, arXiv: 1707.09434 [astro-ph.SR].

A quantitative summary of the models presented in this chapter (mainly the stellar properties and surface abundances at key points of the evolution) is published in electronic form at the Strasbourg astronomical Data Center (http://cdsarc.u-strasbg.fr/viz-bin/qcat?J/A+A/606/A55).

In Chapter 4 we found that some physical mechanism must counter atomic diffusion (gravitational settling and radiative levitation) in CEMP-*s* stars, otherwise it leads to surface abundance anomalies clearly inconsistent with observations. One possibility to inhibit atomic diffusion and bring the models more in line with observations was found to be some additional mixing operating in these stars following mass transfer.

The cause of this extra mixing was left unspecified. But rotational mixing is a promising candidate, since the accreted material should carry with it some angular momentum. In fact, the angular momentum content may be so high that an interesting question is how the accreting star can deal with it and accrete more than a few hundredths of a solar mass of material. This issue is deferred until Chapter 6. In this chapter we simply assume that the newly accreted layers of CEMP-*s* stars, which can have masses up to some tenths of a solar mass, are spinning more rapidly than their interiors. We then follow the post-mass-transfer evolution of these stars, in particular noting the evolution of their surface abundances as a result of rotational mixing, combined with atomic diffusion and thermohaline mixing.

5.1 Methods

All the models presented in this chapter are again produced with the STARS code (Chapters 2 and 3). Briefly, the mass fraction X_i of each chemical species i is governed by the advection-diffusion equation (3.1):

$$\frac{\partial X_i}{\partial t} = R_i + \frac{\partial}{\partial m}\left(\mathcal{D}_{\mathrm{mix},i}\frac{\partial X_i}{\partial m}\right) - \frac{\partial}{\partial m}\left(\mathcal{W}_i X_i\right), \tag{5.1}$$

where $\mathcal{D}_{\mathrm{mix},i} = \left(4\pi r^2 \rho\right)^2 D_{\mathrm{mix},i}$ and $\mathcal{W}_i = 4\pi r^2 \rho w_i$. The total diffusion coefficient $D_{\mathrm{mix},i}$ is given by the sum of the individual mixing coefficients (Eq. (3.8)):

$$D_{\mathrm{mix},i} = D_{\mathrm{conv}} + D_\mu + D_i + f_c D_{\mathrm{rot}}. \tag{5.2}$$

The modifications to the code necessary for modelling rotating stars are described in Sects. 2.2 and 3.2.3. In particular, the internal evolution of the angular momentum $j = \Omega r_P^2$ is governed by Eq. (2.61):

$$\frac{\partial j}{\partial t} = \frac{\partial}{\partial m_P}\left(\mathcal{D}_{\rm rot} r_P^2 \frac{\partial \Omega}{\partial m_P}\right), \tag{5.3}$$

where r_P is the radial coordinate of the isobar enclosing mass m_P (see Sects. 2.2.1 and 2.2.2). The diffusion coefficient entering $\mathcal{D}_{\rm rot} = \left(4\pi r_P^2 \bar{\rho}\right)^2 (D_{\rm rot} + D_{\rm conv})$ in radiative zones is given by Eq. (2.62):

$$D_{\rm rot} = D_{\rm ES} + D_{\rm SSI} + D_{\rm DSI} + D_{\rm GSF} + D_{\rm SH}. \tag{5.4}$$

The evaluation of the individual terms is described in Sect. 2.2.5.

The treatment of mass and angular momentum accretion is described in Sects. 2.1.5 and 2.2.6. The mass accretion rate is again set to $10^{-6}\ M_\odot\ {\rm yr}^{-1}$. The composition on the ZAMS and that of the added material is given in Table 4.1.

We adopt the same grid of initial primary (AGB) masses M_1, initial secondary masses $M_{2,\rm i}$, and accreted masses ΔM as in Chapter 4 (Sect. 4.1.1). In addition, for each combination of M_1, $M_{2,\rm i}$ and ΔM we have one more dimension: the specific angular momentum $j_{\rm a}$ of the added material. We investigate ten values of $j_{\rm a}$ in the range $(0.001\text{–}1) \times 10^{18}\ {\rm cm^2\ s^{-1}}$. While the specific angular momentum of the accreted material in real systems is likely closer to the higher end of these values (Sect. 5.3.1 and Chapter 6), this range can be interpreted as representing different degrees of angular momentum loss during accretion and is suitable to produce CEMP-*s* models with surface rotation velocities between $v_{\rm rot} \lesssim 0.5\ {\rm km\,s^{-1}}$ (i.e. nearly stationary) and $v_{\rm rot} \gtrsim 300\ {\rm km\,s^{-1}}$ (close to critical rotation), once they have settled on the post-mass-transfer main sequence. On the ZAMS the models are uniformly rotating with a surface rotation velocity $v_{\rm rot} \simeq 0.3\ {\rm km\,s^{-1}}$.

The two adjustable parameters in our adopted prescription for rotational mixing, f_c and f_μ (which determine the contribution of the rotationally induced instabilities to chemical transport and the sensitivity of rotational mixing to mean molecular weight gradients, respectively; Sects. 3.2.3 and 2.2.5) are by default set to $f_c = 1/30$ and $f_\mu = 0.05$ following Heger, Langer and Woosley (2000). The influence of these parameters is examined in Sect. 5.3.3.

To save a considerable amount of computational time, we use the OPAL-based (Iglesias and Rogers, 1996) opacity tables of Eldridge and Tout (2004) and ignore radiative levitation in this chapter. As shown in Chapter 4, this is perfectly sufficient to get a handle on the importance of atomic diffusion in a given model (e.g. Fig. 4.3).

5.2 Results

As in Sect. 4.2, we begin the discussion of the results by considering in depth the evolution of a system characterised by $M_1 = 1.25\ M_\odot$, $M_{2,\rm i} = 0.75\ M_\odot$, and $\Delta M = 0.05\ M_\odot$, first under the influence of rotational mixing alone (Sect. 5.2.1), and then together with diffusion and thermohaline mixing (Sect. 5.2.2). The general features of the calculations are summarised in Sect. 5.2.3.

5.2.1 Models with rotational mixing only

Figure 5.1 shows the Hertzsprung-Russel diagram (HRD) and the evolution of the rotation velocity of the secondary of this system when the accreted material is assigned different values of specific angular momentum. In all systems with $M_1 = 1.25\ M_\odot$ the mass transfer is assumed to start at $t = 3.06$ Gyr. This

point is identified by the circle numbered '1' in the figure. The $M_{2,\mathrm{i}} = 0.75\ M_\odot$ secondary at this age is still early on in its main sequence with a central hydrogen mass fraction of $X_{\mathrm{H,c}} = 0.59$ (down from the ZAMS value of 0.758). Once mass transfer starts, the tracks corresponding to different values of j_a separate.

The accretion rate of $\dot{M}_2 = 10^{-6}\ M_\odot\,\mathrm{yr}^{-1}$ is high enough that the accretion timescale $\tau \simeq M_2/\dot{M}_2$ is always much shorter (by a factor of ten or more) than the thermal timescale of any CEMP star progenitor. Accreting material (part of the track between '1' and '2' in Fig. 5.1a) at this rate therefore drives the star out of thermal equilibrium to higher luminosity and effective temperature. Once accretion ends ('2'), the star attempts to return to equilibrium, becoming fainter and cooler in the process.

While returning to thermal equilibrium, the stars spin up for a time, both in absolute terms and as a fraction of the critical velocity (Figs. 5.1b,c). For the highest values of specific angular momentum the stars may reach critical rotation at some point, as in the $j_\mathrm{a} = 7 \times 10^{17}\ \mathrm{cm}^2\,\mathrm{s}^{-1}$ case in this system (yellow line). Since our primary interest in this chapter is the long-term evolution after relaxation, we do not attempt to model this brief ($\delta t \simeq \tau_\mathrm{KH}$) phase accurately, assuming that it is not very important for the subsequent evolution.[1] Instead, we simply limit the centrifugal acceleration, and the resulting structural deformation, while the star is formally rotating at super-critical velocities (dashed portion of the line). After relaxation, this particular model never exceeds $\Omega/\Omega_\mathrm{c} \simeq 0.8$.

Various aspects of the evolution of the star after it settles back on the main sequence ('3') depend on the angular momentum accreted. First, owing to the extra support against gravity from the centrifugal force, rotating stars are normally cooler and less luminous than non-rotating stars – they resemble non-rotating stars of lower mass (Sackmann, 1970). Here this effect is largely compensated for by the unusual chemical structure. The non-rotating model is fairly cool ($T_\mathrm{eff} \simeq 6550$ K at turn-off, same as the $j_\mathrm{a} = 10^{15}\ \mathrm{cm}^2\,\mathrm{s}^{-1}$ track and about 200 K less than a regular $0.8\ M_\odot$ star at $Z = 10^{-4}$) because of the high metallicity of the accreted material. Making the star rotate leads to dilution of this material by rotational mixing (Fig. 5.2), and the corresponding change in the opacity actually makes the star hotter (although not more luminous) at turn-off ('4') than in the non-rotating case.[2] Only for very rapid rotation rates ($\Omega/\Omega_\mathrm{c} \gtrsim 0.5$ or $v_\mathrm{rot} > 100\ \mathrm{km\,s}^{-1}$), when rotational mixing does not lead to significant further changes in the structure of the star, do the mechanical effects shift the track back to cooler temperatures. The resulting spread in turn-off temperatures between all models of this system is only about 100 K.

Second, the internal transport of angular momentum leads to different initial rotational evolution for rapid rotators. Normally, the surface value of Ω/Ω_c somewhat increases during the main sequence evolution of low-mass stars. This is a consequence of their slight expansion, which reduces the critical rotation velocity ($\Omega_\mathrm{c} \propto R^{-3/2}$, Eq. (2.59)). Here, in the rapid rotators, Ω/Ω_c and v_rot first decrease because the accreted momentum is transported inwards. After reaching a minimum, Ω/Ω_c then increases for the rest of the main sequence. All models reach a maximum in the rotation rate somewhere between the turn-off ('4') and the beginning of first dredge-up (FDU; '5').

Figure 5.3 shows the internal evolution of the rotational velocity profile in the star between the beginning of mass transfer and the end of FDU, and Figs. 5.4 and 5.5 show the internal profiles of the specific angular momentum, angular rotation velocity, and carbon and nitrogen abundances near the main sequence turn-off for the different values of j_a. Naturally, accreting more angular momentum leads to deeper and faster transport of angular momentum. By the time the star reaches the turn-off in the $j_\mathrm{a} = 7 \times 10^{16}\ \mathrm{cm}^2\,\mathrm{s}^{-1}$ ($v_\mathrm{rot} \simeq 20\ \mathrm{km\,s}^{-1}$) case, the angular momentum is mixed to about the half-way

[1] Presumably the star must shed the super-critical layers as it contracts. Unless the material is re-accreted later, the star then ends up with a slightly lower mass. In this particular case, losing about 0.004 $M_\odot$ of material during the contraction suffices to keep the star below critical rotation. This amount of mass loss has only a small effect on the subsequent evolution.

[2] To elaborate, models with rotation are indeed slightly cooler and less luminous early on in the post-mass-transfer main sequence. But by the time they reach turn-off, most of them are hotter as a result of the mixing.

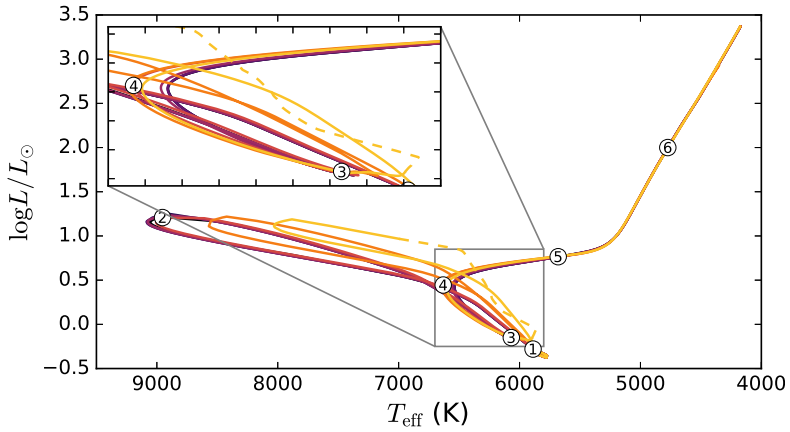

(a) Hertzsprung-Russell diagram

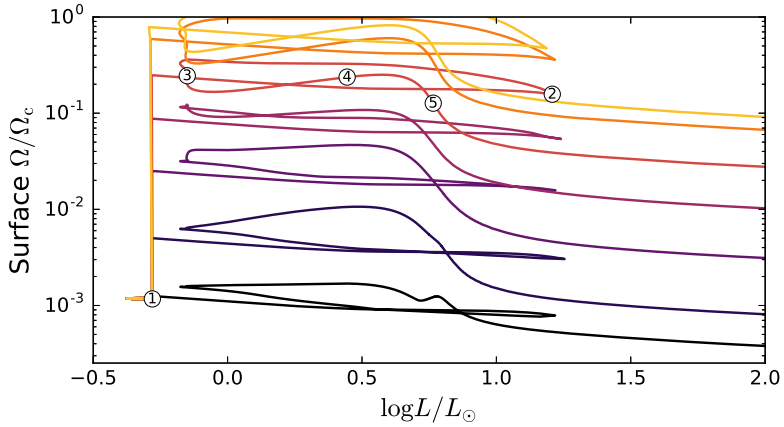

(b) Evolution of surface angular rotation velocity

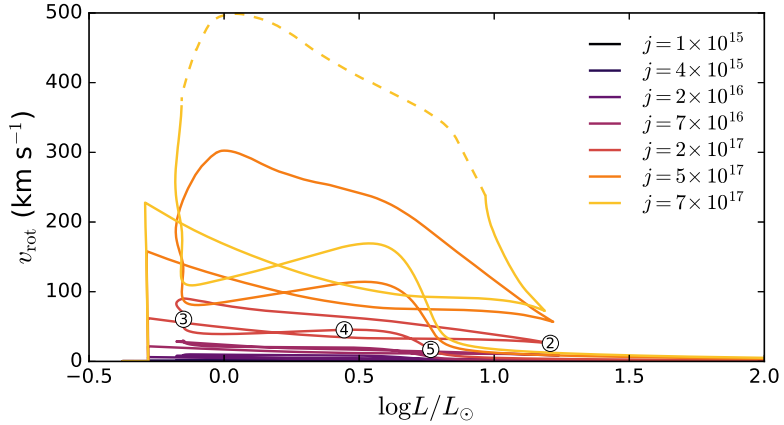

(c) Evolution of surface rotation velocity

Figure 5.1: Evolution of a $M_{2,\rm i} = 0.75\ M_\odot$ secondary accreting $\Delta M = 0.05\ M_\odot$ of material from a primary with initial mass $M_1 = 1.25\ M_\odot$. Tracks distinguish different specific angular momentum of the accreted material. The numbers on top of the $j_{\rm a} = 2 \times 10^{17}$ cm^2 s^{-1} track mark the beginning of mass transfer ('1'), end of mass transfer ('2'), return to the main sequence ('3'), main sequence turn-off ('4'), beginning of first dredge-up ('5'), end of first dredge-up ('6'). The dashed part of the $j_{\rm a} = 7 \times 10^{17}$ cm^2 s^{-1} track marks the phase of the evolution where the star is formally above critical rotation (see text).

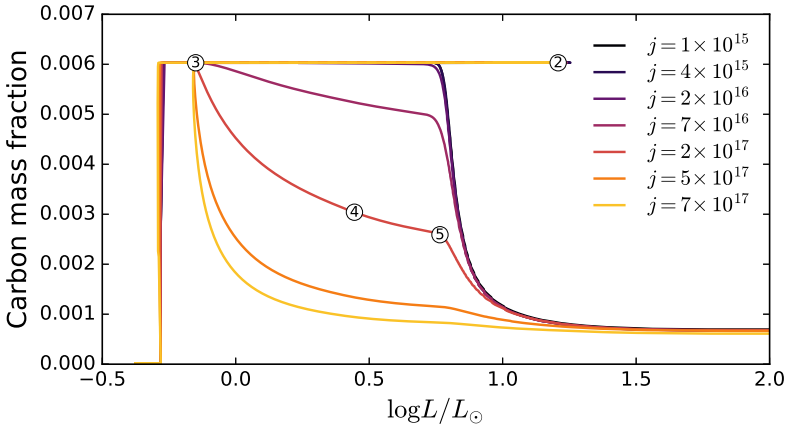

(a) Evolution of carbon

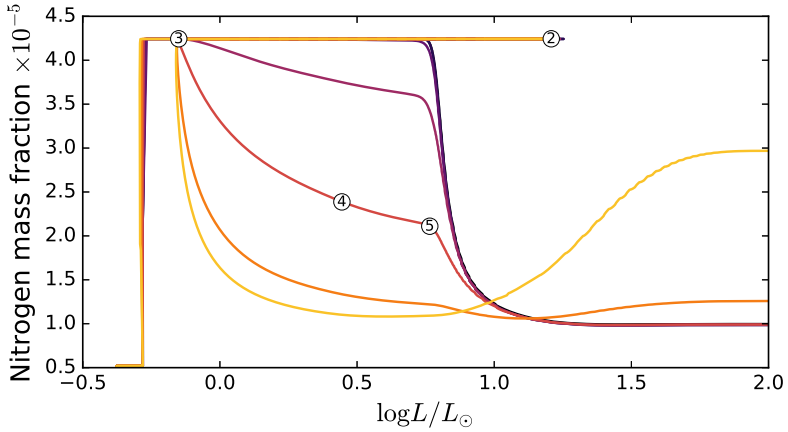

(b) Evolution of nitrogen

Figure 5.2: As Fig. 5.1 but showing the evolution of the carbon and nitrogen surface mass fractions.

point in the star by mass. For the highest values of j_a ($v_{rot} \gtrsim 100$ km s^{-1}) nearly all of the star is mixed by then.

The mixing of angular momentum and of chemical elements does not occur to the same depth (cf. Figs. 5.4a and 5.5a). For example, in the lowest angular momentum case that shows a change in the surface abundances on the main sequence, $j_a = 7 \times 10^{16}$ cm^2 s^{-1} (Fig. 5.2), the chemical elements have been partially mixed down to a mass coordinate of $m \simeq 0.6\ M_\odot$ by the time the star has reached the turn-off. Meanwhile, the angular momentum has been transported about twice as deep. This is a direct consequence of the choice of f_c, the fraction of total angular momentum diffusion coefficient applied to chemical transport, in Eq. (5.2). Had we chosen $f_c = 1$, the depth of chemical and angular momentum transport would coincide. Instead, the timescale for chemical transport is much longer than that for angular momentum transport, and thus angular momentum has been transported to a greater depth at a given time. We return to the influence of f_c and f_μ in Sect. 5.3.3.

Which of the different processes dominates the transport of angular momentum? The answer changes over time (Fig. 5.6). At first, a steep Ω-gradient is present at the interface between the accreted layer and the original surface of the star. This induces shear mixing, which dominates the initial transport with some contribution from the GSF instability. But the transport also smears out the Ω-gradient, quenching the shear instability. For a while, the GSF instability is responsible for the continuing inward transport

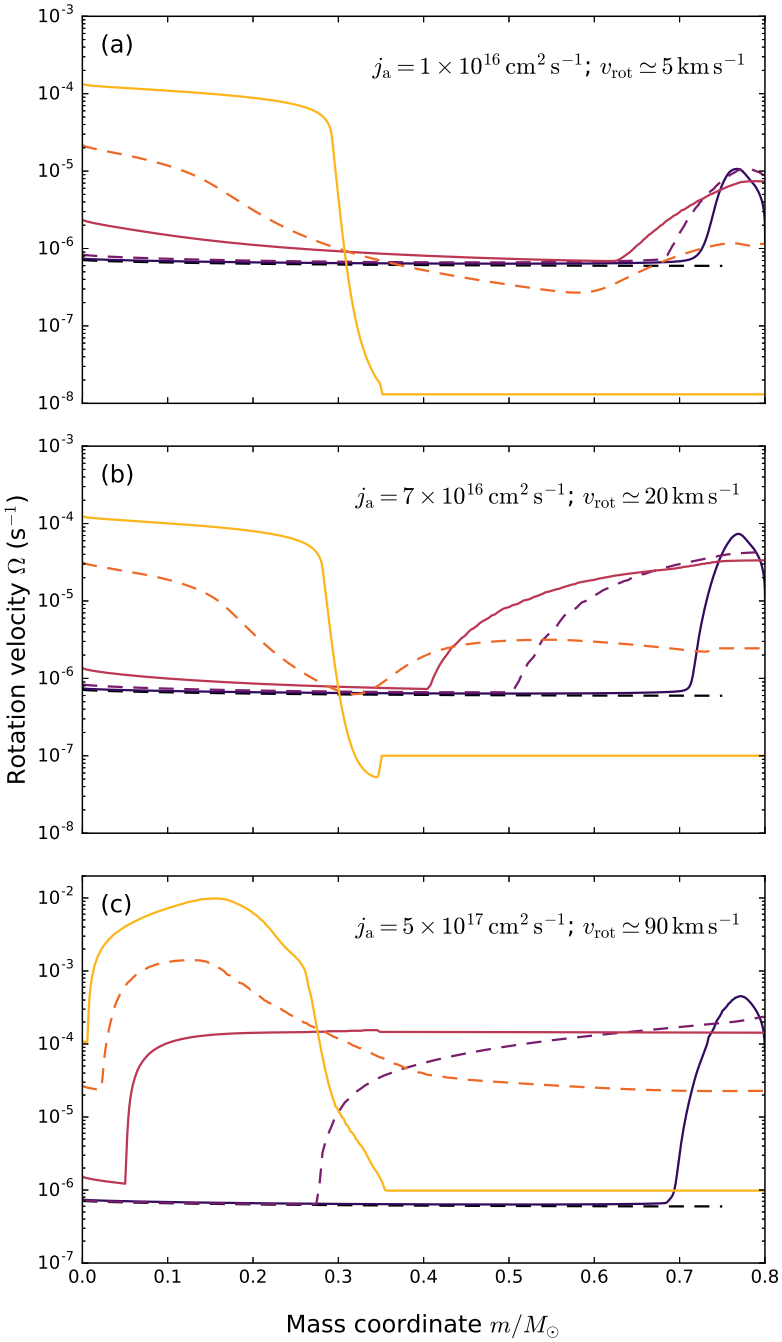

Figure 5.3: Evolution of angular rotation velocity profiles for three different values of j_a. The dashed black profile corresponds to just before mass transfer ('1') and subsequent profiles, plotted in alternating line types of progressively lighter colours, correspond to end of mass transfer ('2'), return to thermal equilibrium ('3'), main sequence (between '3' and '4'), before first dredge-up ('5') and after first dredge-up ('6'). The last two profiles demonstrate the spin-up of the core after the main sequence. Note the different y scales.

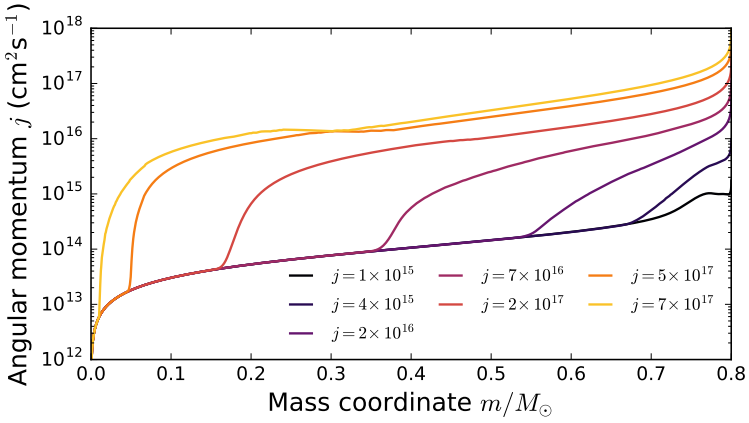

(a) Specific angular momentum

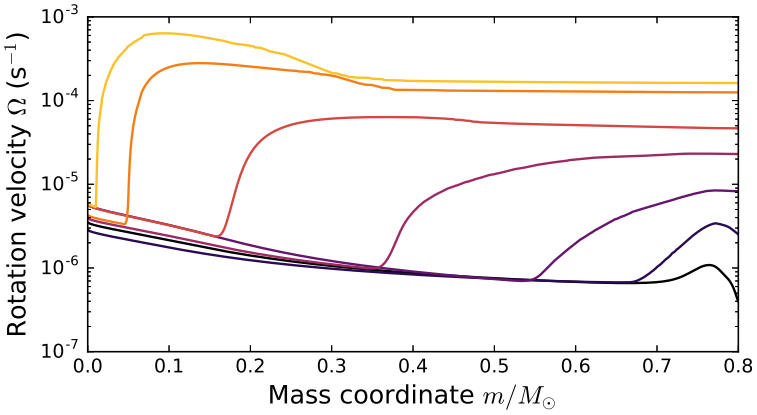

(b) Angular rotation velocity

Figure 5.4: Distribution of specific angular momentum and angular velocity near the end of the main sequence in the rotating models shown in Fig. 5.1.

of angular momentum, until eventually much of the Ω-gradient is removed, and mixing proceeds over longer timescales by the Eddington-Sweet circulation (which is the only term in Eq. (5.4) that depends on Ω and not its gradient, see Sect. 2.2.5). Some Ω-gradients always remain (e.g. Fig. 5.3), but these are either too small to contribute to further mixing and/or the mixing is inhibited by molecular weight gradients. Given the rapid removal of the Ω-gradients, Eddington-Sweet circulation is responsible for most of the chemical mixing.

Once first dredge-up starts ('5'), the tracks again converge, and the evolution up the red giant branch (RGB) is similar in all cases. This is largely the result of FDU erasing most of the differences in the chemical structure between the model sequences. Furthermore, the accreted angular momentum is insufficient to result in large rotation rates (with respect to the critical rate) of any part of a giant because of its much larger moment of inertia.

Overall, below $j_a \lesssim 2 \times 10^{16}$ cm^2 s^{-1} (turn-off velocity of about 10 km s^{-1}) the evolution of the CEMP star in this system is essentially unaffected by the rotation. This is because both the centrifugal acceleration is too small to substantially lower the effective gravity, and the contrast between the accreted layer and the region below is too small to trigger significant chemical mixing of the two (although there is some angular momentum mixing; Fig. 5.4a). For higher values of j_a the timescale for chemical

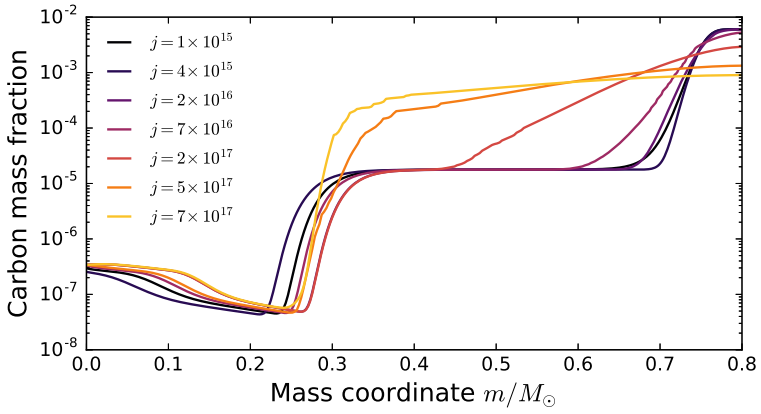

(a) Carbon abundances

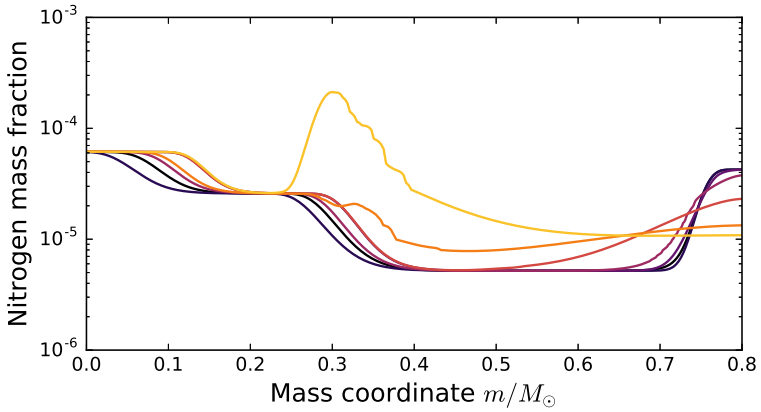

(b) Nitrogen abundances

Figure 5.5: Distribution of abundances near the end of the main sequence in the rotating models shown in Fig. 5.1.

transport is finally short enough, compared to the nuclear timescale, that chemical dilution of the accreted material can occur before FDU (Fig. 5.2), which, as explained above, also shifts the track in the HRD. Naturally, the greater j_a, the more extensive and rapid the mixing. For the highest values of j_a mixing is deep enough that FDU no longer plays a significant role in diluting the accreted material. However, if rotational mixing on the main sequence is extensive enough to bring the accreted carbon down to regions where it can be burnt, FDU can bring the produced nitrogen, visible in Fig. 5.5b around $m \simeq 0.3\ M_\odot$, to the surface. In the two most rapidly rotating models, the nitrogen abundance after FDU ('6') is thus higher than in all others (Fig. 5.2b).

The evolution further up the giant branch is not very eventful in these models. No further abundance changes occur once FDU is over. The contracting core spins up and the expanding envelope slows down – the surface velocities decrease to $v_{\rm rot} \lesssim 10\ {\rm km\,s^{-1}}$. There thus develops a large and ever-increasing contrast between the rotation rate of the core and the envelope (Fig. 5.3). This is not consistent with asteroseismic measurements of red giant core rotation rates (Mosser, Goupil, Belkacem et al., 2012; Deheuvels, Doğan, Goupil et al., 2014), which find much greater coupling between the core and the envelope. This coupling is thought to come about as a result of magnetic fields (Spruit, 2002; Suijs, Langer, Poelarends et al., 2008) and/or gravity waves (Talon and Charbonnel, 2003; Talon and Charbonnel, 2008; Fuller, Lecoanet, Cantiello et al., 2014), neither of which we have modelled at this time. In terms of surface abundances, these processes seem more likely to manifest by altering the

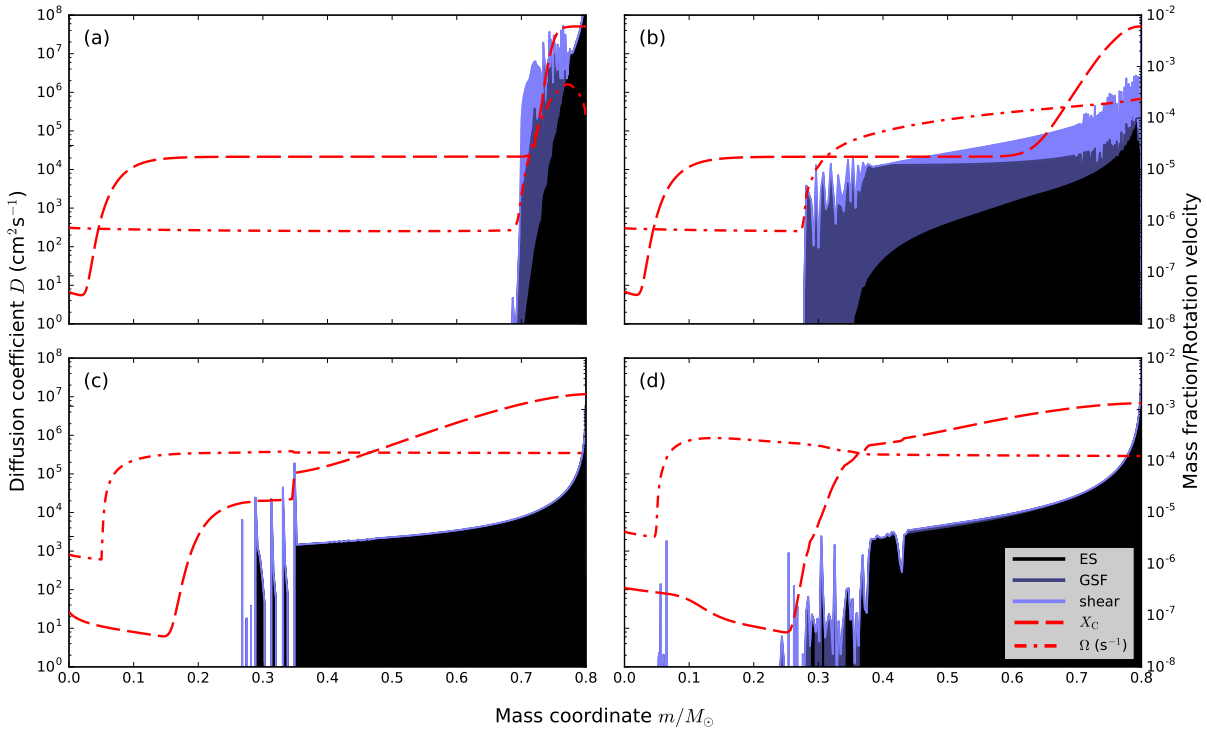

Figure 5.6: Individual contributions of the most important rotational instabilities to the total angular momentum transport coefficient in the $j_a = 5 \times 10^{17}$ cm^2 s^{-1} ($v_{rot} \simeq 100$ km s^{-1}) case at four instances: (a) shortly after mass transfer ends ('2'); (b) near return to equilibrium ('3'); (c) main sequence (between '3' and '4'); (d) main sequence turn-off ('4'). Initially, large Ω-gradients favour the shear and GSF instabilities. Later on, when the Ω-gradients are erased, the overall transport is dominated by the Eddington-Sweet (ES) circulation. The lines show the angular velocity (dash-dotted) and the carbon abundance (dashed) profiles at the corresponding times.

importance of rotational mixing than leading to mixing directly (Talon and Charbonnel, 2005; Maeder and Meynet, 2005; Eggenberger, Meynet, Maeder et al., 2010), an effect that to some extent we probe by considering different rotation rates.

5.2.2 Models with atomic diffusion and thermohaline mixing

Atomic diffusion will tend to modify the surface abundances following mass transfer. In Chapter 4 we saw how, in absence of other mixing processes, in most CEMP-*s* stars the carbon should settle out of the surface convection zone, while the surface abundance of iron should increase as a result of radiative levitation. Near the main sequence turn-off, before the convective envelope begins to move inwards in mass, the resulting abundances (e.g. [C/H] < -1 and [Fe/H] > -1 so that [C/Fe] < 0) can be very different from those of the accreted material ([C/H] $\simeq 0$ and [Fe/H] $\simeq -2$ so that [C/Fe] $\gtrsim 2$; Fig. 4.3).

However, atomic diffusion will be counteracted by rotational mixing. As a result of this competition, abundance variations on the main sequence are expected in models of all rotation rates (Fig. 5.7a). At the lowest rotation velocities atomic diffusion dominates, modifying the surface abundances of metals until the convective envelope mass begins to increase shortly after the turn-off. But even a model rotating at less than a kilometre per second shows a slightly reduced effect compared to the non-rotating case. As one considers higher rotation rates, atomic diffusion near the surface is more and more inhibited up to the $j_a = 2 \times 10^{16}$ cm^2 s^{-1} case (in this system corresponding to a turn-off velocity of $v_{rot} \simeq 9$ km s^{-1}), where

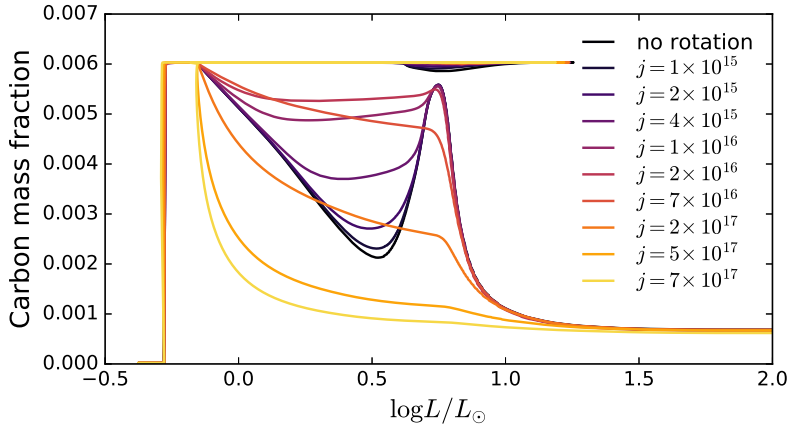

(a) Evolution of carbon

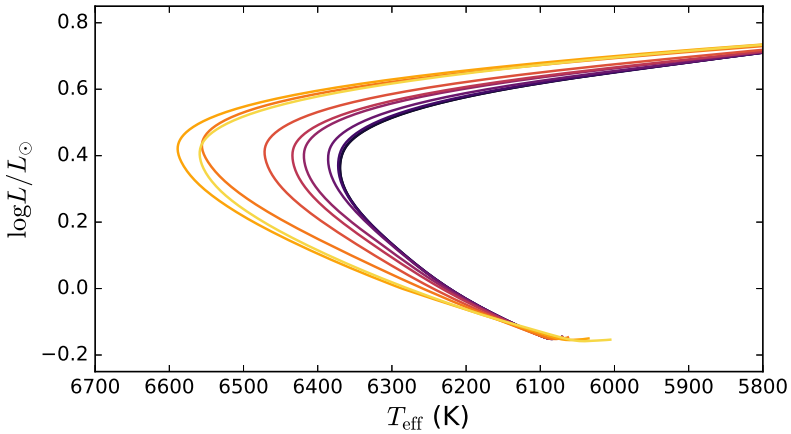

(b) Hertzsprung-Russell diagram

Figure 5.7: Evolution and abundances of a $M_{2,\rm i} = 0.75\ M_\odot$ secondary accreting $\Delta M = 0.05\ M_\odot$ of material from a $M_1 = 1.25\ M_\odot$ primary for different values of specific angular momentum of accreted material (with atomic diffusion).

the abundance variations are smallest, and the surface abundances remain within 15% of the accreted composition. In non-diffusing models this is the highest $j_{\rm a}$ case in which there is practically no change in the abundances prior to first dredge-up (Fig. 5.2). As $j_{\rm a}$ is increased still further, rotational mixing takes over, and the models look more and more like in the purely rotating case in terms of surface abundances.

The competition between diffusion and rotational mixing also has an effect on the global properties of the star. It has been shown (e.g. VandenBerg, Richard, Michaud et al., 2002; Bressan, Marigo, Girardi et al., 2012) that non-rotating models without atomic diffusion are longer-lived and hotter throughout the main sequence evolution than models with diffusion. This holds also for models of CEMP-*s* stars. But, because of partial inhibition of atomic diffusion, accreting even a small amount of angular momentum makes a model more like a non-diffusing one and thus hotter throughout the main sequence than a model with diffusion only (Fig. 5.7b). When the angular momentum accreted is sufficient to cause rotational mixing directly ($j_{\rm a} \gtrsim 7 \times 10^{16}$ cm^2 s^{-1}), the models become still hotter. Since the surface abundance anomalies are actually smaller than in the non-rotating case, this must be due to inhibition of diffusion deeper in the star. Eventually, the mechanical effects from rotation take over such that the models with highest rotation rates are again cooler.

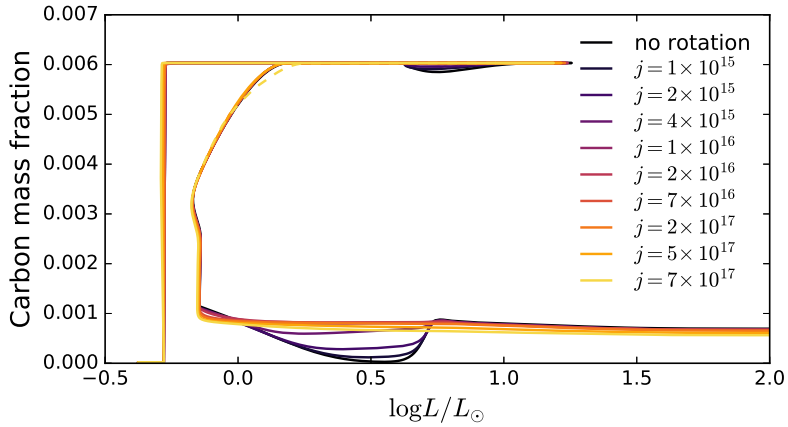

(a) Evolution of carbon

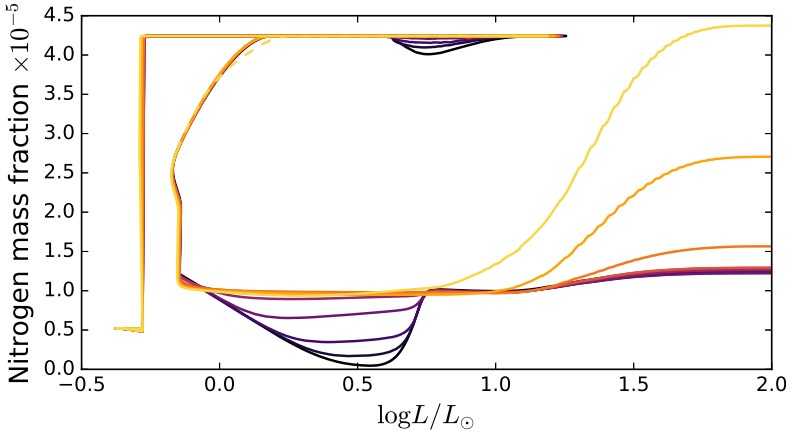

(b) Evolution of nitrogen

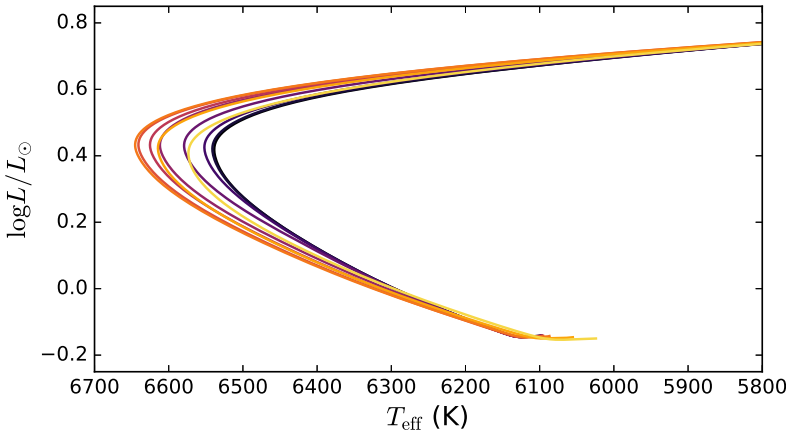

(c) Hertzsprung-Russell diagram

Figure 5.8: As Fig. 5.7 but with thermohaline mixing.

Thermohaline mixing, when modelled as an independent process (see Sect. 5.3.2), always dominates over diffusion and rotational mixing. In this system thermohaline mixing rapidly reduces the carbon abundance by a factor of about six (between $\log L \simeq 0.2$ and -0.1; Fig. 5.8a). Once thermohaline mixing has levelled the inverse μ-gradient, diffusion modifies the surface abundances still further in the slowly rotating models. In the rapidly rotating models the subsequent abundance evolution depends on the depth of thermohaline mixing. When this depth is at least comparable to that of rotational mixing (such as in this system, where thermohaline mixing proceeds down to a mass coordinate of $m \simeq 0.39\ M_\odot$), the chief role of rotational mixing is to inhibit atomic diffusion – it does not lead to significant further abundance changes before FDU. In systems where thermohaline mixing is not as deep (because of a smaller μ-gradient), rotational mixing can lead to further dilution of the accreted material.

A slight increase in the surface nitrogen abundance following FDU is found in this system even without rotation (Fig. 5.8b). This nitrogen has been produced from the accreted carbon transported deep into the star by thermohaline mixing (Stancliffe, Glebbeek, Izzard et al., 2007). Rotational mixing replenishes the carbon at these depths after thermohaline mixing has shut off so that more nitrogen can be produced, boosting the amount of nitrogen that is brought to the surface during FDU. Thermohaline mixing can once again activate following the RGB luminosity bump because of the $^3\mathrm{He}(^3\mathrm{He}, 2\mathrm{p})^4\mathrm{He}$ reaction, which reduces the mean molecular weight just above the hydrogen burning shell (Eggleton, Dearborn and Lattanzio, 2006; Stancliffe, Church, Angelou et al., 2009). A further increase in surface nitrogen abundance follows, but normally by no more than a factor of two because of the low value of the thermohaline mixing coefficient (Denissenkov, 2010).

The mechanical effects are visible earlier and more clearly in models with thermohaline mixing, because most of the chemical mixing is caused by the thermohaline instability. Since this makes rotational mixing of chemical composition largely superfluous, only the mechanical effects from rotation remain. The spread in temperature around the main sequence turn-off is smaller than in models without thermohaline mixing (about 100 K versus 220 K, respectively; cf. Figs. 5.8c and 5.7b).

5.2.3 Abundance anomalies near the main sequence turn-off

We now attempt to characterise how the surface composition changes (from the composition of the accreted material) in all of our simulations collectively. We refer to these changes as abundance anomalies. In models where atomic diffusion dominates, the abundance anomalies are usually largest around the main sequence turn-off, which is thus a convenient point of reference for comparing different systems (Sect. 4.2.2). In models without diffusion, or when diffusion is inhibited, the abundances of most elements instead change monotonically throughout the main sequence and beyond, as the accreted material gets more and more diluted (Fig. 5.2; this is not true for elements like nitrogen that can undergo further nuclear processing). Since a similar point of reference in these models thus cannot be identified, we adopt the same point, the main sequence turn-off, for convenience.

In the system discussed above, accretion of material with specific angular momentum $j_\mathrm{a} \lesssim 2 \times 10^{16}\ \mathrm{cm^2\ s^{-1}}$ has little influence on the evolution following mass transfer, if atomic diffusion is ignored. Figure 5.9 shows that this is the case in other systems (with different values of $M_{2,\mathrm{i}}$ and ΔM) as well. It is the specific angular momentum (instead of, for example, the total angular momentum accreted) that is decisive in determining whether material will mix, because material with higher specific angular momentum establishes a greater gradient in the angular velocity, which aids the shear instability.

In the same system, accretion of material with specific angular momentum $j_\mathrm{a} = 2 \times 10^{16}\ \mathrm{cm^2\ s^{-1}}$ results in a turn-off velocity of about $10\ \mathrm{km\ s^{-1}}$. In systems with other combinations of $M_{2,\mathrm{i}}$, ΔM and M_1 the turn-off velocity can be anywhere between $v_\mathrm{rot} \simeq 1$–$30\ \mathrm{km\ s^{-1}}$ (increasing with ΔM), with the range of possible turn-off velocities increasing with j_a (Fig. 5.10). That is because the rotation velocity of the

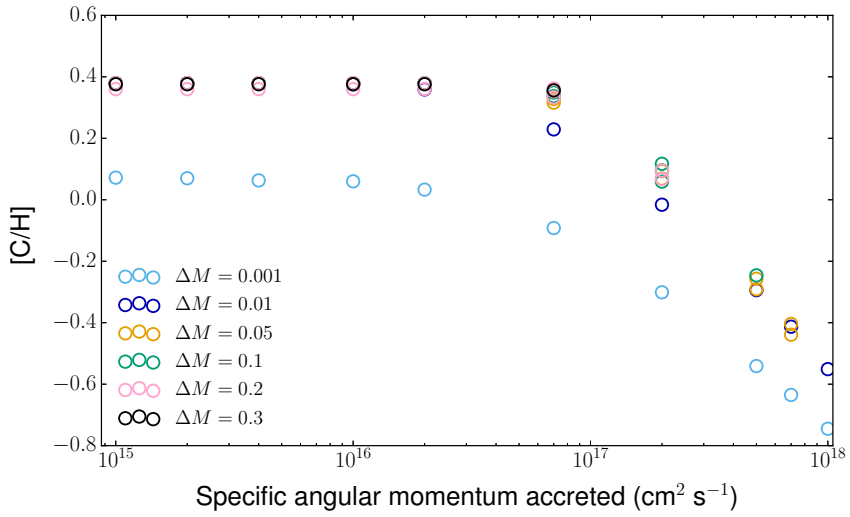

Figure 5.9: Carbon abundance at main sequence turn-off as a function of specific angular momentum of accreted material in models with rotational mixing only. To avoid excessive crowding, only models with $M_1 = 1.25\ M_\odot$ are plotted, in which [C/H] $\simeq 0.38$ after mass transfer in all cases. The general result of little to no dilution for $j_a \lesssim 2 \times 10^{16}$ cm^2 s^{-1} holds for systems with other primary masses.

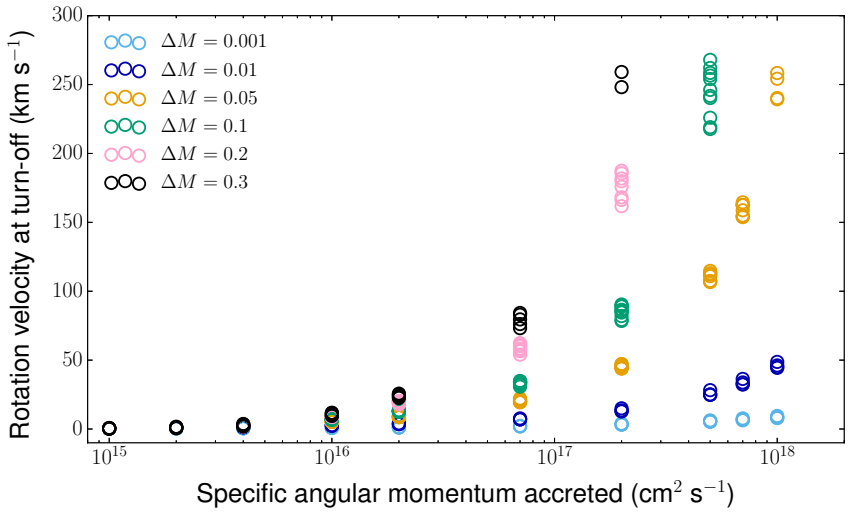

Figure 5.10: Rotation velocities at main sequence turn-off ('4') resulting from accretion of material of different specific angular momentum in all simulations with rotational mixing only. The critical velocity at turn-off is between about 280 and 300 km s^{-1} in the vast majority of cases.

star following mass accretion reflects the total angular momentum accreted. It does not constrain the amount of mass accreted, because the same amount of angular momentum can be obtained by accreting a small amount of material with high specific angular momentum, or a large amount of material with low specific angular momentum.

The rotation velocity is therefore not very informative of the amount of rotational mixing expected, which is unfortunate given that the rotation velocity is an observable quantity. A rotation rate of, for example, 50 km s^{-1} could correspond to a carbon dilution of more than a dex if ΔM is small ($\lesssim 0.01\ M_\odot$) or negligible dilution if ΔM is large ($\gtrsim 0.2\ M_\odot$; Fig. 5.11). The rotation velocity does, however, serve as

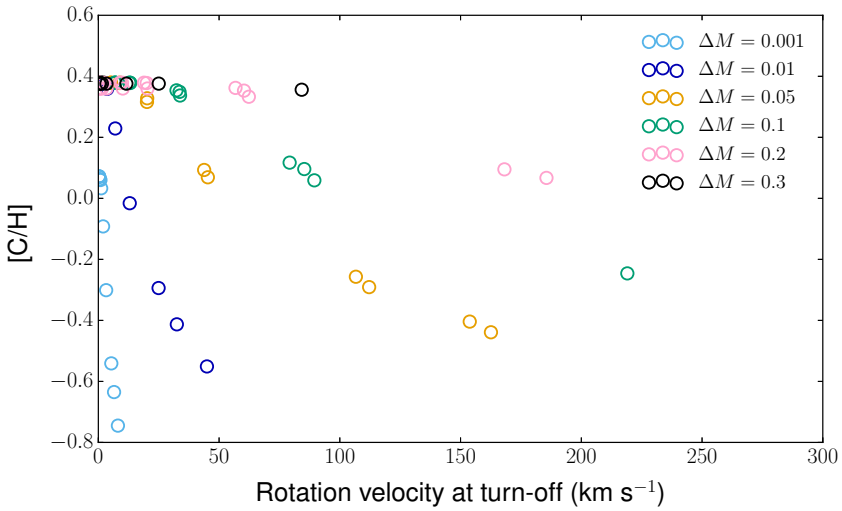

Figure 5.11: Carbon abundance at turn-off ('4') as a function of rotation velocity in models with $M_1 = 1.25\ M_\odot$ and rotational mixing only. After mass transfer [C/H] $\simeq 0.38$ in all cases.

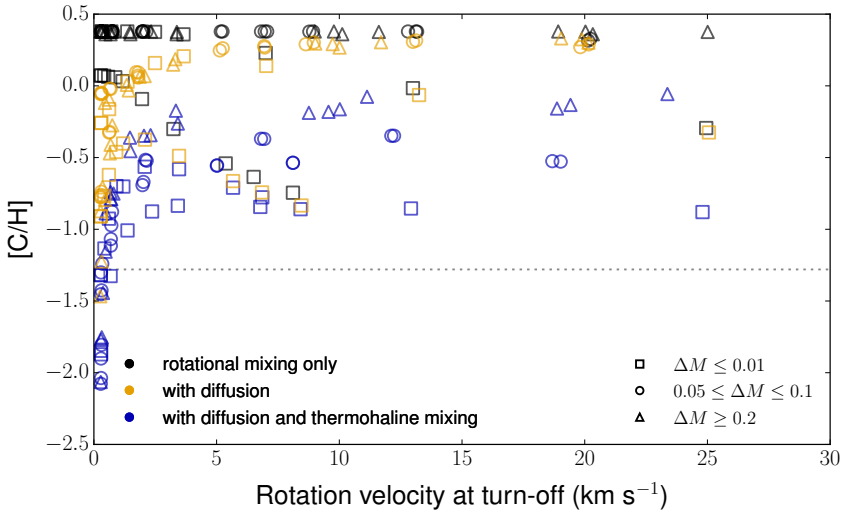

Figure 5.12: Carbon abundance at turn-off ('4') as a function of rotation velocity in all models with $M_1 = 1.25\ M_\odot$. After mass transfer [C/H] $\simeq 0.38$ in all cases. Models above the dotted line are carbon-enhanced ([C/Fe] > 0.9; Masseron, Johnson, Plez et al., 2010).

a good indicator of whether atomic diffusion should be important (Fig. 5.12). If one compares models with rotation alone (black symbols) to those with rotation and diffusion (orange symbols), one sees that only below $v_{\rm rot} \simeq 1$ km s^{-1} does atomic diffusion lead to abundance anomalies of a dex or more. The amount of dilution of carbon drops below a factor of two above rotation velocities of a mere 2–3 km s^{-1} and basically disappears above 5 km s^{-1}. The most severe change in abundances in models with such rotation velocities results from thermohaline mixing (blue symbols), which typically reduces [C/H] by a factor of three or more, depending on the mass accreted and the molecular weight of the accreted material (Stancliffe et al., 2007, Sect. 4.2.3).

For the largest values of specific angular momentum ($j_{\rm a} \gtrsim 7 \times 10^{17}$ cm^2 s^{-1}) abundance differences between models with and without thermohaline mixing also disappear. This is because, when rotational

mixing is rapid enough, it can dilute the material to a similar extent as thermohaline mixing, and the abundances near the turn-off end up being similar (cf. Figs. 5.2a and 5.8a). Nevertheless, thermohaline mixing is still by far the more rapid of the two mixing processes and responsible for most of the dilution when $\Delta M \gtrsim 0.01\ M_\odot$ (as in the high-j_a cases in Fig. 5.8).

Overall then, in models with rotational mixing only, it is the specific angular momentum of the accreted material, and not the rotation velocity or the total angular momentum accreted, that best predicts whether rotational instabilities will directly lead to chemical mixing. For a given progenitor system (combination of M_1, $M_{2,i}$), the dilution on the main sequence is determined almost entirely by the specific angular momentum of the accreted material if more than a couple of hundredths of a solar mass are accreted. The rotation velocity, while not a reliable indicator of the importance of rotational mixing, does reflect the importance of atomic diffusion – large abundance anomalies above rotation velocities of a few $\mathrm{km\,s^{-1}}$ are not expected. Thermohaline mixing is responsible for most of the abundance changes occurring on the main sequence after mass transfer, unless very little mass is accreted (of the order of $10^{-3}\ M_\odot$).

5.3 Discussion

Building on the models presented in Chapter 4, we have presented here models of the evolution of a large number of CEMP-*s* stars originating from a range of putative progenitor systems, for the first time considering in detail the accretion and internal transport of angular momentum by these stars. We now discuss the applicability of the models to real CEMP-*s* stars (Sect. 5.3.1) and then turn to the abundance evolution predicted by the models in context of observations (Sect. 5.3.2). We end with an examination of the importance of the free parameters inherent in our adopted prescription for angular momentum evolution (Sect. 5.3.3).

5.3.1 Angular momentum content of real CEMP-*s* stars

We know of no CEMP-*s* stars rotating at a substantial fraction of their critical velocity. Indeed, typical velocities of CEMP dwarfs seem to be in the 5–15 $\mathrm{km\,s^{-1}}$ range (Masseron, Johnson, Lucatello et al., 2012). These velocities are probably higher than the typical velocities of old Halo dwarfs (by a factor of about two; Lucatello and Gratton, 2003; Cortés, Silva, Recio-Blanco et al., 2009), which supports the idea of angular momentum accretion by these stars. Even so, these velocities are quite low (no more than a few percent of the critical velocity), which indicates that either the stars lose angular momentum after mass transfer, or they accrete little of it to begin with. There are issues with both possibilities.

If a substantial amount of mass is to be accreted, accreting a small amount of angular momentum requires that the specific angular momentum of the accreted material is low, notably much below the Keplerian value of $j_K = \sqrt{GMR} \simeq 2 \times 10^{18}\ \mathrm{cm^2\,s^{-1}}$ (Fig. 5.10). But multi-dimensional hydrodynamic simulations of representative progenitor systems routinely predict accretion disk formation (e.g. Theuns, Boffin and Jorissen, 1996; Huarte-Espinosa, Carroll-Nellenback, Nordhaus et al., 2013; Chen, Frank, Blackman et al., 2017) or otherwise find the specific angular momentum of the material flowing around the accretor to be close to j_K (Liu, Stancliffe, Abate et al., 2017). Although these simulations neglect physical processes that likely play an important role in regulating the angular momentum accreted by the star (particularly magnetic fields; Armitage and Clarke, 1996; Matt and Pudritz, 2005a; Matt and Pudritz, 2005b), the angular momentum would have to effectively be wrong by two orders of magnitude to reconcile the simulations with the observations.[3]

[3] We return to the problem of accreting substantial amounts of mass in Chapter 6.

Alternatively, the stars may have rotated rapidly shortly after mass transfer, but lost much of the accreted angular momentum subsequently. Given that their interior structure (a radiative interior with a surface convective envelope) is qualitatively similar to solar-like stars, one might expect that CEMP stars too lose angular momentum by magnetised winds (Weber and Davis, 1967; Mestel and Spruit, 1987). At solar metallicity this magnetic braking is found to cause the gradual spin-down of stars up to masses of $M \simeq 1.4\ M_\odot$ on timescales of about 0.1–1 Gyr (e.g. Skumanich, 1972; Kawaler, 1987; Meibom, Barnes, Latham et al., 2011; Meibom, Barnes, Platais et al., 2015; Bouvier, Matt, Mohanty et al., 2014). If magnetic braking operates similarly in CEMP stars, they should have had a fair amount of time to spin down, as even the youngest CEMP stars are probably at least a gigayear old.[4]

The magnetised winds are believed to be powered by a dynamo sustained by the interaction between differential rotation near the base of the envelope and convection (Brandenburg and Subramanian, 2005; Charbonneau, 2010). The successful operation of the dynamo thus depends on the properties of the surface convection zone. As a prerequisite, one has to exist, and the progressively longer spin-down timescales of stars in the $1.1 \lesssim M/M_\odot \lesssim 1.4$ range is attributed to the gradual thinning of the surface convection zone (Kraft, 1967; Kawaler, 1987), after the disappearance of which no braking occurs. We find that by various measures that could be relevant for the efficiency of the dynamo (e.g. Noyes, Hartmann, Baliunas et al., 1984; Schrijver, 1993) – the mass contained ($10^{-5} \lesssim M_{\rm env}/M_\odot \lesssim 10^{-3}$), the convective turn-over timescale ($1 \lesssim \tau_{\rm conv}({\rm d}) \lesssim 10$), the fractional radius ($0.05 \lesssim R_{\rm env}/R \lesssim 0.2$) and volume ($0.15 \lesssim V_{\rm env}/V \lesssim 0.5$) – the convective envelopes of $Z = 10^{-4}$ models with $M \simeq 0.75$–$0.85\ M_\odot$ resemble those of $Z = 0.02$ models with $M \simeq 1.15$–$1.4\ M_\odot$ throughout much of the main sequence. The envelopes of CEMP stars are still more sizeable because of the increased metallicity (Z). It thus seems plausible that CEMP stars too could sustain a dynamo and undergo magnetic braking, although possibly on fairly long (gigayear) timescales.

Assuming CEMP stars do undergo magnetic braking, what are the consequences for their evolution? Obviously, one consequence is that their surface rotational velocity decreases over time, but what about the internal transport of angular momentum and chemical elements? To gain some insight into this question, we return to the illustrative case of Sect. 5.2.1 with $j_{\rm a} = 5 \times 10^{17}\ {\rm cm^2\ s^{-1}}$. We restart the model sequence from the end of mass transfer (labelled '2' in Fig. 5.1), this time including angular momentum loss following Kawaler (1988):

$$\frac{{\rm d}J}{{\rm d}t} = -K \left(\frac{R/R_\odot}{M/M_\odot} \right)^{\frac{1}{2}} \Omega \min(\Omega, \Omega_{\rm sat})^2. \tag{5.5}$$

$\Omega_{\rm sat}$ is the surface angular velocity, above which angular momentum loss is found to saturate in rapidly rotating solar-like stars (Chaboyer, Demarque and Pinsonneault, 1995a), here taken to be $10\Omega_\odot$ (Amard, Palacios, Charbonnel et al., 2016), and $K = 2.5 \times 10^{47}$ (g cm^2 s) is a calibrating constant, chosen to reproduce the solar rotation rate at the solar age.

The default $M_{2,{\rm f}} = 0.8\ M_\odot$ model rotates at a velocity of $v_{\rm rot} \simeq 100\ {\rm km\ s^{-1}}$ throughout the post-mass-transfer main sequence (Fig. 5.1c). Such rapid rotation implies a large torque according to Eq. (5.5). Its application to the relatively thin envelope ($0.004\ M_\odot$ shortly after mass transfer) of the star results in a very rapid spin-down: 50 Myr after the end of mass transfer the surface rotation velocity has fallen to $v_{\rm rot} < 10\ {\rm km\ s^{-1}}$ and after about a gigayear it levels off to $v_{\rm rot} \simeq 4\ {\rm km\ s^{-1}}$ (Fig. 5.13a). After that the angular momentum of the envelope no longer changes appreciably, as the angular momentum loss is balanced by the outward transport from the radiative core. In other words, the angular momentum is then extracted from the core (Pinsonneault, Deliyannis and Demarque, 1991; Epstein and Pinsonneault, 2014).

[4] The youngest Halo stars are about 10 Gyr old, while the lifetime of the lowest-mass star that undergoes third dredge-up during the AGB stage at $Z = 10^{-4}$ is about a gigayear less (Stancliffe and Glebbeek, 2008; Karakas, 2010).

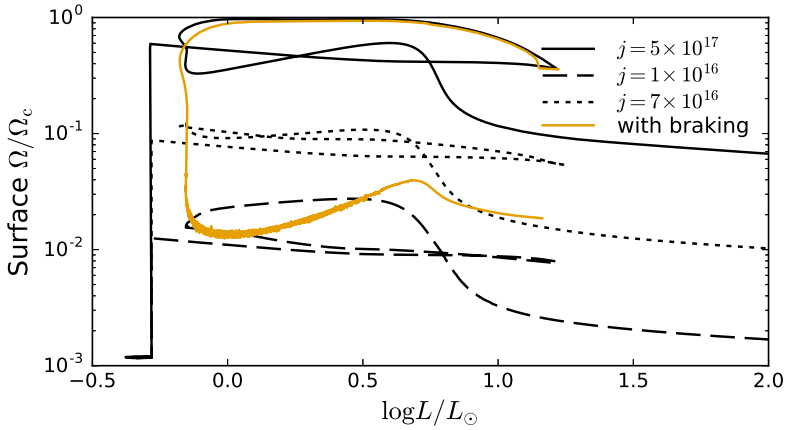

(a) Evolution of surface rotation velocity

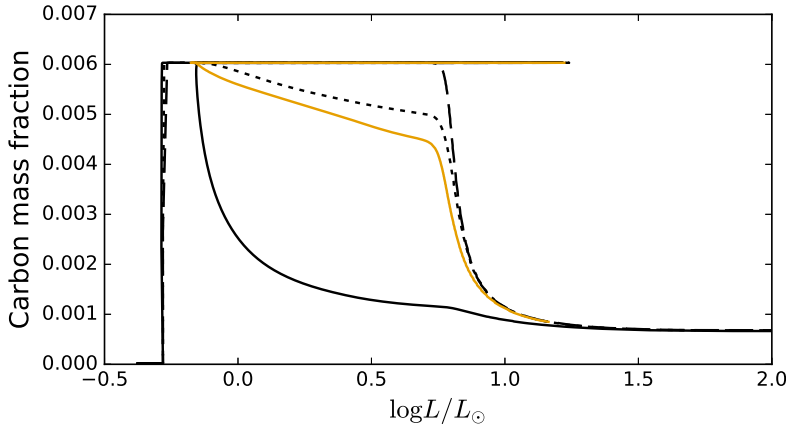

(b) Evolution of carbon

Figure 5.13: Influence of magnetic braking on the $M_1 = 1.25\ M_\odot$, $M_{2,\mathrm{i}} = 0.75\ M_\odot$, $\Delta M = 0.05\ M_\odot$ model with $j_\mathrm{a} = 5\times10^{17}$ cm^2 s^{-1} and rotational mixing only. Out of the models without braking, on the main sequence the $j_\mathrm{a} = 1\times10^{16}$ cm^2 s^{-1} model is the one most similar in terms of surface rotation velocity, and the $j_\mathrm{a} = 7\times10^{16}$ cm^2 s^{-1} model is the one most similar in terms of surface abundances.

The surface rotational velocity of the model with magnetic braking during the main sequence is most similar to that with $j_\mathrm{a} = 10^{16}$ cm^2 s^{-1} and no braking. But the internal angular momentum evolution is not very different from the default model with $j_\mathrm{a} = 5\times10^{17}$ cm^2 s^{-1} because the accreted layer is much larger than the convective envelope. The instabilities at the base of this accreted layer thus still occur, although the continuous removal of angular momentum does reduce the depth to which angular momentum has been transported at a given time (Fig. 5.14). Still, the angular momentum content in the model with braking remains larger than in the $j_\mathrm{a} = 10^{16}$ cm^2 s^{-1} model without braking, and this is reflected by its more rapid rotation during post-main-sequence evolution.

Since the transport of chemical species occurs over a longer timescale, it is more affected by the angular momentum loss at the surface. The depth to which elements are mixed is much smaller in the case with braking ($m \simeq 0.45\ M_\odot$ instead of $m < 0.3\ M_\odot$ at turn-off; Fig. 5.14b), and the surface abundance evolution on the main sequence is closer to the $j_\mathrm{a} = 7\times10^{16}$ cm^2 s^{-1} case, which has a surface rotational velocity of only $v_\mathrm{rot} \simeq 20$ km s^{-1} (Fig. 5.13). Internally, however, the abundance profiles are very smeared out in the model with braking. This results in a prolonged first dredge-up, compared to the

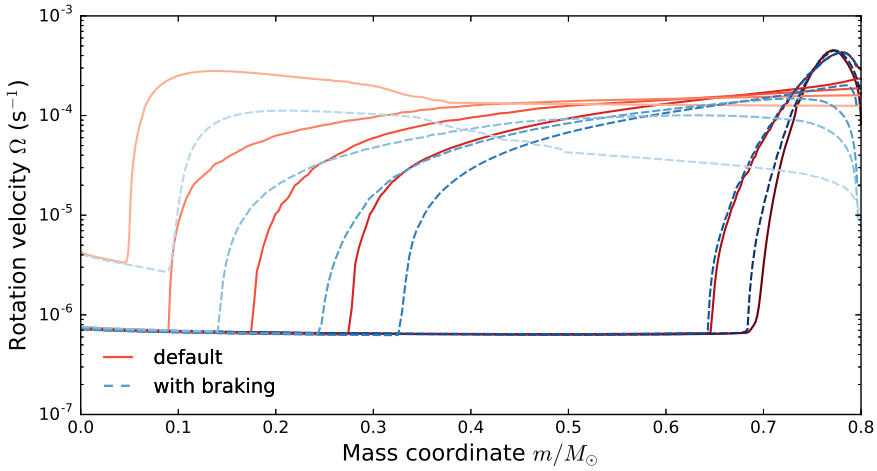

(a) Evolution of internal rotation profile

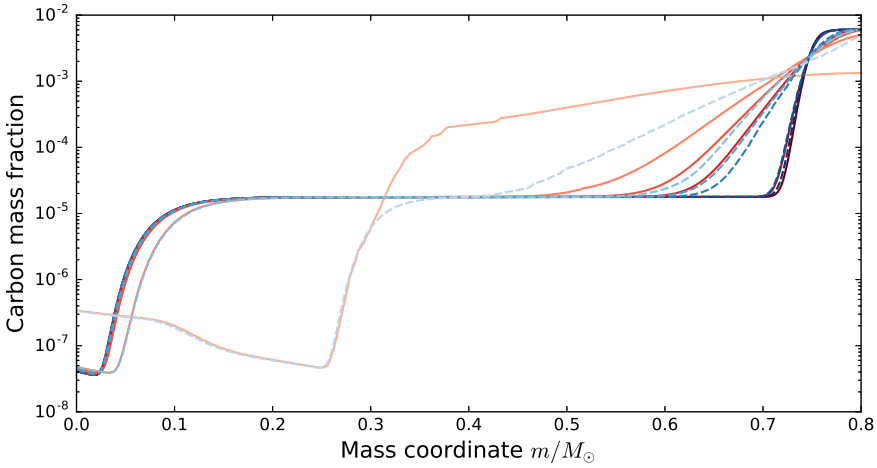

(b) Evolution of internal carbon profile

Figure 5.14: Internal evolution of the model from Fig. 5.13 with and without magnetic braking. The sets of profiles correspond to very similar ages in both cases, and later times are plotted in progressively lighter shades.

$j_a = 7 \times 10^{16}$ cm^2 s^{-1} case.

For this system then, including magnetic braking in the case with $j_a = 5 \times 10^{17}$ cm^2 s^{-1} gives a surface rotational velocity similar to the $j_a = 10^{16}$ cm^2 s^{-1} case, and surface abundance evolution similar to the $j_a = 7 \times 10^{16}$ cm^2 s^{-1} case. The former can be expected to remain true if magnetic braking would be applied to a model with a different value of $j_a > 10^{16}$ cm^2 s^{-1}, or to some extent even a different system (i.e. combination of M_1, $M_{2,i}$, ΔM) altogether. The reason is that the surface velocity after the envelope has spun down largely depends on the constant K in Eq. (5.5). But the non-braking model with the most similar evolution of surface abundances would however change (to a case somewhere between that which gives the most similar rotation velocity, and that from which we start). But generally, magnetic braking is expected to reduce the surface abundance anomalies stemming from rotational mixing. For example, all the points in Fig. 5.11 would shift towards lower velocities and to higher [C/H], the shift in velocity being more important for models with $\Delta M \gtrsim 0.05\ M_\odot$, and the shift in [C/H] dominating for models with $\Delta M \lesssim 0.01\ M_\odot$.

5.3.2 Comparison with observations

In Sect. 4.3 we saw that atomic diffusion should lead to very large abundance anomalies (e.g. [C/Fe] < -1) near the main sequence turn-off, a result clearly at odds with observational data (Fig. 4.6). Here we again juxtapose some of our model sequences with the measured carbon abundances ([C/H]) of CEMP stars from the Sloan Digital Sky Survey (SDSS; Lee, Beers, Masseron et al., 2013), the largest homogeneous data set of carbon abundances in metal-poor stars. We restrict the comparison to models with $v_{\rm rot} \lesssim 100$ km s^{-1} at turn-off. While this limit considerably exceeds the highest observed velocities of CEMP stars, these rapidly rotating models serve to illustrate the effect of rotational mixing in systems other than the one discussed so far, and can be taken to mimic the surface chemical evolution of initially still more rapidly rotating models with magnetic braking.

We also restrict the comparison to models with atomic diffusion. We can easily see when diffusion, or more accurately gravitational settling and thermal diffusion, becomes important by considering the [C/H] abundance evolution in models with different rotation velocities. In all cases in Fig. 5.15 we see that the hallmark pattern of atomic diffusion – continuous decrease of heavy element abundances until the turn-off ($\log g \simeq 4$ in these stars) followed by a reversal as the convective envelope moves inwards – is severely disrupted, compared to the non-rotating case, already at $v_{\rm rot} \simeq 0.7$ km s^{-1}. For $v_{\rm rot} \simeq 2$ km s^{-1} the variation of [C/H] over the main sequence is below 0.3 dex. This is what we already concluded in Sect. 5.2.3 (Fig. 5.12). In these models we have ignored radiative levitation, which can drastically alter the relative abundances of metals (e.g. the [C/Fe] ratio). But as we saw in Chapter 4, levitation will only be important together with the other microscopic diffusion processes, that is, in the slowly rotating models ($v_{\rm rot} \lesssim 2$ km s^{-1}).

If rotational mixing is indeed responsible for inhibiting atomic diffusion in metal-poor stars, the lack of stars with [C/H] < -2.5 between $-2.5 <$ [Fe/H] < -2 seems to require that all stars rotate, even if very slowly ($v_{\rm rot} \gtrsim 0.5$ km s^{-1}). Otherwise we should observe some carbon-depleted stars around the main sequence turn-off. Whether there are stars that rotate still slower seems unclear. Spectroscopically such low velocities are difficult to disentangle from other line broadening mechanisms (Valenti and Fischer, 2005), and photometric missions are currently restricted to rotation rates above about the same limit ($P_{\rm rot} \lesssim 100$ d; Affer, Micela, Favata et al., 2012; McQuillan, Mazeh and Aigrain, 2014).

Whether thermohaline mixing should activate in rotating stars is a matter of debate. Following Cantiello and Langer (2010) and Charbonnel and Lagarde (2010), we have treated the thermohaline and rotational instabilities independently, neglecting their possible interaction (although, they still influence each other by changing the structure of the stellar models). Thus modelled, thermohaline mixing results in a relatively immediate and substantial (Δ[C/H] > 0.3) reduction of [C/H] following mass transfer. Therefore, large quantities ($\Delta M > 0.2\ M_\odot$) of high molecular weight material are required to reproduce the largest observed carbon enhancements. Also, mixing proceeds to slightly greater depths in more rapidly rotating models. In models with $\Delta M \gtrsim 0.05\ M_\odot$ the depth of thermohaline mixing generally exceeds the maximum depth reached by the convective envelope at the end of first dredge-up. In these models there is thus little to no change in [C/H] during FDU (but [N/H] can increase substantially; see Stancliffe et al., 2007).

However, many authors (Denissenkov and Pinsonneault, 2008a; Vauclair and Théado, 2012; Maeder, Meynet, Lagarde et al., 2013) have argued that the strong horizontal turbulence expected in rotating stars (Zahn, 1992) should at least curtail thermohaline mixing, if not outright suppress it (but see Medrano, Garaud and Stellmach, 2014). If so, it might be more appropriate to exclude thermohaline mixing. But it is worth noting that the μ-inversion on the red giant branch, on which much of the cited discussion is focused, is much smaller than established by accretion of material ($\Delta\mu/\mu \propto 10^{-4}$ versus $\Delta\mu/\mu \gtrsim 0.01$) and develops gradually as a result of ^{3}He-burning instead of instantaneously, so complete suppression of

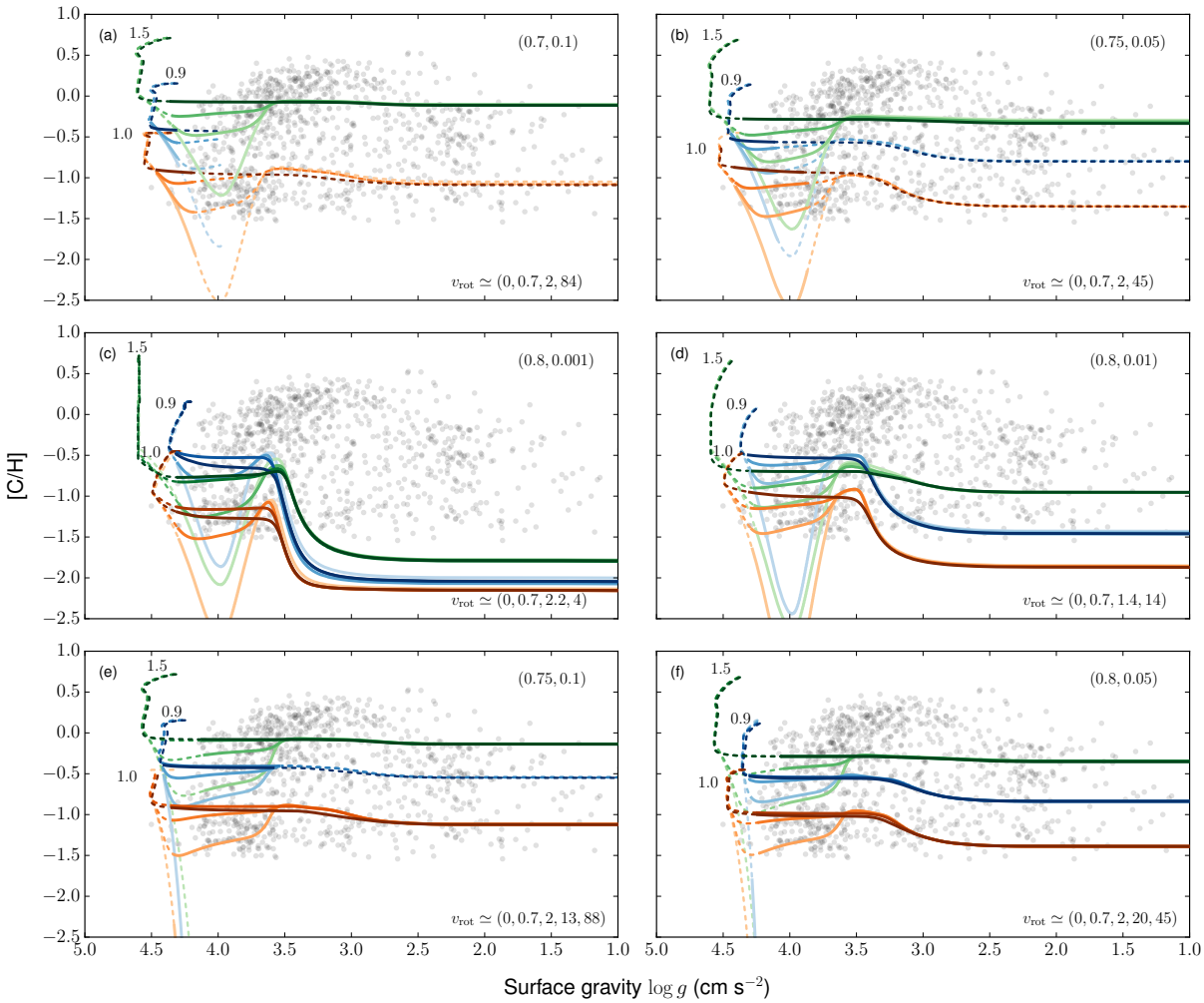

Figure 5.15: Evolution of [C/H] in CEMP-*s* star models of different initial and accreted masses (given in solar masses in the top right corner of each panel) with rotational mixing, gravitational settling, and thermohaline mixing. The three sets of lines correspond to different AGB donor masses (marked on the left). The colour intensity indicates the specific angular momentum of accreted material. From brightest to darkest, the lines correspond to $j_{\rm a} = 0$ (no rotation), $0.02, 0.04, 0.2, 0.7, 2.0$ ($\times 10^{17}$ cm^2 s^{-1}). The corresponding rotation velocities are listed in the bottom right corner of each panel (to reduce crowding not all $j_{\rm a}$ cases are shown in every panel). The solid part of each line delimits ages between 10 and 13.8 Gyr (for panel (a) computations were stopped at $t = 16$ Gyr). The points are CEMP stars ([C/Fe] ≥ 0.9; Masseron, Johnson, Plez et al., 2010) from SDSS with $-2.5 \leq$ [Fe/H] ≤ -2.0 (Lee, Beers, Masseron et al., 2013).

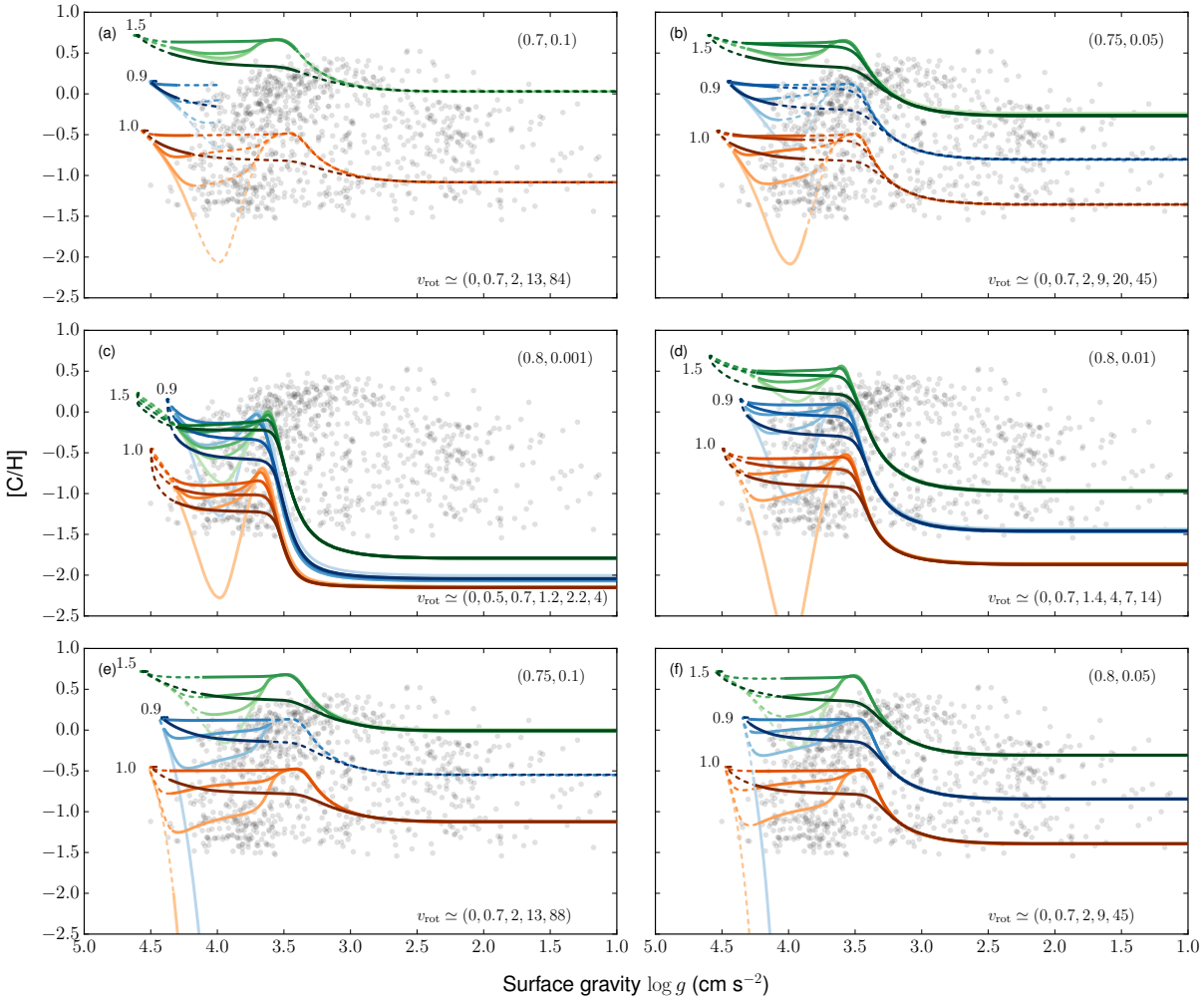

Figure 5.16: As Fig. 5.15 but without thermohaline mixing.

thermohaline mixing seems less likely in CEMP-*s* stars. Given this theoretical uncertainty, in Fig. 5.16 we also show models without thermohaline mixing.

At rotation velocities typical of CEMP stars ($v_{\rm rot} \simeq$ 5–10 km s^{-1}) these models look very similar to previously published models with only convective mixing (Stancliffe et al., 2007; Stancliffe and Glebbeek, 2008). That is, no significant changes in surface abundances occur in these models before FDU dilutes the accreted material. Before that point, rotational mixing prevents atomic diffusion but does not cause any significant dilution of the accreted material by itself (unless very little mass is accreted as in Figs. 5.16c and 5.16d). Based on the SDSS data, it is difficult to ascertain whether models with or without thermohaline mixing ought to be preferred. Some dilution of the accreted material around FDU may be required (e.g. few stars have [C/H] $\gtrsim 0$ beyond $\log g \simeq 3$; see also Denissenkov and Pinsonneault, 2008b), but without any thermohaline mixing the dilution is too large unless ΔM commonly exceeds 0.2 $M_\odot$.

There is a conspicuous lack of unevolved ($\log g \gtrsim 4.2$) CEMP stars in the SDSS data, particularly ones with [C/Fe] $\gtrsim 1.5$. As discussed in detail in Sect. 4.3, this dearth cannot be explained as an effect of (inhibited) atomic diffusion. Unsurprisingly then, the models with rotational mixing also

predict the existence of stars with $\log g \gtrsim 4.2$ and [C/Fe] > 1. In particular, lower-mass CEMP-*s* stars ($M_{2,\mathrm{f}} \lesssim 0.8\ M_\odot$) and most CEMP-*s* stars with low-mass AGB companions ($M_1 \lesssim 1\ M_\odot$) should populate this region, assuming the ages of these stars are between 10 and 13.8 Gyr (solid sections of the lines in Figs. 5.15 and 5.16). Since a similar scarcity of CEMP dwarfs is not evident from high-resolution studies (e.g. as compiled in the SAGA database; Suda, Katsuta, Yamada et al., 2008; Suda, Yamada, Katsuta et al., 2011; Suda, Hidaka, Aoki et al., 2017), we do not believe the issue rests with the models.

5.3.3 Influence of the rotational mixing parameters

The diffusion coefficients in Eq. (5.4) have been derived making use of order-of-magnitude estimates of some of the length- and timescales involved, and are thus rather uncertain. The rotational mixing parameters, f_c and f_μ, have been introduced to somewhat correct for this (Pinsonneault, Kawaler, Sofia et al., 1989; Heger et al., 2000). These efficiency parameters are typically calibrated against observed surface chemical enrichment of rapidly rotating massive stars (e.g. Yoon, Langer and Norman, 2006; Brott, de Mink, Cantiello et al., 2011) or the destruction of fragile elements in the Sun and other stars (Pinsonneault et al., 1989; Chaboyer, Demarque and Pinsonneault, 1995b; Fliegner, Langer and Venn, 1996; Venn, Brooks, Lambert et al., 2002), and our default values (Heger et al., 2000) fall in their typically adopted ranges: $0.01 \lesssim f_c \lesssim 0.1$ and $0 \lesssim f_\mu \lesssim 0.2$.

In effect, f_c simply sets the timescale for the chemical transport compared to angular momentum transport. Therefore, increasing f_c increases the rate and extent of chemical mixing. But the influence of f_μ, which sets the sensitivity of the rotational instabilities to molecular weight gradients, is more subtle. Since the various instabilities depend on μ-gradients in different ways (Sect. 2.2.5), changing f_μ alters their relative importance in different regions of the star and over time. Normally stars build up positive molecular weight gradients in their interiors as they evolve, i.e. $\nabla_\mu > 0$. Accretion of AGB ejecta instead forms a negative ∇_μ in the transition region between the original and accreted material. In that region shear instabilities are more likely to set in as a result, independently of f_μ.[5] But in the central regions, where $\nabla_\mu > 0$, increasing f_μ stabilises the medium against shear. For the Eddington-Sweet circulation and the GSF instability μ-gradients are always considered inhibiting (Eqs. (2.63) and (2.65)), so only the absolute value of ∇_μ matters. Reducing f_μ thus always helps these transport processes, while increasing f_μ suppresses them. Overall then, increasing f_μ will reduce the extent of both angular momentum and chemical transport.

To glean the importance of the rotational mixing parameters in our CEMP star models, we have experimented with changing one of them at a time. For $f_\mu = 0.05$ we have run additional models with $f_c = 0.01$ or $f_c = 0.1$, and for $f_c = 1/30$ models with $f_\mu = 0$ or $f_\mu = 1$. We restrict ourselves to $M_1 = 1$ and 1.25 $M_\odot$ and the following pairs of $M_{2,\mathrm{i}}, \Delta M$: $(0.65, 0.2), (0.7, 0.1), (0.8, 0.01), (0.8, 0.05)$.

Figures 5.17 and 5.18 show the effect f_c and f_μ have on the internal evolution of a CEMP star model characterised by $M_1 = 1.25\ M_\odot$, $M_{2,\mathrm{i}} = 0.8\ M_\odot$, $\Delta M = 0.05\ M_\odot$, and $j_\mathrm{a} = 5 \times 10^{17}$ cm^2 s^{-1}. As expected, while f_c has almost no effect on the angular momentum evolution within the star (Fig. 5.17a), the extent and rate of chemical mixing correlates with f_c (Fig. 5.17b). Meanwhile, variation of f_μ affects the transport of both angular momentum and material (Fig. 5.18). At $f_\mu = 1$ the transport of both is reduced, and by the end of the main sequence less of the star is mixed than in the default case.

The case with $f_\mu = 0$ is theoretically the most interesting one. Since the μ-gradients do not interfere with the transport, the extent of mixing depends primarily on its timescale. When it is sufficiently short compared to the evolutionary timescale, as is the case here, the angular momentum can be transported all

[5] Strictly, as can be seen from Eq. (2.69), increasing f_μ when $\nabla_\mu < 0$ does make the dynamical shear instability more likely. However, we find the secular shear instability, which is favoured for any $\nabla_\mu < 0$ regardless of f_μ (Eq. (2.72)), to set in far more often.

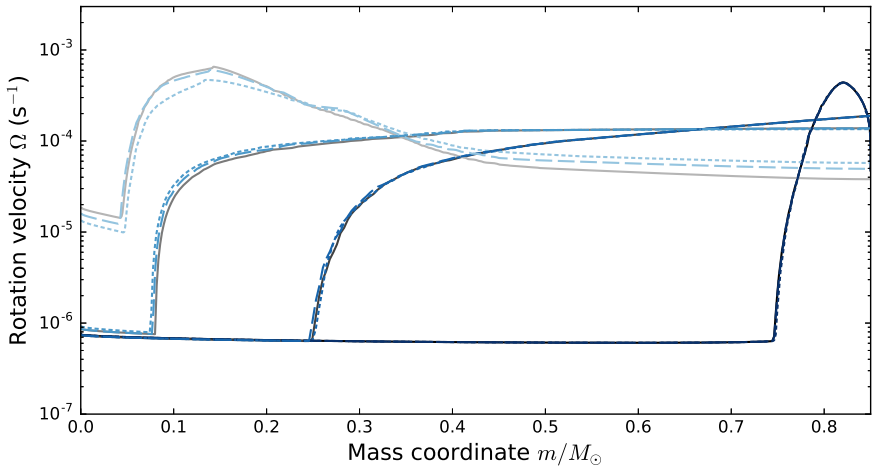

(a) Evolution of internal rotation profile

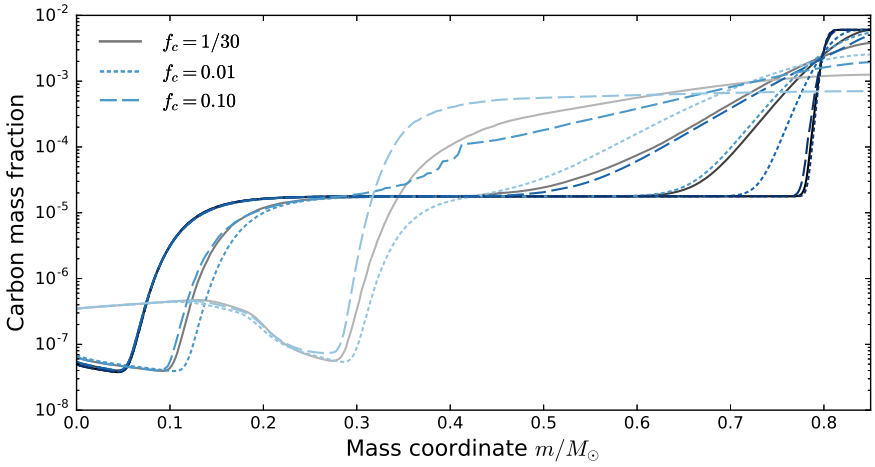

(b) Evolution of internal carbon profile

Figure 5.17: Internal profiles for different values of the rotational mixing parameter f_c in the system with M_1 = 1.25 $M_\odot$, $M_{2,\mathrm{i}}$ = 0.8 $M_\odot$, ΔM = 0.05 $M_\odot$, $j_\mathrm{a} = 5 \times 10^{17}$ cm^2 s^{-1}. The sets of profiles correspond to ages of about 3.06005 (darkest), 3.1, 4.5, and 11 Gyr (brightest) in both cases. Models with rotational mixing only.

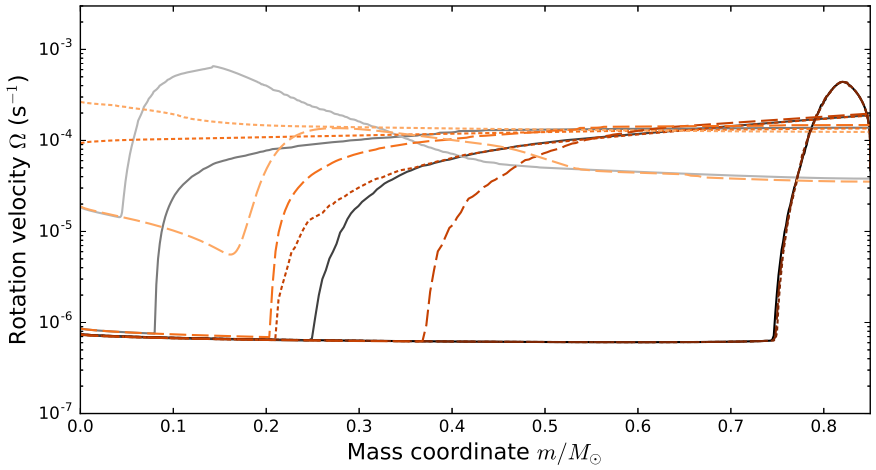

(a) Evolution of internal rotation profile

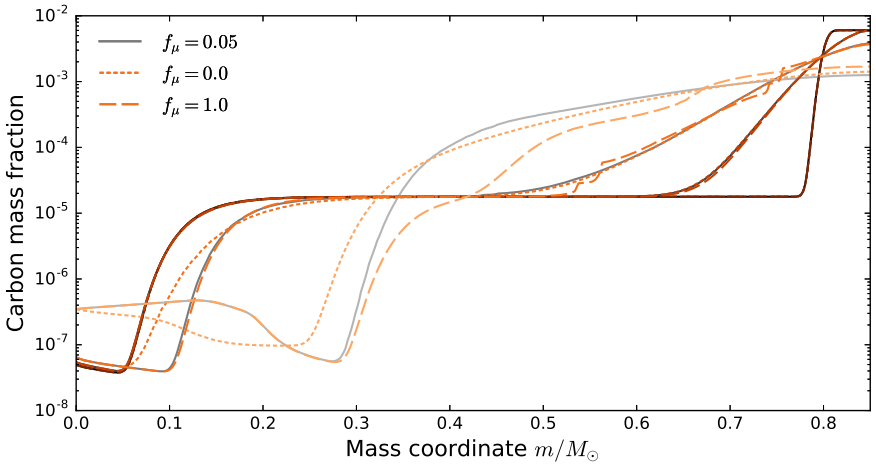

(b) Evolution of internal carbon profile

Figure 5.18: As Fig. 5.17, but for the rotational mixing parameter f_μ.

the way to the centre of the star. In this particular case, starting from about a gigayear after mass transfer, the central regions rotate about a factor of a hundred faster than in the default model. This allows mixing of additional hydrogen into the burning regions and extends the main sequence lifetime by about 0.7 Gyr. Not only are such models longer lived (Fig. 5.19a), they also evolve considerably hotter because of their larger helium content, reaching much higher surface temperatures at turn-off ($T_{\rm eff} > 7000$ K; Fig. 5.19b). Such temperatures are not measured in CEMP stars, so rotational mixing in these stars cannot be efficient enough to cause substantial chemical mixing of the central regions. Observations would thus seem to rule out models with $f_\mu = 0$, but perhaps CEMP stars never acquire enough angular momentum, or lose it too rapidly, to allow for extensive rotational mixing in the first place (Sect. 5.3.1).

The internal evolution is naturally reflected by the surface abundances, as Figs. 5.19c and 5.19d demonstrate. In terms of surface abundances there is thus somewhat of a degeneracy between the specific angular momentum assigned to the accreted material and f_c (and f_μ to a lesser extent). For example, models with $f_c = 0.1$ resemble models with $f_c = 1/30$ and higher $j_{\rm a}$. While this ambiguity is difficult to disentangle on a case-by-case basis, it does not influence some of the broader conclusions reached in previous sections. For example, in models with diffusion substantial abundance anomalies are still

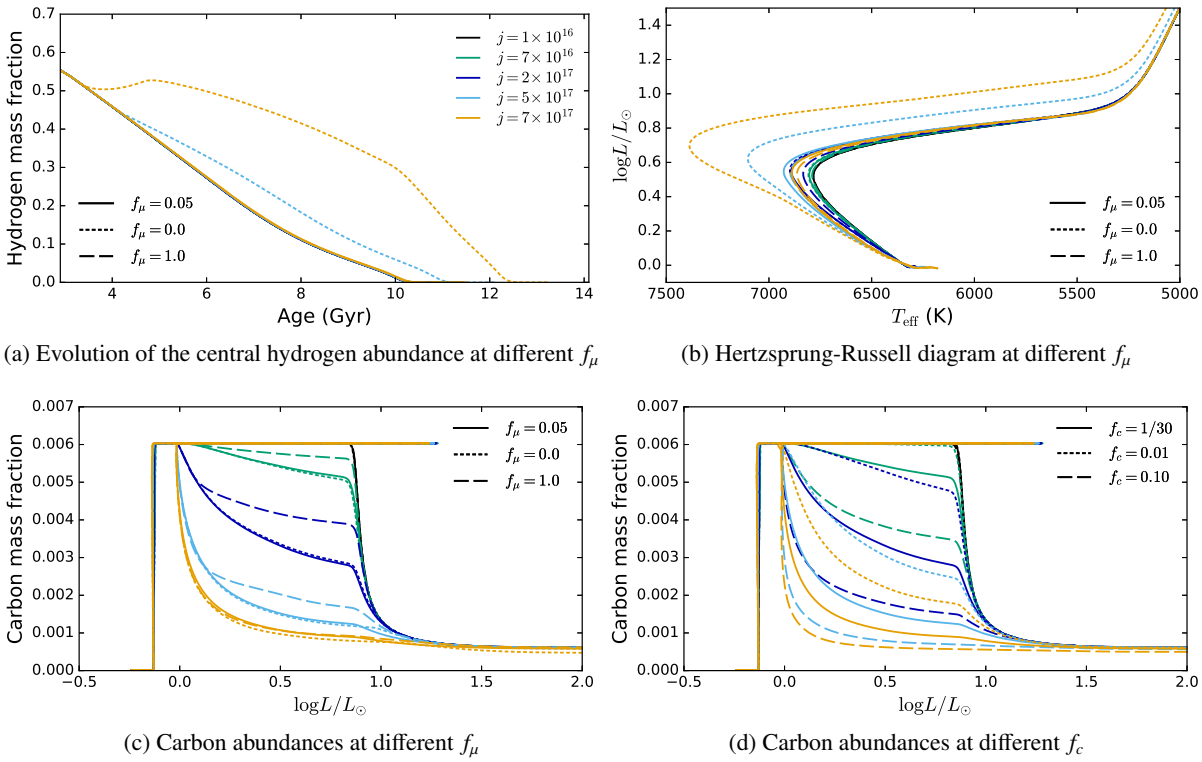

(a) Evolution of the central hydrogen abundance at different f_μ

(b) Hertzsprung-Russell diagram at different f_μ

(c) Carbon abundances at different f_μ

(d) Carbon abundances at different f_c

Figure 5.19: Effect of changing the values of the rotational mixing parameters f_μ (panels a-c) and f_c (d) in the system with $M_1 = 1.25\ M_\odot$, $M_{2,\rm i} = 0.8\ M_\odot$, $\Delta M = 0.05\ M_\odot$. Models with rotational mixing only.

expected only at rotational velocities $v_{\rm rot} \lesssim 2$ km s^{-1} even in the two unfavourable cases with $f_c = 0.01$ and $f_\mu = 1.0$ (cf. Figs. 5.12 and 5.20).

Thus there are no strong constraints on f_c in the range [0.01, 0.1]. Outside of this range we expect that at least from the lower end f_c could be constrained (assuming that rotational mixing is indeed responsible for suppressing atomic diffusion). Eventually, for $f_c \ll 0.01$, the chemical transport due to rotational instabilities must become so slow that atomic diffusion would be expected to dominate the surface abundance evolution of CEMP stars, at odds with observations. Overall, because of the many steps involved in creating CEMP-*s* stars (nucleosynthesis in the AGB donor, mass and angular momentum accretion, and subsequent mixing of the accreted material), they could offer only loose constraints on f_c (and f_μ), which would in any case be consistent with more stringent constraints from other types of stars.

5.4 Conclusions

In this chapter we have investigated what effect angular momentum accretion has on the chemical evolution of CEMP-*s* stars. The angular momentum deposited in the outer layers of the stars triggers rotational instabilities that induce mixing of angular momentum and the stellar material. This rotational mixing modifies the internal chemical structure of the stars in addition to the other physical processes (atomic diffusion and thermohaline mixing).

The relevance of each of the processes included in the models to different CEMP-*s* stars can be broadly summarised as follows. In the slowest rotating ($v_{\rm rot} \lesssim 1$ km s^{-1}) massive ($M_{2,\rm f} \gtrsim 0.85\ M_\odot$) stars the greatest abundance changes are caused by atomic diffusion near the main sequence turn-off ($\log L \simeq 0.5$;

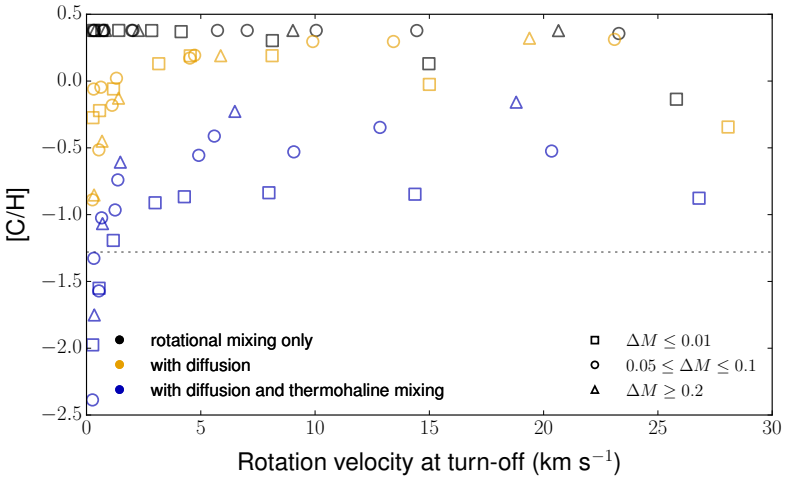

(a) $f_\mu = 1.0$

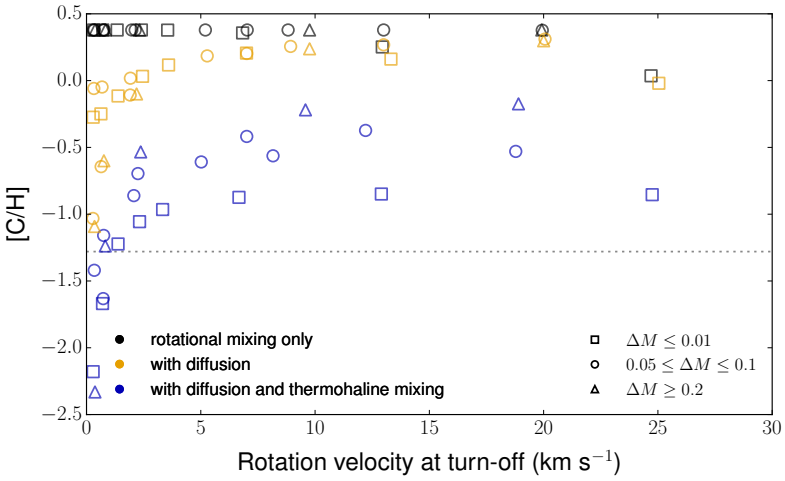

(b) $f_c = 0.01$

Figure 5.20: As Fig. 5.12 but with different values of f_c and f_μ.

$\log g \simeq 4$). Depending on the amount of mass accreted (and also the mean molecular weight of the accreted material), either first dredge-up (occurring during $3.5 \gtrsim \log g \gtrsim 3$) or thermohaline mixing ($\log g \simeq 4.5$) is more important in stars with moderate rotation velocities ($v_{\rm rot} \lesssim 20\,{\rm km\,s^{-1}}$), and also less massive CEMP-*s* stars ($M_{2,\rm f} \lesssim 0.8\ M_\odot$). Rotational mixing could be important for (internally) more rapidly rotating stars, but only if thermohaline mixing is somehow rendered ineffective, or the accreted mass is only of the order of $10^{-3}\ M_\odot$. Then rotational mixing could lead to similar abundances as thermohaline mixing but gradually, over timescales comparable to the main sequence lifetime.

Importantly, even in models with the lowest rotation velocities ($v_{\rm rot} \lesssim 1\,{\rm km\,s^{-1}}$) rotational mixing is able to severely inhibit atomic diffusion, compared to non-rotating models. It thus seems to offer a natural solution to the problem posed by atomic diffusion. However, while rotational mixing probably cannot be neglected in models of CEMP-*s* stars, accretion of angular momentum might present new challenges to the formation of CEMP-*s* stars, as we will see in the next chapter.

CHAPTER 6

On the angular momentum content of the accreted material

Material from this chapter is published as:

E. Matrozis, C. Abate and R. J. Stancliffe (2017), *How much mass and angular momentum can the progenitors of carbon-enriched stars accrete?*, A&A **606** A137, arXiv: 1707.08224 [astro-ph.SR].

In the previous chapter we saw that rotational mixing provides a plausible answer as to why atomic diffusion does not lead to large surface abundance anomalies in CEMP-*s* (and perhaps metal-poor in general) stars. However, there the ratio of angular momentum to mass accreted, i.e. the specific angular momentum of the accreted material, was treated as a free parameter spanning three orders of magnitude, whereas its range could be much more restricted in real systems.

In studies on the origin of CEMP-*s* stars and their more metal-rich counterparts (barium and CH stars) it is common to consider only the mass of the AGB star and the orbital parameters of the system (separation and eccentricity) as the key factors in determining how much mass is transferred onto the lower-mass main sequence companion (e.g. Han, Eggleton, Podsiadlowski et al., 1995; Pols, Karakas, Lattanzio et al., 2003; Abate, Pols, Izzard et al., 2013). The angular momentum of the accreted material, which should spin up the accreting star, is usually neglected. However, it seems plausible that, if the accreted material has enough angular momentum to spin the accreting star up to critical rotation, no further accretion can take place before the star either loses the excess angular momentum, or somehow redistributes it in its interior. Packet (1981) estimated analytically that a star needs to accrete only about ten percent of its own mass before it reaches critical rotation. However, the properties of many observed barium (Ba) and CEMP-*s* stars are hard to explain unless they have accreted over 30% of their initial mass (e.g. Miszalski, Boffin, Jones et al., 2013; Abate, Pols, Izzard et al., 2015a; Abate, Pols, Karakas et al., 2015b).

Dedicated multi-dimensional simulations are required to answer the question of how much angular momentum is accreted by the progenitors of carbon-enriched stars. In this chapter we instead investigate a simpler problem, namely, how much angular momentum can these stars accrete before they reach critical rotation. While we do not treat the physics of the accretion process in detail, we consider different accretion rates and values of the specific angular momentum of the accreted material. We thus attempt to deduce if (and what amount of) angular momentum loss is necessary to allow accreting enough mass to explain the chemical abundances of observed CEMP-*s* and Ba stars. While the focus is mainly on

the favourable case of instantaneous redistribution of angular momentum throughout the star, such that uniform rotation is enforced at all times, the effect of a more realistic treatment of angular momentum redistribution based on the diffusion approximation is also demonstrated.

6.1 Methods

The models presented in this chapter are produced with the STARS code described in Chapters 2 and 3. The modifications necessary for modelling rotating stars are described in Sect. 2.2. In this chapter we focus on the mass accretion stage (Sect. 2.1.5). Briefly, mass accretion is modelled by simply increasing the mass M of a model at a particular rate $\dot{M}$. The added mass is assigned specific angular momentum j_a, so that addition of mass ΔM results in the addition of total angular momentum $\Delta J = j_\mathrm{a}\Delta M$ (Sect. 2.2.6). To find the upper limit of ΔM for a given value of j_a, we set the ZAMS rotation velocity to be small ($\Omega < 0.01\Omega_\mathrm{c}$), so that the initial angular momentum is negligible. The mass is added until Ω reaches Ω_c anywhere in the model (usually the surface). Unlike in the previous chapters, the added mass is set to have the same composition as the surface at all times by using the surface boundary conditions given by Eq. (2.33), i.e. the surface composition changes that result from accretion of material are ignored. While this makes some difference to the angular momentum that a star can accrete (Sect. 6.2), none of the conclusions depend on this simplification. The critical rotation velocity throughout the star is given by Eq. (2.59):

$$\Omega_\mathrm{c}(r_P) \approx \sqrt{0.45\frac{Gm_P}{r_{P,\mathrm{c}}^3}}, \tag{6.1}$$

where $r_{P,\mathrm{c}}$ is the radius r_P of an isobar (see Sects. 2.2.1 and 2.2.2) at critical rotation.

The added angular momentum is instantaneously distributed throughout the star so that uniform rotation results. This gives a plausible upper limit to the amount of material with j_a that a star can accrete (Packet, 1981). In addition, in some models we follow the internal transport of angular momentum as described in Sects. 2.2.4 and 2.2.5. In these models the specific angular momentum evolves according to Eq. (2.61):

$$\frac{\partial j}{\partial t} = \frac{\partial}{\partial m_P}\left(\mathcal{D}_\mathrm{rot} r_P^2 \frac{\partial \Omega}{\partial m_P}\right). \tag{6.2}$$

The models are characterised by the following set of parameters: metallicity Z, initial primary mass M_AGB (which here only sets the age at the onset of mass transfer and limits the maximum mass that can be accreted by the secondary to the total amount lost by the primary), initial secondary mass M, mass accretion rate $\dot{M}$, and specific angular momentum of accreted material j_a. We restrict ourselves to $Z = 10^{-4}$ and $M \simeq 0.6$–$0.825\ M_\odot$ for CEMP stars (Abate et al., 2015a; Abate, Pols, Stancliffe et al., 2015c), and $Z = 0.008$ and $M \simeq 1.0$–$2.5\ M_\odot$ for Ba stars (e.g. McClure and Woodsworth, 1990; Pols et al., 2003; Izzard, Dermine and Church, 2010). The mass accretion rate and specific angular momentum are varied between $\dot{M} \simeq 10^{-8}$–$10^{-5}\ M_\odot\,\mathrm{yr}^{-1}$ and $j_\mathrm{a} = (0.2$–$3) \times 10^{18}\ \mathrm{cm}^2\,\mathrm{s}^{-1}$. The upper limit of $\dot{M}$ is close to typical mass-loss rates of the donor stars near the end of their lives (Vassiliadis and Wood, 1993; van Loon, Cioni, Zijlstra et al., 2005; Ramstedt and Olofsson, 2014), and the upper limit for j_a is comparable to the Keplerian value $j_\mathrm{K} = \sqrt{GMR} \simeq (2$–$5) \times 10^{18}\ \mathrm{cm}^2\,\mathrm{s}^{-1}$ of the different progenitors. At all times we prevent j_a from exceeding j_K.

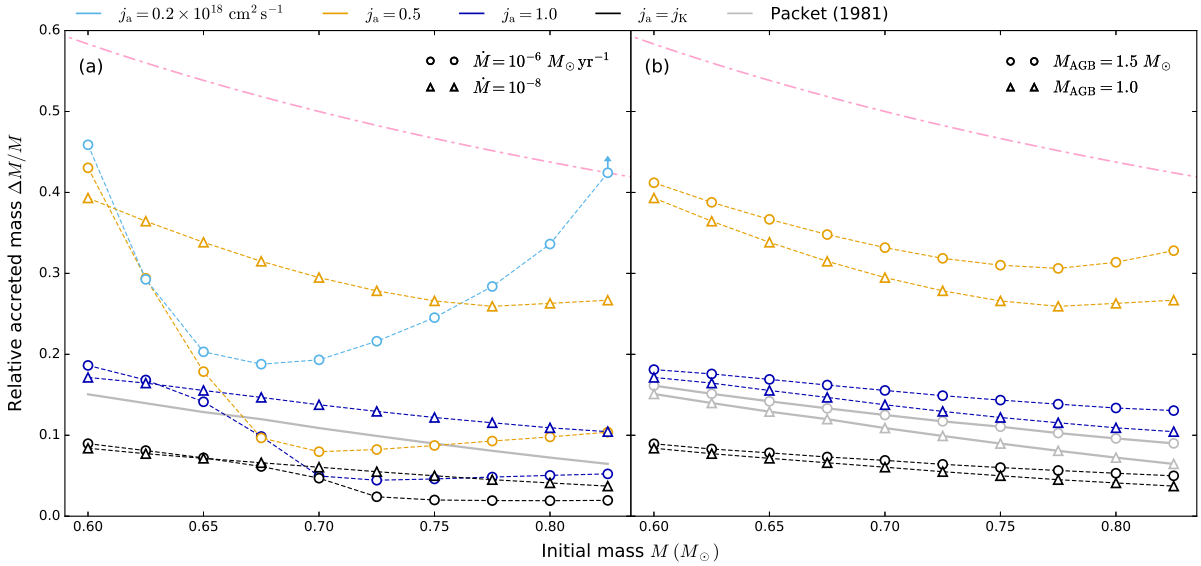

Figure 6.1: Mass accreted before critical rotation is reached (relative to initial mass) by uniformly rotating CEMP-*s* star progenitors for different values of the specific angular momentum of accreted material j_a: (a) effect of different mass accretion rates in the $M_{AGB} = 1\ M_\odot$ case); (b) effect of different primary masses (age at the onset of mass transfer) in the $\dot{M} = 10^{-8}\ M_\odot\ \mathrm{yr}^{-1}$ case. The case of $j_a = 2 \times 10^{17}$ cm^2 s^{-1}, $\dot{M} = 10^{-8}\ M_\odot\ \mathrm{yr}^{-1}$ is not shown because in all models ΔM exceeds 0.35 $M_\odot$ (dash-dotted line), at which point the computations were stopped.

6.2 Results

A summary of all calculations of the amount of mass progenitors of carbon-enriched stars can accrete prior to reaching critical rotation is given in Table 6.1. We now highlight the main features of the models.

Figure 6.1 shows the amount of mass CEMP-*s* star progenitors of different masses can add before reaching critical rotation. This amount is a complicated function of the initial structure of the star, the angular momentum of the added material, and the rate at which the material is added. Much of this complexity is an outcome of the response of the star as it gains mass. Thus one crucial parameter is the ratio between the mass accretion timescale $\tau_{\dot{M}} = M/\dot{M}$ (here varied between about 10^5 and 10^8 years) and the thermal adjustment (Kelvin-Helmholtz) timescale τ_{KH} of the star (between about 10^6 and close to 10^8 years for the different progenitors). Generally when $\tau_{\dot{M}} \gg \tau_{KH}$ the star is able to stay close to thermal equilibrium, and its global properties change slowly. The star evolves as if replaced at every instant by a slightly more massive and more rapidly rotating star. In this case ΔM depends almost entirely on the angular momentum of the added material alone (this is more clearly seen in Fig. 6.1b, where $\dot{M} = 10^{-8}\ M_\odot\ \mathrm{yr}^{-1}$ and $\tau_{\dot{M}} > \tau_{KH}$ in all cases).

When $\tau_{\dot{M}} \lesssim \tau_{KH}$, the star is driven out of thermal equilibrium, forcing its outer layers to expand while the inner regions are compressed. In this case seemingly minor differences in the initial structure can lead to large differences in the response of the star to mass addition. In particular, the response is related to the convective stability of its outer layers. As long as there is a substantial convective outer region, the star slowly expands and heats up as mass is added. But if in the process of gaining mass convection becomes inefficient and the convective region disappears, the star experiences a brief phase of rapid expansion, during which very little mass (and angular momentum) is accreted (Fig. 6.2). As the star continues gaining mass, the expansion gradually slows down and the surface layers begin to cool. In stars that initially have a more massive convective region this phase plays a larger role in bringing the star closer to critical rotation, but it also occurs later (Figs. 6.3 and 6.4). The result can be a minimum in the

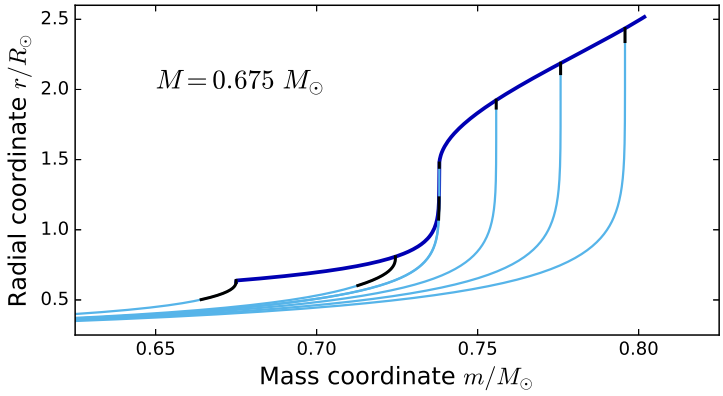

Figure 6.2: Evolution of the mass distribution in a uniformly rotating model with an initial mass of 0.675 $M_\odot$ when adding matter with $j_a = 2 \times 10^{17}$ cm^2 s^{-1} at a rate of $\dot{M} = 10^{-6}$ $M_\odot$ yr^{-1}. The light-blue lines show the radius variation with mass in six models from just prior to mass addition to near critical rotation ($\Delta M \simeq 0.125\ M_\odot$). The black sections of the profiles indicate convective regions. The upper (dark-blue) envelope shows the evolution of the surface radius during mass addition.

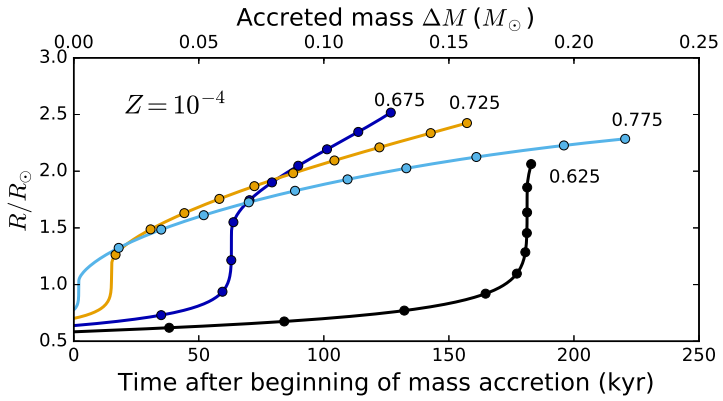

Figure 6.3: Evolution of the radius in uniformly rotating models of the indicated initial masses when adding matter with $j_a = 2 \times 10^{17}$ cm^2 s^{-1} at a rate of $\dot{M} = 10^{-6}$ $M_\odot$ yr^{-1}. The markers indicate every 10% in Ω/Ω_c with the last marker indicating $\Omega = \Omega_c$. Prior to mass addition the stars have a small outer convective region, which is more massive in less massive stars. The disappearance of this region is followed by a rapid expansion phase, after which the stars are closer to critical rotation. The line corresponding to the $M = 0.675\ M_\odot$ case is the same as the upper envelope in Fig. 6.2.

$\Delta M(M)$ relation, as is the case, for example, at $M \simeq 0.675\ M_\odot$ when $j_a = 2 \times 10^{17}$ cm^2 s^{-1} (Fig. 6.1a).

The evolution of accreting Ba star progenitors is often simpler. Owing to their higher mass, the thermal timescale of such stars is about a factor of ten smaller than that of CEMP-*s* star progenitors. They are thus closer to thermal equilibrium during mass accretion. Furthermore, except in the lowest mass cases ($M \simeq 1\ M_\odot$), these stars never have substantial convective envelopes. The disappearance of the convective region and the rapid expansion phase, as observed in the CEMP star case, therefore does not happen in most of these models. Instead the critical rotation rate is reached more gradually, and there is a smaller dependence on $\dot{M}$ (Fig. 6.5).

Packet (1981) presents analytical estimates of the amount of mass a star can accrete when $j_a = j_K$. For an initially non-rotating star he finds approximately

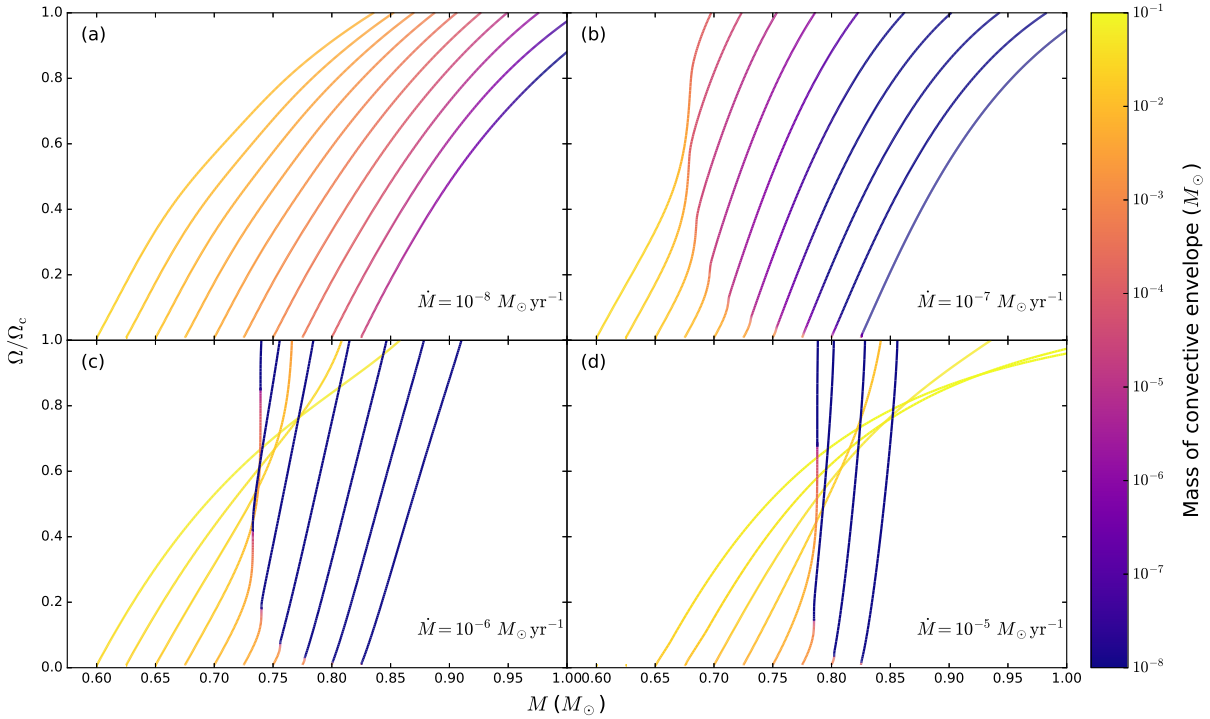

Figure 6.4: Evolution of the surface rotation velocity (starting from $\Omega/\Omega_c \approx 0$) of uniformly rotating CEMP-*s* star progenitors of different initial masses when adding mass with $j_a = 5 \times 10^{17}$ cm^2 s^{-1}. The colour coding shows that the disappearance of the convective envelope is accompanied by a rapid expansion phase, during which Ω/Ω_c increases.

$$\Delta M \simeq 2\left(\sqrt{1+k^2} - 1\right) M, \tag{6.3}$$

where $k^2 = I/MR^2$, the square of the normalised gyration radius, characterises the distribution of mass inside a star with moment of inertia I (a smaller value of k^2 corresponds to a steeper, more centrally concentrated mass distribution). While for CEMP-*s* star progenitors $k^2 \simeq 0.06$–0.12, for Ba star progenitors $k^2 \lesssim 0.05$. Thus the value given by Eq. (6.3) is similar for both sets of progenitors (approximately 0.07–0.09 $M_\odot$). Our computed ΔM values in the $j_a = j_K$ case are also similar for the two sets, but they are about a factor of two smaller than given by Eq. (6.3). The difference arises because the response of the star to mass addition (for example, its change in R and k^2) is not taken into account by Packet (1981). In particular, k^2 decreases during accretion when the outer layers expand (Fig. 6.2), which implies a lower value of ΔM. Moreover, ΔM shows considerable variation with $\dot{M}$ (more so in the CEMP-*s* star case; Table 6.1) because the response of the star depends on the rate at which mass is added.

The distribution of mass in the progenitors of carbon-enriched stars changes during their evolution such that k^2 decreases (the stars become more centrally concentrated). As a consequence, the amount of angular momentum the stars can accommodate also decreases over time. Therefore, somewhat more material can be transferred in systems hosting a more massive donor star in which mass transfer occurs earlier (Fig. 6.1b). But note that we have ignored the composition of the transferred material. Accretion of material with a different composition will alter the opacity, and hence the structure, of the outer layers. The composition will thus also play a role in the response of the star to mass accretion and the amount of mass needed to reach critical rotation. Test models indicate that taking the composition into account can

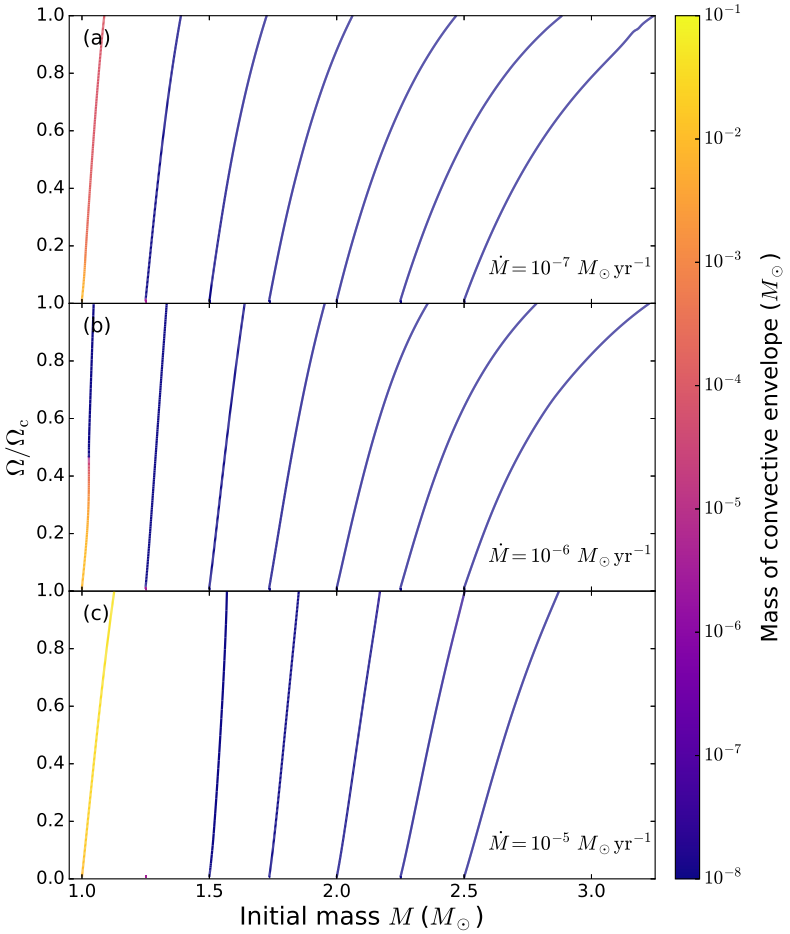

Figure 6.5: The evolution of the surface rotation velocity (starting from $\Omega/\Omega_c \approx 0$) of uniformly rotating Ba star progenitors of different initial masses when adding mass with $j_a = 1 \times 10^{18}$ cm^2 s^{-1}. Except for the $M = 1\ M_\odot$ case, the outer regions of Ba star progenitors remain radiative at all times.

alter ΔM by some ten percent.

What is the minimum specific angular momentum that material must have such that accreting it can spin the star up to critical rotation? More explicitly, what is $\langle j \rangle$ when going from $J_0 = I_0\Omega_0 = 0$ to $J = I\Omega_c = \langle j \rangle \Delta M$ for large ΔM? Ignoring the change in R and k^2 we can crudely estimate that

$$\langle j \rangle \simeq k^2 R^2 \left(1 + \frac{M}{\Delta M}\right) \sqrt{G\left(M + \Delta M\right)/R^3}. \tag{6.4}$$

For large ΔM (say $\Delta M \simeq M$) $\langle j \rangle \simeq 3k^2 j_K$, which for typical values of k^2 gives $\langle j \rangle \gtrsim 0.3\, j_K \simeq$ (5–7) $\times\ 10^{17}$ cm^2 s^{-1} (CEMP stars) and $\langle j \rangle \gtrsim 0.1\, j_K \simeq$ (5–8) $\times\ 10^{17}$ cm^2 s^{-1} (Ba stars). These values are a bit high (Figs. 6.1, 6.6), but give a reasonable estimate when the assumption of a constant radius is closer to being satisfied (e.g. at low accretion rates when thermal equilibrium is maintained). However, models that do swell up can reach critical rotation for even lower values of j_a (Fig. 6.1a).

When the redistribution of angular momentum is not instantaneous, the angular momentum is rapidly distributed only in some outer part of the star (e.g. the convective envelope, when present) instead of throughout, and differential rotation results. One might then expect that generally much less mass is necessary to spin the star up to critical rotation. This is true for j_a close to j_K (having $j_a = j_K$ by

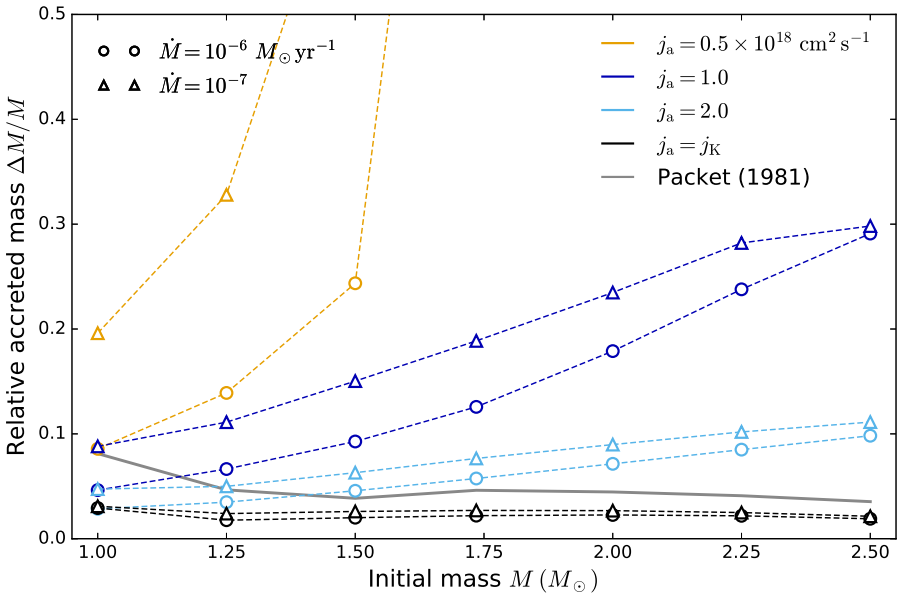

Figure 6.6: Mass accreted before critical rotation is reached (relative to initial mass) by uniformly rotating Ba star progenitors for different values of the specific angular momentum of accreted material. For progenitors with $M \geq 1.75\ M_\odot$ addition of material with $j_\mathrm{a} \leq 5 \times 10^{17}\ \mathrm{cm}^2\,\mathrm{s}^{-1}$ does not result in critical rotation even for $\Delta M > 2\ M_\odot$.

definition sets the surface to $\Omega = \Omega_\mathrm{c}$). However, when j_a is substantially smaller than j_K, sometimes even more mass can be added than in the uniformly rotating case (cf. Figs. 6.1a and 6.7). For example, a $M = 0.7\ M_\odot$ CEMP star progenitor rotating uniformly can only add about 0.05 $M_\odot$ of material (when $\dot{M} = 10^{-6}\ M_\odot\,\mathrm{yr}^{-1}$) with $j_\mathrm{a} = 5 \times 10^{17}\ \mathrm{cm}^2\,\mathrm{s}^{-1} \simeq 0.25\, j_\mathrm{K}$ before reaching critical rotation. But in the differentially rotating case even after adding 0.35 $M_\odot$ no part of the star has reached $\Omega = \Omega_\mathrm{c}$. Figure 6.8 illustrates why this is the case. When Ω/Ω_c reaches unity at the surface in the uniformly rotating case, most of the interior of the star still has $\Omega/\Omega_\mathrm{c} \ll 1$ (solid black line). If more angular momentum could be stored in the interior, the surface could be prevented from reaching Ω_c. This is what happens in the differentially rotating case where more of the angular momentum is stored in the outer 0.1 $M_\odot$ of material at the corresponding time (compare the red lines). By the time 0.35 $M_\odot$ of material have been added (0.35 Myr after the onset of mass accretion) the angular momentum has been transported down to a mass coordinate of $m \simeq 0.3\ M_\odot$, and $\Omega/\Omega_\mathrm{c} > 0.1$ in the outer 0.5 $M_\odot$.

6.3 Discussion

We have stopped the computations and recorded the accreted mass ΔM at the point when the model reaches critical rotation. But this ΔM is subject to change if critical rotation is reached when the star is out of thermal equilibrium. Once accretion stops, the star will attempt to regain equilibrium. Whether the star will tend to spin up or down with respect to the critical rate as it evolves towards equilibrium can be reasonably predicted by comparing ΔM with ΔM_TE, the value of ΔM in the case closest to thermal equilibrium (case with the lowest $\dot{M}$).

Models with $\Delta M < \Delta M_\mathrm{TE}$ usually experience a phase in which very little mass and angular momentum are accreted while R and Ω/Ω_c increase rapidly (Fig. 6.3). After accretion these stars tend to contract and spin down with respect to the critical rate. After moving away from critical rotation, they could in

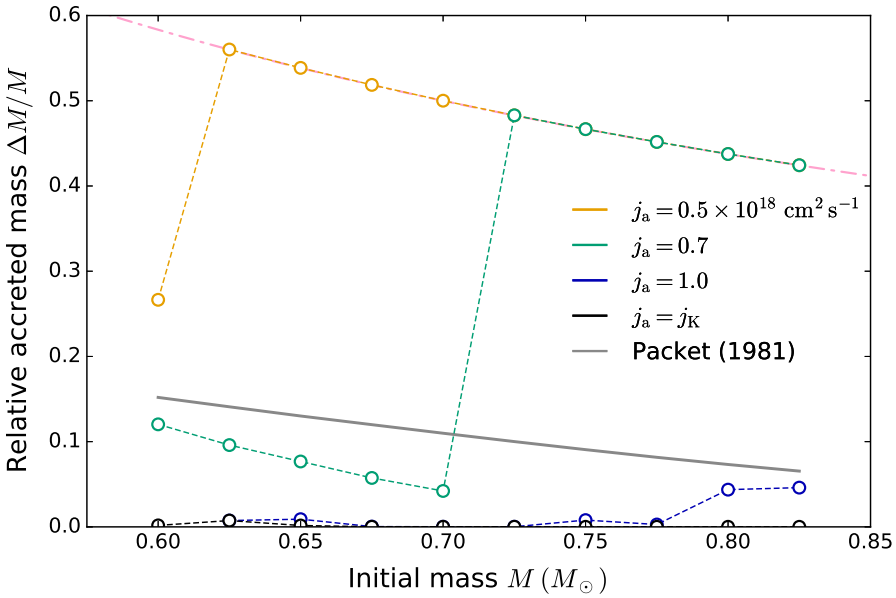

Figure 6.7: Mass accreted before critical rotation is reached (relative to initial mass) by differentially rotating CEMP-*s* star progenitors for different values of the specific angular momentum of accreted material. Here $\dot{M} = 10^{-6}\ M_\odot\ \mathrm{yr}^{-1}$. The models were stopped at $\Delta M = 0.35\ M_\odot$ (dash-dotted line) if critical rotation had not been reached by that point.

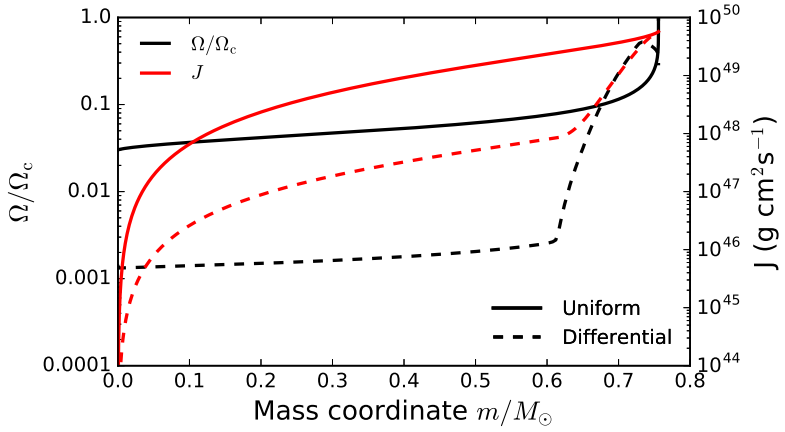

Figure 6.8: The cumulative angular momentum and Ω/Ω_c in a $M = 0.7\ M_\odot$ model that has added about $0.055\ M_\odot$ of matter with $j_a = 5 \times 10^{17}$ cm^2 s^{-1} at a rate of $\dot{M} = 10^{-6}\ M_\odot\ \mathrm{yr}^{-1}$. For the uniformly rotating model this is just enough to bring it to critical rotation, whereas in the differentially rotating model enough of the angular momentum has been transported to layers deeper in the star (between $m \simeq 0.65$–$0.75\ M_\odot$) to prevent the surface from rotating critically.

principle go on to accrete more material (up to about $\Delta M_{\rm TE} - \Delta M$ such that $\Delta M_{\rm final} \simeq \Delta M_{\rm TE}$). Conversely, in cases where $\Delta M > \Delta M_{\rm TE}$, the stars tend to expand and spin up with respect to the critical rate. Since this is not possible, they must somehow lose angular momentum to return to equilibrium. This could happen by mass shedding (Meynet, Ekström and Maeder, 2006; Krtička, Owocki and Meynet, 2011) so that some of the accreted material is, at least temporarily, lost.

The final ΔM thus depends on how the thermal relaxation timescale compares to the accretion timescale. Given the large mass-loss rates near the end of the AGB phase ($\dot{M}_{\rm AGB} \gtrsim 10^{-5}\,M_\odot\,{\rm yr}^{-1}$; van Loon et al., 2005; Ramstedt and Olofsson, 2014), the mass accretion rate in real systems is likely closer to the higher range of values investigated here ($\dot{M} \simeq 10^{-6\ldots-5}\,M_\odot\,{\rm yr}^{-1}$, depending on separation, see estimate based on Bondi-Hoyle-Lyttleton accretion in Sect. 2.1.5). Furthermore, this last stage, during which the AGB star loses most of its envelope, lasts only a small fraction of the overall thermally pulsing AGB lifetime of about 1 Myr (Vassiliadis and Wood, 1993; Marigo and Girardi, 2007) and is considerably shorter than the thermal timescales of the prospective CEMP and Ba stars. It is thus difficult to envision how the progenitors of carbon-enriched stars could maintain thermal equilibrium (and end up with $\Delta M \simeq \Delta M_{\rm TE}$) as they are accreting mass from their AGB companion.

We have thus far not discussed the nature of mass transfer. Because Roche lobe overflow from an AGB star will in most cases be unstable, most carbon-enriched stars probably form through wind accretion or wind Roche lobe overflow (Mohamed and Podsiadlowski, 2007; Abate et al., 2013). The specific angular momentum of accreted material in the canonical BHL accretion (Sect. 1.2.2) can be less than a few percent of $j_{\rm K}$ (Blondin and Raymer, 2012) and would impose no limit on the accreted mass. But because of their slow wind velocities, wind accretion from an AGB star is very different from the BHL case. As the slowly expanding material cools and falls towards the accretor, it gains angular momentum from Coriolis forces. Once the angular momentum exceeds the local Keplerian value $\sqrt{GMr}$ ($r > R$), the material is expected to settle in a disk around the accretor (Eggleton, 2006). Both analytical estimates (Soker and Rappaport, 2000; Perets and Kenyon, 2013) and numerical simulations (e.g. Theuns, Boffin and Jorissen, 1996; Mastrodemos and Morris, 1998; de Val-Borro, Karovska and Sasselov, 2009; Huarte-Espinosa, Carroll-Nellenback, Nordhaus et al., 2013; Chen, Frank, Blackman et al., 2017) suggest that disk formation in typical progenitor systems should be common ($j_{\rm a} \simeq j_{\rm K}$).[1]

If the mass accretion in real systems indeed occurs at high rates via a Keplerian disk, our results imply that most CEMP-*s* (and Ba) star progenitors can gain only up to about $\Delta M \simeq 0.05\,M_\odot$ even if we assume that the angular momentum is rapidly distributed throughout the star. This is a much smaller amount than the vast majority of CEMP-*s* stars in the population synthesis calculations of Abate et al. (2015c), who find that the median mass accreted is about $0.15\,M_\odot$ when angular momentum accretion is ignored. Whether accounting for angular momentum accretion would present difficulties explaining the observed fraction of CEMP stars (more than ten percent of all stars with [Fe/H] $\lesssim -2$ are carbon-enhanced; Lucatello, Beers, Christlieb et al., 2006; Lee, Beers, Masseron et al., 2013; Placco, Frebel, Beers et al., 2014) would require a careful accounting of the number of systems expected to be lost and gained as a result of severely limiting the accreted masses. Most of the CEMP star progenitors in the simulations of Abate et al. (2015c) have initial masses well below $0.8\,M_\odot$. Stars with larger initial masses ($M \simeq 0.8\,M_\odot$) rapidly evolve after accreting a large amount of mass and become white dwarfs. If such stars were not able to gain as much mass, they might be around for long enough to still be observable as CEMP stars. At the same time, some of the lower mass stars, if they were to gain less mass, would no longer be luminous enough to be observable (Abate et al., 2015c). Hence, we can only conclude that angular momentum

[1] Direct impact ($j_{\rm a} < j_{\rm K}$) of the transferring material is unlikely because in all but the closest mass ratio binaries the accreting star will be on the main sequence (North and Duquennoy, 1991; Böhm-Vitense, Carpenter, Robinson et al., 2000) and thus well within its Roche lobe. This remains true even if the stars swell up as a result of the accretion.

considerations suggest an initially more massive progenitor population of CEMP-*s* stars, compared to that found by Abate et al. (2015c), but not whether CEMP-*s* stars should be more or less common.

We also saw in Chapter 5 that stars that accrete less than 0.05 $M_\odot$ can still remain CEMP-*s* stars throughout their evolution (Figs. 5.15 and 5.16). However, the properties of individual Ba and CEMP stars often point to much higher accreted masses. For example, Miszalski et al. (2013) require accreting about 0.5 $M_\odot$ onto a $M \simeq 1.5\ M_\odot$ (from a primary with initial mass $M_{\rm AGB} = 1.8\ M_\odot$), or 0.8 $M_\odot$ onto a $M \simeq 2\ M_\odot$ ($M_{\rm AGB} = 3\ M_\odot$) star to explain the surface abundances of the Ba star in the planetary nebula Hen 2-39. Many of the CEMP-*s* stars considered by Abate et al. (2015a,b) are also best fit with accreted masses in excess of 0.1 $M_\odot$, given the current AGB nucleosynthesis model predictions (Karakas, 2010; Lugaro, Karakas, Stancliffe et al., 2012).

In many cases the accreted masses needed to explain the surface chemistry of carbon-enriched stars are a significant fraction of the total mass lost by the AGB star, so the accretor must have captured nearly all of the material entering its Roche lobe. If the star can somehow deal with the angular momentum, this is not implausible. As the inner part of the disk is accreted, the disk spreads outwards to compensate the loss of angular momentum onto the accreting object (Pringle, 1981; Lodato, 2008). If a disk with initial radius $R_{\rm d}$ spreads beyond the Roche lobe radius R_L, the fraction of material lost that allows the rest to fall to the central object is approximately $\sqrt{R_{\rm d}/R_L}$ (Lin and Pringle, 1976). For disks initially well inside the Roche lobe this is a negligible amount. Furthermore, once the disk spreads enough to approach $R_{\rm d} \simeq R_L$, tides from the AGB donor (or its remnant) should efficiently transfer angular momentum from the outer disk edge back to the orbit, with little to no mass lost from the Roche volume (Papaloizou and Pringle, 1977; Schwarzenberg-Czerny and Rozyczka, 1988; Ichikawa and Osaki, 1994; Hameury and Lasota, 2005).[2]

If the star is spun up to critical rotation in the process, it needs to lose angular momentum before it can accrete more of the disk. This could be achieved by depositing the angular momentum back in the disk. Popham and Narayan (1991) show that, once the star approaches critical rotation, outward transport of angular momentum by shear stresses ($\dot{J} \propto \Sigma \nu\, {\rm d}\Omega\,/\,{\rm d}r$, where Σ and ν are respectively the surface density and viscosity of the disk) can dominate the inward transport by accretion ($\dot{J} = \dot{M} j_{\rm a}$), and thus angular momentum can even be removed from the accreting object as it gains mass, if there is sufficient viscous coupling between the star and the disk. This coupling between the accreting star and its disk could perhaps be magnetic in nature. For example, in T Tauri stars (pre-main-sequence stars still surrounded by an accretion disk) the magnetic field of the central star anchors in the disk, which then exerts a negative torque on the star, preventing it from reaching critical rotation (e.g. Armitage and Clarke, 1996; Hartmann, Calvet, Gullbring et al., 1998; Matt and Pudritz, 2005b).

Also, some of the energy liberated during accretion could be used to drive strong winds from the stellar surface. Ejecting a mere ten percent of the accreted mass could suffice to remove enough angular momentum to prevent critical rotation (Matt and Pudritz, 2005a; Dervişoglu, Tout and Ibanoglu, 2010). However, surface magnetic field strengths in excess of $B \sim$ 100–1000 G are required for this mechanism or disk torques to be effective. While such fields are probably uncommon in the progenitors of carbon-enriched stars, they could perhaps be generated during the accretion if a strong differential rotation results (Dervişoglu et al., 2010).

Whatever the mechanism, according to the calculations presented here, for the accreted masses to be large enough to satisfy the chemistry constraints (some tenths of a solar mass), $j_{\rm a}$ must effectively be below about 5×10^{17} cm^2 s^{-1} (Figs. 6.1, 6.6), or about 10 and 25% of $j_{\rm K}$ for Ba and CEMP stars, respectively. Put differently, above 75% of the angular momentum supplied to the accretor by the disk

[2] The tidal influence on the accretor itself should be negligible since the timescale for angular momentum transfer from the accretor back to the orbit scales as $\tau_{\rm sync} \sim (R/a)^{-6}$ (Zahn, 1977), where $a \gg R$ is the orbital separation.

has to be removed on average.

Nevertheless, the newly born carbon-enriched stars should rotate fairly rapidly after the mass transfer ends. Indeed, a few younger Ba-enriched stars with relatively rapid rotation velocities (tens of $\mathrm{km\,s^{-1}}$ or more) are known (e.g. Kellett, Bromage, Brown et al., 1995; Jeffries and Smalley, 1996; Vennes, Christian and Thorstensen, 1998; Bond, Pollacco and Webbink, 2003; Miszalski, Boffin, Frew et al., 2012), indicating that some angular momentum accretion has occurred. As noted before, carbon-enhanced metal-poor dwarfs also rotate more rapidly on average than other metal-poor Halo stars (about 10 and $3\,\mathrm{km\,s^{-1}}$, respectively; Masseron, Johnson, Lucatello et al., 2012; Lucatello and Gratton, 2003), although the difference is small, which likely points to further angular momentum loss following mass transfer. Given the large amount of time elapsed since mass transfer took place, magnetic braking seems a plausible candidate for allowing the stars to spin down, assuming it can work in stars with such small convective envelopes (Sect. 5.3.1).

6.4 Conclusions

The specific angular momentum of the accreted material strongly affects the amount of mass that can be added to the progenitors of carbon-enriched (i.e. Ba and CEMP) stars before they are spun up to critical rotation. Material assumed to originate from a Keplerian accretion disk brings the stars to critical rotation after only a few percent of their initial mass is added, even if the angular momentum is allowed to rapidly redistribute throughout the star. If instead the specific angular momentum of the accreted material is a few tenths of the Keplerian value or less, the angular momentum no longer limits the amount of mass that can be added.

Taken at face value, these results have major implications for the progenitor systems of carbon-enriched stars, as many likely do accrete matter through an accretion disk. The large accreted masses inferred from observations of particular Ba and CEMP stars (in some instances comparable to the initial mass of the progenitor) are at odds with these results. However, a way to reconcile them with the necessity of substantial mass accretion would be to invoke some mechanism, such as viscous or magnetic coupling to the accretion disk, that would allow the accreting star to transfer its spin angular momentum back to the orbit with the help of tidal torques from the donor star. In this way the accretor could possibly avoid critical rotation and accrete much more of the material entering its Roche lobe.

Table 6.1: Mass accreted before critical rotation is reached (ΔM) by the different models. The first five columns list the initial mass of the secondary (M); its Kelvin-Helmholtz timescale before mass addition ($\tau_{\rm KH}$, Myr); its gyration radius before mass addition ($k^2 = I/MR^2$); estimate of ΔM based on Packet (1981) ($\Delta M_{\rm P81}$); mass accretion rate ($\dot{M}/10^{-6}\ M_\odot\ {\rm yr}^{-1}$). The remaining columns list pairs of specific angular momentum of the accreted material ($j_{\rm a}$ in units of 10^{18} cm^2 s^{-1}) and the corresponding ΔM. The last pair in each row corresponds to $j_{\rm a} = j_{\rm K}$ and the listed value of $j_{\rm a}$ is the Keplerian specific angular momentum at the surface prior to mass addition. The table is sectioned according to the metallicity Z and initial primary mass $M_{\rm AGB}$ ($t_{\rm mt}$ is the age at which mass addition starts).

M	$\tau_{\rm KH}$	k^2	$\Delta M_{\rm P81}$	$\dot{M}$	$j_{\rm a}$	ΔM	$j_{\rm a}$	ΔM	$j_{\rm a}$	ΔM	$j_{\rm a}$	ΔM	$j_{\rm a}$	ΔM	$j_{\rm a}$	ΔM
$Z = 10^{-4}$; $M_{\rm AGB} = 1.0\ M_\odot$; $t_{\rm mt} = 6.3$ Gyr; uniform rotation																
0.600	65.0	0.128	0.091	0.01	0.2	> 0.35	0.5	0.236	1.0	0.103	2.0	0.050	1.758	0.050	…	…
…	…	…	…	0.1	0.2	> 0.35	0.5	0.098	1.0	0.079	2.0	0.050	1.758	0.050	…	…
…	…	…	…	1.0	0.2	0.275	0.5	0.258	1.0	0.112	2.0	0.054	1.758	0.054	…	…
…	…	…	…	10.0	0.2	–	0.5	–	1.0	–	2.0	–	1.758	–	…	…
0.625	56.2	0.120	0.088	0.01	0.2	> 0.35	0.5	0.228	1.0	0.103	2.0	0.049	1.836	0.048	…	…
…	…	…	…	0.1	0.2	> 0.35	0.5	0.099	1.0	0.060	2.0	0.045	1.836	0.044	…	…
…	…	…	…	1.0	0.2	0.183	0.5	0.184	1.0	0.105	2.0	0.051	1.836	0.051	…	…
…	…	…	…	10.0	0.2	–	0.5	–	1.0	–	2.0	–	1.836	–	…	…
0.650	48.7	0.112	0.085	0.01	0.2	> 0.35	0.5	0.220	1.0	0.101	2.0	0.047	1.914	0.046	…	…
…	…	…	…	0.1	0.2	> 0.35	0.5	0.104	1.0	0.052	2.0	0.038	1.914	0.037	…	…
…	…	…	…	1.0	0.2	0.132	0.5	0.116	1.0	0.092	2.0	0.048	1.914	0.047	…	…
…	…	…	…	10.0	0.2	–	0.5	> 0.35	1.0	–	2.0	–	1.914	–	…	…
0.675	42.1	0.105	0.081	0.01	0.2	> 0.35	0.5	0.213	1.0	0.099	2.0	0.047	1.995	0.045	…	…
…	…	…	…	0.1	0.2	> 0.35	0.5	0.111	1.0	0.052	2.0	0.029	1.995	0.028	…	…
…	…	…	…	1.0	0.2	0.127	0.5	0.065	1.0	0.066	2.0	0.044	1.995	0.041	…	…
…	…	…	…	10.0	0.2	> 0.35	0.5	> 0.35	1.0	0.109	2.0	0.048	1.995	0.046	…	…
0.700	36.5	0.097	0.077	0.01	0.2	> 0.35	0.5	0.206	1.0	0.096	2.0	0.047	2.080	0.042	…	…
…	…	…	…	0.1	0.2	> 0.35	0.5	0.123	1.0	0.054	2.0	0.028	2.080	0.024	…	…
…	…	…	…	1.0	0.2	0.135	0.5	0.056	1.0	0.035	2.0	0.034	2.080	0.033	…	…
…	…	…	…	10.0	0.2	0.297	0.5	0.236	1.0	0.099	2.0	0.046	2.080	0.042	…	…
0.725	31.6	0.089	0.073	0.01	0.2	> 0.35	0.5	0.202	1.0	0.094	2.0	0.046	2.168	0.040	…	…
…	…	…	…	0.1	0.2	> 0.35	0.5	0.137	1.0	0.056	2.0	0.029	2.168	0.024	…	…
…	…	…	…	1.0	0.2	0.157	0.5	0.060	1.0	0.032	2.0	0.019	2.168	0.017	…	…
…	…	…	…	10.0	0.2	0.118	0.5	0.117	1.0	0.079	2.0	0.042	2.168	0.036	…	…
0.750	27.3	0.082	0.068	0.01	0.2	> 0.35	0.5	0.199	1.0	0.091	2.0	0.045	2.262	0.037	…	…
…	…	…	…	0.1	0.2	> 0.35	0.5	0.152	1.0	0.060	2.0	0.030	2.262	0.023	…	…
…	…	…	…	1.0	0.2	0.184	0.5	0.066	1.0	0.035	2.0	0.020	2.262	0.015	…	…
…	…	…	…	10.0	0.2	0.051	0.5	0.037	1.0	0.039	2.0	0.032	2.262	0.028	…	…
0.775	23.6	0.075	0.063	0.01	0.2	> 0.35	0.5	0.201	1.0	0.089	2.0	0.043	2.361	0.035	…	…
…	…	…	…	0.1	0.2	> 0.35	0.5	0.168	1.0	0.064	2.0	0.030	2.361	0.023	…	…
…	…	…	…	1.0	0.2	0.220	0.5	0.072	1.0	0.037	2.0	0.020	2.361	0.015	…	…
…	…	…	…	10.0	0.2	0.048	0.5	0.027	1.0	0.018	2.0	0.012	2.361	0.011	…	…
0.800	20.2	0.067	0.058	0.01	0.2	> 0.35	0.5	0.210	1.0	0.087	2.0	0.042	2.466	0.033	…	…
…	…	…	…	0.1	0.2	> 0.35	0.5	0.183	1.0	0.068	2.0	0.032	2.466	0.023	…	…
…	…	…	…	1.0	0.2	0.269	0.5	0.078	1.0	0.040	2.0	0.022	2.466	0.015	…	…
…	…	…	…	10.0	0.2	0.053	0.5	0.029	1.0	0.019	2.0	0.011	2.466	0.008	…	…
0.825	17.4	0.061	0.054	0.01	0.2	> 0.35	0.5	0.220	1.0	0.086	2.0	0.041	2.578	0.031	…	…
…	…	…	…	0.1	0.2	> 0.35	0.5	0.196	1.0	0.072	2.0	0.034	2.578	0.024	…	…
…	…	…	…	1.0	0.2	> 0.35	0.5	0.086	1.0	0.043	2.0	0.023	2.578	0.016	…	…
…	…	…	…	10.0	0.2	0.059	0.5	0.031	1.0	0.020	2.0	0.012	2.578	0.008	…	…
$Z = 10^{-4}$; $M_{\rm AGB} = 1.5\ M_\odot$; $t_{\rm mt} = 1.8$ Gyr; uniform rotation																
0.600	72.2	0.135	0.098	0.01	0.2	> 0.35	0.5	0.247	1.0	0.109	2.0	0.054	1.736	0.054	…	…
…	…	…	…	0.1	0.2	> 0.35	0.5	0.113	1.0	0.089	2.0	0.054	1.736	0.054	…	…
…	…	…	…	1.0	0.2	–	0.5	0.330	1.0	0.120	2.0	0.058	1.736	0.058	…	…
…	…	…	…	10.0	0.2	–	0.5	–	1.0	–	2.0	–	1.736	–	…	…
0.625	63.5	0.128	0.095	0.01	0.2	> 0.35	0.5	0.242	1.0	0.110	2.0	0.052	1.809	0.052	…	…
…	…	…	…	0.1	0.2	> 0.35	0.5	0.104	1.0	0.072	2.0	0.050	1.809	0.050	…	…
…	…	…	…	1.0	0.2	0.229	0.5	0.228	1.0	0.116	2.0	0.055	1.809	0.055	…	…
…	…	…	…	10.0	0.2	–	0.5	–	1.0	–	2.0	–	1.809	–	…	…
0.650	56.1	0.122	0.093	0.01	0.2	> 0.35	0.5	0.238	1.0	0.110	2.0	0.051	1.881	0.051	…	…
…	…	…	…	0.1	0.2	> 0.35	0.5	0.108	1.0	0.055	2.0	0.045	1.881	0.044	…	…
…	…	…	…	1.0	0.2	0.164	0.5	0.160	1.0	0.108	2.0	0.053	1.881	0.052	…	…
…	…	…	…	10.0	0.2	–	0.5	–	1.0	–	2.0	–	1.881	–	…	…

Table 6.1: continued.

M	$\tau_{\rm KH}$	k^2	$\Delta M_{\rm P81}$	$\dot{M}$	$j_{\rm a}$	ΔM	$j_{\rm a}$	ΔM	$j_{\rm a}$	ΔM	$j_{\rm a}$	ΔM	$j_{\rm a}$	ΔM	$j_{\rm a}$	ΔM
0.675	49.6	0.115	0.091	0.01	0.2	> 0.35	0.5	0.235	1.0	0.109	2.0	0.051	1.954	0.049	…	…
…	…	…	…	0.1	0.2	> 0.35	0.5	0.117	1.0	0.055	2.0	0.037	1.954	0.036	…	…
…	…	…	…	1.0	0.2	0.142	0.5	0.102	1.0	0.092	2.0	0.051	1.954	0.049	…	…
…	…	…	…	10.0	0.2	–	0.5	–	1.0	–	2.0	–	1.954	–	…	…
0.700	44.1	0.109	0.088	0.01	0.2	> 0.35	0.5	0.232	1.0	0.109	2.0	0.052	2.028	0.048	…	…
…	…	…	…	0.1	0.2	> 0.35	0.5	0.130	1.0	0.057	2.0	0.031	2.028	0.028	…	…
…	…	…	…	1.0	0.2	0.152	0.5	0.066	1.0	0.064	2.0	0.047	2.028	0.044	…	…
…	…	…	…	10.0	0.2	> 0.35	0.5	0.349	1.0	0.121	2.0	0.053	2.028	0.049	…	…
0.725	39.3	0.103	0.086	0.01	0.2	> 0.35	0.5	0.231	1.0	0.108	2.0	0.052	2.102	0.046	…	…
…	…	…	…	0.1	0.2	> 0.35	0.5	0.148	1.0	0.060	2.0	0.031	2.102	0.027	…	…
…	…	…	…	1.0	0.2	0.176	0.5	0.064	1.0	0.038	2.0	0.036	2.102	0.035	…	…
…	…	…	…	8.0	0.2	0.228	0.5	0.210	1.0	0.107	2.0	0.051	2.102	0.046	…	…
0.750	35.2	0.098	0.083	0.01	0.2	> 0.35	0.5	0.233	1.0	0.108	2.0	0.052	2.178	0.045	…	…
…	…	…	…	0.1	0.2	> 0.35	0.5	0.168	1.0	0.064	2.0	0.032	2.178	0.026	…	…
…	…	…	…	1.0	0.2	0.215	0.5	0.069	1.0	0.037	2.0	0.022	2.178	0.020	…	…
…	…	…	…	10.0	0.2	0.142	0.5	0.143	1.0	0.093	2.0	0.048	2.178	0.042	…	…
0.775	31.6	0.092	0.080	0.01	0.2	> 0.35	0.5	0.237	1.0	0.107	2.0	0.052	2.255	0.044	…	…
…	…	…	…	0.1	0.2	> 0.35	0.5	0.192	1.0	0.070	2.0	0.034	2.255	0.026	…	…
…	…	…	…	1.0	0.2	0.278	0.5	0.077	1.0	0.040	2.0	0.022	2.255	0.018	…	…
…	…	…	…	8.0	0.2	0.067	0.5	0.061	1.0	0.061	2.0	0.042	2.255	0.036	…	…
0.800	28.4	0.087	0.077	0.01	0.2	> 0.35	0.5	0.251	1.0	0.107	2.0	0.052	2.334	0.042	…	…
…	…	…	…	0.1	0.2	> 0.35	0.5	0.220	1.0	0.076	2.0	0.036	2.334	0.027	…	…
…	…	…	…	1.0	0.2	> 0.35	0.5	0.085	1.0	0.044	2.0	0.024	2.334	0.018	…	…
…	…	…	…	10.0	0.2	–	0.5	–	1.0	–	2.0	0.024	2.334	0.024	…	…
0.825	25.6	0.082	0.075	0.01	0.2	> 0.35	0.5	0.271	1.0	0.108	2.0	0.052	2.412	0.041	…	…
…	…	…	…	0.1	0.2	> 0.35	0.5	0.247	1.0	0.082	2.0	0.038	2.412	0.027	…	…
…	…	…	…	1.0	0.2	> 0.35	0.5	0.093	1.0	0.048	2.0	0.026	2.412	0.019	…	…
…	…	…	…	10.0	0.2	0.059	0.5	0.033	1.0	0.021	2.0	0.014	2.412	0.011	…	…
$Z = 0.008$; $M_{\rm AGB} = 3.0\ M_\odot$; $t_{\rm mt} = 422$ Myr; uniform rotation																
1.000	25.27	0.075	0.082	0.01	0.2	> 2.0	0.5	0.275	1.0	0.136	2.0	0.070	3.0	0.045	2.954	0.045
…	…	…	…	0.1	0.2	> 2.0	0.5	0.196	1.0	0.088	2.0	0.047	3.0	0.033	2.954	0.031
…	…	…	…	1.0	0.2	0.255	0.5	0.086	1.0	0.046	2.0	0.029	3.0	0.029	2.954	0.029
…	…	…	…	10.0	0.2	0.181	0.5	0.181	1.0	0.127	2.0	0.067	3.0	0.045	2.954	0.043
1.250	12.60	0.045	0.059	0.01	0.2	> 2.0	0.5	0.490	1.0	0.160	2.0	0.071	3.0	0.046	3.844	0.035
…	…	…	…	0.1	0.2	> 2.0	0.5	0.410	1.0	0.139	2.0	0.062	3.0	0.041	3.844	0.030
…	…	…	…	1.0	0.2	> 2.0	0.5	0.174	1.0	0.083	2.0	0.044	3.0	0.031	3.844	0.022
…	…	…	…	10.0	0.2	–	0.5	–	1.0	–	2.0	–	3.0	–	3.844	–
1.500	7.27	0.044	0.069	0.01	0.2	> 2.0	0.5	1.052	1.0	0.240	2.0	0.102	3.0	0.065	4.370	0.042
…	…	…	…	0.1	0.2	> 2.0	0.5	1.041	1.0	0.225	2.0	0.094	3.0	0.060	4.370	0.039
…	…	…	…	1.0	0.2	> 2.0	0.5	0.365	1.0	0.139	2.0	0.069	3.0	0.047	4.370	0.030
…	…	…	…	10.0	0.2	0.286	0.5	–	1.0	0.069	2.0	–	3.0	–	4.370	–
1.735	4.63	0.044	0.080	0.01	0.2	> 2.0	0.5	> 2.0	1.0	0.338	2.0	0.137	3.0	0.087	4.954	0.049
…	…	…	…	0.1	0.2	> 2.0	0.5	> 2.0	1.0	0.327	2.0	0.133	3.0	0.083	4.954	0.047
…	…	…	…	1.0	0.2	> 2.0	0.5	> 2.0	1.0	0.218	2.0	0.100	3.0	0.066	4.954	0.038
…	…	…	…	8.0	0.2	> 2.0	0.5	0.234	1.0	0.117	2.0	0.064	3.0	0.045	4.954	0.027
2.000	2.84	0.042	0.089	0.1	0.2	> 2.0	0.5	> 2.0	1.0	0.470	2.0	0.180	3.0	0.112	5.770	0.054
…	…	…	…	1.0	0.2	> 2.0	0.5	> 2.0	1.0	0.358	2.0	0.143	3.0	0.092	5.770	0.045
…	…	…	…	10.0	0.2	> 2.0	0.5	0.379	1.0	0.171	2.0	0.089	3.0	0.062	5.770	0.032
2.250	1.77	0.039	0.093	0.1	0.2	> 2.0	0.5	> 2.0	1.0	0.635	2.0	0.229	3.0	0.141	6.809	0.056
…	…	…	…	1.0	0.2	> 2.0	0.5	> 2.0	1.0	0.535	2.0	0.191	3.0	0.120	6.809	0.049
…	…	…	…	10.0	0.2	> 2.0	0.5	0.732	1.0	0.253	2.0	0.124	3.0	0.085	6.809	0.037
2.500	1.07	0.034	0.088	0.1	0.2	> 2.0	0.5	> 2.0	1.0	0.746	2.0	0.278	3.0	0.170	8.460	0.054
…	…	…	…	1.0	0.2	> 2.0	0.5	> 2.0	1.0	0.728	2.0	0.246	3.0	0.149	8.460	0.048
…	…	…	…	10.0	0.2	> 2.0	0.5	> 2.0	1.0	0.373	2.0	0.168	3.0	0.112	8.460	0.039
$Z = 10^{-4}$; $M_{\rm AGB} = 1.0\ M_\odot$; $t_{\rm mt} = 6.3$ Gyr; differential rotation																
0.600	65.0	0.128	0.091	0.01	0.2	> 0.35	0.5	> 0.35	1.0	–	2.0	–	1.758	–	…	…
…	…	…	…	0.1	0.2	> 0.35	0.5	> 0.35	1.0	0.004	2.0	0.004	1.758	0.004	…	…
…	…	…	…	1.0	0.2	–	0.5	0.160	0.7	0.072	1.0	0.001	2.0	–	1.758	0.001
…	…	…	…	10.0	0.2	–	0.5	–	1.0	–	2.0	–	1.758	–	…	…
0.625	56.2	0.120	0.088	0.01	0.2	> 0.35	0.5	> 0.35	1.0	0.000	2.0	–	1.836	–	…	…
…	…	…	…	0.1	0.2	> 0.35	0.5	> 0.35	1.0	0.000	2.0	0.000	1.836	0.000	…	…
…	…	…	…	1.0	0.2	> 0.35	0.5	> 0.35	0.7	0.056	1.0	0.005	2.0	0.005	1.836	0.005

Table 6.1: continued.

M	$\tau_{\rm KH}$	k^2	$\Delta M_{\rm P81}$	$\dot{M}$	$j_{\rm a}$	ΔM	$j_{\rm a}$	ΔM	$j_{\rm a}$	ΔM	$j_{\rm a}$	ΔM	$j_{\rm a}$	ΔM	$j_{\rm a}$	ΔM
…	…	…	…	10.0	0.2	–	0.5	–	1.0	–	2.0	–	1.836	–	…	…
0.650	48.7	0.112	0.085	0.01	0.2	> 0.35	0.5	> 0.35	1.0	0.000	2.0	0.000	1.914	0.000	…	…
…	…	…	…	0.1	0.2	> 0.35	0.5	> 0.35	1.0	0.000	2.0	0.000	1.914	0.000	…	…
…	…	…	…	1.0	0.2	> 0.35	0.5	> 0.35	0.7	0.050	1.0	0.006	2.0	0.001	1.914	0.001
…	…	…	…	10.0	0.2	–	0.5	–	1.0	–	2.0	–	1.914	–	…	…
0.675	42.2	0.105	0.081	0.01	0.2	> 0.35	0.5	> 0.35	1.0	0.000	2.0	–	1.995	–	…	…
…	…	…	…	0.1	0.2	> 0.35	0.5	> 0.35	1.0	0.000	2.0	0.000	1.995	0.000	…	…
…	…	…	…	1.0	0.2	> 0.35	0.5	> 0.35	0.7	0.039	1.0	0.000	2.0	0.000	1.995	0.000
…	…	…	…	10.0	0.2	–	0.5	–	1.0	–	2.0	–	1.995	–	…	…
0.700	36.5	0.097	0.077	0.01	0.2	> 0.35	0.5	> 0.35	1.0	0.000	2.0	–	2.080	–	…	…
…	…	…	…	0.1	0.2	> 0.35	0.5	–	1.0	0.000	2.0	0.000	2.080	0.000	…	…
…	…	…	…	1.0	0.2	> 0.35	0.5	> 0.35	0.7	0.029	1.0	0.000	2.0	0.000	2.080	0.000
…	…	…	…	10.0	0.2	–	0.5	–	1.0	–	2.0	–	2.080	–	…	…
0.725	31.6	0.089	0.073	0.01	0.2	> 0.35	0.5	> 0.35	1.0	0.000	2.0	–	2.168	–	…	…
…	…	…	…	0.1	0.2	> 0.35	0.5	> 0.35	1.0	0.000	2.0	0.000	2.168	0.000	…	…
…	…	…	…	1.0	0.2	> 0.35	0.5	> 0.35	0.7	> 0.35	1.0	0.000	2.0	0.000	2.168	0.000
…	…	…	…	10.0	0.2	> 0.35	0.5	> 0.35	1.0	0.014	2.0	0.006	2.168	–	…	…
0.750	27.3	0.082	0.068	0.01	0.2	> 0.35	0.5	> 0.35	1.0	0.012	2.0	0.000	2.262	0.000	…	…
…	…	…	…	0.1	0.2	> 0.35	0.5	> 0.35	1.0	0.004	2.0	0.000	2.262	0.000	…	…
…	…	…	…	1.0	0.2	> 0.35	0.5	> 0.35	0.7	> 0.35	1.0	0.006	2.0	0.000	2.262	0.000
…	…	…	…	10.0	0.2	> 0.35	0.5	> 0.35	1.0	0.009	2.0	0.004	2.262	–	…	…
0.775	23.6	0.075	0.063	0.01	0.2	> 0.35	0.5	> 0.35	1.0	0.015	2.0	0.000	2.361	0.000	…	…
…	…	…	…	0.1	0.2	> 0.35	0.5	> 0.35	1.0	0.001	2.0	0.000	2.361	0.000	…	…
…	…	…	…	1.0	0.2	> 0.35	0.5	> 0.35	0.7	> 0.35	1.0	0.002	2.0	0.000	2.361	0.000
…	…	…	…	10.0	0.2	> 0.35	0.5	> 0.35	1.0	0.004	2.0	0.000	2.361	–	…	…
0.800	20.2	0.067	0.059	0.01	0.2	> 0.35	0.5	> 0.35	1.0	0.015	2.0	0.000	2.466	–	…	…
…	…	…	…	0.1	0.2	> 0.35	0.5	> 0.35	1.0	0.001	2.0	0.000	2.466	0.000	…	…
…	…	…	…	1.0	0.2	> 0.35	0.5	> 0.35	0.7	> 0.35	1.0	0.035	2.0	0.000	2.466	0.000
…	…	…	…	10.0	0.2	> 0.35	0.5	> 0.35	1.0	0.001	2.0	0.000	2.466	–	…	…
0.825	17.4	0.061	0.054	0.01	0.2	> 0.35	0.5	> 0.35	1.0	–	2.0	0.000	2.578	–	…	…
…	…	…	…	0.1	0.2	> 0.35	0.5	> 0.35	1.0	0.016	2.0	0.000	2.578	–	…	…
…	…	…	…	1.0	0.2	> 0.35	0.5	> 0.35	0.7	> 0.35	1.0	0.038	2.0	0.000	2.578	0.000
…	…	…	…	10.0	0.2	> 0.35	0.5	> 0.35	1.0	> 0.35	2.0	0.000	2.578	–	…	…

Notes. All masses are in solar masses. If critical rotation was not reached by then, the CEMP and Ba star progenitor models were stopped when, respectively, 0.35 $M_\odot$ and 2 $M_\odot$ of material were accreted. A minus indicates failure of convergence. The values of $t_{\rm mt}$ are from Lugaro et al. (2012) and Pols, Schröder, Hurley et al. (1998) for stars of $Z = 10^{-4}$ and $Z = 0.008$, respectively.

CHAPTER 7

Summary and conclusions

In this thesis we have investigated the evolution of carbon-enhanced metal-poor stars that are believed to originate from mass transfer in binaries with an asymptotic giant branch companion. In particular, we have focused on the chemical evolution of these stars following mass transfer. To that end we have used the STARS stellar evolution code to compute grids of stellar models corresponding to different combinations of the initial masses of the AGB (M_1 = 0.9–1.5 $M_\odot$) and CEMP-*s* ($M_{2,\mathrm{i}}$ = 0.6–0.8 $M_\odot$) stars and the mass accreted by the CEMP-*s* star (ΔM = 0.001–0.3 $M_\odot$).

The effect of multiple physical processes on the evolution of CEMP-*s* stars has been considered. Some, like thermohaline mixing and atomic diffusion, had already been investigated before in this context. We have built upon the earlier work of Stancliffe, Glebbeek, Izzard et al. (2007) and Stancliffe and Glebbeek (2008) by accounting for radiative forces in the STARS prescription for atomic diffusion. We have shown in Chapter 4 that many of the resulting models in which atomic diffusion is allowed to act unhindered develop chemical abundance patterns on the main sequence that are clearly inconsistent with those observed in real stars (e.g. vastly sub-solar ratios of carbon-to-iron abundances are predicted), which indicates that some other physical process(es) must inhibit atomic diffusion to a large extent.

We then show in Chapter 5 that rotational mixing could well be responsible for this inhibition since CEMP-*s* stars should naturally have some degree of rotation as a result of angular momentum accretion. In particular, accretion of angular momentum likely establishes differential rotation in these stars which favours mixing of angular momentum and chemical elements. Real CEMP-*s* stars appear to rotate at rates that are sufficiently rapid to explain why atomic diffusion is severely inhibited, but not rapid enough for the chemical mixing to substantially affect the structure or evolution of these stars in other ways.

However, as discussed in Chapter 6, the angular momentum of the accreted material is expected to be fairly high, which could impose severe limitations on the amount of mass the star can accrete by spinning it up to critical rotation. If so, a potential difficulty in explaining the origin of many CEMP-*s* stars arises: how do they avoid accreting too much angular momentum? The answer may involve some sort of mass loss concurrent with the mass accretion, or an interaction of the star with an accretion disk, but this issue merits further study.

Main sequence CEMP-*s* stars have been supposed to be particularly suitable for testing models of low-metallicity AGB stars because they are supposed to be simple: since there is hardly any outer convection zone on the main sequence, the surface of CEMP-*s* dwarfs should largely consist of the accreted material. We reemphasise that this is actually not what should be expected. In fact, many of the physical processes investigated here are more manifest in main sequence stars. Are post-main-sequence stars more easily interpretable? Perhaps, but one should still keep in mind that we always observe the

integrated effect of the prior evolution. The further (in evolutionary terms) we move from the time of mass transfer, the more other considerations come into play. For example, on the lower half of the red giant branch the star is still undergoing first dredge-up. Unless the luminosity of the stars can be precisely measured, the degree of mixing from first dredge-up is uncertain, and following FDU the abundances of some elements (e.g. lithium and nitrogen; Stancliffe et al., 2007; Stancliffe, 2009) may have changed as a result of nuclear processing. And further up the RGB at least some giants experience additional mixing, the cause of which is still debated (e.g. Stancliffe, Church, Angelou et al., 2009; Denissenkov and Merryfield, 2011).

7.1 Future directions

The most straightforward extension of the work presented here would be to explore more of the parameter space. The combinations of M_1, $M_{2,\mathrm{i}}$ and ΔM were limited to those that are most probable according to the population synthesis calculations of Abate, Pols, Stancliffe et al. (2015c). As a result, particularly the range of M_1 is limited, and extending the grid to include AGB stars with higher initial masses might be of some interest. Also, detailed model sets applicable to the more massive ($M > 1\ M_\odot$) and metal-rich ([Fe/H] $\gtrsim -1$) barium and CH stars appear not to be available at the moment. Such model sets could be tested against blue straggler stars, stars in stellar clusters that are hotter and brighter than the most massive stars still on the main sequence. Many blue stragglers are believed to have originated from mass transfer (Geller and Mathieu, 2011), and some have been found to be Ba-rich, which suggests that they have formed by accreting material from an AGB star (Milliman, Mathieu and Schuler, 2015).

We have assumed that all the physical processes considered here are essentially independent of one another, and simply summed up the transport coefficients associated with them. The interaction of the processes is only indirect, via modifying the structure of the star. Here this left some uncertainty as to whether the growth of the thermohaline instability would be suppressed in rotating stars. This question should be addressed in the future and an approach on how to integrate rotational instabilities with thermohaline mixing has been put forth by Maeder, Meynet, Lagarde et al. (2013). They derive a general quadratic equation whose solution yields a single transport coefficient. In its current formulation their approach can only be applied when the meridional currents are modelled as an advective process, but adapting it to the diffusive approach we have used should be possible.

The physical phenomena considered in this work are rather naturally expected to be relevant for CEMP-*s* stars. But others could be important as well. One intriguing possibility is magnetic fields. We have briefly discussed them as possible means of angular momentum loss, both during and following mass transfer, but magnetic fields would also modify the internal transport of angular momentum and chemical species (Spruit, 2002; Heger, Woosley and Spruit, 2005). Internal gravity waves generated on the boundaries between convective and radiative regions could alter the transport in the interior as well (Talon and Charbonnel, 2004; Talon and Charbonnel, 2005).

Finally, while the code development during this research was driven by the aim of modelling CEMP-*s* stars, the potential applications of the updated code are certainly wider, and the code can be used to investigate the various physical processes in other kinds of (binary) stars. For example, atomic diffusion and radiative levitation is relevant for some types of chemically peculiar stars (e.g. slowly rotating A and F stars; Richer, Michaud and Turcotte, 2000), as well as old low-mass stars and some subdwarf stars (Hu, Glebbeek, Thoul et al., 2010). Thermohaline convection should be relevant whenever a star accretes material from an evolved companion. And it is safe to say that all stars rotate. Rotation is particularly important for the evolution of massive stars, strongly influencing their structure, chemical evolution, rate of mass loss, and final fate (Maeder and Meynet, 2000; Langer, 2012).

APPENDIX A

Opacity Project data

As described in Sect. 3.3.4, the Opacity Project provides the monochromatic absorption cross-sections $\sigma_i(\nu)$ and corrections for momentum transfer to electrons $\sigma_i^e(\nu)$ on a temperature-electron density grid. However, for practical reasons the frequency coordinate in the OP data is not ν but υ. The two are related via

$$\upsilon(u_0) = \int_0^{\nu_0} \left(\frac{\partial B_\nu / \partial T}{\partial B / \partial T} \right) \mathrm{d}\nu = \int_0^{u_0} b_u \, \mathrm{d}u \,, \tag{A.1}$$

$$b_u = \left(\frac{15}{4\pi^4} \right) \frac{u^4 e^{-u}}{(1 - e^{-u})^2}, \tag{A.2}$$

$$u = \frac{h\nu}{k_\mathrm{B} T}, \tag{A.3}$$

where h and k_B are the Planck and Boltzmann constants, T is temperature, and B_ν is given by Eq. (2.18). The Rosseland mean opacity and the γ factors can then be written as

$$\frac{1}{\kappa_\mathrm{R}} = \int_0^\infty \frac{1}{\kappa_\nu} \left(\frac{\partial B_\nu / \partial T}{\partial B / \partial T} \right) \mathrm{d}\nu = \int_0^\infty \frac{1}{\kappa_u} b_u \, \mathrm{d}u = \int_0^{\upsilon_\mathrm{max}} \frac{1}{\kappa_u} \, \mathrm{d}\upsilon \,, \tag{A.4}$$

$$\gamma_i = \int_0^\infty f_i(\nu) \frac{(\partial B_\nu / \partial T)}{(\partial B / \partial T)} \, \mathrm{d}\nu = \int_0^\infty f_i(u) b_u \, \mathrm{d}u = \int_0^{\upsilon_\mathrm{max}} f_i(u) \, \mathrm{d}\upsilon \,, \tag{A.5}$$

with $\upsilon_\mathrm{max} = \upsilon(u \to \infty) = 1$ and f_i given by Eq. (3.22). Use of the υ mesh allows for more accurate integrations as more integration points are present in regions with large contributions to the integrals (Fig. A.1; Badnell, Bautista, Butler et al., 2005).

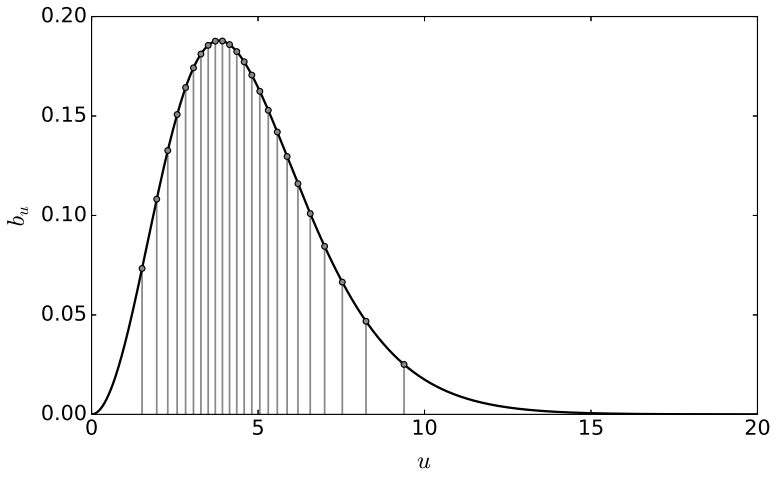

Figure A.1: The weighting function b_u (black line) defined by Eq. (A.2) in the range $0 < u \equiv h\nu/k_{\rm B}T < 20$. The monochromatic data in the Opacity Project are tabulated at frequencies corresponding to equal intervals of v (vertical lines), i.e. constant areas under the curve, instead of ν or u. This allows efficient sampling of the monochromatic data in regions where the radiative flux is large, and fewer integration points are needed to obtain a given accuracy in the opacities and accelerations.

Acknowledgements

So, a year tardy appears to be my way of doing things. Anyhow, job somehow nearly done, me! I suppose I should mention some people here. I'll start with the obvious. Richard, I think you did a fantastic job striking the right balance between allowing me to work on my own and guiding me when necessary. I have certainly learned a lot from you, and I always felt like I could expect good advice and honest feedback from you, work-related or otherwise. The environment of our mini-group has been incredibly enjoyable thanks to you, Carlo, and Zheng-Wei, and our weekly Friday morning get-togethers were almost always immensely fun (and sometimes educational as well!). Simply put, I could not have wished for a better supervisor, and I hope many other students have the pleasure of working with you in the future.

Some parts of the preceding chapters were read by a number of people: Richard, Abel, Nathan, Carlo, Elīna, Sandra. I really appreciate the effort these people made trying to improve this thesis by giving many valuable comments, even though I flippantly dismissed most of them. The original papers benefited from discussions and/or feedback from some people not appearing on the author lists: Carlo, Zheng-Wei, Rob Izzard, Luca Fossati, Chris Tout, Olivier Richard, Evert Glebbeek, and Georges Meynet. And many thanks to Alessandro, as well as Norbert, Pablo, Debashis, and Luca, for kindly answering all my dumb questions about the thesis submission process.

I am glad to have met many of my coworkers. Some of them I even sometimes enjoy spending time with outside of working hours. In this regard, I want to particularly mention Nathan, Abel, Sandra, Richard, Benjamin, JC, Zheng-Wei, Carlo, and the (other) (semi-)regulars at the Friday drinks: Ana, David, Toma, and, of course, The Chief.

Anyone who knows me a bit both on and off the court knows that I take basketball perhaps more seriously than anything else. So I would be remiss not to acknowledge my time as a member of the Blazing Suns! During my time here the Blazing Suns have grown from a bunch of people getting together once a week to shoot some hoops to an actual team with practices and competitive (at least in the opening minutes) games. I want to particularly thank the people that I believe to have been instrumental in making this so: Sarah, Tally, Benjamin, and Nils. I wish the Blazing Suns to go on to become bigger and better, and get that Basketballliga Bonn title! I am going to miss playing with you.

Last but not least, there is one other person besides Richard who deserves special recognition (or blame, perhaps). Elīna, your continued friendship and support throughout the last ten years has been invaluable. Without you I would certainly not be in a position to write these words.

Bibliography

Abate, C., O. R. Pols, R. G. Izzard and A. I. Karakas (2015a), *Carbon-enhanced metal-poor stars: a window on AGB nucleosynthesis and binary evolution. II. Statistical analysis of a sample of 67 CEMP-s stars*, A&A **581** A22, arXiv: 1507.04662 [astro-ph.SR] (cit. on pp. 55, 107, 108, 116).

Abate, C., O. R. Pols, R. G. Izzard, S. S. Mohamed and S. E. de Mink (2013), *Wind Roche-lobe overflow: Application to carbon-enhanced metal-poor stars*, A&A **552** A26, arXiv: 1302.4441 [astro-ph.SR] (cit. on pp. 15, 107, 115).

Abate, C., O. R. Pols, A. I. Karakas and R. G. Izzard (2015b), *Carbon-enhanced metal-poor stars: a window on AGB nucleosynthesis and binary evolution. I. Detailed analysis of 15 binary stars with known orbital periods*, A&A **576** A118, arXiv: 1502.07759 [astro-ph.SR] (cit. on pp. 107, 116).

Abate, C., O. R. Pols, R. J. Stancliffe, R. G. Izzard, A. I. Karakas, T. C. Beers and Y. S. Lee (2015c), *Modelling the observed properties of carbon-enhanced metal-poor stars using binary population synthesis*, A&A **581** A62, arXiv: 1507.04969 [astro-ph.SR] (cit. on pp. 57, 64, 108, 115, 116, 122).

Abate, C., R. J. Stancliffe and Z.-W. Liu (2016), *How plausible are the proposed formation scenarios of CEMP-r/s stars?*, A&A **587** A50, arXiv: 1601.00976 [astro-ph.SR] (cit. on p. 18).

Abbott, B. P., R. Abbott, T. D. Abbott, M. R. Abernathy, F. Acernese, K. Ackley, C. Adams, T. Adams et al. (2016a), *GW151226: Observation of Gravitational Waves from a 22-Solar-Mass Binary Black Hole Coalescence*, Physical Review Letters **116** 241103, arXiv: 1606.04855 [gr-qc] (cit. on p. 11).

– (2016b), *Observation of Gravitational Waves from a Binary Black Hole Merger*, Physical Review Letters **116** 061102, arXiv: 1602.03837 [gr-qc] (cit. on p. 11).

Abbott, B. P., R. Abbott, T. D. Abbott, F. Acernese, K. Ackley, C. Adams, T. Adams, P. Addesso et al. (2017), *GW170104: Observation of a 50-Solar-Mass Binary Black Hole Coalescence at Redshift 0.2*, Physical Review Letters **118** 221101, arXiv: 1706.01812 [gr-qc] (cit. on p. 11).

Affer, L., G. Micela, F. Favata and E. Flaccomio (2012), *The rotation of field stars from CoRoT data*, MNRAS **424** 11, arXiv: 1202.4947 [astro-ph.SR] (cit. on p. 97).

Ahn, C. P., R. Alexandroff, C. Allende Prieto, F. Anders, S. F. Anderson, T. Anderton, B. H. Andrews, É. Aubourg et al. (2014), *The Tenth Data Release of the Sloan Digital Sky Survey: First Spectroscopic Data from the SDSS-III Apache Point Observatory Galactic Evolution Experiment*, ApJS **211** 17, arXiv: 1307.7735 [astro-ph.IM] (cit. on p. 67).

Ahn, C. P., R. Alexandroff, C. Allende Prieto, S. F. Anderson, T. Anderton, B. H. Andrews, É. Aubourg, S. Bailey et al. (2012), *The Ninth Data Release of the Sloan Digital Sky Survey: First Spectroscopic Data from the SDSS-III Baryon Oscillation Spectroscopic Survey*, ApJS **203** 21, arXiv: 1207.7137 [astro-ph.IM] (cit. on p. 67).

Allen, D. M., S. G. Ryan, S. Rossi, T. C. Beers and S. A. Tsangarides (2012), *Elemental abundances and classification of carbon-enhanced metal-poor stars*, A&A **548** A34, arXiv: 1210.5009 [astro-ph.SR] (cit. on p. 17).

Amard, L., A. Palacios, C. Charbonnel, F. Gallet and J. Bouvier (2016), *Rotating models of young solar-type stars. Exploring braking laws and angular momentum transport processes*, A&A **587** A105, arXiv: 1601.01904 [astro-ph.SR] (cit. on p. 94).

Anders, E. and N. Grevesse (1989), *Abundances of the elements - Meteoritic and solar*, Geochim. Cosmochim. Acta **53** 197 (cit. on pp. 8, 10).

Aoki, W., T. C. Beers, N. Christlieb, J. E. Norris, S. G. Ryan and S. Tsangarides (2007), *Carbon-enhanced Metal-poor Stars. I. Chemical Compositions of 26 Stars*, ApJ **655** 492, eprint: astro-ph/0609702 (cit. on pp. 17, 18).

Aoki, W., T. C. Beers, Y. S. Lee, S. Honda, H. Ito, M. Takada-Hidai, A. Frebel, T. Suda et al. (2013), *High-resolution Spectroscopy of Extremely Metal-poor Stars from SDSS/SEGUE. I. Atmospheric Parameters and Chemical Compositions*, AJ **145** 13, arXiv: 1210.1946 [astro-ph.SR] (cit. on p. 69).

Aoki, W., T. C. Beers, T. Sivarani, B. Marsteller, Y. S. Lee, S. Honda, J. E. Norris, S. G. Ryan et al. (2008), *Carbon-Enhanced Metal-Poor Stars. III. Main-Sequence Turnoff Stars from the SDSS SEGUE Sample*, ApJ **678** 1351, arXiv: 0801.4187 (cit. on p. 69).

Arlandini, C., F. Käppeler, K. Wisshak, R. Gallino, M. Lugaro, M. Busso and O. Straniero (1999), *Neutron Capture in Low-Mass Asymptotic Giant Branch Stars: Cross Sections and Abundance Signatures*, ApJ **525** 886, eprint: astro-ph/9906266 (cit. on pp. 8, 9).

Armitage, P. J. and C. J. Clarke (1996), *Magnetic braking of T Tauri stars*, MNRAS **280** 458, eprint: astro-ph/9512018 (cit. on pp. 93, 116).

Asplund, M., N. Grevesse, A. J. Sauval and P. Scott (2009), *The Chemical Composition of the Sun*, ARA&A **47** 481, arXiv: 0909.0948 [astro-ph.SR] (cit. on pp. 10, 56).

Badnell, N. R., M. A. Bautista, K. Butler, F. Delahaye, C. Mendoza, P. Palmeri, C. J. Zeippen and M. J. Seaton (2005), *Updated opacities from the Opacity Project*, MNRAS **360** 458, eprint: astro-ph/0410744 (cit. on pp. 48, 123).

Bailyn, C. D. (1995), *Blue Stragglers and Other Stellar Anomalies:Implications for the Dynamics of Globular Clusters*, ARA&A **33** 133 (cit. on p. 11).

Beers, T. C. and N. Christlieb (2005), *The Discovery and Analysis of Very Metal-Poor Stars in the Galaxy*, ARA&A **43** 531 (cit. on pp. 11, 17, 63).

Beers, T. C., G. W. Preston and S. A. Shectman (1985), *A search for stars of very low metal abundance. I*, AJ **90** 2089 (cit. on p. 17).

– (1992), *A search for stars of very low metal abundance. II*, AJ **103** 1987 (cit. on p. 17).

Behara, N. T., P. Bonifacio, H.-G. Ludwig, L. Sbordone, J. I. González Hernández and E. Caffau (2010), *Three carbon-enhanced metal-poor dwarf stars from the SDSS. Chemical abundances from CO^{5}BOLD 3D hydrodynamical model atmospheres*, A&A **513** A72, arXiv: 1002.1670 [astro-ph.SR] (cit. on p. 69).

Belczyński, K., J. Mikołajewska, U. Munari, R. J. Ivison and M. Friedjung (2000), *A catalogue of symbiotic stars*, A&AS **146** 407, eprint: astro-ph/0005547 (cit. on p. 11).

Berger, E. (2014), *Short-Duration Gamma-Ray Bursts*, ARA&A **52** 43, arXiv: 1311.2603 [astro-ph.HE] (cit. on p. 11).

Bidelman, W. P. and P. C. Keenan (1951), *The BA II Stars.*, ApJ **114** 473 (cit. on p. 17).

Bisterzo, S., R. Gallino, O. Straniero, S. Cristallo and F. Käppeler (2010), *s-Process in low-metallicity stars - I. Theoretical predictions*, MNRAS **404** 1529, arXiv: 1001.5376 [astro-ph.SR] (cit. on p. 10).

– (2011), *The s-process in low-metallicity stars - II. Interpretation of high-resolution spectroscopic observations with asymptotic giant branch models*, MNRAS **418** 284, arXiv: 1108.0500 [astro-ph.SR] (cit. on p. 55).

– (2012), *The s-process in low-metallicity stars - III. Individual analysis of CEMP-s and CEMP-s/r with asymptotic giant branch models*, MNRAS **422** 849, arXiv: 1201.6198 [astro-ph.SR] (cit. on p. 55).

Bisterzo, S., C. Travaglio, R. Gallino, M. Wiescher and F. Käppeler (2014), *Galactic Chemical Evolution and Solar s-process Abundances: Dependence on the ^{13}C-pocket Structure*, ApJ **787** 10, arXiv: 1403.1764 [astro-ph.SR] (cit. on pp. 9, 10, 19).

Blondin, J. M. and E. Raymer (2012), *Hoyle-Lyttleton Accretion in Three Dimensions*, ApJ **752** 30, arXiv: 1204.0717 [astro-ph.SR] (cit. on p. 115).

Bode, M. F. and A. Evans (2012), *Classical Novae* (cit. on p. 11).

Boercker, D. B. (1987), *Collective effects on Thomson scattering in the solar interior*, ApJ **316** L95 (cit. on p. 49).

Boffin, H. M. and A. Jorissen (1988), *Can a barium star be produced by wind accretion in a detached binary?*, A&A **205** 155 (cit. on p. 14).

Böhm-Vitense, E. (1958), *Über die Wasserstoffkonvektionszone in Sternen verschiedener Effektivtemperaturen und Leuchtkräfte. Mit 5 Textabbildungen*, ZAp **46** 108 (cit. on p. 30).

Böhm-Vitense, E., K. Carpenter, R. Robinson, T. Ake and J. Brown (2000), *Do All BA II Stars Have White Dwarf Companions?*, ApJ **533** 969 (cit. on pp. 17, 115).

Bonaca, A., J. D. Tanner, S. Basu, W. J. Chaplin, T. S. Metcalfe, M. J. F. Monteiro, J. Ballot, T. R. Bedding et al. (2012), *Calibrating Convective Properties of Solar-like Stars in the Kepler Field of View*, ApJ **755** L12, arXiv: 1207.2765 [astro-ph.SR] (cit. on p. 71).

Bond, H. E. (1974), *The subgiant CH stars.*, ApJ **194** 95 (cit. on p. 17).

Bond, H. E., D. L. Pollacco and R. F. Webbink (2003), *WeBo 1: A Young Barium Star Surrounded by a Ringlike Planetary Nebula*, AJ **125** 260, eprint: astro-ph/0209418 (cit. on p. 117).

Bondi, H. (1952), *On spherically symmetrical accretion*, MNRAS **112** 195 (cit. on p. 14).

Bondi, H. and F. Hoyle (1944), *On the mechanism of accretion by stars*, MNRAS **104** 273 (cit. on p. 14).

Bouvier, J., S. P. Matt, S. Mohanty, A. Scholz, K. G. Stassun and C. Zanni (2014), *Angular Momentum Evolution of Young Low-Mass Stars and Brown Dwarfs: Observations and Theory*, Protostars and Planets VI 433, arXiv: 1309.7851 [astro-ph.SR] (cit. on p. 94).

Brandenburg, A. and K. Subramanian (2005), *Astrophysical magnetic fields and nonlinear dynamo theory*, Phys. Rep. **417** 1, eprint: astro-ph/0405052 (cit. on p. 94).

Bressan, A., P. Marigo, L. Girardi, B. Salasnich, C. Dal Cero, S. Rubele and A. Nanni (2012), *PARSEC: stellar tracks and isochrones with the PAdova and TRieste Stellar Evolution Code*, MNRAS **427** 127, arXiv: 1208.4498 [astro-ph.SR] (cit. on pp. 64, 88).

Brott, I., S. E. de Mink, M. Cantiello, N. Langer, A. de Koter, C. J. Evans, I. Hunter, C. Trundle et al. (2011), *Rotating massive main-sequence stars. I. Grids of evolutionary models and isochrones*, A&A **530** A115, arXiv: 1102.0530 [astro-ph.SR] (cit. on p. 100).

Brown, J. M., P. Garaud and S. Stellmach (2013), *Chemical Transport and Spontaneous Layer Formation in Fingering Convection in Astrophysics*, ApJ **768** 34, arXiv: 1212.1688 [astro-ph.SR] (cit. on pp. 20, 44, 45).

Budding, E., A. Erdem, C. Çiçek, I. Bulut, F. Soydugan, E. Soydugan, V. Bakiş and O. Demircan (2004), *Catalogue of Algol type binary stars*, A&A **417** 263 (cit. on p. 11).

Burgers, J. M. (1969), *Flow Equations for Composite Gases* (cit. on pp. 46, 71).

Busso, M., R. Gallino, D. L. Lambert, C. Travaglio and V. V. Smith (2001), *Nucleosynthesis and Mixing on the Asymptotic Giant Branch. III. Predicted and Observed s-Process Abundances*, ApJ **557** 802, eprint: astro-ph/0104424 (cit. on pp. 9, 10).

Busso, M., R. Gallino and G. J. Wasserburg (1999), *Nucleosynthesis in Asymptotic Giant Branch Stars: Relevance for Galactic Enrichment and Solar System Formation*, ARA&A **37** 239 (cit. on p. 8).

Busso, M., D. L. Lambert, L. Beglio, R. Gallino, C. M. Raiteri and V. V. Smith (1995), *Nucleosynthesis and Mixing on the Asymptotic Giant Branch. II. Carbon and Barium Stars in the Galactic Disk*, ApJ **446** 775 (cit. on p. 17).

Cameron, A. G. (1955), *Origin of Anomalous Abundances of the Elements in Giant Stars.*, ApJ **121** 144 (cit. on p. 9).

– (1960), *New Neutron Sources of Possible Astrophysical Importance.*, AJ **65** 485 (cit. on p. 9).

Cantiello, M. and N. Langer (2010), *Thermohaline mixing in evolved low-mass stars*, A&A **521** A9, arXiv: 1006.1354 [astro-ph.SR] (cit. on p. 97).

Canuto, V. (1970), *Electrical Conductivity and Conductive Opacity of a Relativistic Electron Gas*, ApJ **159** 641 (cit. on p. 50).

Carney, B. W., D. W. Latham, R. P. Stefanik, J. B. Laird and J. A. Morse (2003), *Spectroscopic Binaries, Velocity Jitter, and Rotation in Field Metal-poor Red Giant and Red Horizontal-Branch Stars*, AJ **125** 293 (cit. on p. 18).

Carollo, D., T. C. Beers, J. Bovy, T. Sivarani, J. E. Norris, K. C. Freeman, W. Aoki, Y. S. Lee et al. (2012), *Carbon-enhanced Metal-poor Stars in the Inner and Outer Halo Components of the Milky Way*, ApJ **744** 195, arXiv: 1103.3067 (cit. on p. 18).

Cassisi, S., A. Y. Potekhin, A. Pietrinferni, M. Catelan and M. Salaris (2007), *Updated Electron-Conduction Opacities: The Impact on Low-Mass Stellar Models*, ApJ **661** 1094, eprint: astro-ph/0703011 (cit. on pp. 50, 52).

Castellani, V. and S. degl'Innocenti (1999), *Microscopic diffusion and the calibration of globular cluster ages*, A&A **344** 97 (cit. on p. 64).

Catalán, S., J. Isern, E. García-Berro and I. Ribas (2008), *The initial-final mass relationship of white dwarfs revisited: effect on the luminosity function and mass distribution*, MNRAS **387** 1693, arXiv: 0804.3034 (cit. on p. 7).

Caughlan, G. R. and W. A. Fowler (1988), *Thermonuclear Reaction Rates V*, Atomic Data and Nuclear Data Tables **40** 283 (cit. on p. 44).

Chaboyer, B., C. P. Deliyannis, P. Demarque, M. H. Pinsonneault and A. Sarajedini (1992), *The effect of helium diffusion on the ages of globular clusters*, ApJ **388** 372 (cit. on p. 23).

Chaboyer, B., P. Demarque and M. H. Pinsonneault (1995a), *Stellar models with microscopic diffusion and rotational mixing. 1: Application to the Sun*, ApJ **441** 865, eprint: astro-ph/9408058 (cit. on p. 94).

– (1995b), *Stellar models with microscopic diffusion and rotational mixing. 2: Application to open clusters*, ApJ **441** 876, eprint: astro-ph/9408059 (cit. on p. 100).

Chaboyer, B. and J.-P. Zahn (1992), *Effect of horizontal turbulent diffusion on transport by meridional circulation*, A&A **253** 173 (cit. on p. 45).

Chandrasekhar, S. (1961), *Hydrodynamic and hydromagnetic stability* (cit. on p. 21).

Chapman, S. and T. G. Cowling (1970), *The mathematical theory of non-uniform gases. an account of the kinetic theory of viscosity, thermal conduction and diffusion in gases* (cit. on p. 46).

Charbonneau, P. (2010), *Dynamo Models of the Solar Cycle*, Living Reviews in Solar Physics **7** 3 (cit. on p. 94).

Charbonnel, C. and N. Lagarde (2010), *Thermohaline instability and rotation-induced mixing. I. Low- and intermediate-mass solar metallicity stars up to the end of the AGB*, A&A **522** A10, arXiv: 1006.5359 [astro-ph.SR] (cit. on p. 97).

Chen, Z., A. Frank, E. G. Blackman, J. Nordhaus and J. Carroll-Nellenback (2017), *Mass transfer and disc formation in AGB binary systems*, MNRAS **468** 4465, arXiv: 1702.06160 [astro-ph.SR] (cit. on pp. 21, 93, 115).

Christensen-Dalsgaard, J. (2002), *Helioseismology*, Reviews of Modern Physics **74** 1073, eprint: astro-ph/0207403 (cit. on p. 23).

Christensen-Dalsgaard, J., C. R. Proffitt and M. J. Thompson (1993), *Effects of diffusion on solar models and their oscillation frequencies*, ApJ **403** L75 (cit. on p. 23).

Christlieb, N., P. J. Green, L. Wisotzki and D. Reimers (2001), *The stellar content of the Hamburg/ESO survey II. A large, homogeneously-selected sample of high latitude carbon stars*, A&A **375** 366, eprint: astro-ph/0106240 (cit. on p. 17).

Cortés, C., J. R. Silva, A. Recio-Blanco, M. Catelan, J. D. Do Nascimento Jr. and J. R. De Medeiros (2009), *An Overview of the Rotational Behavior of Metal-poor Stars*, ApJ **704** 750, arXiv: 1009.4951 [astro-ph.SR] (cit. on pp. 21, 93).

Couch, R. G., A. B. Schmiedekamp and W. D. Arnett (1974), *S-PROCESS Nucleosynthesis in Massive Stars: Core Helium Burning*, ApJ **190** 95 (cit. on p. 9).

Cowan, J. J. and W. K. Rose (1977), *Production of C-14 and neutrons in red giants*, ApJ **212** 149 (cit. on p. 18).

Cranmer, S. R. and S. H. Saar (2011), *Testing a Predictive Theoretical Model for the Mass Loss Rates of Cool Stars*, ApJ **741** 54, arXiv: 1108.4369 [astro-ph.SR] (cit. on p. 74).

Cyburt, R. H., B. D. Fields, K. A. Olive and T.-H. Yeh (2016), *Big bang nucleosynthesis: Present status*, Reviews of Modern Physics **88** 015004, arXiv: 1505.01076 (cit. on p. 10).

De Marco, O. and R. G. Izzard (2017), *Dawes Review 6: The Impact of Companions on Stellar Evolution*, PASA **34** e001, arXiv: 1611.03542 [astro-ph.SR] (cit. on pp. 11, 17).

de Val-Borro, M., M. Karovska and D. Sasselov (2009), *Numerical Simulations of Wind Accretion in Symbiotic Binaries*, ApJ **700** 1148, arXiv: 0905.3542 [astro-ph.SR] (cit. on pp. 21, 115).

Deheuvels, S., G. Doğan, M. J. Goupil, T. Appourchaux, O. Benomar, H. Bruntt, T. L. Campante, L. Casagrande et al. (2014), *Seismic constraints on the radial dependence of the internal rotation profiles of six Kepler subgiants and young red giants*, A&A **564** A27, arXiv: 1401.3096 [astro-ph.SR] (cit. on p. 86).

Denissenkov, P. A. (2010), *Numerical Simulations of Thermohaline Convection: Implications for Extra-mixing in Low-mass RGB Stars*, ApJ **723** 563, arXiv: 1006.5481 [astro-ph.SR] (cit. on pp. 20, 45, 90).

Denissenkov, P. A. and W. J. Merryfield (2011), *Thermohaline Mixing: Does it Really Govern the Atmospheric Chemical Composition of Low-mass Red Giants?*, ApJ **727** L8, arXiv: 1011.2191 [astro-ph.SR] (cit. on p. 122).

Denissenkov, P. A. and M. Pinsonneault (2008a), *^{3}He-driven Mixing in Low-Mass Red Giants: Convective Instability in Radiative and Adiabatic Limits*, ApJ **684** 626, arXiv: 0708.3864 (cit. on pp. 72, 97).

– (2008b), *The Impact of Carbon Enhancement on Extra Mixing in Metal-poor Stars*, ApJ **679** 1541, arXiv: 0709.4240 (cit. on p. 99).

Denissenkov, P. A. and C. A. Tout (2003), *Partial mixing and formation of the ^{13}C pocket by internal gravity waves in asymptotic giant branch stars*, MNRAS **340** 722 (cit. on p. 9).

Dervişoglu, A., C. A. Tout and C. Ibanoglu (2010), *Spin angular momentum evolution of the long-period Algols*, MNRAS **406** 1071, arXiv: 1003.4392 [astro-ph.SR] (cit. on p. 116).

Doherty, C. L., P. Gil-Pons, L. Siess, J. C. Lattanzio and H. H. Lau (2015), *Super- and massive AGB stars - IV. Final fates - initial-to-final mass relation*, MNRAS **446** 2599, arXiv: 1410.5431 [astro-ph.SR] (cit. on p. 7).

Dupuis, J., G. Fontaine, C. Pelletier and F. Wesemael (1992), *A study of metal abundance patterns in cool white dwarfs. I - Time-dependent calculations of gravitational settling*, ApJS **82** 505 (cit. on p. 23).

Duquennoy, A. and M. Mayor (1991), *Multiplicity among solar-type stars in the solar neighbourhood. II - Distribution of the orbital elements in an unbiased sample*, A&A **248** 485 (cit. on p. 11).

Eddington, A. S. (1925), *Circulating currents in rotating stars*, The Observatory **48** 73 (cit. on p. 22).
Edgar, R. (2004), *A review of Bondi-Hoyle-Lyttleton accretion*, New A Rev. **48** 843, eprint: astro-ph/0406166 (cit. on pp. 14, 15).
Edvardsson, B., J. Andersen, B. Gustafsson, D. L. Lambert, P. E. Nissen and J. Tomkin (1993), *The Chemical Evolution of the Galactic Disk - Part One - Analysis and Results*, A&A **275** 101 (cit. on p. 17).
Eggenberger, P., G. Meynet, A. Maeder, A. Miglio, J. Montalban, F. Carrier, S. Mathis, C. Charbonnel et al. (2010), *Effects of rotational mixing on the asteroseismic properties of solar-type stars*, A&A **519** A116, arXiv: 1009.4541 [astro-ph.SR] (cit. on p. 87).
Eggleton, P. (2006), *Evolutionary Processes in Binary and Multiple Stars* (cit. on pp. 11, 115).
Eggleton, P. P. (1971), *The evolution of low mass stars*, MNRAS **151** 351 (cit. on pp. 27, 32).
– (1972), *Composition changes during stellar evolution*, MNRAS **156** 361 (cit. on pp. 27, 44).
Eggleton, P. P., D. S. Dearborn and J. C. Lattanzio (2006), *Deep Mixing of ^{3}He: Reconciling Big Bang and Stellar Nucleosynthesis*, Science **314** 1580, eprint: astro-ph/0611039 (cit. on pp. 20, 90).
Eggleton, P. P., J. Faulkner and B. P. Flannery (1973), *An Approximate Equation of State for Stellar Material*, A&A **23** 325 (cit. on p. 27).
Eichler, D., M. Livio, T. Piran and D. N. Schramm (1989), *Nucleosynthesis, neutrino bursts and gamma-rays from coalescing neutron stars*, Nature **340** 126 (cit. on p. 8).
Ekström, S., G. Meynet, A. Maeder and F. Barblan (2008), *Evolution towards the critical limit and the origin of Be stars*, A&A **478** 467, arXiv: 0711.1735 (cit. on p. 38).
Eldridge, J. J. and C. A. Tout (2004), *A more detailed look at the opacities for enriched carbon and oxygen mixtures*, MNRAS **348** 201, eprint: astro-ph/0310255 (cit. on pp. 50, 80).
Endal, A. S. and S. Sofia (1976), *The evolution of rotating stars. I - Method and exploratory calculations for a 7-solar-mass star*, ApJ **210** 184 (cit. on pp. 34, 35).
– (1978), *The evolution of rotating stars. II - Calculations with time-dependent redistribution of angular momentum for 7- and 10-solar-mass stars*, ApJ **220** 279 (cit. on p. 39).
Epstein, C. R. and M. H. Pinsonneault (2014), *How Good a Clock is Rotation? The Stellar Rotation-Mass-Age Relationship for Old Field Stars*, ApJ **780** 159, arXiv: 1203.1618 [astro-ph.SR] (cit. on p. 94).
ESA, ed. (1997), *The HIPPARCOS and TYCHO catalogues. Astrometric and photometric star catalogues derived from the ESA HIPPARCOS Space Astrometry Mission*, vol. 1200, ESA Special Publication (cit. on p. 2).
Fliegner, J., N. Langer and K. A. Venn (1996), *Boron in main sequence B stars: a critical test for rotational mixing.*, A&A **308** L13 (cit. on p. 100).
Frebel, A. and J. E. Norris (2015), *Near-Field Cosmology with Extremely Metal-Poor Stars*, ARA&A **53** 631, arXiv: 1501.06921 [astro-ph.SR] (cit. on pp. 11, 18).
Freiburghaus, C., S. Rosswog and F.-K. Thielemann (1999), *R-Process in Neutron Star Mergers*, ApJ **525** L121 (cit. on p. 8).
Fricke, K. (1968), *Instabilität stationärer Rotation in Sternen*, ZAp **68** 317 (cit. on p. 39).
Fryer, C. L., F. Herwig, A. Hungerford and F. X. Timmes (2006), *Supernova Fallback: A Possible Site for the r-Process*, ApJ **646** L131, eprint: astro-ph/0606450 (cit. on p. 8).
Fuller, J., D. Lecoanet, M. Cantiello and B. Brown (2014), *Angular Momentum Transport via Internal Gravity Waves in Evolving Stars*, ApJ **796** 17, arXiv: 1409.6835 [astro-ph.SR] (cit. on p. 86).
Gallino, R., C. Arlandini, M. Busso, M. Lugaro, C. Travaglio, O. Straniero, A. Chieffi and M. Limongi (1998), *Evolution and Nucleosynthesis in Low-Mass Asymptotic Giant Branch Stars. II. Neutron Capture and the S-Process*, ApJ **497** 388 (cit. on p. 9).

Gallino, R., M. Busso, G. Picchio, C. M. Raiteri and A. Renzini (1988), *On the role of low-mass asymptotic giant branch stars in producing a solar system distribution of s-process isotopes*, ApJ **334** L45 (cit. on p. 9).

Garaud, P. (2014), *Double-Diffusive Convection*, ArXiv e-prints, arXiv: 1401.0928 [astro-ph.EP] (cit. on p. 20).

Geller, A. M. and R. D. Mathieu (2011), *A mass transfer origin for blue stragglers in NGC 188 as revealed by half-solar-mass companions*, Nature **478** 356, arXiv: 1110.3793 [astro-ph.SR] (cit. on p. 122).

Georgy, C., G. Meynet and A. Maeder (2011), *Effects of anisotropic winds on massive star evolution*, A&A **527** A52, arXiv: 1011.6581 [astro-ph.SR] (cit. on p. 38).

Glebbeek, E., O. R. Pols and J. R. Hurley (2008), *Evolution of stellar collision products in open clusters. I. Blue stragglers in N-body models of M 67*, A&A **488** 1007, arXiv: 0806.0863 (cit. on p. 27).

Goldman, S. R., J. T. van Loon, A. A. Zijlstra, J. A. Green, P. R. Wood, A. Nanni, H. Imai, P. A. Whitelock et al. (2017), *The wind speeds, dust content, and mass-loss rates of evolved AGB and RSG stars at varying metallicity*, MNRAS **465** 403, arXiv: 1610.05761 [astro-ph.SR] (cit. on p. 8).

Goldreich, P. and G. Schubert (1967), *Differential Rotation in Stars*, ApJ **150** 571 (cit. on p. 39).

Gonzalez, J.-F., F. LeBlanc, M.-C. Artru and G. Michaud (1995), *Improvements on radiative acceleration calculations in stellar envelopes*, A&A **297** 223 (cit. on p. 56).

Gray, R. O., C. E. McGahee, R. E. Griffin and C. J. Corbally (2011), *First Direct Evidence That Barium Dwarfs Have White Dwarf Companions*, AJ **141** 160 (cit. on p. 17).

Grevesse, N. and A. J. Sauval (1998), *Standard Solar Composition*, Space Sci. Rev. **85** 161 (cit. on p. 10).

Grevesse, N., P. Scott, M. Asplund and A. J. Sauval (2015), *The elemental composition of the Sun. III. The heavy elements Cu to Th*, A&A **573** A27, arXiv: 1405.0288 [astro-ph.SR] (cit. on p. 10).

Gruyters, P., T. Nordlander and A. J. Korn (2014), *Atomic diffusion and mixing in old stars. V. A deeper look into the globular cluster NGC 6752*, A&A **567** A72, arXiv: 1405.6543 [astro-ph.SR] (cit. on p. 72).

Hameury, J.-M. and J.-P. Lasota (2005), *Tidal torques, disc radius variations, and instabilities in dwarf novae and soft X-ray transients*, A&A **443** 283, eprint: astro-ph/0508509 (cit. on p. 116).

Hampel, M., R. J. Stancliffe, M. Lugaro and B. S. Meyer (2016), *The Intermediate Neutron-capture Process and Carbon-enhanced Metal-poor Stars*, ApJ **831** 171, arXiv: 1608.08634 [astro-ph.SR] (cit. on p. 18).

Han, Z., P. P. Eggleton, P. Podsiadlowski and C. A. Tout (1995), *The formation of barium and CH stars and related objects*, MNRAS **277** 1443 (cit. on p. 107).

Hansen, T. T., J. Andersen, B. Nordström, T. C. Beers, V. M. Placco, J. Yoon and L. A. Buchhave (2016a), *The role of binaries in the enrichment of the early Galactic halo. II. Carbon-enhanced metal-poor stars: CEMP-no stars*, A&A **586** A160, arXiv: 1511.08197 [astro-ph.SR] (cit. on p. 18).

– (2016b), *The role of binaries in the enrichment of the early Galactic halo. III. Carbon-enhanced metal-poor stars - CEMP-s stars*, A&A **588** A3, arXiv: 1601.03385 [astro-ph.SR] (cit. on p. 18).

Harris, H. C. and R. D. McClure (1983), *Radial velocities of a random sample of K giant stars and implications concerning multiplicity among giant stars in clusters*, ApJ **265** L77 (cit. on p. 17).

Hartmann, L., N. Calvet, E. Gullbring and P. D'Alessio (1998), *Accretion and the Evolution of T Tauri Disks*, ApJ **495** 385 (cit. on p. 116).

Heger, A., N. Langer and S. E. Woosley (2000), *Presupernova Evolution of Rotating Massive Stars. I. Numerical Method and Evolution of the Internal Stellar Structure*, ApJ **528** 368, eprint: astro-ph/9904132 (cit. on pp. 39, 40, 45, 80, 100).

Heger, A., S. E. Woosley and H. C. Spruit (2005), *Presupernova Evolution of Differentially Rotating Massive Stars Including Magnetic Fields*, ApJ **626** 350, eprint: astro-ph/0409422 (cit. on p. 122).

Henyey, L. G., J. E. Forbes and N. L. Gould (1964), *A New Method of Automatic Computation of Stellar Evolution.*, ApJ **139** 306 (cit. on p. 32).
Henyey, L. G., L. Wilets, K. H. Böhm, R. Lelevier and R. D. Levee (1959), *A Method for Automatic Computation of Stellar Evolution.*, ApJ **129** 628 (cit. on p. 32).
Herwig, F. (2000), *The evolution of AGB stars with convective overshoot*, A&A **360** 952, eprint: astro-ph/0007139 (cit. on p. 9).
– (2005), *Evolution of Asymptotic Giant Branch Stars*, ARA&A **43** 435 (cit. on p. 7).
Herwig, F., N. Langer and M. Lugaro (2003), *The s-Process in Rotating Asymptotic Giant Branch Stars*, ApJ **593** 1056, eprint: astro-ph/0305491 (cit. on p. 9).
Hinshaw, G., D. Larson, E. Komatsu, D. N. Spergel, C. L. Bennett, J. Dunkley, M. R. Nolta, M. Halpern et al. (2013), *Nine-year Wilkinson Microwave Anisotropy Probe (WMAP) Observations: Cosmological Parameter Results*, ApJS **208** 19, arXiv: 1212.5226 (cit. on p. 69).
Hirschi, R. (2007), *Very low-metallicity massive stars:. Pre-SN evolution models and primary nitrogen production*, A&A **461** 571, eprint: astro-ph/0608170 (cit. on p. 18).
Holzwarth, V. and M. Jardine (2007), *Theoretical mass loss rates of cool main-sequence stars*, A&A **463** 11, eprint: astro-ph/0611430 (cit. on p. 74).
Hoyle, F. and R. A. Lyttleton (1939), *The effect of interstellar matter on climatic variation*, Proceedings of the Cambridge Philosophical Society **35** 405 (cit. on p. 14).
Hu, H., E. Glebbeek, A. A. Thoul, M.-A. Dupret, R. J. Stancliffe, G. Nelemans and C. Aerts (2010), *Gravitational settling in pulsating subdwarf B stars and their progenitors*, A&A **511** A87, arXiv: 0912.4665 [astro-ph.SR] (cit. on pp. 71, 122).
Huarte-Espinosa, M., J. Carroll-Nellenback, J. Nordhaus, A. Frank and E. G. Blackman (2013), *The formation and evolution of wind-capture discs in binary systems*, MNRAS **433** 295, arXiv: 1211.1672 [astro-ph.SR] (cit. on pp. 21, 93, 115).
Hubbard, W. B. and M. Lampe (1969), *Thermal Conduction by Electrons in Stellar Matter*, ApJS **18** 297 (cit. on p. 50).
Iben Jr., I. and A. Renzini (1983), *Asymptotic giant branch evolution and beyond*, ARA&A **21** 271 (cit. on p. 7).
Ichikawa, S. and Y. Osaki (1994), *Tidal torques on accretion disks in close binary systems*, PASJ **46** 621 (cit. on p. 116).
Iglesias, C. A. and F. J. Rogers (1996), *Updated Opal Opacities*, ApJ **464** 943 (cit. on pp. 50, 80).
Ivanova, N., S. Justham, X. Chen, O. De Marco, C. L. Fryer, E. Gaburov, H. Ge, E. Glebbeek et al. (2013), *Common envelope evolution: where we stand and how we can move forward*, A&A Rev. **21** 59, arXiv: 1209.4302 [astro-ph.HE] (cit. on p. 14).
Izzard, R. G., T. Dermine and R. P. Church (2010), *White-dwarf kicks and implications for barium stars*, A&A **523** A10, arXiv: 1008.3818 [astro-ph.SR] (cit. on p. 108).
Jeffries, R. D. and B. Smalley (1996), *Excess barium in a K dwarf-white dwarf binary system.*, A&A **315** L19 (cit. on p. 117).
Johnstone, C. P., M. Güdel, I. Brott and T. Lüftinger (2015), *Stellar winds on the main-sequence. II. The evolution of rotation and winds*, A&A **577** A28, arXiv: 1503.07494 [astro-ph.SR] (cit. on p. 74).
Jorissen, A., S. Van Eck, M. Mayor and S. Udry (1998), *Insights into the formation of barium and Tc-poor S stars from an extended sample of orbital elements*, A&A **332** 877, eprint: astro-ph/9801272 (cit. on p. 17).
Jorissen, A., S. Van Eck, H. Van Winckel, T. Merle, H. M. Boffin, J. Andersen, B. Nordström, S. Udry et al. (2016), *Binary properties of CH and carbon-enhanced metal-poor stars*, A&A **586** A158, arXiv: 1510.05840 [astro-ph.SR] (cit. on pp. 17, 18).

Käppeler, F., R. Gallino, S. Bisterzo and W. Aoki (2011), *The s process: Nuclear physics, stellar models, and observations*, Reviews of Modern Physics **83** 157, arXiv: 1012.5218 [astro-ph.SR] (cit. on p. 9).

Karakas, A. I. (2010), *Updated stellar yields from asymptotic giant branch models*, MNRAS **403** 1413, arXiv: 0912.2142 [astro-ph.SR] (cit. on pp. 9, 10, 94, 116).

Karakas, A. I. and J. C. Lattanzio (2014), *The Dawes Review 2: Nucleosynthesis and Stellar Yields of Low- and Intermediate-Mass Single Stars*, PASA **31** e030, arXiv: 1405.0062 [astro-ph.SR] (cit. on p. 7).

Kawaler, S. D. (1987), *Angular momentum in stars - The Kraft curve revisited*, PASP **99** 1322 (cit. on p. 94).

– (1988), *Angular momentum loss in low-mass stars*, ApJ **333** 236 (cit. on pp. 21, 94).

Keenan, P. C. (1942), *The Spectra of CH Stars*, ApJ **96** 101 (cit. on p. 17).

Kellett, B. J., G. E. Bromage, A. Brown, R. D. Jeffries, D. J. James, D. Kilkenny, R. M. Robb, D. Wonnacott et al. (1995), *RE 0044+09: A new K dwarf rapid rotator with a white dwarf companion?*, ApJ **438** 364 (cit. on p. 117).

Kippenhahn, R. (1974), "Circulation and Mixing", *Late Stages of Stellar Evolution*, ed. by R. J. Tayler and J. E. Hesser, vol. 66, IAU Symposium 20 (cit. on pp. 39, 40).

Kippenhahn, R., G. Ruschenplatt and H.-C. Thomas (1980), *The time scale of thermohaline mixing in stars*, A&A **91** 175 (cit. on pp. 19, 20, 45, 55).

Kippenhahn, R. and H.-C. Thomas (1970), "A Simple Method for the Solution of the Stellar Structure Equations Including Rotation and Tidal Forces", *IAU Colloq. 4: Stellar Rotation*, ed. by A. Slettebak 20 (cit. on pp. 34, 35).

Kippenhahn, R., A. Weigert and A. Weiss (2012), *Stellar Structure and Evolution* (cit. on pp. 27, 32).

Kobayashi, C., A. I. Karakas and H. Umeda (2011), *The evolution of isotope ratios in the Milky Way Galaxy*, MNRAS **414** 3231, arXiv: 1102.5312 (cit. on p. 19).

Korn, A. J., F. Grundahl, O. Richard, P. S. Barklem, L. Mashonkina, R. Collet, N. Piskunov and B. Gustafsson (2006), *A probable stellar solution to the cosmological lithium discrepancy*, Nature **442** 657, eprint: astro-ph/0608201 (cit. on p. 72).

Korobkin, O., S. Rosswog, A. Arcones and C. Winteler (2012), *On the astrophysical robustness of the neutron star merger r-process*, MNRAS **426** 1940, arXiv: 1206.2379 [astro-ph.SR] (cit. on p. 9).

Kraft, R. P. (1967), *Studies of Stellar Rotation. V. The Dependence of Rotation on Age among Solar-Type Stars*, ApJ **150** 551 (cit. on pp. 21, 94).

Krtička, J., S. P. Owocki and G. Meynet (2011), *Mass and angular momentum loss via decretion disks*, A&A **527** A84, arXiv: 1101.1732 [astro-ph.SR] (cit. on p. 115).

Kunze, E. (2003), *A review of oceanic salt-fingering theory*, Progress in Oceanography **56** 399 (cit. on p. 19).

Lamb, S. A., W. M. Howard, J. W. Truran and I. Iben Jr. (1977), *Neutron-capture nucleosynthesis in the helium-burning cores of massive stars*, ApJ **217** 213 (cit. on p. 9).

Langer, N. (2012), *Presupernova Evolution of Massive Single and Binary Stars*, ARA&A **50** 107, arXiv: 1206.5443 [astro-ph.SR] (cit. on p. 122).

Lee, Y. S., T. C. Beers, T. Masseron, B. Plez, C. M. Rockosi, J. Sobeck, B. Yanny, S. Lucatello et al. (2013), *Carbon-enhanced Metal-poor Stars in SDSS/SEGUE. I. Carbon Abundance Estimation and Frequency of CEMP Stars*, AJ **146** 132, arXiv: 1310.3276 [astro-ph.SR] (cit. on pp. 18, 67–69, 74, 97, 98, 115).

Lewin, W. H. and M. van der Klis (2006), *Compact Stellar X-ray Sources* (cit. on p. 11).

Lin, D. N. and J. E. Pringle (1976), "Numerical Simulation of Mass Transfer and Accretion Disc Flow in Binary Systems", *Structure and Evolution of Close Binary Systems*, ed. by P. Eggleton, S. Mitton and J. Whelan, vol. 73, IAU Symposium 237 (cit. on p. 116).

Liu, Q. Z., J. van Paradijs and E. P. van den Heuvel (2006), *Catalogue of high-mass X-ray binaries in the Galaxy (4th edition)*, A&A **455** 1165, arXiv: 0707.0549 (cit. on p. 11).

Liu, Z.-W., R. J. Stancliffe, C. Abate and E. Matrozis (2017), *Three-dimensional Hydrodynamical Simulations of Mass Transfer in Binary Systems by a Free Wind*, ApJ **846** 117, arXiv: 1708.03639 [astro-ph.SR] (cit. on pp. 21, 93).

Lodato, G. (2008), *Classical disc physics*, New A Rev. **52** 21 (cit. on p. 116).

Lodders, K. (2003), *Solar System Abundances and Condensation Temperatures of the Elements*, ApJ **591** 1220 (cit. on p. 10).

Lucatello, S., T. C. Beers, N. Christlieb, P. S. Barklem, S. Rossi, B. Marsteller, T. Sivarani and Y. S. Lee (2006), *The Frequency of Carbon-enhanced Metal-poor Stars in the Galaxy from the HERES Sample*, ApJ **652** L37, eprint: astro-ph/0609730 (cit. on p. 115).

Lucatello, S. and R. G. Gratton (2003), *Rotation in Globular Cluster stars. Turn-off and subgiant stars in NGC 104, NGC 6397 and NGC 6752*, A&A **406** 691 (cit. on pp. 21, 93, 117).

Lucatello, S., R. G. Gratton, T. C. Beers and E. Carretta (2005a), *Observational Evidence for a Different Initial Mass Function in the Early Galaxy*, ApJ **625** 833, eprint: astro-ph/0412423 (cit. on pp. 19, 55).

Lucatello, S., S. Tsangarides, T. C. Beers, E. Carretta, R. G. Gratton and S. G. Ryan (2005b), *The Binary Frequency Among Carbon-enhanced, s-Process-rich, Metal-poor Stars*, ApJ **625** 825, eprint: astro-ph/0412422 (cit. on p. 18).

Luck, R. E. and H. E. Bond (1991), *Subgiant CH stars. II - Chemical compositions and the evolutionary connection with barium stars*, ApJS **77** 515 (cit. on pp. 17, 18).

Lugaro, M., A. I. Karakas, R. J. Stancliffe and C. Rijs (2012), *The s-process in Asymptotic Giant Branch Stars of Low Metallicity and the Composition of Carbon-enhanced Metal-poor Stars*, ApJ **747** 2, arXiv: 1112.2757 [astro-ph.SR] (cit. on pp. 33, 56, 69, 70, 116, 120).

MacConnell, D. J., R. L. Frye and A. R. Upgren (1972), *The absolute magnitude of the barium stars.*, AJ **77** 384 (cit. on p. 18).

Maeder, A. (1999), *Stellar evolution with rotation IV: von Zeipel's theorem and anisotropic losses of mass and angular momentum*, A&A **347** 185 (cit. on p. 45).

– (2009), *Physics, Formation and Evolution of Rotating Stars* (cit. on pp. 21, 34, 37, 39, 41).

Maeder, A. and G. Meynet (2000), *The Evolution of Rotating Stars*, ARA&A **38** 143, eprint: astro-ph/0004204 (cit. on p. 122).

– (2005), *Stellar evolution with rotation and magnetic fields. III. The interplay of circulation and dynamo*, A&A **440** 1041, eprint: astro-ph/0506347 (cit. on p. 87).

Maeder, A., G. Meynet and C. Chiappini (2015), *The first stars: CEMP-no stars and signatures of spinstars*, A&A **576** A56, arXiv: 1412.5754 [astro-ph.SR] (cit. on p. 18).

Maeder, A., G. Meynet, N. Lagarde and C. Charbonnel (2013), *The thermohaline, Richardson, Rayleigh-Taylor, Solberg-Høiland, and GSF criteria in rotating stars*, A&A **553** A1, arXiv: 1303.3230 [astro-ph.SR] (cit. on pp. 97, 122).

Maeder, A. and J.-P. Zahn (1998), *Stellar evolution with rotation. III. Meridional circulation with MU -gradients and non-stationarity*, A&A **334** 1000 (cit. on pp. 38, 45).

Maoz, D., F. Mannucci and G. Nelemans (2014), *Observational Clues to the Progenitors of Type Ia Supernovae*, ARA&A **52** 107, arXiv: 1312.0628 (cit. on p. 11).

Marigo, P. (2002), *Asymptotic Giant Branch evolution at varying surface C/O ratio: effects of changes in molecular opacities*, A&A **387** 507, eprint: astro-ph/0203036 (cit. on p. 7).

Marigo, P. and L. Girardi (2007), *Evolution of asymptotic giant branch stars. I. Updated synthetic TP-AGB models and their basic calibration*, A&A **469** 239, eprint: astro-ph/0703139 (cit. on p. 115).

Masseron, T., J. A. Johnson, S. Lucatello, A. Karakas, B. Plez, T. C. Beers and N. Christlieb (2012), *Lithium Abundances in Carbon-enhanced Metal-poor Stars*, ApJ **751** 14, arXiv: 1203.3295 [astro-ph.SR] (cit. on pp. 93, 117).

Masseron, T., J. A. Johnson, B. Plez, S. van Eck, F. Primas, S. Goriely and A. Jorissen (2010), *A holistic approach to carbon-enhanced metal-poor stars*, A&A **509** A93, arXiv: 0901.4737 [astro-ph.SR] (cit. on pp. 17, 18, 92, 98).

Mastrodemos, N. and M. Morris (1998), *Bipolar Preplanetary Nebulae: Hydrodynamics of Dusty Winds in Binary Systems. I. Formation of Accretion Disks*, ApJ **497** 303 (cit. on pp. 21, 115).

Mathis, S., A. Palacios and J.-P. Zahn (2004), *On shear-induced turbulence in rotating stars*, A&A **425** 243, eprint: astro-ph/0403580 (cit. on p. 45).

Matrozis, E., C. Abate and R. J. Stancliffe (2017), *How much mass and angular momentum can the progenitors of carbon-enriched stars accrete?*, A&A **606** A137, arXiv: 1707.08224 [astro-ph.SR] (cit. on pp. 25, 107).

Matrozis, E. and R. J. Stancliffe (2016), *Radiative levitation in carbon-enhanced metal-poor stars with s-process enrichment*, A&A **592** A29, arXiv: 1605.02791 [astro-ph.SR] (cit. on pp. 25, 55).

– (2017), *Rotational mixing in carbon-enhanced metal-poor stars with s-process enrichment*, A&A **606** A55, arXiv: 1707.09434 [astro-ph.SR] (cit. on pp. 25, 79).

Matt, S. and R. E. Pudritz (2005a), *Accretion-powered Stellar Winds as a Solution to the Stellar Angular Momentum Problem*, ApJ **632** L135, eprint: astro-ph/0510060 (cit. on pp. 93, 116).

– (2005b), *The spin of accreting stars: dependence on magnetic coupling to the disc*, MNRAS **356** 167, eprint: astro-ph/0409701 (cit. on pp. 93, 116).

McClure, R. D. (1983), *The binary nature of the barium stars. II - Velocities, binary frequency, and preliminary orbits*, ApJ **268** 264 (cit. on p. 17).

– (1984), *The binary nature of the CH stars*, ApJ **280** L31 (cit. on p. 17).

McClure, R. D., J. M. Fletcher and J. M. Nemec (1980), *The binary nature of the barium stars*, ApJ **238** L35 (cit. on p. 17).

McClure, R. D. and A. W. Woodsworth (1990), *The binary nature of the barium and CH stars. III - Orbital parameters*, ApJ **352** 709 (cit. on pp. 17, 108).

McQuillan, A., T. Mazeh and S. Aigrain (2014), *Rotation Periods of 34,030 Kepler Main-sequence Stars: The Full Autocorrelation Sample*, ApJS **211** 24, arXiv: 1402.5694 [astro-ph.SR] (cit. on p. 97).

Medrano, M., P. Garaud and S. Stellmach (2014), *Double-diffusive mixing in stellar interiors in the presence of horizontal gradients*, ApJ **792** L30, arXiv: 1407.4648 [astro-ph.SR] (cit. on p. 97).

Meibom, S., S. A. Barnes, D. W. Latham, N. Batalha, W. J. Borucki, D. G. Koch, G. Basri, L. M. Walkowicz et al. (2011), *The Kepler Cluster Study: Stellar Rotation in NGC 6811*, ApJ **733** L9, arXiv: 1104.2912 [astro-ph.SR] (cit. on p. 94).

Meibom, S., S. A. Barnes, I. Platais, R. L. Gilliland, D. W. Latham and R. D. Mathieu (2015), *A spin-down clock for cool stars from observations of a 2.5-billion-year-old cluster*, Nature **517** 589, arXiv: 1501.05651 [astro-ph.SR] (cit. on p. 94).

Mendoza, C., M. J. Seaton, P. Buerger, A. Bellorín, M. Meléndez, J. González, L. S. Rodríguez, F. Delahaye et al. (2007), *OPserver: interactive online computations of opacities and radiative accelerations*, MNRAS **378** 1031, arXiv: 0704.1583 (cit. on p. 49).

Merrill, P. W. (1952), *Spectroscopic Observations of Stars of Class*, ApJ **116** 21 (cit. on p. 9).

Mestel, L. (1953), *Rotation and stellar evolution*, MNRAS **113** 716 (cit. on p. 40).

Mestel, L. and H. C. Spruit (1987), *On magnetic braking of late-type stars*, MNRAS **226** 57 (cit. on p. 94).
Meyer, B. S. (1994), *The r-, s-, and p-Processes in Nucleosynthesis*, ARA&A **32** 153 (cit. on p. 8).
Meynet, G., S. Ekström and A. Maeder (2006), *The early star generations: the dominant effect of rotation on the CNO yields*, A&A **447** 623, eprint: astro-ph/0510560 (cit. on pp. 18, 115).
Meynet, G. and A. Maeder (1997), *Stellar evolution with rotation. I. The computational method and the inhibiting effect of the μ-gradient.*, A&A **321** 465 (cit. on pp. 34, 35).
Michaud, G. (1977), *Diffusion time scales and accretion in the sun*, Nature **266** 433 (cit. on p. 62).
Michaud, G., J. Dupuis, G. Fontaine and T. Montmerle (1987), *Selective Mass Loss, Abundance Anomalies, and Helium-rich Stars*, ApJ **322** 302 (cit. on p. 74).
Michaud, G., J. Richer and O. Richard (2010), *Atomic diffusion during red giant evolution*, A&A **510** A104 (cit. on p. 62).
Mikołajewska, J. (2012), *Symbiotic Stars: Observations Confront Theory*, Baltic Astronomy **21** 5, arXiv: 1110.2361 [astro-ph.SR] (cit. on p. 11).
Miller Bertolami, M. M. (2016), *New models for the evolution of post-asymptotic giant branch stars and central stars of planetary nebulae*, A&A **588** A25, arXiv: 1512.04129 [astro-ph.SR] (cit. on p. 7).
Milliman, K. E., R. D. Mathieu and S. C. Schuler (2015), *Barium Surface Abundances of Blue Stragglers in the Open Cluster NGC 6819*, AJ **150** 84, arXiv: 1508.01236 [astro-ph.SR] (cit. on p. 122).
Miszalski, B., H. M. Boffin, D. J. Frew, A. Acker, J. Köppen, A. F. Moffat and Q. A. Parker (2012), *A barium central star binary in the Type I diamond ring planetary nebula Abell 70*, MNRAS **419** 39, arXiv: 1108.3957 [astro-ph.SR] (cit. on p. 117).
Miszalski, B., H. M. Boffin, D. Jones, A. I. Karakas, J. Köppen, A. A. Tyndall, S. S. Mohamed, P. Rodríguez-Gil et al. (2013), *SALT reveals the barium central star of the planetary nebula Hen 2-39*, MNRAS **436** 3068, arXiv: 1309.5239 [astro-ph.SR] (cit. on pp. 107, 116).
Mohamed, S. and P. Podsiadlowski (2007), "Wind Roche-Lobe Overflow: a New Mass-Transfer Mode for Wide Binaries", *15th European Workshop on White Dwarfs*, ed. by R. Napiwotzki and M. R. Burleigh, vol. 372, Astronomical Society of the Pacific Conference Series 397 (cit. on pp. 15, 115).
– (2012), *Mass Transfer in Mira-type Binaries*, Baltic Astronomy **21** 88 (cit. on p. 15).
Mosser, B., M. J. Goupil, K. Belkacem, J. P. Marques, P. G. Beck, S. Bloemen, J. De Ridder, C. Barban et al. (2012), *Spin down of the core rotation in red giants*, A&A **548** A10, arXiv: 1209.3336 [astro-ph.SR] (cit. on p. 86).
Muchmore, D. (1984), *Diffusion in white dwarf stars*, ApJ **278** 769 (cit. on p. 23).
Nomoto, K., C. Kobayashi and N. Tominaga (2013), *Nucleosynthesis in Stars and the Chemical Enrichment of Galaxies*, ARA&A **51** 457 (cit. on pp. 9, 18).
Nordlander, T., A. J. Korn, O. Richard and K. Lind (2012), *Atomic Diffusion and Mixing in Old Stars. III. Analysis of NGC 6397 Stars under New Constraints*, ApJ **753** 48, arXiv: 1204.5600 [astro-ph.SR] (cit. on p. 72).
Norris, J. E., D. Yong, M. S. Bessell, N. Christlieb, M. Asplund, G. Gilmore, R. F. Wyse, T. C. Beers et al. (2013), *The Most Metal-poor Stars. IV. The Two Populations with [Fe/H] < −3.0*, ApJ **762** 28, arXiv: 1211.3157 (cit. on p. 18).
North, P., S. Berthet and T. Lanz (1994), *The nature of the F STR lambda 4077 stars. 3: Spectroscopy of the barium dwarfs and other CP stars*, A&A **281** 775 (cit. on p. 17).
North, P. and A. Duquennoy (1991), *The nature of the F STR 4077-A stars. II - Frequency, kinematics, metallicity, binarity and rotational velocities*, A&A **244** 335 (cit. on p. 115).
North, P., A. Jorissen and M. Mayor (2000), "Binarity among Barium Dwarfs and CH Subgiants: Will They Become Barium Giants?", *The Carbon Star Phenomenon*, ed. by R. F. Wing, vol. 177, IAU Symposium 269 (cit. on p. 17).

North, P. and T. Lanz (1991), *The nature of the F STR 4077-A stars. IV - Search for white dwarfs around barium dwarfs*, A&A **251** 489 (cit. on p. 17).

Noyes, R. W., L. W. Hartmann, S. L. Baliunas, D. K. Duncan and A. H. Vaughan (1984), *Rotation, convection, and magnetic activity in lower main-sequence stars*, ApJ **279** 763 (cit. on p. 94).

Packet, W. (1981), *On the spin-up of the mass accreting component in a close binary system*, A&A **102** 17 (cit. on pp. 21, 107, 108, 110, 111, 118).

Paczyński, B. (1965), *Cataclysmic Variables among Binary Stars I. U Geminorum Stars*, Acta Astron. **15** 89 (cit. on p. 14).

Paczynski, B. and S. D. Tremaine (1977), *Core helium flash and the origin of CH and carbon stars*, ApJ **216** 57 (cit. on p. 17).

Papaloizou, J. and J. E. Pringle (1977), *Tidal torques on accretion discs in close binary systems*, MNRAS **181** 441 (cit. on p. 116).

Paquette, C., C. Pelletier, G. Fontaine and G. Michaud (1986), *Diffusion coefficients for stellar plasmas*, ApJS **61** 177 (cit. on pp. 45, 46, 62).

Paxton, B., L. Bildsten, A. Dotter, F. Herwig, P. Lesaffre and F. Timmes (2011), *Modules for Experiments in Stellar Astrophysics (MESA)*, ApJS **192** 3, arXiv: 1009.1622 [astro-ph.SR] (cit. on p. 71).

Paxton, B., M. Cantiello, P. Arras, L. Bildsten, E. F. Brown, A. Dotter, C. Mankovich, M. H. Montgomery et al. (2013), *Modules for Experiments in Stellar Astrophysics (MESA): Planets, Oscillations, Rotation, and Massive Stars*, ApJS **208** 4, arXiv: 1301.0319 [astro-ph.SR] (cit. on p. 39).

Paxton, B., P. Marchant, J. Schwab, E. B. Bauer, L. Bildsten, M. Cantiello, L. Dessart, R. Farmer et al. (2015), *Modules for Experiments in Stellar Astrophysics (MESA): Binaries, Pulsations, and Explosions*, ApJS **220** 15, arXiv: 1506.03146 [astro-ph.SR] (cit. on p. 71).

Pelletier, C., G. Fontaine, F. Wesemael, G. Michaud and G. Wegner (1986), *Carbon pollution in helium-rich white dwarf atmospheres Time-dependent calculations of the dredge-up process*, ApJ **307** 242 (cit. on p. 45).

Perets, H. B. and S. J. Kenyon (2013), *Wind-accretion Disks in Wide Binaries, Second-generation Protoplanetary Disks, and Accretion onto White Dwarfs*, ApJ **764** 169, arXiv: 1203.2918 [astro-ph.SR] (cit. on p. 115).

Piersanti, L., S. Cristallo and O. Straniero (2013), *The Effects of Rotation on s-process Nucleosynthesis in Asymptotic Giant Branch Stars*, ApJ **774** 98, arXiv: 1307.2017 [astro-ph.SR] (cit. on p. 9).

Pinsonneault, M. H., C. P. Deliyannis and P. Demarque (1991), *Evolutionary models of halo stars with rotation. I - Evidence for differential rotation with depth in stars*, ApJ **367** 239 (cit. on p. 94).

Pinsonneault, M. H., S. D. Kawaler, S. Sofia and P. Demarque (1989), *Evolutionary models of the rotating sun*, ApJ **338** 424 (cit. on pp. 39, 40, 45, 100).

Placco, V. M., A. Frebel, T. C. Beers and R. J. Stancliffe (2014), *Carbon-enhanced Metal-poor Star Frequencies in the Galaxy: Corrections for the Effect of Evolutionary Status on Carbon Abundances*, ApJ **797** 21, arXiv: 1410.2223 [astro-ph.SR] (cit. on pp. 18, 115).

Podsiadlowski, P. and S. Mohamed (2007), *The Origin and Evolution of Symbiotic Binaries*, Baltic Astronomy **16** 26 (cit. on p. 15).

Podsiadlowski, P., S. Rappaport and E. D. Pfahl (2002), *Evolutionary Sequences for Low- and Intermediate-Mass X-Ray Binaries*, ApJ **565** 1107, eprint: astro-ph/0107261 (cit. on p. 11).

Pols, O. R., A. I. Karakas, J. C. Lattanzio and C. A. Tout (2003), "Can Standard Evolution Models Explain the Properties of Barium Stars?", *Symbiotic Stars Probing Stellar Evolution*, ed. by R. L. Corradi, J. Mikolajewska and T. J. Mahoney, vol. 303, Astronomical Society of the Pacific Conference Series 290 (cit. on pp. 107, 108).

Pols, O. R., K.-P. Schröder, J. R. Hurley, C. A. Tout and P. P. Eggleton (1998), *Stellar evolution models for Z = 0.0001 to 0.03*, MNRAS **298** 525 (cit. on p. 120).

Pols, O. R., C. A. Tout, P. P. Eggleton and Z. Han (1995), *Approximate input physics for stellar modelling*, MNRAS **274** 964, eprint: astro-ph/9504025 (cit. on p. 27).

Popham, R. and R. Narayan (1991), *Does accretion cease when a star approaches breakup?*, ApJ **370** 604 (cit. on p. 116).

Potter, A. T. (2012), *Rotation and magnetism in massive stars*, PhD thesis: University of Cambridge (cit. on p. 41).

Potter, A. T., C. A. Tout and I. Brott (2012a), *Towards a unified model of stellar rotation - II. Model-dependent characteristics of stellar populations*, MNRAS **423** 1221, arXiv: 1204.1973 [astro-ph.SR] (cit. on p. 40).

Potter, A. T., C. A. Tout and J. J. Eldridge (2012b), *Towards a unified model of stellar rotation*, MNRAS **419** 748, arXiv: 1109.0993 [astro-ph.SR] (cit. on pp. 27, 38, 40, 41).

Pringle, J. E. (1981), *Accretion discs in astrophysics*, ARA&A **19** 137 (cit. on p. 116).

Proffitt, C. R. and G. Michaud (1991), *Diffusion and mixing of lithium and helium in population II dwarfs*, ApJ **371** 584 (cit. on p. 45).

Raghavan, D., H. A. McAlister, T. J. Henry, D. W. Latham, G. W. Marcy, B. D. Mason, D. R. Gies, R. J. White et al. (2010), *A Survey of Stellar Families: Multiplicity of Solar-type Stars*, ApJS **190** 1, arXiv: 1007.0414 [astro-ph.SR] (cit. on p. 11).

Raiteri, C. M., R. Gallino, M. Busso, D. Neuberger and F. Kaeppeler (1993), *The Weak s-Component and Nucleosynthesis in Massive Stars*, ApJ **419** 207 (cit. on p. 9).

Ramstedt, S. and H. Olofsson (2014), *The $^{12}CO/^{13}CO$ ratio in AGB stars of different chemical type. Connection to the $^{12}C/^{13}C$ ratio and the evolution along the AGB*, A&A **566** A145, arXiv: 1405.6404 [astro-ph.SR] (cit. on pp. 7, 34, 108, 115).

Reimers, D. (1975), *Circumstellar absorption lines and mass loss from red giants*, Memoires of the Societe Royale des Sciences de Liege **8** 369 (cit. on p. 72).

Richard, O., G. Michaud and J. Richer (2002a), *Models of Metal-poor Stars with Gravitational Settling and Radiative Accelerations. III. Metallicity Dependence*, ApJ **580** 1100, eprint: astro-ph/0112113 (cit. on p. 55).

– (2005), *Implications of WMAP Observations on Li Abundance and Stellar Evolution Models*, ApJ **619** 538, eprint: astro-ph/0409672 (cit. on pp. 71, 72).

Richard, O., G. Michaud, J. Richer, S. Turcotte, S. Turck-Chièze and D. A. VandenBerg (2002b), *Models of Metal-poor Stars with Gravitational Settling and Radiative Accelerations. I. Evolution and Abundance Anomalies*, ApJ **568** 979 (cit. on pp. 55, 61, 70).

Richard, O., S. Vauclair, C. Charbonnel and W. A. Dziembowski (1996), *New solar models including helioseismological constraints and light-element depletion.*, A&A **312** 1000, eprint: astro-ph/9601136 (cit. on p. 23).

Richardson, L. F. (1911), *The Approximate Arithmetical Solution by Finite Differences of Physical Problems Involving Differential Equations, with an Application to the Stresses in a Masonry Dam*, Philosophical Transactions of the Royal Society of London A: Mathematical, Physical and Engineering Sciences **210** 307 (cit. on p. 41).

Richer, J., G. Michaud and S. Turcotte (2000), *The Evolution of AMFM Stars, Abundance Anomalies, and Turbulent Transport*, ApJ **529** 338 (cit. on pp. 24, 71, 122).

Ricker, P. M. and R. E. Taam (2008), *The Interaction of Stellar Objects within a Common Envelope*, ApJ **672** L41, arXiv: 0710.3631 (cit. on p. 14).

Ritossa, C., E. García-Berro and I. Iben Jr. (1999), *On the Evolution of Stars that Form Electron-degenerate Cores Processed by Carbon Burning. V. Shell Convection Sustained by Helium Burning, Transient Neon Burning, Dredge-out, Urca Cooling, and Other Properties of an 11 M_{solar} Population I Model Star*, ApJ **515** 381 (cit. on p. 7).

Roederer, I. U., J. J. Cowan, A. I. Karakas, K.-L. Kratz, M. Lugaro, J. Simmerer, K. Farouqi and C. Sneden (2010), *The Ubiquity of the Rapid Neutron-capture Process*, ApJ **724** 975, arXiv: 1009.4496 [astro-ph.SR] (cit. on p. 19).

Romberg, W. (1955), *Vereinfachte numerische Integration*, Det Kong. Norske Videnskabers Selskab Forhandlinger **28** 30 (cit. on p. 41).

Sackmann, I. J. (1970), *Rapid Uniform Rotation Along the Main Sequence II*, A&A **8** 76 (cit. on p. 81).

Salaris, M., A. Serenelli, A. Weiss and M. Miller Bertolami (2009), *Semi-empirical White Dwarf Initial-Final Mass Relationships: A Thorough Analysis of Systematic Uncertainties Due to Stellar Evolution Models*, ApJ **692** 1013, arXiv: 0807.3567 (cit. on p. 7).

Scalo, J. M. (1976), *A composite Hertzsprung-Russell diagram for the peculiar red giants*, ApJ **206** 474 (cit. on p. 17).

Scalo, J. M. and G. E. Miller (1979), *Constraints on the evolution of peculiar red giants. II - Masses and space densities*, ApJ **233** 596 (cit. on p. 18).

Schatzman, E. (1977), *Turbulent transport and lithium destruction in main sequence stars*, A&A **56** 211 (cit. on p. 39).

Schrijver, C. J. (1993), *Magnetic activity in dwarf stars with shallow convective envelopes*, A&A **269** 446 (cit. on p. 94).

Schwarzenberg-Czerny, A. and M. Rozyczka (1988), *On tidal effects in accretion disks*, Acta Astron. **38** 189 (cit. on p. 116).

Schwarzschild, M. and R. Härm (1965), *Thermal Instability in Non-Degenerate Stars.*, ApJ **142** 855 (cit. on p. 4).

Scott, P., M. Asplund, N. Grevesse, M. Bergemann and A. J. Sauval (2015a), *The elemental composition of the Sun. II. The iron group elements Sc to Ni*, A&A **573** A26, arXiv: 1405.0287 [astro-ph.SR] (cit. on p. 10).

Scott, P., N. Grevesse, M. Asplund, A. J. Sauval, K. Lind, Y. Takeda, R. Collet, R. Trampedach et al. (2015b), *The elemental composition of the Sun. I. The intermediate mass elements Na to Ca*, A&A **573** A25, arXiv: 1405.0279 [astro-ph.SR] (cit. on p. 10).

Seaton, M. J. (1997), *Radiative accelerations in stellar envelopes*, MNRAS **289** 700 (cit. on pp. 47–49, 56).

– (2007), *Updated Opacity Project radiative accelerations*, MNRAS **382** 245 (cit. on pp. 48, 56).

Seeger, P. A., W. A. Fowler and D. D. Clayton (1965), *Nucleosynthesis of Heavy Elements by Neutron Capture.*, ApJS **11** 121 (cit. on p. 8).

Sivarani, T., P. Bonifacio, P. Molaro, R. Cayrel, M. Spite, F. Spite, B. Plez, J. Andersen et al. (2004), *First stars IV. CS 29497-030: Evidence for operation of the s-process at very low metallicity*, A&A **413** 1073, eprint: astro-ph/0310291 (cit. on p. 19).

Skumanich, A. (1972), *Time Scales for CA II Emission Decay, Rotational Braking, and Lithium Depletion*, ApJ **171** 565 (cit. on p. 94).

Smith, J. A. and P. Demarque (1980), *CH subgiants and the mixing hypothesis*, A&A **92** 163 (cit. on p. 17).

Smith, V. V., H. Coleman and D. L. Lambert (1993), *Abundances in CH Subgiants: Evidence of Mass Transfer onto Main-Sequence Companions*, ApJ **417** 287 (cit. on p. 17).

Soker, N. and S. Rappaport (2000), *The Formation of Very Narrow Waist Bipolar Planetary Nebulae*, ApJ **538** 241, eprint: astro-ph/9911140 (cit. on p. 115).

Spite, M., E. Caffau, P. Bonifacio, F. Spite, H.-G. Ludwig, B. Plez and N. Christlieb (2013), *Carbon-enhanced metal-poor stars: the most pristine objects?*, A&A **552** A107, arXiv: 1303.1791 (cit. on p. 18).

Spruit, H. C. (2002), *Dynamo action by differential rotation in a stably stratified stellar interior*, A&A **381** 923, eprint: astro-ph/0108207 (cit. on pp. 86, 122).

Stancliffe, R. J. (2009), *Light element abundances in carbon-enhanced metal-poor stars*, MNRAS **394** 1051, arXiv: 0812.3187 (cit. on pp. 55, 122).

Stancliffe, R. J., R. P. Church, G. C. Angelou and J. C. Lattanzio (2009), *The depletion of carbon by extra mixing in metal-poor giants*, MNRAS **396** 2313, arXiv: 0904.2393 [astro-ph.SR] (cit. on pp. 62, 90, 122).

Stancliffe, R. J. and J. J. Eldridge (2009), *Modelling the binary progenitor of Supernova 1993J*, MNRAS **396** 1699, arXiv: 0904.0282 [astro-ph.SR] (cit. on p. 27).

Stancliffe, R. J., L. Fossati, J.-C. Passy and F. R. Schneider (2016), *Confronting uncertainties in stellar physics. II. Exploring differences in main-sequence stellar evolution tracks*, A&A **586** A119, arXiv: 1601.03054 [astro-ph.SR] (cit. on p. 30).

Stancliffe, R. J. and E. Glebbeek (2008), *Thermohaline mixing and gravitational settling in carbon-enhanced metal-poor stars*, MNRAS **389** 1828, arXiv: 0807.1758 (cit. on pp. 9, 24, 34, 45, 46, 55, 57, 66, 69, 94, 99, 121).

Stancliffe, R. J., E. Glebbeek, R. G. Izzard and O. R. Pols (2007), *Carbon-enhanced metal-poor stars and thermohaline mixing*, A&A **464** L57 (cit. on pp. 20, 33, 55, 62, 69, 90, 92, 97, 99, 121, 122).

Stancliffe, R. J., C. R. Kennedy, H. H. Lau and T. C. Beers (2013), *Modelling the nucleosynthetic properties of carbon-enhanced metal-poor RR Lyrae stars*, MNRAS **435** 698, arXiv: 1307.4762 [astro-ph.SR] (cit. on p. 64).

Stancliffe, R. J., C. A. Tout and O. R. Pols (2004), *Deep dredge-up in intermediate-mass thermally pulsing asymptotic giant branch stars*, MNRAS **352** 984, eprint: astro-ph/0405150 (cit. on pp. 4, 7).

Starkenburg, E., M. D. Shetrone, A. W. McConnachie and K. A. Venn (2014), *Binarity in carbon-enhanced metal-poor stars*, MNRAS **441** 1217, arXiv: 1404.0385 [astro-ph.SR] (cit. on p. 18).

Stern, M. E. (1960), *The salt-fountain and thermohaline convection*, Tellus **12** 172 (cit. on p. 19).

Straniero, O., A. Chieffi, M. Limongi, M. Busso, R. Gallino and C. Arlandini (1997), *Evolution and Nucleosynthesis in Low-Mass Asymptotic Giant Branch Stars. I. Formation of Population I Carbon Stars*, ApJ **478** 332 (cit. on p. 7).

Straniero, O., S. Cristallo and R. Gallino (2009), *The ^{13}C Pocket in Low-Mass AGB Stars*, PASA **26** 133, arXiv: 0904.4163 [astro-ph.SR] (cit. on p. 10).

Suda, T., J. Hidaka, W. Aoki, Y. Katsuta, S. Yamada, M. Y. Fujimoto, Y. Ohtani, M. Masuyama et al. (2017), *Stellar Abundances for Galactic Archaeology IV - Compilation of Stars in Dwarf Spheroidal Galaxies*, ArXiv e-prints, arXiv: 1703.10009 (cit. on p. 100).

Suda, T., Y. Katsuta, S. Yamada, T. Suwa, C. Ishizuka, Y. Komiya, K. Sorai, M. Aikawa et al. (2008), *Stellar Abundances for the Galactic Archeology (SAGA) Database — Compilation of the Characteristics of Known Extremely Metal-Poor Stars*, PASJ **60** 1159, arXiv: 0806.3697 (cit. on pp. 18, 67, 100).

Suda, T., S. Yamada, Y. Katsuta, Y. Komiya, C. Ishizuka, W. Aoki and M. Y. Fujimoto (2011), *The Stellar Abundances for Galactic Archaeology (SAGA) data base - II. Implications for mixing and nucleosynthesis in extremely metal-poor stars and chemical enrichment of the Galaxy*, MNRAS **412** 843, arXiv: 1010.6272 (cit. on pp. 18, 67, 100).

Suijs, M. P., N. Langer, A.-J. Poelarends, S.-C. Yoon, A. Heger and F. Herwig (2008), *White dwarf spins from low-mass stellar evolution models*, A&A **481** L87, arXiv: 0802.3286 (cit. on p. 86).

Suzuki, T. K. (2007), *Structured Red Giant Winds with Magnetized Hot Bubbles and the Corona/Cool Wind Dividing Line*, ApJ **659** 1592, eprint: astro-ph/0608195 (cit. on p. 74).

Sweet, P. A. (1950), *The importance of rotation in stellar evolution*, MNRAS **110** 548 (cit. on p. 22).

Swenson, F. J. (1995), *Lithium in halo dwarfs: The undoing of diffusion by mass loss*, ApJ **438** L87 (cit. on p. 72).

Takahashi, K., J. Witti and H.-T. Janka (1994), *Nucleosynthesis in neutrino-driven winds from protoneutron stars II. The r-process*, A&A **286** 857 (cit. on p. 8).

Talon, S. (2008), "Transport Processes in Stars: Diffusion, Rotation, Magnetic fields and Internal Waves", *EAS Publications Series*, ed. by C. Charbonnel and J.-P. Zahn, vol. 32, EAS Publications Series 81, arXiv: 0708.1499 (cit. on p. 46).

Talon, S. and C. Charbonnel (2003), *Angular momentum transport by internal gravity waves. I - Pop I main sequence stars*, A&A **405** 1025, eprint: astro-ph/0305151 (cit. on p. 86).

– (2004), *Angular momentum transport by internal gravity waves. II. Pop II stars from the Li plateau to the horizontal branch*, A&A **418** 1051, eprint: astro-ph/0401474 (cit. on p. 122).

– (2005), *Hydrodynamical stellar models including rotation, internal gravity waves, and atomic diffusion. I. Formalism and tests on Pop I dwarfs*, A&A **440** 981, eprint: astro-ph/0505229 (cit. on pp. 87, 122).

– (2008), *Angular momentum transport by internal gravity waves. IV. Wave generation by surface convection zone, from the pre-main sequence to the early-AGB in intermediate mass stars*, A&A **482** 597, arXiv: 0801.4643 (cit. on p. 86).

Theuns, T., H. M. Boffin and A. Jorissen (1996), *Wind accretion in binary stars - II. Accretion rates*, MNRAS **280** 1264, eprint: astro-ph/9602089 (cit. on pp. 21, 93, 115).

Thompson, I. B., I. I. Ivans, S. Bisterzo, C. Sneden, R. Gallino, S. Vauclair, G. S. Burley, S. A. Shectman et al. (2008), *CS 22964-161: A Double-lined Carbon- and s-Process-enhanced Metal-poor Binary Star*, ApJ **677** 556, arXiv: 0712.3228 (cit. on pp. 24, 55, 66).

Thoul, A. A., J. N. Bahcall and A. Loeb (1994), *Element diffusion in the solar interior*, ApJ **421** 828, eprint: astro-ph/9304005 (cit. on p. 71).

Trampedach, R., R. F. Stein, J. Christensen-Dalsgaard, Å. Nordlund and M. Asplund (2014), *Improvements to stellar structure models, based on a grid of 3D convection simulations - II. Calibrating the mixing-length formulation*, MNRAS **445** 4366, arXiv: 1410.1559 [astro-ph.SR] (cit. on p. 71).

Travaglio, C., D. Galli, R. Gallino, M. Busso, F. Ferrini and O. Straniero (1999), *Galactic Chemical Evolution of Heavy Elements: From Barium to Europium*, ApJ **521** 691, eprint: astro-ph/9903451 (cit. on pp. 9, 19).

Travaglio, C., R. Gallino, E. Arnone, J. Cowan, F. Jordan and C. Sneden (2004), *Galactic Evolution of Sr, Y, And Zr: A Multiplicity of Nucleosynthetic Processes*, ApJ **601** 864, eprint: astro-ph/0310189 (cit. on p. 9).

Travaglio, C., R. Gallino, M. Busso and R. Gratton (2001), *Lead: Asymptotic Giant Branch Production and Galactic Chemical Evolution*, ApJ **549** 346, eprint: astro-ph/0011050 (cit. on p. 19).

Traxler, A., P. Garaud and S. Stellmach (2011), *Numerically Determined Transport Laws for Fingering ("Thermohaline") Convection in Astrophysics*, ApJ **728** L29, arXiv: 1011.3461 [astro-ph.SR] (cit. on p. 20).

Turcotte, S., J. Richer and G. Michaud (1998), *Consistent Evolution of F Stars: Diffusion, Radiative Accelerations, and Abundance Anomalies*, ApJ **504** 559 (cit. on p. 24).

Ulrich, R. K. (1972), *Thermohaline Convection in Stellar Interiors.*, ApJ **172** 165 (cit. on pp. 19, 20, 55).

Umeda, H. and K. Nomoto (2003), *First-generation black-hole-forming supernovae and the metal abundance pattern of a very iron-poor star*, Nature **422** 871, eprint: astro-ph/0301315 (cit. on p. 18).

Valenti, J. A. and D. A. Fischer (2005), *Spectroscopic Properties of Cool Stars (SPOCS). I. 1040 F, G, and K Dwarfs from Keck, Lick, and AAT Planet Search Programs*, ApJS **159** 141 (cit. on p. 97).

van Loon, J. T., M.-R. L. Cioni, A. A. Zijlstra and C. Loup (2005), *An empirical formula for the mass-loss rates of dust-enshrouded red supergiants and oxygen-rich Asymptotic Giant Branch stars*, A&A **438** 273, eprint: astro-ph/0504379 (cit. on pp. 7, 108, 115).
van Winckel, H. (2003), *Post-AGB Stars*, ARA&A **41** 391 (cit. on p. 7).
VandenBerg, D. A., O. Richard, G. Michaud and J. Richer (2002), *Models of Metal-poor Stars with Gravitational Settling and Radiative Accelerations. II. The Age of the Oldest Stars*, ApJ **571** 487 (cit. on pp. 23, 64, 88).
Vanture, A. D. (1992), *The CH Stars. III. Heavy Element Abundances*, AJ **104** 1997 (cit. on p. 17).
Vassiliadis, E. and P. R. Wood (1993), *Evolution of low- and intermediate-mass stars to the end of the asymptotic giant branch with mass loss*, ApJ **413** 641 (cit. on pp. 7, 8, 34, 108, 115).
Vauclair, S. and S. Théado (2012), *Thermohaline Instabilities inside Stars: A Synthetic Study Including External Turbulence and Radiative Levitation*, ApJ **753** 49, arXiv: 1205.1329 [astro-ph.SR] (cit. on p. 97).
Venn, K. A., A. M. Brooks, D. L. Lambert, M. Lemke, N. Langer, D. J. Lennon and F. P. Keenan (2002), *Boron Abundances in B-Type Stars: A Test of Rotational Depletion during Main-Sequence Evolution*, ApJ **565** 571, eprint: astro-ph/0108263 (cit. on p. 100).
Vennes, S., D. J. Christian and J. R. Thorstensen (1998), *Hot White Dwarfs in the Extreme-Ultraviolet Explorer Survey. IV. DA White Dwarfs with Bright Companions*, ApJ **502** 763 (cit. on p. 117).
Vick, M., G. Michaud, J. Richer and O. Richard (2010), *AmFm and lithium gap stars. Stellar evolution models with mass loss*, A&A **521** A62, arXiv: 1006.5711 [astro-ph.SR] (cit. on p. 74).
Vogt, H. (1925), *Zum Strahlungsgleichgewicht der Sterne*, Astronomische Nachrichten **223** 229 (cit. on p. 22).
von Zeipel, H. (1924), *The radiative equilibrium of a rotating system of gaseous masses*, MNRAS **84** 665 (cit. on p. 22).
Wachter, A., K.-P. Schröder, J. M. Winters, T. U. Arndt and E. Sedlmayr (2002), *An improved mass-loss description for dust-driven superwinds and tip-AGB evolution models*, A&A **384** 452 (cit. on p. 7).
Wang, Y.-M. (1998), "Cyclic Magnetic Variations of the Sun", *Cool Stars, Stellar Systems, and the Sun*, ed. by R. A. Donahue and J. A. Bookbinder, vol. 154, Astronomical Society of the Pacific Conference Series 131 (cit. on p. 72).
Warner, B. (1965), *The barium stars*, MNRAS **129** 263 (cit. on p. 17).
– (2003), *Cataclysmic Variable Stars* 592 (cit. on p. 11).
Wasiutynski, J. (1946), *Studies in Hydrodynamics and Structure of Stars and Planets*, Astrophysica Norvegica **4** 1 (cit. on p. 39).
Weber, E. J. and L. Davis Jr. (1967), *The Angular Momentum of the Solar Wind*, ApJ **148** 217 (cit. on p. 94).
Wehmeyer, B., M. Pignatari and F.-K. Thielemann (2015), *Galactic evolution of rapid neutron capture process abundances: the inhomogeneous approach*, MNRAS **452** 1970, arXiv: 1501.07749 (cit. on p. 8).
Weiss, A. and J. W. Ferguson (2009), *New asymptotic giant branch models for a range of metallicities*, A&A **508** 1343, arXiv: 0903.2155 [astro-ph.SR] (cit. on p. 7).
Willson, L. A. (2000), *Mass Loss From Cool Stars: Impact on the Evolution of Stars and Stellar Populations*, ARA&A **38** 573 (cit. on p. 7).
Winteler, C., R. Käppeli, A. Perego, A. Arcones, N. Vasset, N. Nishimura, M. Liebendörfer and F.-K. Thielemann (2012), *Magnetorotationally Driven Supernovae as the Origin of Early Galaxy r-process Elements?*, ApJ **750** L22, arXiv: 1203.0616 [astro-ph.SR] (cit. on p. 8).
Wood, B. E., H.-R. Müller, G. P. Zank and J. L. Linsky (2002), *Measured Mass-Loss Rates of Solar-like Stars as a Function of Age and Activity*, ApJ **574** 412, eprint: astro-ph/0203437 (cit. on p. 74).

Wood, B. E., H.-R. Müller, G. P. Zank, J. L. Linsky and S. Redfield (2005), *New Mass-Loss Measurements from Astrospheric Lyα Absorption*, ApJ **628** L143, eprint: astro-ph/0506401 (cit. on p. 74).

Woosley, S. E., J. R. Wilson, G. J. Mathews, R. D. Hoffman and B. S. Meyer (1994), *The r-process and neutrino-heated supernova ejecta*, ApJ **433** 229 (cit. on p. 8).

Yanny, B., C. Rockosi, H. J. Newberg, G. R. Knapp, J. K. Adelman-McCarthy, B. Alcorn, S. Allam, C. Allende Prieto et al. (2009), *SEGUE: A Spectroscopic Survey of 240,000 Stars with g = 14-20*, AJ **137** 4377, arXiv: 0902.1781 [astro-ph.GA] (cit. on p. 67).

Yong, D., J. E. Norris, M. S. Bessell, N. Christlieb, M. Asplund, T. C. Beers, P. S. Barklem, A. Frebel et al. (2013), *The Most Metal-poor Stars. III. The Metallicity Distribution Function and Carbon-enhanced Metal-poor Fraction*, ApJ **762** 27, arXiv: 1208.3016 (cit. on p. 18).

Yoon, S.-C. and N. Langer (2004), *Presupernova evolution of accreting white dwarfs with rotation*, A&A **419** 623, eprint: astro-ph/0402287 (cit. on p. 39).

Yoon, S.-C., N. Langer and C. Norman (2006), *Single star progenitors of long gamma-ray bursts. I. Model grids and redshift dependent GRB rate*, A&A **460** 199, eprint: astro-ph/0606637 (cit. on p. 100).

Yoon, S.-C., N. Langer and M. van der Sluys (2004), *On the stability of thermonuclear shell sources in stars*, A&A **425** 207, eprint: astro-ph/0406164 (cit. on p. 4).

York, D. G., J. Adelman, J. E. Anderson Jr., S. F. Anderson, J. Annis, N. A. Bahcall, J. A. Bakken, R. Barkhouser et al. (2000), *The Sloan Digital Sky Survey: Technical Summary*, AJ **120** 1579, eprint: astro-ph/0006396 (cit. on p. 67).

Zahn, J.-P. (1977), *Tidal friction in close binary stars*, A&A **57** 383 (cit. on p. 116).

– (1992), *Circulation and turbulence in rotating stars*, A&A **265** 115 (cit. on pp. 34, 38, 41, 45, 97).

Zemskova, V., P. Garaud, M. Deal and S. Vauclair (2014), *Fingering Convection Induced by Atomic Diffusion in Stars: 3D Numerical Computations and Applications to Stellar Models*, ApJ **795** 118, arXiv: 1407.1437 [astro-ph.SR] (cit. on p. 20).

List of Figures

List of Tables